

CERN/LHCC 2002–016
Addendum
to ALICE TDR 8
24 April 2002

A L I C E

Addendum

to the

Technical Design Report

of the

Time of Flight System (TOF)

Cover design by Fabienne Marcastel

Printed at CERN
April 2002

ISBN 92-9083-192-8

ALICE Collaboration

Alessandria, Italy, Facoltà di Scienze dell’Università:
P. Cortese, G. Dellacasa, L. Ramello, E. Scalas and M. Sitta.

Aligarh, India, Physics Department, Aligarh Muslim University:
N. Ahmad, S. Ahmad, T. Ahmad, W. Bari, M. Irfan,. and M. Zafar.

Bari, Italy, Dipartimento di Fisica dell’Università and Sezione INFN:
R. Caliandro, M. Caselle, D. Cozza, G. De Cataldo, D. Di Bari, D. Elia, R.A. Fini, B. Ghidini, V. Lenti,
V. Manzari, E. Nappi, F. Navach and F. Posa.

Bari, Italy, Politecnico and Sezione INFN:
M. Castellano, F. Corsi, D. De Venuto and C. Marzocca.

Beijing, China, China Institute of Atomic Energy:
X. Li, S. Lu, Z. Lu, B. Sa, J. Yuan, J. Zhou, S. Zhou and X. Zhu.

Bergen, Norway, Bergen University College, Faculty of Engineering:
H. Helstrup and J.A. Lien.

Bergen, Norway, University of Bergen, Institute of Physics:
K. Fanebust, A. Klovning, O.A. Mæland, O.H. Odland, D. Röhrich, R. Rongved, K. Ullaland and
A.S. Vestbø.

Bhubaneswar, India, Institute of Physics:
R.K. Choudhury, A.K. Dubey, D.P. Mahapatra, D.K. Mishra, B. Mohanty, S.C. Phatak and R. Sahoo.

Birmingham, United Kingdom, School of Physics and Space Research, University of Birmingham:
I.J. Bloodworth, D. Evans, G.T. Jones, P. Jovanović, J.B. Kinson, R. Lietava, P.I. Norman and
O. Villalobos Baillie.

Bologna, Italy, Dipartimento di Fisica dell’Università and Sezione INFN:
A. Alici, F. Anselmo, P. Antonioli, G. Bari, M. Basile, Y.-W. Baek, L. Bellagamba, D. Boscherini,
A. Bruni, G. Bruni, G. Cara Romeo, E. Cerron-Zeballos, L. Cifarelli, F. Cindolo, M. Corradi,
D. Falchieri, A. Gabrielli, E. Gandolfi, P. Giusti, D. Hatzifotiadou, G. Laurenti, M.L. Luvisetto,
A. Margotti, M. Masetti, S. Morozov, R. Nania, P. Otiougova, F. Palmonari, A. Pesci, F. Pierella,
A. Polini, G. Sartorelli, G. Scioli, G.P. Vacca, G. Valenti, G. Venturi, M.C.S. Williams¹⁾ and A. Zichichi.

Bratislava, Slovakia, Faculty of Mathematics and Physics, Comenius University:
J. Braciňík, V. Černý, J. Ftáčník, V. Hlinka, R. Janík, M. Pikna, J. Pišút, N. Pišútová, P. Rosinsky,
B. Sitar, P. Strmeň, I. Szarka and M. Zagiba.

Bucharest, Romania, National Institute for Physics and Nuclear Engineering:
C. Aifimie, A. Andronic, V. Catanea, M. Ciobanu, M. Duma, C.I. Legrand, M. Petrovici and
G. Stoica.

Budapest, Hungary, KFKI Research Institute for Particle and Nuclear Physics, Hungarian Academy
of Sciences:
E. Denes, Z. Fodor and G. Palla.

Cagliari, Italy, Dipartimento di Fisica dell'Università and Sezione INFN:
 C. Cicalóo, A. De Falco, M.P. Macciotta-Serpi, A. Masoni, D. Mura, G. Puddu, S. Serci, E. Siddi,
 L. Tocco and G. Usai.

Catania, Italy, Dipartimento di Fisica dell'Università and Sezione INFN:
 A. Badalà, R. Barbera, F. Librizzi, G. Lo Re, A. Palmeri, G.S. Pappalardo and F. Riggi.

CERN, Switzerland, European Organization for Nuclear Research:
 G. Anelli, I. Augustin, A. Augustinus, J. Bächler, A. Braem, R. Brun, P. Buncic, R. Campagnolo,
 M. Campbell, F. Carena, W. Carena, F. Carminati, N. Carrer, P. Chochula, J. Christiansen, J. Chudoba,
 M. Davenport, J. de Groot, A. Di Mauro, R. Dinapoli, R. Divià, C. Engster, R. Esteve Bosch, C. Fabjan,
 A. Fasso, F. Formenti, A. Gheata, P. Giubellino, I. Gonzalez Caballero, C. Gregory, M. Hoch,
 P. Hristov, P. Jarron, A. Jimenez de Parga, L. Jirden, C. Joram, A. Kluge, L. Leistam, C. Lourenço,
 J.-C. Marin, P. Martinengo, M. Masera, T. Meyer, A.K. Mohanty, P.R. Moreira, A. Morsch, B. Mota,
 L. Musa, G. Paic, D. Perini, F. Piuz, S. Popescu, F. Rademakers, J.-P. Revol, P. Riedler, K. Šafářík,
 P. Saiz, J.-C. Santiard, K. Schossmaier, J. Schukraft, E. Schyns, C. Soos, G. Stefanini, D. Swoboda,
 P. Szymanski, H. Taureg, P. Vande Vyvre, A. Vascotto, M.C.S. Williams and K. Wyllie.

Chandigarh, India, Physics Department, Panjab University:
 M.M. Aggarwal, A.K. Bhatia, V.S. Bhatia and G. Sood.

Clermont-Ferrand, France, Laboratoire de Physique Corpusculaire (LPC), IN2P3-CNRS and
 Université Blaise Pascal:
 IN2P3: A. Baldit, V. Barret, N. Bastid, G. Blanchard, J. Castor, T. Chambon, P. Crochet, F. Daudon,
 A. Devaux, P. Dupieux, B. Espagnon, P. Force, B. Forestier, A. Genoux-Lubain, C. Insa, F. Jouve,
 L. Lamoine, J. Lecoq, F. Manso, L. Royer, P. Saturnini, G. Savinel and P. Rosnet.

Columbus, U.S.A., Department of Physics, Ohio State University:
 T.J. Humanic, D. Johnson, I.V. Kotov, M. Lisa, B.S. Nilsen, G. Paic¹⁾, T.C. Randles and E. Sugarbaker.

Copenhagen, Denmark, Niels Bohr Institute:
 I. Bearden, H. Bøggild, P. Christiansen, J.J. Gaardhøje, O. Hansen, A. Holm, B.S. Nielsen and
 D. Ouerdane.

Cracow, Poland, Henryk Niewodniczanski Institute of Nuclear Physics, High Energy Physics
 Department:
 J. Bartke, E. Gładysz-Dziaduś, E. Górnicki, E. Kornaś, M. Kowalski, A. Rybicki and Z. Włodarczyk⁵⁾.

Darmstadt, Germany, Gesellschaft für Schwerionenforschung (GSI):
 E. Badura, C. Blume, P. Braun-Munzinger, O. Busch, A. Castillo-Ramirez, M. Dahlinger, H.W. Daues,
 A. Devismes, C. Finck, P. Foka, U. Frankenfeld, C. Garabatos, I. Giese, H. Göringer, H.H. Gutbrod,
 G. Hering, M. Ivanov⁴⁾, J. Lühning, P. Malzacher, A. Marin, A. Mischke, D. Miśkowiec, W.F.J. Müller,
 H. Sako, A. Sandoval, H. Sann, H.R. Schmidt, K. Schwarz, S. Sedykh, H. Stelzer, R. Veenhof and
 D. Vranic.

Darmstadt, Germany, Institut für Kernphysik, Technische Universität:
 U. Bonnes, A. Förster, H. Oeschler and F. Uhlig.

Frankfurt, Germany, Institut für Kernphysik, Johann Wolfgang Goethe-Universität:
 C. Adler, W. Amend, J. Berger, J. Berschin, A. Billmeier, P. Buncic¹⁾, D. Flierl, M. Gaździcki,
 J. Hehner, S. Lange, R. Renfordt, H. Rheinfels-Immans, C. Roland, G. Roland, R. Stock, H. Ströbele
 and C. Struck.

Gatchina, Russia, St. Petersburg Nuclear Physics Institute:

B. Komkov, N. Miftakhov, V. Nikouline, V. Polyakov, E. Roschin, V. Samsonov, V. Tarasenkov, O. Tarasenkova, G. Solodov, S. Volkov and Y.A. Berdnikov.

Heidelberg, Germany, Kirchhoff Institute for Physics:

R. Achenbach, V. Angelov, J. de Cuveland, M. Dorn, P. Hanke, L. Hess, F.O. Lesser, V. Lindenstruth, S. Martens, S. Philipp, F. Pister, C. Reichling, F. Rettig, T. Steinbeck, R. Schneider and A. Wiebalck.

Heidelberg, Germany, Physikalisches Institut, Ruprecht-Karls Universität:

H. Appelshäuser, V. Catanescu, S. Damjanovic, D. Emschermann, P. Glässel, N. Herrmann, W. Ludolphs, T. Mahmoud, J. Milosevic, V. Petráček, I. Rusanov, R. Schicker, J. Slivova, H.K. Soltveit, H.J. Specht, J. Stachel, H. Tilsner, B. Vulpescu, J.P. Wessels, B. Windelband, C.C. Xu and S. Yurevich.

Jaipur, India, Physics Department, University of Rajasthan:

R. Raniwala and S. Raniwala.

Jammu, India, Physics Department, Jammu University:

S.K. Badyal, A. Bhasin, A. Gupta, V.K. Gupta, S. Mahajan, L.K. Mangotra, B.V.K.S. Potukuchi, N.K. Rao and S.S. Sambyal.

JINR, Russia, Joint Institute for Nuclear Research:

V.A. Arefiev, B.V. Batiounia, G.S. Chabratova, S. Chernenko, V.K. Dodokhov, V.G. Kadychevsky, Y.A. Panebrattsev, V.N. Penev, M.K. Suleimanov, A.S. Vodopianov, V. Yurevich, Y. Zanevsky and A. Zintchenko.

V. Kuznetsov⁶⁾ and V. Shestakov⁶⁾.

Ts. Baatar⁷⁾, B. Khurelbaatar⁷⁾ and R. Togoo⁷⁾.

K.G. Akhobadze⁸⁾, A.K. Djavrishvili⁸⁾, T. Grigalashvili⁸⁾, E.S. Ioramashvili⁸⁾, A.V. Kharadze⁸⁾, L. Khizanishvili⁸⁾, T.V. Khuskivadze⁸⁾, L.V. Shalamberidze⁸⁾ and N. Shubitidze⁸⁾.

N. Grigalashvili⁹⁾, M. Nioradze⁹⁾, M. Tabidze⁹⁾ and Y. Tevzadze⁹⁾.

D. Felea¹⁰⁾, M. Gheata¹⁰⁾, M. Haiduc¹⁰⁾, D. Hasegan¹⁰⁾, R. Marginean¹⁰⁾, C. Ristea and S.I. Zgura¹⁰⁾.

Jyväskylä, Finland, Department of Physics, University of Jyväskylä and Helsinki Institute of Physics: M. Bondila¹⁰⁾, M. Komogorov, V. Lyapin, V. Ruuskanen and W. Trzaska.

Kangnung, South Korea, Kangnung National University:

C. Choi, J. Jeong, K.S. Kang, D.W. Kim, J. Kim, K. Lee and S. Lee.

Kharkov, Ukraine, National Scientific Centre ‘Kharkov Institute of Physics and Technology’:

G.L. Bochek, A.N. Dovbnya, V.I. Kulibaba, N.I. Maslov, S.V. Naumov, S.M. Potin, O.S. Shevchenko and A.F. Starodubtsev.

Kharkov, Ukraine, Scientific and Technological Research Institute of Instrument Engineering:

V.N. Borshchov, S.K. Kiprich, O.M. Listratenko, G. Protsay, A.N. Reznik and V.E. Starkov.

Kiev, Ukraine, Department of High Energy Density Physics, Bogolyubov Institute for Theoretical Physics, National Academy of Sciences of Ukraine:

E.S. Martynov, S.V. Molodtsov O.P. Pavlenko, Y.M. Sinyukov and G. Zinovjev.

Kolkata, India, Saha Institute of Nuclear Physics:

P. Bhattacharya, S. Bose, Sukalyan Chattopadhyay, L. Das, P. Datta, T. Ghosh, N. Majumdar, S. Mukhopadhyay, S. Pal, R. Saha, A. Sanyal, S. Sarkar, P. Sen, S.K. Sen, B.C. Sinha and T. Sinha.

Kolkata, India, Variable Energy Cyclotron Centre:

Subhasis Chattopadhyay, S. Das, M.R. Dutta Majumdar, M.S. Ganti, P. Ghosh, T.K. Nayak, S. Pal, R.N. Singaraju, Bikash Sinha, M.D. Trivedi and Y.P. Viyogi.

Košice, Slovakia, Institute of Experimental Physics, Slovak Academy of Sciences and Faculty of Science P.J. Šafárik University:

J. Bán, M. Bombara, M. Hnatič, A. Jusko, I. Králik, A. Kravčáková, F. Kriváň, M. Krivda, G. Martinská, B. Pastirčák, L. Šándor, J. Urbán, S. Vokál and J. Vrláková.

Lausanne, Switzerland, Integrated System Laboratory (ISL), Ecole Polytechnique Fédérale de Lausanne (EPFL):

A. Aizza, F.A. Cherigui, M. Mattavelli and D. Mlynek.

Legnaro, Italy, Laboratori Nazionali di Legnaro:

M. Cinausero, M. Lombardi, R.A. Ricci and L. Vannucci.

Lisbon, Portugal, Departamento de Física, Instituto Superior Técnico:

P. Branco, R. Carvalho, J. Seixas and R. Vilela Mendes.

Lund, Sweden, Division of Cosmic and Subatomic Physics, University of Lund:

H.-A. Gustafsson, J. Nystrand, A. Oskarsson, L. Osterman, I. Otterlund, R. du Rietz, E.A. Stenlund and H. Tydesjo.

Lyon, France, Institut de Physique Nucléaire de Lyon (IPNL), IN2P3-CNRS and Université Claude Bernard Lyon-I:

M.Y. Chartoire, B. Cheynis, L. Ducroux, E. Gangler, J.Y. Grossiord, A. Guichard and J.C. Ianigro.

Mexico City, Mexico, Centro de Investigación y de Estudios Avanzados (CINVESTAV) and Instituto de Ciencias Nucleares and Instituto de Física (UNAM):

R. Alfaro, A. Ayala, E. Belmont, J.G. Contreras, E. Cuautle, J.C. D'Olivo, G. Herrera Corral, A. Martinez, J. Martinez, A. Menchaca, L.M. Montaño and L. Nellen.

Moscow, Russia, Institute for Nuclear Research, Academy of Science:

K.A. Chileev, M.B. Goloubtseva, F.F. Gouber, O. Karavichev, T.L. Karavitcheva, E. Karpechev, A.B. Kurepin, A.I. Maevskaia, V. Marin, I. Pshenichnov, V.I. Razine, A.I. Rechetine, V. Tiflov and N.S. Topilskaia.

Moscow, Russia, Institute for Theoretical and Experimental Physics:

A.N. Akhmedinov, V. Golovine, A.B. Kaidalov, M.M. Kats, I.T. Kiselev, S.M. Kiselev, E. Lioublev, M. Martemyanov, A.N. Martemyanov, P.A. Polozov, V.S. Serov, A.V. Smirnitski, M.M. Tchoumakov, I.A. Veltitski, K.G. Volochine, L.S. Vorobiev and B.V. Zagreev.

Moscow, Russia, Russian Research Center ‘Kurchatov Institute’:

V. Antonenko, S. Beliaev, I. Doubrovik, S. Fokine, M. Ippolitov, K. Karadjev, A.L. Lebedev, V. Lebedev, V.I. Manko, T. Moukhanova, A. Nianine, S. Nikolaev, S. Nikouline, O. Patarakine, D. Peressounko, I. Sibiriak, A. Vasiliev, A. Vinogradov and M. Volkov.

Moscow, Russia, Moscow Engineering Physics Institute:
V.A. Grigoriev, V.A. Kapline and V.A. Loguinov.

Münster, Germany, Institut für Kernphysik, Westfälische Wilhelms Universität:
D. Bucher, R. Glasow, N. Heine, S. Keßen, T. Lister, T. Peitzmann, K. Reygers, R. Santo,
W. Verhoeven, O. Winkelmann and O. Zaudtke.

Nantes, France, Laboratoire de Physique Subatomique et des Technologies Associées (SUBATECH),
Ecole des Mines de Nantes, IN2P3-CNRS and Université de Nantes:
L. Aphectche, A. Boucham, S. Bouvier, H. Carduner, D. Charrier, J.P. Cussonneau, H. Delagrange,
D. D'Enterria, M. Dialinas, M. Diaz, C. Drancourt, B. Erazmus, L. Lakehal-Ayat, P. Lautridou,
F. Lefèvre, M. Le Guay, L. Luquin, L. Martin, G. Martinez-Garcia, P. Pichot, G. Puil, O. Ravel,
C.S. Roy, D. Roy, Y. Schutz and A. Tournaire.

NIKHEF, The Netherlands, National Institute for Nuclear and High Energy Physics:
M. Botje¹¹⁾, A. Buijs¹²⁾, J.J.F. Buskop¹¹⁾, A.P. De Haas¹²⁾, R. Kamermans^{11,12)}, P.G. Kuijer^{11,12)},
G. Nooren¹¹⁾, C.J. Oskamp¹²⁾, A. Van Den Brink¹²⁾ and N. Van Eijndhoven¹²⁾.

Novosibirsk, Russia, Budker Institute for Nuclear Physics:
A.R. Frolov and I.N. Pestov.

Oak Ridge, U.S.A., Instrumentation and Controls Division, Oak Ridge National Laboratory:
T. Awes, C.L. Britton, W.L. Bryan and A.L. Wintenberg.

Orsay, France, Institut de Physique Nucléaire (IPNO), IN2P3-CNRS and Université de Paris-Sud:
M.-P. Comets, P.F. Courtat, P. Edelbruck, B. Espagnon, R. Guernane, D. Guez, Y. Le Bornec,
M. Mac Cormick, J. Peyré, J. Pouthas, S. Rousseau and N. Willis.

Oslo, Norway, Department of Physics, University of Oslo:
A.K. Holme, G. Løvhøiden, B. Skaali, T.S. Tveter, T. Vik and D. Wormald.

Padua, Italy, Dipartimento di Fisica dell'Università and Sezione INFN:
F. Antinori¹⁾ N. Carrer, A. Dainese, D. Fabris, M. Morando, G. Nebbia, A. Pepato, E. Quercigh,
F. Scarlassara, G. Segato, R. Turrisi and G. Viesti.

Pohang, South Korea, Pohang Accelerator Laboratory:
J. Choi, M.G. Kim, T.Y. Lee and E.S. Park.

Prague, Czech Republic, Institute of Physics, Academy of Science:
A. Bejtlerova, J.A. Mareš, E. Mihoková, M. Nikl, K. Píška, K. Polák and P. Závada.

Protvino, Russia, Institute for High Energy Physics:
M.Yu. Bogoliubski, I.V. Kharlov, S.A. Konstantinov, M.O. Lobanov, V.A. Petrov, B.V. Polichtchouk,
S.A. Sadovski and V.A. Victorov.

Řež u Prahy, Czech Republic, Academy of Sciences of Czech Republic, Nuclear Physics Institute:
D. Adamová, V. Hanzal, J. Hošek, I. Hřivnáčová¹⁾, S. Kouchpil, V. Kouchpil, A. Kugler, M. Šumbera,
P. Tlustý, V. Wagner and D. Zákoucký.

Rome, Italy, Dipartimento di Fisica, Università di Roma 'La Sapienza' and Sezione INFN:
S. Di Liberto, M.A. Mazzoni, F. Meddi and G.M. Urciuoli.

Saclay, France, Centre d'Etudes Nucléaires, DAPNIA:

A. Baldisseri, H. Borel, P. De Girolamo, J. Gosset, J.-C. Lugol, F. Orsini, S. Salasca and F.M. Staley.

Salerno, Italy, Dipartimento di Fisica ‘E.R.Caianiello’ dell’Università and INFN:

A. De Caro, S. De Pasquale, A. Di Bartolomeo, M. Fusco Girard, G. Grella, M. Guida, J. Quartieri, G. Romano, S. Sellitto, D. Vicinanza and T. Virgili.

Sarov, Russia, Russian Federal Nuclear Center (VNIIEF):

V. Basmanov, D. Budnikov, V. Ianowski, R. Ilkaev, L. Ilkaeva, A. Ivanov, A. Khlebnikov, E. Kolokolnikov, S. Nazarenko, V. Punin, S. Poutevskoi, I. Selin, I. Vinogradov, S. Zhelezov and A. Zhitnik.

St. Petersburg, Russia, V.A. Fock Institute for Physics of St. Petersburg State University, Mendeleev Institute for Metrology and Meson Scientific Association:

L.Y. Abramova, V.S. Alexandrov, P.A. Bolokhov, A.A. Bolonine, M.A. Braun, V.M. Dobulevitch, G.A. Feofilov, S.F. Guerassimov, S.N. Igolkine, A.A. Kolojvari, V.P. Kondratiev, I.A. Novikov, P.A. Otiougova, S.V. Potapov, O.I. Stolyarov, A.M. Switchev, T.A. Toulina, F.A. Tsimbal, F.F. Valiev, V.V. Vetchernine and L.I. Vinogradov.

Strasbourg, France, Institut de Recherches Subatomiques (IReS), IN2P3-CNRS and Université Louis Pasteur:

L. Arnold, J. Baudot, D. Bonnet, J.P. Coffin, M. Germain, C. Gojak, M. Guedon, B. Hippolyte, C. Kuhn, J. Lutz, C. Suire and A. Tarchini.

Trieste, Italy, Dipartimento di Fisica dell’Università and Sezione INFN:

V. Bonvicini, L. Bosisio, M. Bregant, P. Camerini, S. Dittongo, E. Fragiacomo, N. Grion, R. Grossi, G.-V. Margagliotti, S. Piano, C. Piemonte, A. Rashevski, R. Rui F. Soramel¹⁴⁾ and A. Vacchi.

Turin, Italy, Dipartimenti di Fisica dell’Università and INFN:

G. Alberici, B. Alessandro, R. Arnaldi, S. Beolé, P. Cerello, E. Chiavassa, S. Coli, A. Colla, E. Crescio, F. Daudo, N. De Marco, A. Ferretti, L. Gaido, M. Gallio, G. Giraudo, P. Giubellino¹⁾, M. Idzik, P.G. Innocenti, E. Lopez Torres, M.I. Martinez, A. Marzari-Chiesa, M. Masera¹⁾, G. Mazza, P. Mereu, M. Monteno, A. Musso, D. Nouais, C. Oppedisano, A. Piccotti, G. Piragino, F. Prino, L. Riccati, A. Rivetti, E. Scomparin, F. Sigaudo, F. Tosello, G. Travaglia, E. Vercellin, A. Werbrouck, R. Wheadon and F. Yermia.

Warsaw, Poland, Soltan Institute for Nuclear Studies:

A. Deloff, K. Karpio, M. Kozlowski, H. Malinowski, K. Redlich¹³⁾, T. Siemiarczuk, G. Stefanek, L. Tykarski and G. Wilk.

Warsaw, Poland, University of Technology, Institute of Physics:

J. Grabinski, M. Janik, A. Kisiel, T.J. Pawlak, W.S. Peryt, J. Pluta, M. Przewlocki, P. Skowronski¹⁾ and P. Szarwas

Wuhan, China, Institute of Particle Physics, Huazhong Normal University:

X. Cai, S.Q. Feng, Y. Hu, W. Li, F. Liu, F.M. Liu, H. Liu, L.S. Liu, Y. Liu, W.Y. Qian, X.R. Wang, S.Q. Wu, T. Wu, C.C. Xu, C.B. Yang, Z.B. Yin, D.C. Zhou and D.M. Zhou.

Yerevan, Armenia, Yerevan Physics Institute:

M. Atayan, V. Danielyan, A. Grigorian, S. Grigoryan, H. Gulkanyan, V. Kakoyan, Yu. Margaryan, L. Parlakyan, G. Sargsyan, R. Shahoyan and H. Vardanyan.

Zagreb, Croatia, Ruder Bošković Institute:
T. Anticic, K. Kadija and T. Susa.

Zagreb, Croatia, Prirodoslovno-Matematicki Fakultet:
R. Manger, M. Marusic, G. Nogo, R. Piskac, K. Puljic and V. Sego.

-
- ¹⁾ Also at CERN, Geneva, Switzerland.
 - ²⁾ On leave from JINR, Dubna, Russia.
 - ³⁾ On leave from Comenius University, Bratislava, Slovakia.
 - ⁴⁾ Institut Universitaire de Technologie de Monluçon, Allier, France.
 - ⁵⁾ Institute of Physics, Pedagogical University, Kielce, Poland.
 - ⁶⁾ Research Centre for Applied Nuclear Physics (RCANP), Dubna, Russia.
 - ⁷⁾ Institute of Physics and Technology, Mongolian Academy of Sciences, Ulaanbaatar, Mongolia.
 - ⁸⁾ Institute of Physics, Georgian Academy of Sciences, Tbilisi, Georgia.
 - ⁹⁾ High Energy Physics Institute, Tbilisi State University, Tbilisi, Georgia.
 - ¹⁰⁾ Institute of Space Sciences, Bucharest, Romania.
 - ¹¹⁾ Foundation of Fundamental Research of Matter in The Netherlands.
 - ¹²⁾ Utrecht University, Utrecht, The Netherlands.
 - ¹³⁾ University of Wroclaw, Poland.
 - ¹⁴⁾ Dipartimento di Fisica di Udine.

Acknowledgements

The work presented in the present Addendum to the Technical Design Report of the TOF System is the result of the contribution of many people.

We would like to thank the following people from INFN-Bologna: M. Guerzoni, S. Serra and R. Michinelli for the mechanical drawings; I. D'Antone, S. Meneghini, M. Zuffa and M. Rizzi for electronics support; F. Massera, G. Molinari, G. Pancaldi, R. Pilastrini and A. Zucchini for technical support.

From ITEP-Moscow we thank M. Duline, I. Melnikov and V. Plotnikov for technical support and Y. Grishuk for engineering and technical support.

We also thank M. Mota for his work on the development of the HPTDC, F. Anghinolfi and R. Szczygiel for valuable assistance with the analogue electronics.

Important contributions to the analogue electronics are due to the LAA project; we thank H. Wenninger and E. Oussenko.

We would like to thank P. Ijzermans for valuable assistance at T10; and S. Witoszynskyj for invaluable assistance with data taking and subsequent analysis.

The intensive R&D program that led to the design of the TOF System would not have been possible without the PS and SPS test beams; we are indebted to the CERN staff who run the PS/SPS complex so well.

We made full use of the CERN surface mounting workshop thanks to C. Millerin, N. Wauquier and M. Primadei; we are also indebted to A. Gandi of the CERN printed circuit shop; and to R. Dye for help with cutting the glass for the RPC plates.

Installing in the T10 test beam was only made possible due to Christian Recour, his fellow crane drivers and other transport personnel who were always very helpful, especially at hectic times.

We also thank the staff of the Desktop Publishing Service for their professional help with the editing.

Contents

1	Introduction	1
2	R&D program, prototype test results	3
2.1	Introduction	3
2.2	R&D during the year 2000 - Full size MRPC strips	3
2.2.1	The experimental set-up	3
2.2.2	The first full size MRPC strips - Strips 1 and 2	4
2.2.3	Strips 6,7 and 8 - Study of the gap width	11
2.2.4	Conclusion	13
2.3	R&D during 2001 - The double stack MRPC	13
2.3.1	Efficiency and time resolution	14
2.3.2	Average charge	16
2.3.3	Charge spectrum simulation	17
2.3.4	Boundaries	19
2.3.5	Test of the Time Over Threshold method	20
2.3.6	Conclusion	25
2.4	Rate tests of double stack MRPC strips at the GIF	25
2.4.1	Description of the GIF and the experimental set-up	26
2.4.2	Some results of the measurements	27
2.4.3	Rate capability	31
2.4.4	Power dissipation	31
2.4.5	Conclusion	31
2.5	Tests of first prototypes of a central module of the TOF system	31
2.5.1	The prototype modules and the MRPC strips	32
2.5.2	Test beam results	35
2.5.3	Conclusion	38
2.6	Summary and proposed design	39
2.6.1	Summary of the R&D Program	39
2.6.2	Proposed design for the detector element for the TOF	39
3	Detector engineering design	41
3.1	Introduction	41
3.2	General module description	42
3.3	The module cooling system	48
3.4	Installation procedure and services to the modules	51
3.5	Assembly procedure	53
3.5.1	Assembly of the MRPC strips	53
3.5.2	Assembly of the modules	57
3.6	Quality assurance and test facilities	57
3.7	Weights of the TOF modules	58
3.8	Material budget for the TOF modules.	58
4	The readout system	61
4.1	Introduction	61
4.2	The Front End Analogue card: FEA	61
4.3	The TDC readout module: TRM	63

4.3.1	The HPTDC - a summary	63
4.3.2	The TRM	67
4.3.3	Tests of the HPTDC	68
4.4	The Data Readout Module: DRM	70
4.5	Expected readout bandwidth	74
4.6	Timing and the T0 array	75
4.6.1	LHC timing	75
4.6.2	T0 array	76
4.7	Cosmic and multiplicity TOF trigger	76
4.7.1	Cosmic trigger	77
4.7.2	Topology trigger	78
4.8	Monitoring and Calibration	79
4.9	Grounding scheme	79
4.10	Power consumption estimates	79
4.11	Basic time resolution of the TOF detector and electronics	79
5	TOF Detector Performance	81
5.1	Introduction	81
5.2	Detector description	81
5.2.1	Software tools for detector description and particle tracking	81
5.2.2	Detector layout for Monte Carlo simulation studies	81
5.3	Monte Carlo event generators	82
5.4	Detector acceptance studies	83
5.4.1	Momentum spectra and acceptances	83
5.4.2	Incident angle studies	89
5.4.3	Occupancy	89
5.5	Track matching	93
5.5.1	Matching with TPC tracks	93
5.5.2	Matching efficiency and contamination	93
5.6	Particle identification (PID)	101
5.6.1	PID basic method	101
5.6.2	PID efficiency and contamination	101
5.6.3	PID in p-p interactions	108
5.6.4	Conclusion on PID	114
5.7	Measurement of the t_0 event time with TOF	115
5.7.1	The statistical method	115
5.7.2	t_0 determination in Monte Carlo events	116
5.8	Monte Carlo event production in the framework of ALICE-GRID	119
6	Services	121
6.1	Low Voltage Power Distribution	121
6.1.1	Distribution schemes	121
6.2	High Voltage Distribution	122
6.2.1	HV power consumption	122
6.2.2	Distribution system	124
6.3	TOF gas system	124
6.3.1	Introduction	124
6.3.2	The Closed Loop Distribution System	125
6.3.3	Distribution Pipework	129
6.4	Space requirements	134

7 Schedule, costs and responsibilities	137
7.1 Schedule and milestones	137
7.2 Budget	137
7.3 Responsibilities	137
References	141

1 Introduction

The Time-Of-Flight (TOF) detector was proposed in 1999 and presented in the ALICE TDR n°8 at the beginning of 2000 [1] with the purpose of providing the ALICE experiment with the best instrument for identifying charged particles over the full central region, in the intermediate momentum range above the ITS/TPC PID capability and partly overlapping the HMPID higher momentum range. The physics goals of the TOF detector dictate the following requirements:

- large acceptance (~ 2 rapidity units)
- high efficiency ($> 95\%$)
- excellent intrinsic time resolution (< 100 ps)
- high granularity/low occupancy ($\sim 10^5$ channels)
- rate capability adequate to the ALICE environment (≤ 50 Hz/cm²)
- good uniformity of response
- modularity and simplicity of construction.

In the TOF TDR it was shown that the innovative technique of the Multigap RPCs allows to fulfil all these requirements.

However several details of the final detector had yet to be studied and tested with a full-size MRPC strip: the type of glass both in terms of resistivity and of practical thickness, the definition of the edge of the active area, the best value of the gas gaps and the type of spacers to define them, the sharpness of boundaries between adjacent pads, the choice of the front-end electronic components and the scheme for providing the time-over-threshold signal.

During the intensive R&D activity carried out in 2000 and 2001 all these topics have been addressed and a final solution has been found. The most relevant change with respect to the TDR proposal is the new MRPC strip design that has evolved from a single-stack to a double-stack structure. This design has allowed to improve the performance of the basic detector element pushing to the limits its efficiency and time resolution. The results of the first mass preproduction of strips and the construction of two central module prototypes accomplished in the autumn of 2001 show that the technique for building a large number of MRPC strips is under control and that the uniformity of performance is very promising.

One of the most important benefits of the new strip design, the double-stack structure, is the intrinsic detector efficiency, now really close to 100% in a broad range of operating voltages. Since the global PID efficiency is a product of several efficiencies (track finding and reconstruction in the ITS and TPC, TPC-TOF track matching, TOF PID procedure) starting from a full intrinsic efficiency detector is an advantage.

Concerning the services (LV, HV, cooling and gas distribution) the relevant choices have been made and the details have been worked out. The same applies to the readout modules beyond the front-end analogue card and the trigger logic. The assembly and test procedures for the strips and the modules, and the installation procedure of the modules inside the space frame have also been established.

The schedule of the project and the cost of the different components of the detector have been updated; a new set of milestones is therefore proposed in this addendum.

The present document is organised as follows: in Chapter 2 the results and the conclusions of the R&D program carried out during the last two years are presented, in Chapter 3 the proposed detector engineering design is described, in Chapter 4 the electronics readout system is presented, in Chapter 5 the detector performance in terms of acceptance, occupancy, PID capability and offline data processing are reported, in Chapter 6 the services and in Chapter 7 the planning and cost of this project are reviewed.

2 R&D program, prototype test results

2.1 Introduction

The Multigap Resistive Plate Chamber (MRPC) was developed 6 years ago [1]. It consists of a stack of resistive plates, spaced one from the other with equal sized spacers creating a series of gas gaps. Electrodes are connected to the outer surfaces of the stack of resistive plates while all the internal plates are left electrically floating. Initially the voltage on these internal plates is given by electrostatics, but they are kept at the correct voltage due to the flow of electrons and ions created in the avalanches. The MRPCs described in this document are designed for timing purposes; thus the gas gaps need to be small. The final design we have selected has ten gaps of $250\ \mu\text{m}$; thus through-going particles traverse a total of 2.5 mm of gas so that the efficiency will be high. The details of the R&D program leading to this choice will be covered in this chapter.

Initially tests were performed using small detectors with a readout pad of dimensions $3 \times 3\ \text{cm}^2$ to prove that good timing can be obtained by such a detector. Even though it is conceivable to build the $160\ \text{m}^2$ ALICE array from 160,000 individual readout cells, it is much easier to build larger detector units and segment the readout. The Time-of-Flight array proposed [2] for ALICE consists of detector elements that are long strips with an active area of $7 \times 120\ \text{cm}^2$. These strips have 96 readout pads, each with an area of $3.5 \times 2.5\ \text{cm}^2$, arranged in two rows of 48 pads.

The principal goal of the R&D effort during the year 2000 was to investigate the problems associated with scaling up from a small test MRPC discussed in the original TDR (MRPC strip with 2×8 readout pads of $3 \times 3\ \text{cm}^2$) to a full size MRPC strip.

Various issues were addressed, such as: (a) material and thickness of resistive plates (b) definition of the edge of the active area (c) connection between readout pads and electronics (d) assembly problems and (e) front-end electronics.

In the following section, 2.2, we present results from full size MRPC strips, built with small differences in the details of construction. By the end of 2000 it had been established that the full size MRPC strips had the required performance. However, as there was still space for improvement, in 2001 a new, slightly different design was introduced : the double stack MRPC. The aim was to push the performance to the limits (maximise efficiency and optimise time resolution). In section 2.3 we present results from a number of such double stack MRPC strips. Section 2.4 presents results from tests of MRPCs at the Gamma Irradiation Facility (GIF) of CERN, aimed to determine the rate capability of these devices. Section 2.5 describes tests with first prototypes of the central module of the ALICE TOF, where we increased the size and complexity by an order of magnitude and confirmed that the performance remains unchanged. Finally section 2.6 contains the proposed design of the detector element for the TOF system.

2.2 R&D during the year 2000 - Full size MRPC strips

2.2.1 The experimental set-up

The experimental set-up, located at the T10 beam line of the CERN Proton Synchrotron East Hall, consists of the following :

- Two pairs of crossed scintillators, the coincidence of which defines a $1\ \text{cm}^2$ area and provides the trigger.
- A small MRPC, of $10\ \text{cm}^2$ active area, which acts as a pre-trigger providing the start to the TDCs and the gate to the ADCs.

- Three tracking chambers, each consisting of 2 planes of strips with 4 mm pitch, to provide information on the beam position.
- Two fast scintillator bars ($2 \times 2 \times 10 \text{ cm}^3$) equipped with two photomultipliers each, to provide accurate time reference.
- The detector under study (MRPC strip), contained in an aluminium box, of dimensions 125 cm x 20 cm x 20 cm; one side of the box is closed by ‘interface cards’ so that a connection can be made between the front-end electronics and the pick-up pads.

The electronics used for the readout of the above detectors were CAMAC TDCs (LRS 2228A with the bin width set to 50 ps) and CAMAC ADCs (LRS 2249W). For the readout of the tracking chambers VME ADCs were used (CRAMS with pedestal subtraction and zero suppression).

The trigger system worked in the following manner. A pre-trigger was generated by the ‘start’ MRPC; this pre-trigger was used to generate the gates and start signals for the CAMAC ADCs and TDCs. A trigger was provided by the two pairs of crossed scintillators at a later time than the pre-trigger. If no trigger was produced, the ADCs and TDCs were cleared. We used this system since the CAMAC TDCs could only work in ‘common start’ mode and we wanted to have the cables between the front-end electronics and the TDCs as short as possible. However even with this scheme we were obliged to use cables of 15 m length. It should be noted that this system is a test system for measuring the efficiency and time resolution of the MRPCs during the R&D phase; over the next 18 months we will install a DAQ system which will follow exactly the scheme discussed in chapter 4. It should also be noted that the start MRPC was a small chamber consisting of a single stack of glass defining 5 gaps of 230 μm ; it has been used as a beam counter in our test beam for two years and has given no problems. Even though this can not be regarded as an aging test, it does give us confidence in the stability of this technology.

All tests have been performed with a gas mixture of 90 % $\text{C}_2\text{F}_4\text{H}_2$, 5 % SF_6 and 5 % C_4H_{10} ; this is a non-flammable gas that has given us no problems. The measurements presented here have been taken using a 7 GeV/c beam of negative particles (π, μ). The numbering of the strips reflects the chronological order of construction.

2.2.2 The first full size MRPC strips - Strips 1 and 2

The first full sized strips that we constructed had good efficiency (98%) but ‘bad’ time resolution of ~ 150 ps. We eventually decided this was due to non-uniformity of the size of the gas gaps. Our initial plan had been to have glass sheets larger than the active area, and to use this extra region to place the spacers. The region would be made dead by placing mylar between the glass plates; thus there would be no spacers within the active area. This is shown in Fig. 2.1. However increasing the width of the active area from 6 cm used for the small MRPC [2] to the 7 cm of the full-sized TOF strips allowed the glass sheets to distort, and maybe even to touch in places. We decided to space the glass sheets by running a fiber across the width of the active area. Our first tests were made with 250 μm diameter optical fiber, each one cut and glued in place. Later we started to use nylon fishing line; this is more flexible and could be wrapped around plastic posts so the fiber was continuous. This is shown in fig. 2.2. These fibers are aligned with each other and will not create a significant dead region since they are small (250 μm diameter) and if the traversing particles are not normal to the glass plates, it is likely that they would only pass through one fiber at most and be able to initiate gas avalanches in the other four gas gaps. The edge of the active area for strip 1 is defined by the cut edge of the internal glass sheets, while for strip 2 this edge is defined by the mylar foil. We had the worry that streamers could be produced by this sharp edge of glass, but on studying the performance at the edge we could find no evidence of this.

The first two full-sized TOF strips with sub 100 ps time resolution (labelled strip 1 and strip 2) had the construction characteristics given below:

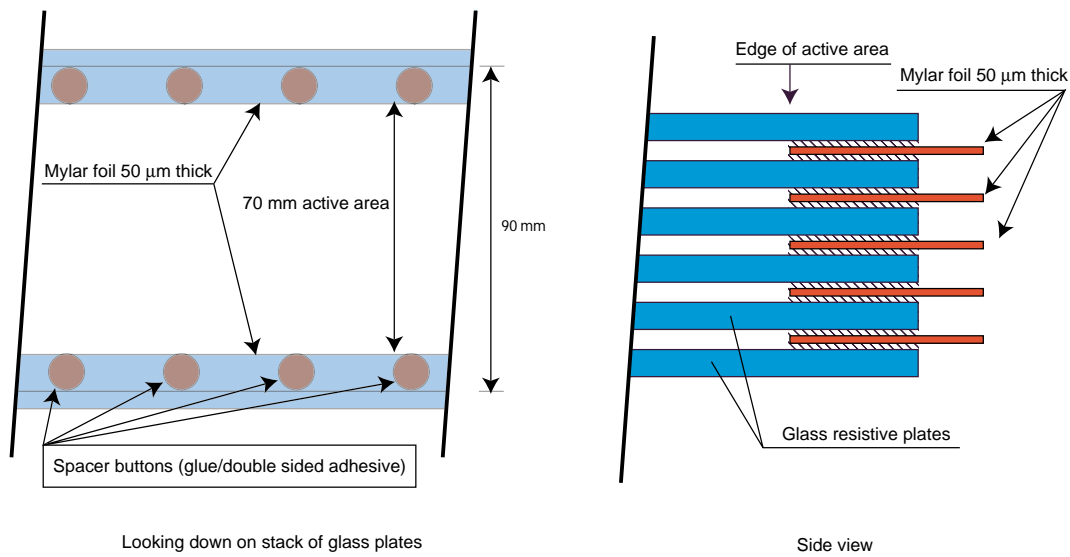


Figure 2.1: Original scheme for spacing resistive plates. The outer 1 cm of the glass plate was used to place the spacer button; this outer region was made dead with the mylar foil, with the edge of this mylar foil defining the edge of the active area. This is the method used for strip 2 (see text).

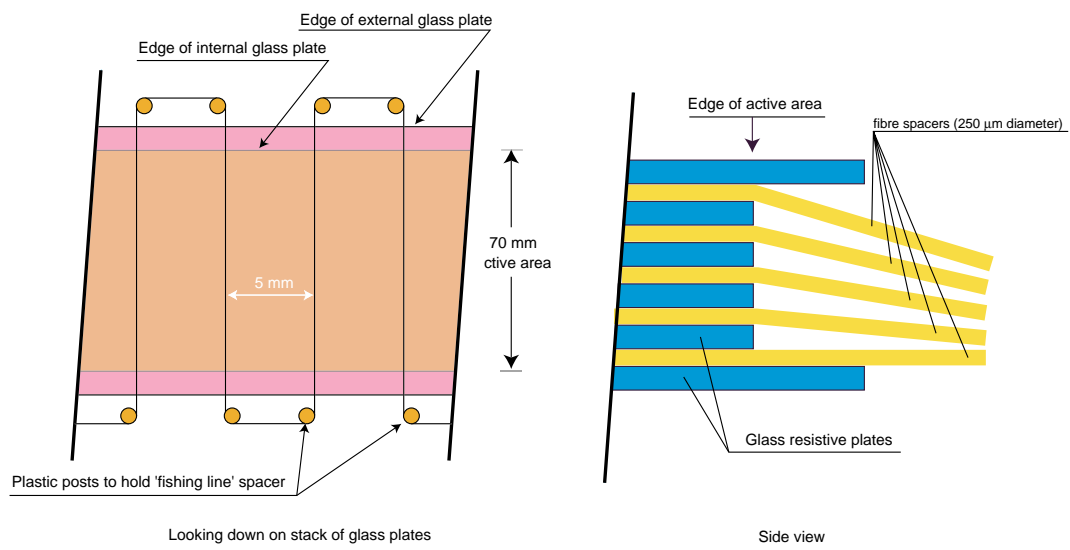


Figure 2.2: Selected scheme for spacing resistive plates. A fiber (first tests were with optical fibers, however nylon fishing line was found to be a more practical solution) is run across the width of the active area and around a plastic screw (to hold it in position). The edge of the active area is defined by the cut edge of the internal glass sheets. This is the method used for strip 1 (see text).

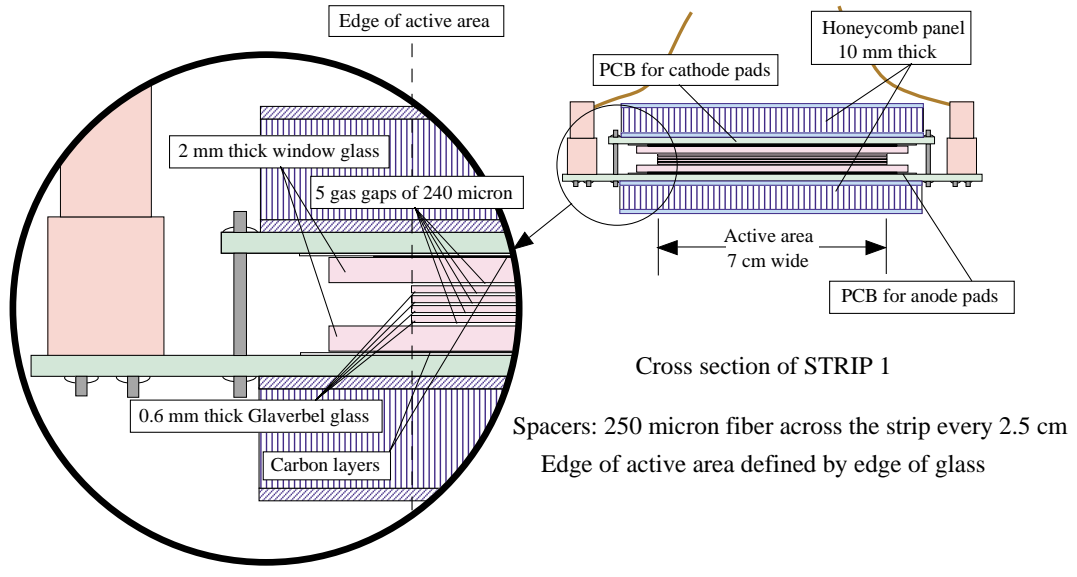


Figure 2.3: Cross section of MRPC strip 1.

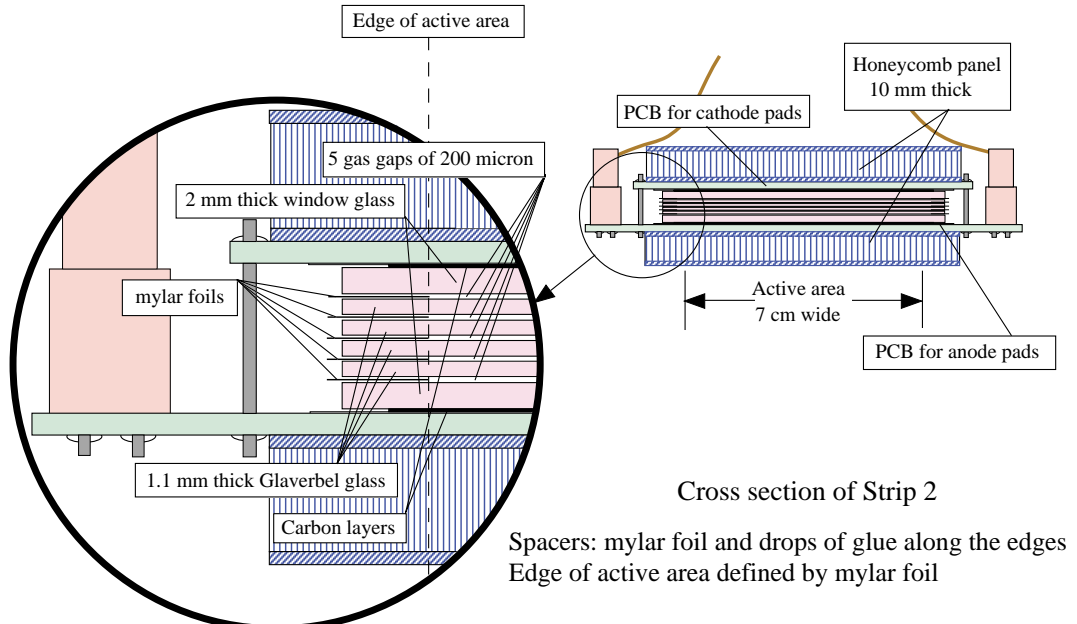


Figure 2.4: Cross section of MRPC strip 2.

Strip 1

- 600 μm internal resistive plates from Glaverbel float glass
- 2 mm external resistive plates from window glass
- 5 gas gaps of 250 μm each
- fiber spacers across the width of the strip, placed every 2.5 cm
- The edge of the active area was defined by the edge of the internal glass plates

Strip 2

- 1.1 mm internal resistive plates from Glaverbel glass
- 2 mm external resistive plates from window glass
- 5 gas gaps of 200 μm each
- spacers made of mylar foil and drops of glue along the perimeter of the active area
- The edge of the active area was defined by inserting mylar foil in the gas gaps

A cross section of strip 1 is shown in Fig. 2.3 and of strip 2 in Fig. 2.4. The important characteristics are (a) the thickness of the internal glass and (b) the spacers. Strip 2 is similar to the 16 pad MRPC described in the original TDR, except that the width of the active area is 7 cm and the internal glass plates are thicker (1.1 mm compared to 0.6 mm used previously); strip 1 has 600 μm internal glass with fiber spacers running across the width of the active area.

2.2.2.1 Performance of strips 1 and 2

Fig. 2.5 shows the efficiency and the time resolution σ for strips 1 and 2 as a function of the applied voltage. The efficiency, in the >96 % range, is slightly higher for strip 1. This is expected, since the total gas gap is 1.25 mm compared to 1 mm of strip 2. However the observed shift of 125 V between the 2 efficiency curves is smaller than expected due to the difference in electric field (higher by 20 % for strip 2 than for strip 1). This will be discussed in Sect. 2.3.3. Both strips have a time resolution of ~ 70 ps.

2.2.2.2 Electronics

In order to obtain the best time resolution, the time measurement has to be corrected according to the measured amplitude. The time of the hit and the value of the pulse height are recorded; a 5th order polynomial is fitted to the data, to describe the time - amplitude correlation; then a correction is made to the measured time with a function that depends on the pulse height (derived from the fit); this correction we refer to as the T(A) correction. To simplify the readout electronics, the idea is to substitute the amplitude measurement (done with an ADC) by Time Over Threshold (TOT) using a TDC measuring both leading and trailing edge of the pulse. For this reason, at the time of the TDR we added an integration stage after the fast amplifier. The front-end electronics in use at that time is schematically shown in Fig. 2.6. Tests of this scheme showed that similar time resolutions could be obtained using corrections based on the ADC or TOT (the status of the TOT will be discussed in a later section of this chapter); however the time spectrum had long tails outside the gaussian fit. The reason for this was that the slow decay of the signal after integration produces baseline noise; this coupled with the finite rise time of the signal at the output of the amplifier produced a rate-dependent tail of early and late signals.

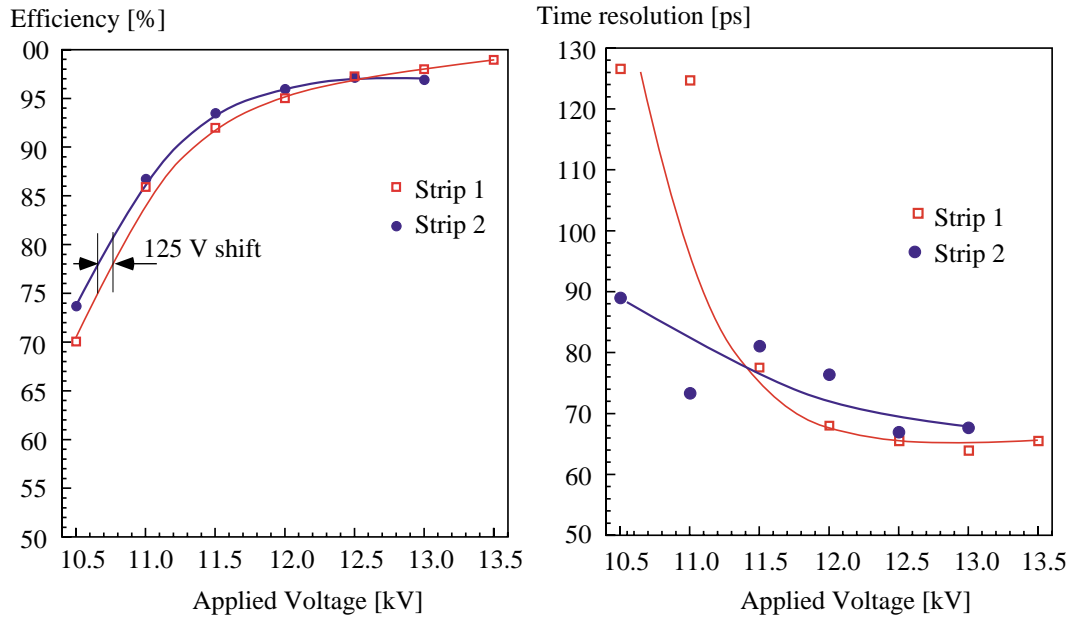


Figure 2.5: Efficiency and time resolution σ for strips 1 and 2 as a function of the applied voltage.

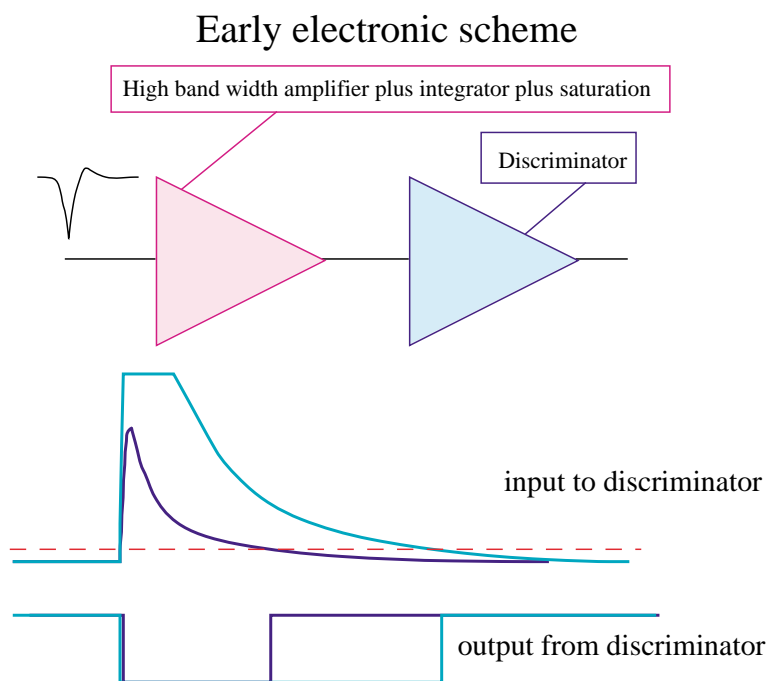


Figure 2.6: Layout of front-end electronics used in 1999.

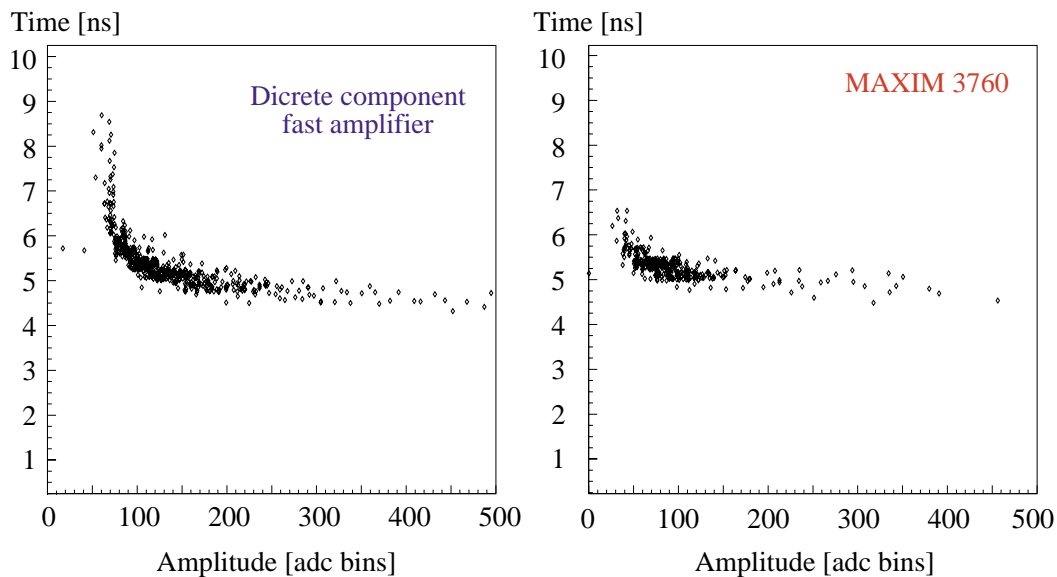


Figure 2.7: Time-amplitude correlation with the discrete component fast amplifier and with the MAXIM 3760.

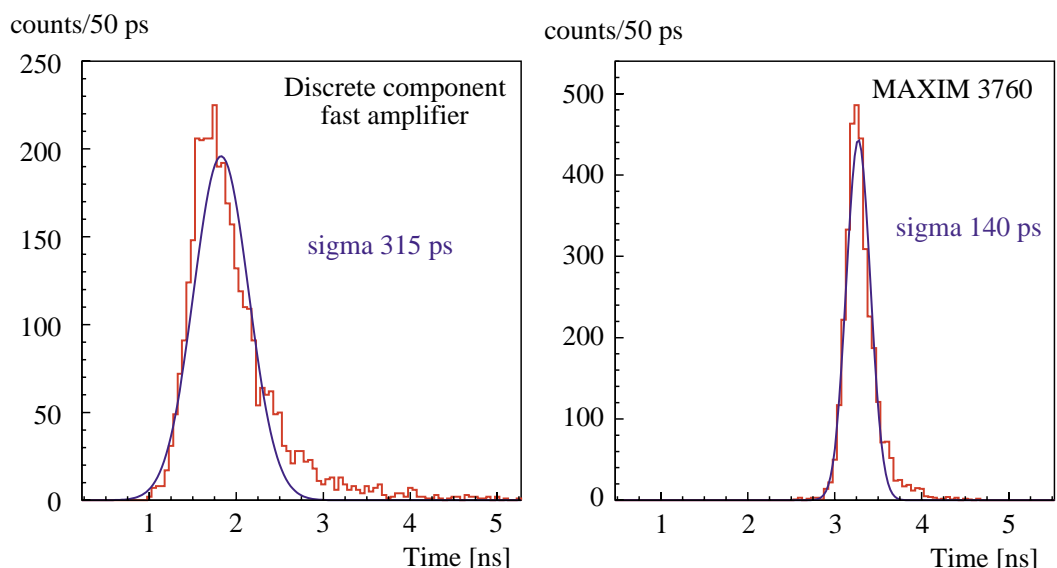


Figure 2.8: Time distributions (no T(A) correction applied) with the discrete component fast amplifier and with the MAXIM 3760.

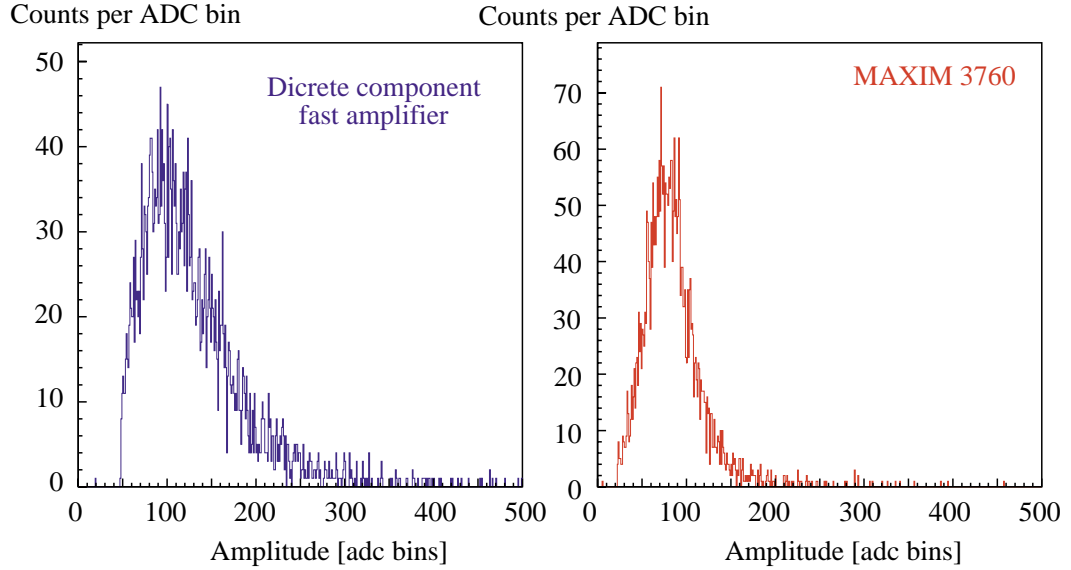


Figure 2.9: Charge distributions with the discrete component fast amplifier and with the MAXIM 3760.

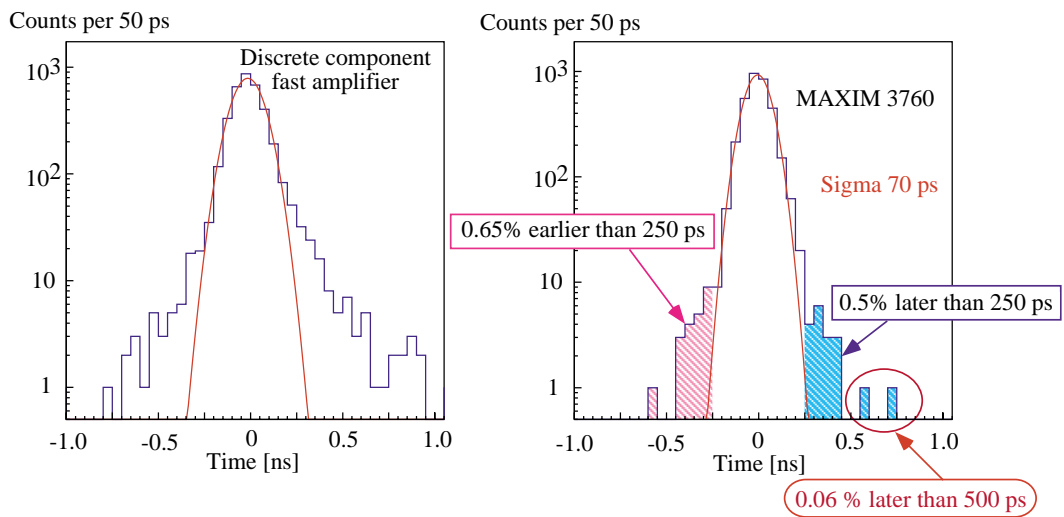


Figure 2.10: T(A) corrected time distributions with the discrete component fast amplifier and with the MAXIM 3760.

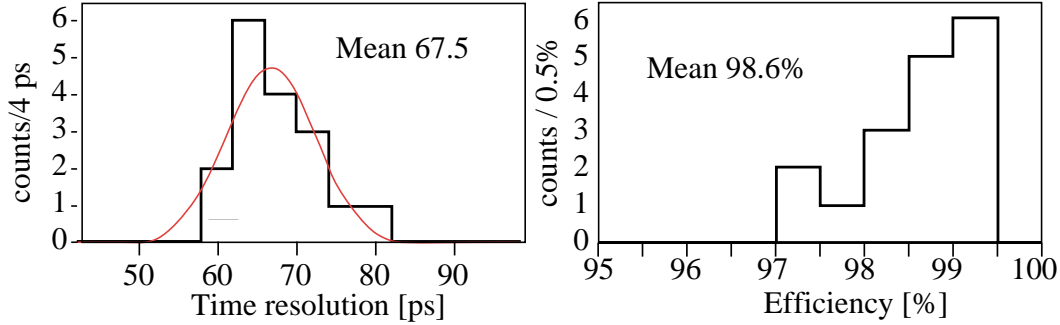


Figure 2.11: Time resolution and efficiency distributions for strip 1.

By substituting the discrete component fast amplifier by a commercial low-noise transimpedance preamplifier (MAXIM 3760) designed as a 622 Mbit LAN optical receiver with a 560 MHz bandwidth, we observed a significant reduction in the slewing of small pulses; this is shown in Fig. 2.7.

The uncorrected time distributions, shown in Fig. 2.8, have $\sigma = 315$ ps, for the case of the discrete component amplifier and $\sigma = 140$ ps for the MAXIM 3760. In Fig. 2.9 we show for comparison the charge spectra measured with the two types of amplifiers. It is clear that the MAXIM has a significant higher gain for very small signals and it is probably this fact that brings about the improvements to the time spectrum (both the reduction in width of the uncorrected time and the reduction in the tails seen on the time spectrum after T(A) corrections).

In Fig. 2.10 we show the T(A) corrected time spectra for the two cases. It is obvious that the tails of the distributions are significantly reduced when the MAXIM is used.

From this point on all measurements shown have been taken using the MAXIM 3760 instead of the discrete component fast amplifier.

2.2.2.3 Uniformity

The uniformity of response of strip 1 was tested by centering the beam on many pads, randomly distributed along the MRPC strip. To do these measurement we had to physically move the front-end electronics cards in different positions. The results are shown in Fig. 2.11. The plot on the left of Fig. 2.11 shows the distribution of time resolution values, with a mean of 67.5 ps; the plot on the right of Fig. 2.11 shows the distribution of efficiency values, with a mean of 98.6%.

2.2.3 Strips 6,7 and 8 - Study of the gap width

One of the frequently asked questions is: how precisely can the gap width be controlled? Hence, how large is the non-uniformity of performance due to variations in the thickness of the spacers and the glass sheets? In the previous subsection we considered strips 1 and 2 and noted that they operated at very similar voltages even though one had gas gaps of $200\ \mu\text{m}$ and the other had $250\ \mu\text{m}$ gaps; however it was not a complete test as glass sheets of different thickness were used for the two strips.

We studied the effect of the variation of the gap width by constructing 3 MRPC strips, each with 6 gas gaps, with identical characteristics (plate material and thickness) apart from the gap width. For these strips we used nylon fishing line as a spacer rather than the optical fiber used for strip 1, but again ran it across the width of the active area every 2.5 cm. This nylon fishing line comes in a variety of thicknesses ($20\ \mu\text{m}$ steps in the range around $200\ \mu\text{m}$) and is very uniform; we have adopted this as the spacer material for all the following strips and for the final design of the TOF MRPC strips.

It should be noted that we have tested the effectiveness of this fishing line as a spacer by taking two sheets of glass and creating a gap by running the fishing line across the width. We found that the gap

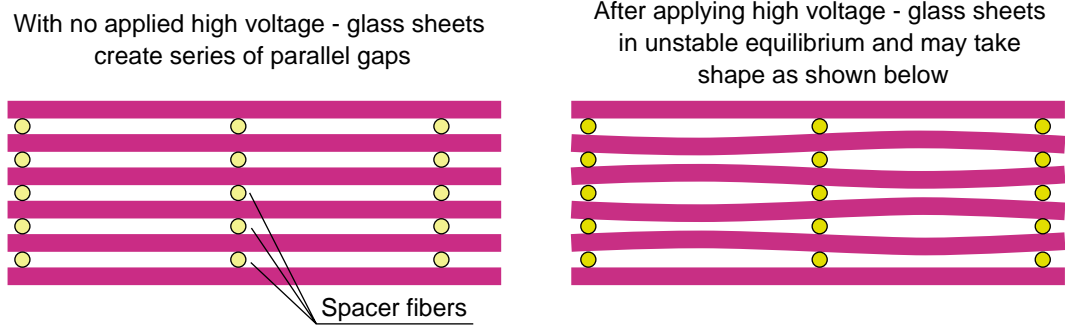


Figure 2.12: Schematic representation of possible variation in size of gas gap after applying high voltage.

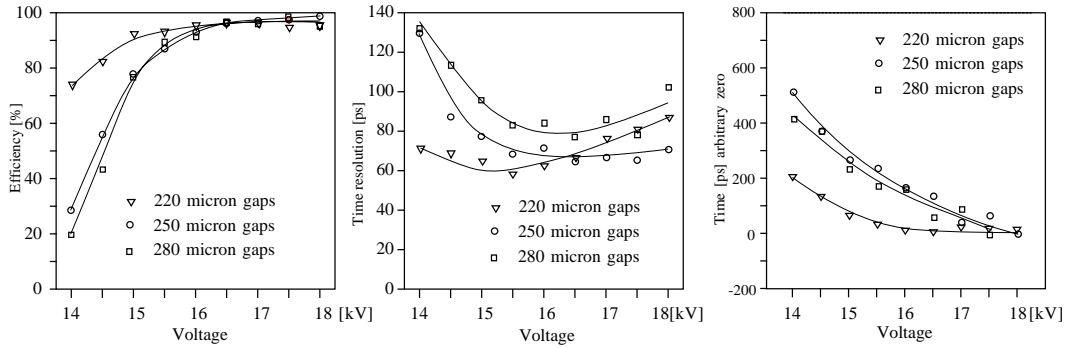


Figure 2.13: Efficiency, time resolution σ and time walk for strips 6, 7 and 8 as a function of the applied voltage.

size was very uniform (within $\pm 10 \mu\text{m}$) and that it was very difficult to compress this fishing line. The electrostatic forces on the two sides of the glass are equal and opposite when all the voltages are exactly as they should be and all gas gaps are exactly the same size. However, since there is a natural tolerance in the exact gap width, the electrostatic forces will become unbalanced; the result is shown schematically in the right-hand picture of fig. 2.12. Therefore the average gap size is as stated below (i.e. 220, 250 and 280 μm), but there will be variations in the exact gap width.

Strips 6, 7 and 8 have the following characteristics:

- 550 μm internal plates from Glaverbel glass
- 2.5 mm external plates from Schott black welding glass (type A10)
- 6 gas gaps of : 250 μm each (strip 6), 220 μm each (strip 7), 280 μm each (strip 8)
- fishing line spacers across the width of the strip, placed every 2.5 cm
- edge defined by the edge of the glass.

2.2.3.1 Performance of strips 6, 7 and 8

Since the key purpose of these tests was to study the dependence of the performance on the gap width, special care was taken to use exactly the same electronics for comparative measurements. In Fig. 2.13 we show plots of efficiency, resolution and time walk as a function of the applied high voltage, for all 3 strips. The measurements were taken with the same electronics channel (same MAXIM preamplifier, same discriminator etc on the front end card, same ADC and TDC channels for the readout). As can be

seen the ‘knee’ of the efficiency plateau is roughly at 16 kV applied high voltage for all three strips. Also at 16 kV one is operating at the best time resolution for a given strip. The right hand plot in Fig. 2.13 shows the time walk versus applied voltage. This is the change in absolute time after T(A) corrections. For each MRPC strip the same T(A) correction has been used for all voltages (the function used for the T(A) correction has been calculated from the data taken at the highest voltage, 18 kV). The MRPC with the smallest gas gap of 220 μm has a very low value of time walk (< 50 ps/1 kV change).

2.2.4 Conclusion

We started the year with the goal of understanding which parameters were critical so that we can build full sized TOF MRPC strips with ease. Since we want to use the thinnest practical glass for the stack (to keep the material budget as low as possible) we found that we had to have sufficient spacers to keep the gaps uniform and to stop the glass distorting (when the electric field was applied). We have arrived at a solution using nylon fishing line stretched across the width of the active area. These spacer lines are placed every 2.5 cm.

The absolute size of the gas gap is not so critical; the gap can be varied from 220 to 280 μm without changing the operating voltage. Smaller gaps give better time resolution and lower time walk, while larger gaps increase the ‘streamer-free’ region of the plateau and enhance the efficiency. We finally selected the gap size of 250 μm . This invariance with gap size is a key ingredient to building large strips. It would be impossible to build units of this size if all the gas gaps had to be uniform to better than, for example, 5 μm as is common for parallel plate chambers with metallic plates. The distribution of efficiency and time resolution shown for strip 1 indicates that devices of this active area (7 cm \times 120 cm) are a realistic choice.

2.3 R&D during 2001 - The double stack MRPC

In the year 2001, the design of the MRPC strips for the TOF was changed. Instead of the single stack MRPC, described up to this point, the double stack MRPC was introduced. The two different types of MRPC are shown schematically in Fig. 2.14. The double stack structure consists of 2 MRPCs, built on each side of the anode pickup pads. The signal we measure in this case is the sum of the signals of the two MRPCs.

The motivations for this change in design were the following :

- The signal from the double stack MRPC is larger by a factor of 2 compared to that from a single stack MRPC with the same characteristics (same number of gaps and gap width).
- We can move the anode and cathode closer, as compared to the single-stack device, thus making the charge footprint of the avalanche smaller; this could sharpen the boundaries between pads.
- A single stack needs a factor 2 higher applied voltage than a double stack (for the case that each stack in the double stack has half the number of gaps of the single stack)
- As a consequence of the above, devices with increased number of gaps can be built, since the practical limitations (high voltage power supplies) become less critical.

A number of such double stack MRPC strips were built and tested during the spring and summer of 2001. Following the numbering of full size MRPC prototypes built in 2000, these were strips 9-12 and had the following characteristics:

- Strip 9 : 2 stacks of 3 gaps of 220 μm .
- Strip 10 : 2 stacks of 5 gaps of 220 μm .

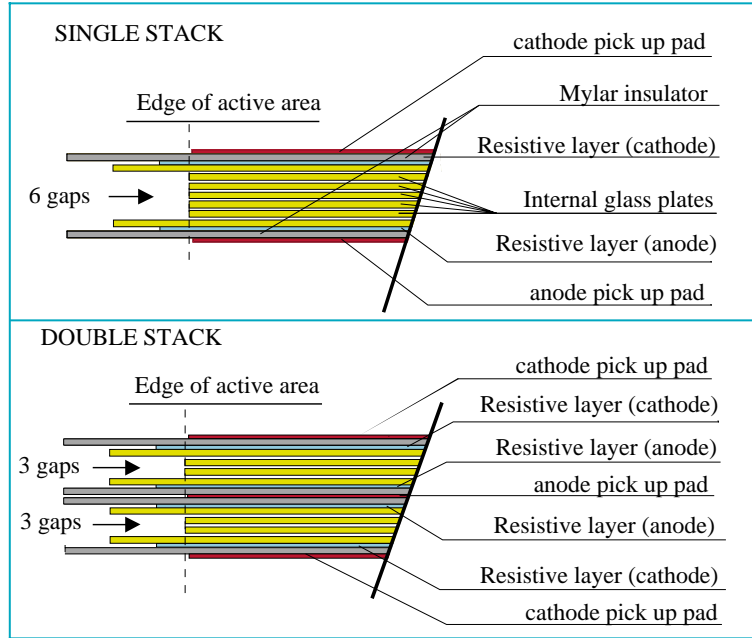


Figure 2.14: Cross section of single stack and double stack MRPC with a total of 6 gas gaps.

- Strip 11 : 2 stacks of 5 gaps of 140 μm .
- Strip 12 : 2 stacks of 5 gaps of 220 μm .

All these strips had internal plates of 550 μm thick Glaverbel glass, external plates of 620 μm thick Glaverbel glass, and fishing line spacers were used every 2.5 cm. The HV electrodes were made out of double-sided adhesive carbon tape with 200 k Ω/square ¹ for strips 9, 10 and 11; for strip 12 a resistive layer of 5 M Ω/square was used, and the technique for applying it on the glass was different: one surface of the glass was painted with acrylic paint loaded with metal oxides².

Strips 9-12 were tested in the usual T10 setup during April-June 2001. In what follows we present a selection of results of their performance.

2.3.1 Efficiency and time resolution

Fig. 2.15 shows the efficiency as a function of the applied differential high voltage (equal and opposite voltages applied to the anode and cathode) for strips 9 and 10. The results are more meaningful and easier to compare if plotted as a function of the electric field inside the gas gap. The electric field is calculated by dividing the applied voltage by the total gas gap. This is shown in Fig. 2.16, where in addition to the efficiency of strips 9 and 10, we show the efficiency for a single stack MRPC with 6 gaps of 220 μm (strip 7). We observe that the efficiency of the 10 gap MRPC is close to 100% and reaches the plateau at lower electric field, thereby extending the plateau of operating voltage (5.7 kV to 6.6 kV). Note that the boundary for streamer production at 120 kV/cm was deduced from the 6 gap stacks (streamers show up as a second peak in the pulse height distribution and by a worsening of time resolution). The maximum voltage of ± 6.25 kV that was applied to the 10 gap stack during this test merely reflects caution on our part and limited beam time; this 10 gap MRPC strip was tested up to ± 7 kV in later tests with no ill effects.

¹Nissin T-9149 Carbon Tape, Kokosai Kinzoku Yakuhin Co. Ltd, Tokyo, Japan

²DETEC di Orietti M.L., viale E. Thovez 16/a, 10131 Torino, Italy

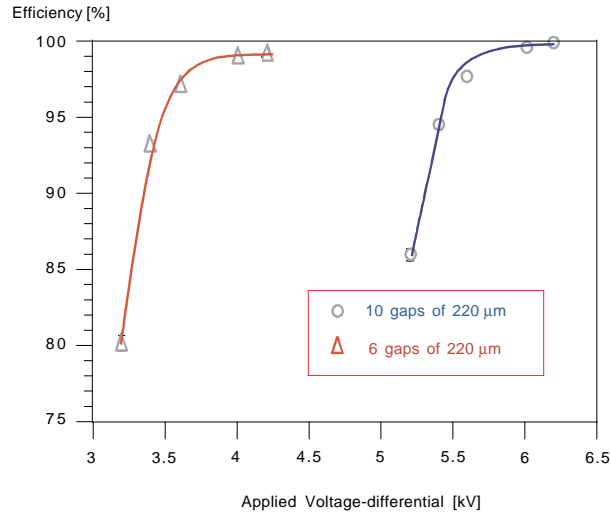


Figure 2.15: Efficiency versus differential high voltage for double stack strips 9 and 10.

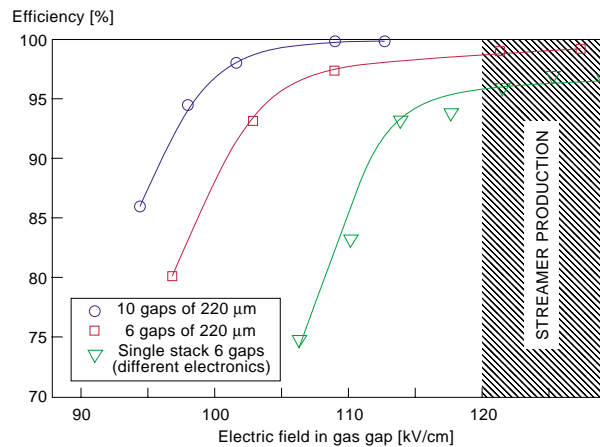


Figure 2.16: Efficiency versus electric field in the gas gap for double stack strips 9 and 10 and single stack strip 6.

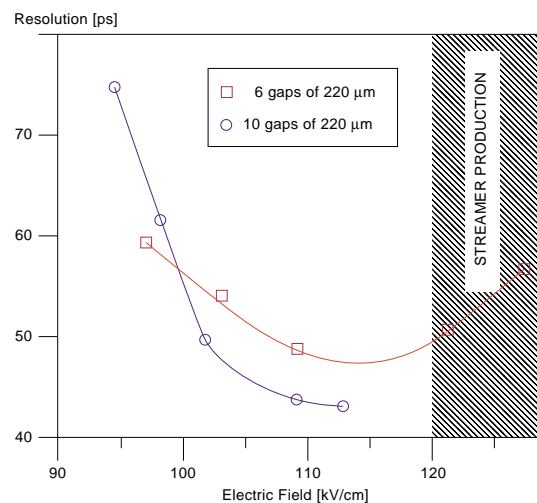


Figure 2.17: Time resolution σ as a function of the electric field for double stack strips 9 and 10.

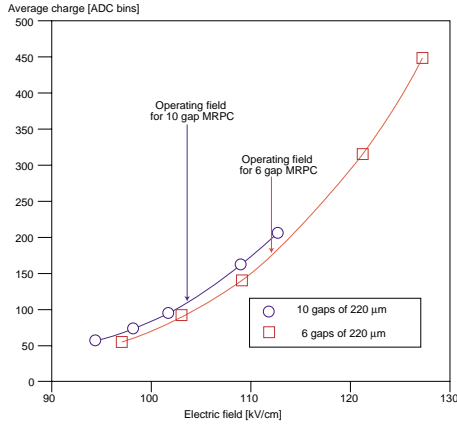


Figure 2.18: Average charge as a function of the electric field for double stack strips 9 and 10.

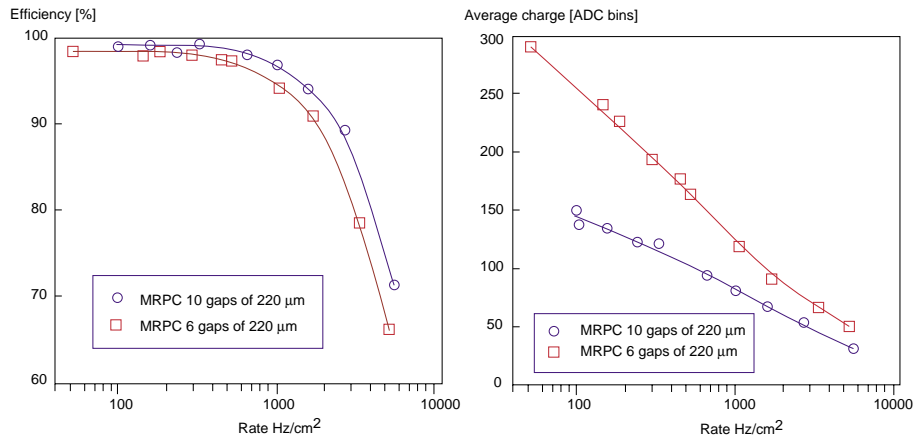


Figure 2.19: Efficiency and average charge versus rate (see text) for double stack strips 9 and 10.

Fig.2.17 shows the time resolution as a function of the electric field for strips 9 and 10. For the electric field corresponding to the knee of the high voltage plateau, time resolution σ between 40 ps and 50 ps is observed.

2.3.2 Average charge

Fig.2.18 shows the average charge of the fast signal (in ADC bins) as a function of the electric field for strips 9 and 10. Since the ‘knee’ of the efficiency plateau for the 10 gap MRPC occurs at a lower electric field, the gas gain will be lower. Less charge being produced for each through-going particle implies that the rate capability should have a corresponding improvement for the 10 gap MRPC. The rate capability in the T10 test beam is shown in Fig. 2.19, where the efficiency and the average charge is plotted as a function of the rate; indeed there is a factor of 2 improvement in the rate capability of the 10 gap MRPC. It should be noted that the rates quoted here are from the pulsed beam at the PS, where we get 2, 3 or 4 spills of 300 ms every supercycle of 15 s; the rate thus calculated in Hz/cm^2 is not equivalent to the same continuous rate as will be the case for ALICE. The rate capability will be discussed in section 2.4, devoted to tests performed at the Gamma Irradiation Facility (GIF) at CERN. Fig. 2.19 is shown here in order to explain the improvement in rate capability with a 10 gap MRPC and not as a measurement of the performance in the continuous flux expected in LHC environments.

2.3.3 Charge spectrum simulation

The almost Gaussian charge distribution obtained with the MRPCs is a key ingredient to their performance. If the avalanches grew following Townsend's formula the charge distribution would be exponential in shape. We have speculated in the past [3] that space charge effects must play a role. Based on the article of Riebler et al. [4] and ref. [3] we have carried out some simple simulations of the avalanche development in the MRPC for a different number of gaps. The aim was to see if we could reproduce the data for the charge distribution in the detector with such a simple scheme and to understand the reasons for the observation that the 10 gap configuration is significantly better than the 6 gap one.

The input parameters for the simulation program are: the Townsend coefficient α , the attachment coefficient η , the average distance between clusters λ and the probability distribution of the number of electrons per cluster. In addition, a maximum number of electrons in an avalanche (cutoff value) is specified. All these pieces of information can be obtained, for a given gas mixture and given conditions (pressure and temperature) and electric field, by the programs HEED [5] and MAGBOLTZ [6], [7].

In a given gap, we generate a number of clusters with distances exponentially distributed with average distance λ . For each cluster, we then generate a certain number of electrons, according to the distribution obtained by the program HEED.

The distance between the cluster and the anode is then divided into a number of steps of fixed size. Each electron will give rise to a number of electrons in the following step, generated according to an exponential probability law.

For each cluster, the avalanche growth is stopped when the total charge generated reaches a certain cutoff value, as originally suggested in ref. [8] to take into account space charge effects in the avalanche development. This cutoff value has been set to be 1.6×10^7 electrons.

In Fig. 2.20 we show the results of two simulations, one for a 6 gap chamber and the other for a 10 gap chamber, compared to experimental data. In both cases the gap size is $220 \mu\text{m}$. The gas mixture was 90% freon, 5% isobutane and 5% SF_6 in normal conditions of pressure and temperature. The value of λ used was 0.1 mm, derived from the HEED program.

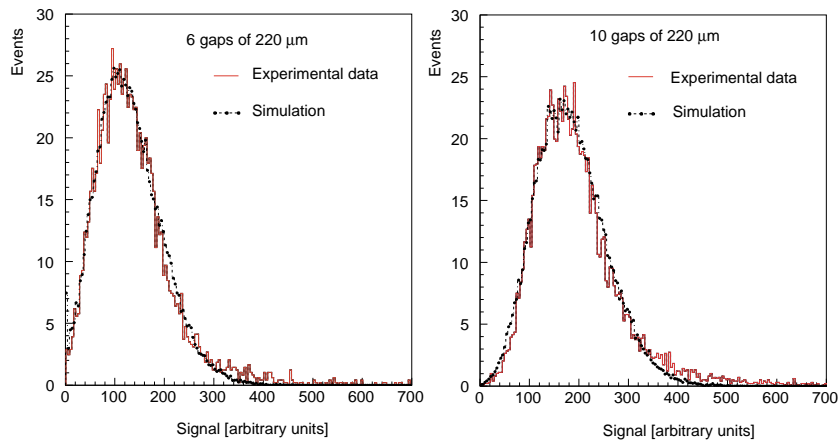


Figure 2.20: Simulated and measured charge distribution for a 6 and 10 gap MRPC operated at the same electric field. The normalisation of the simulated spectra to the data was done by forcing the peaks of the two distributions to coincide.

The charge distribution has an almost Gaussian form, especially for the 10 gap MRPC. The left side of the distribution (very few events at values near zero) is due to the fact that the MRPC operates at high gain, $\alpha D \approx 30$. This means that avalanches starting in the middle of the gap width, which only avalanche over half the distance, give a detectable signal. The charge distribution is the superposition of several probability distributions which, according to the central limit theorem, will tend to a Gaussian form. The

right side of the charge distribution (the fact that the tails are not very long) indicates that indeed the space charge effects stop the development of the avalanche.

With our program we are able to reproduce the qualitative features described in ref. [4].

We then proceeded to simulate the charge distribution for 10 gap MRPCs, varying the gap width and keeping the high voltage fixed. The simulation technique described up to this point takes into account only the avalanche development inside the gas. The signal we measure is the induced signal on the pickup pads due to the movement of the charge, during the avalanche development; this also needs to be considered. In order to calculate the coupling of the movement of the charge to the induced current on the pickup pad we use the weighting field technique [9].

The induced current on a pickup pad is $j = -q\vec{E}_W \cdot \vec{v}$, where \vec{E}_W is the normalised weighting field and \vec{v} is the velocity with which the charge (in the avalanche) is moving. The normalised weighting field is calculated by applying 1 V to the electrode of interest and 0 V to all other electrodes. This normalised weighting field is used only to calculate the coupling of moving charges to the pick-up electrodes; it has no connection with the actual electric field in the device itself. The weighting fields were computed by the commercial program Maxwell of the Ansoft corporation [10].

The electric field inside the 6-gap chamber we considered was 109 kV/cm, the weighting field 0.35 V/mm. The values for the 10-gap chamber are shown in Table 2.1.

In Fig. 2.21 three spectra are shown that are the results of simulation for a 10 gap chamber with different gap sizes (140 μ m, 220 μ m and 300 μ m). The high voltage has been kept fixed at 12 kV across the 5-gap stack. In Table 2.1 we show the values of the input parameters used (Townsend coefficient α , attachment coefficient η , step size, electric field and weighting field for the three gap sizes); the last column shows the average charge of each simulated charge distribution.

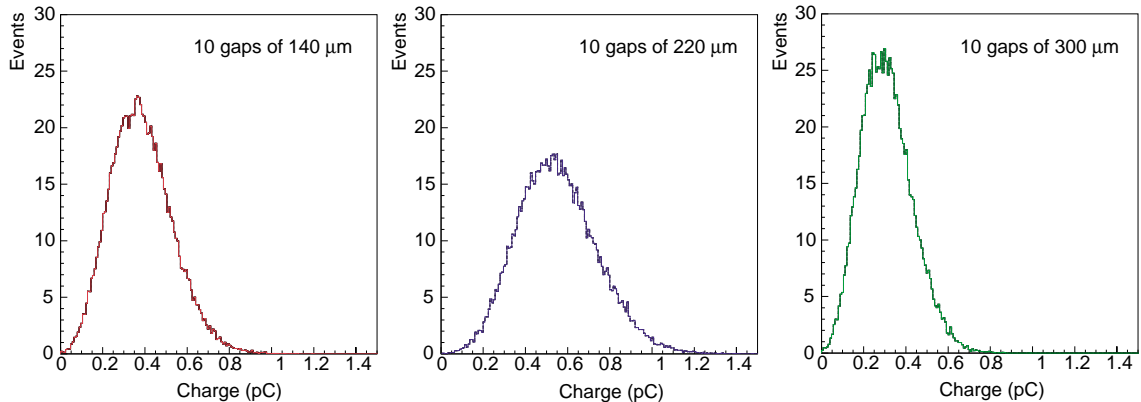


Figure 2.21: Charge spectrum simulation with 3 different gap sizes for a 10 gap chamber.

Table 2.1: Values of the input parameters used for the 10 gap chamber simulation of Fig. 2.21, together with the mean values of the charge.

gap size	$\alpha(\text{mm}^{-1})$	$\eta(\text{mm}^{-1})$	$\Delta x(\mu\text{m})$	E (kV/cm)	E_W (V/mm)	average charge (pC)
140 μ m	384.9	3.2	0.1	170	0.33	0.39
220 μ m	173.4	5.8	0.3	109	0.30	0.55
300 μ m	86.9	9.2	0.6	80	0.27	0.31

One can see that the gap size is not very crucial for the total charge. A reason for this insensitivity could be as follows: at a given applied voltage a device with a smaller gas gap has a higher electric field and therefore a higher Townsend coefficient, as shown in Table 2.1; thus the gain will be higher.

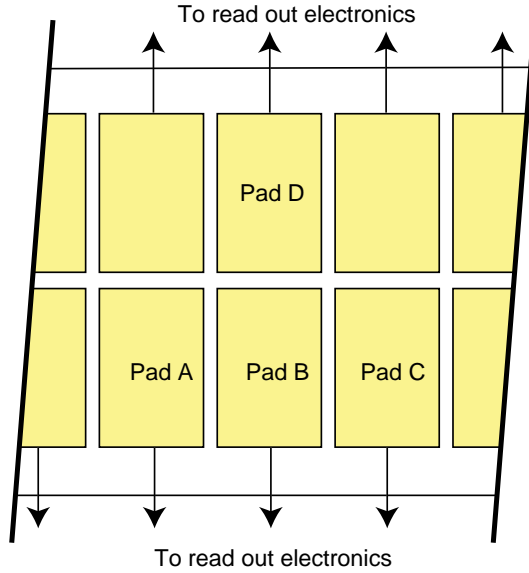


Figure 2.22: The boundaries were evaluated by scanning along the length and across the width of the strip; the labelling of the pads used in other figures is shown here to clarify which boundaries were under test.

However the avalanche grows in size with the distance it travels; thus a smaller gap results in a smaller distance and thus the gain is lower. It seems that we are working in a regime where these effects cancel. This has also been discussed in [11].

2.3.4 Boundaries

The fact that the TOF system consists of long strips read out by individual pads, with some mm spacing between them, means that, at the boundaries between pads, there will be charge sharing between the pads. This will lead to a loss in efficiency on one hand and a probability for double hits on the other hand. In the final system the boundaries have to be optimised so that these two effects are minimised.

To study the boundary effects we scanned all MRPC strips (see Fig. 2.22) along the length of the strip (pad A-pad B-pad C) and across the width of the strip (pad B-pad D), moving the chambers by 5 mm steps.

The factors that play a role in the change of performance at the boundaries of the pads are :

- The exact threshold and the dynamic range of the charge spectrum.
- The size of the ‘charge footprint’ of the avalanche on the pickup pads.

To elaborate the first point, let us consider an event close to the boundary between two neighbouring pads A and B, producing 90% of the charge on pad A and 10% of the charge on pad B : in the ideal case we want pad A to see a hit and pad B to see nothing. To achieve this, the threshold has to be set so that in most cases the 10% level of charge seen on pad B does not fire the discriminator; however the discriminator has to be set at a low enough level so that the efficiency on pad A is not compromised. Obviously the more gaussian shaped and narrow the charge spectrum is, the easier this task becomes.

Fig. 2.23 shows the charge spectrum for strips 9 and 10, at the same electric field. From the different shape of the two distributions near zero (discussed in the previous section) one can see that a very low threshold is needed for the 6 gap MRPC for the efficiency to be high and this would result in the boundaries not being ‘sharp’. The 10 gap MRPC can be operated at a higher threshold with no significant loss in efficiency; thus this produces sharper boundaries.

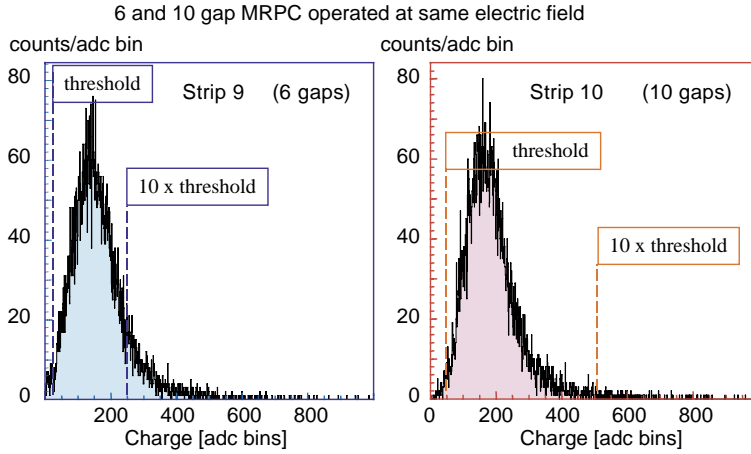


Figure 2.23: Charge distribution for double stack strips 9 and 10.

Concerning the second point, the size of ‘charge footprint’ of the avalanche depends on the total distance between anode and cathode. However there is an additional question: does the carbon layer ‘spread’ the charge footprint? This is shown schematically in Fig. 2.24.

In Fig. 2.25 we show the average charge as a function of the beam position along the strip, for strips 10 and 12. It is clear that the higher resistivity coating makes the boundaries sharper (right-hand plot); thus the lower resistivity carbon layer does spread the charge footprint.

In Fig. 2.26 we show the efficiency as a function of the beam position along the strip, for strips 10 and 12. Here the sharpness of the boundaries is similar, due to the finite dynamic range of the charge spectrum of the 10 gap MRPC.

The uniformity of charge seen for strip 12 affects the time resolution. In Fig. 2.27 we show the time resolution σ as a function of the beam position along the strip, for both strips. Strip 12, which has the $5\text{ M}\Omega/\text{square}$ coating, has much more uniform resolution, which is expected due to the uniformity of the charge.

Fig. 2.28 shows the double hit probability and the global efficiency (OR of neighbouring pads) as a function of the beam position along the strip, for strips 10 and 12. For strip 10 (left) we observe a 1.5% drop in global efficiency at the boundary and 12.5% double hit probability; for strip 12 (right) we observe a 2% drop in global efficiency at the boundary and 8.5% double hit probability.

Fig. 2.29 shows the time walk (variation of absolute time after slewing correction) as a function of the beam position along the strip, for strips 10 and 12. Again the variation of charge at the boundaries shows up as deviation in absolute time - and the high resistivity coating of strip 12 is better, because these deviations are much smaller.

From the measurements of the vertical scan (across the central boundary), we show in Fig. 2.30 the global efficiency (OR of neighbouring pads) and the double hit probability as a function of the beam position across the strip, for strips 10 and 12. For strip 10 (left), the double hit probability from this boundary is 3.8%, whereas for strip 12 (right) it is 3.2%.

2.3.5 Test of the Time Over Threshold method

To verify that a Time-over-Threshold(TOT) measurement is equivalent to direct measuring of the pulse amplitude with an ADC, we calculated the time resolution using the time width (trailing edge - leading edge) of the pulse for slewing corrections. It should be noted here that, since the TDC used during the tests can only register a single hit, we used two separate digital outputs from the front-end analogue card: one for the leading edge timing and one for the trailing edge.

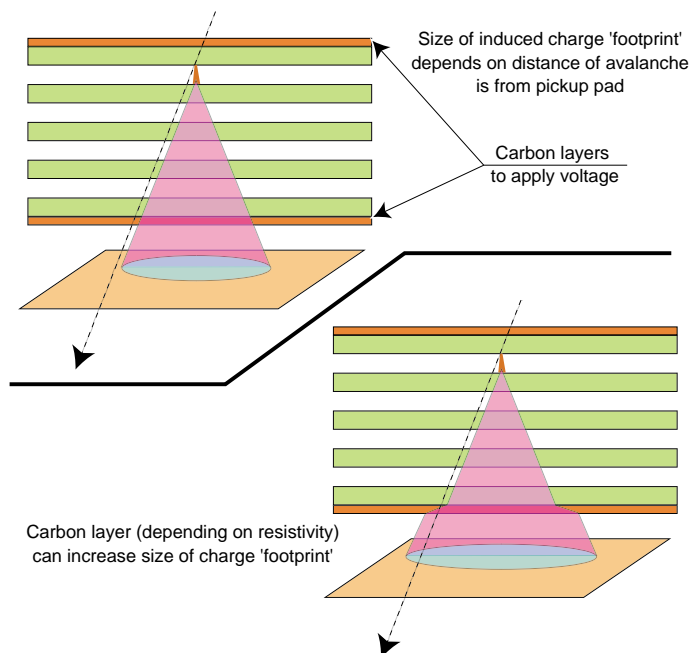


Figure 2.24: Schematic diagram of the avalanche footprint.

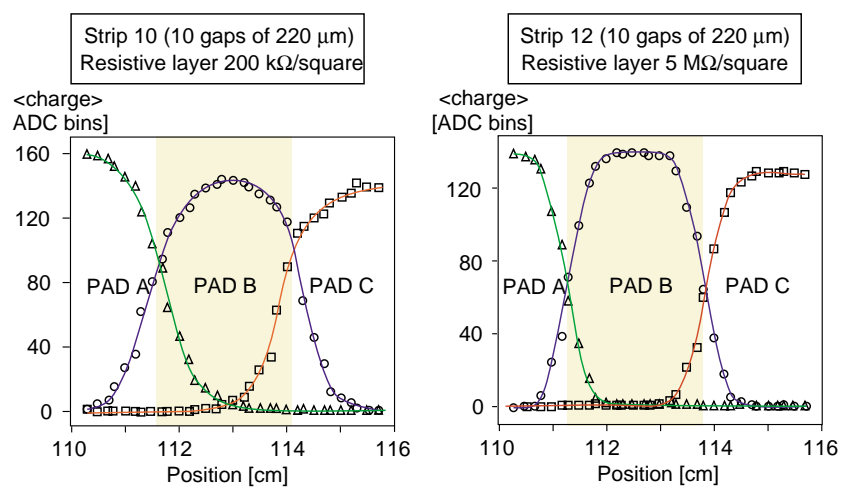


Figure 2.25: Average charge as a function of the beam position along the strip, for strips 10 and 12.

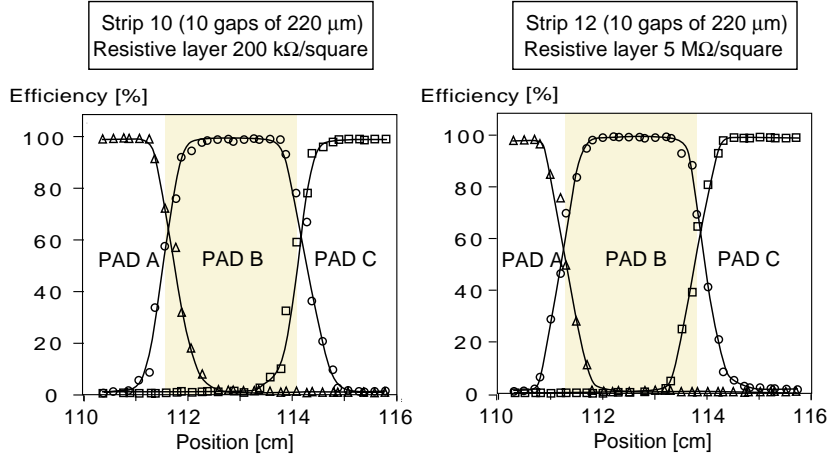


Figure 2.26: Efficiency as a function of the beam position along the strip, for strips 10 and 12.

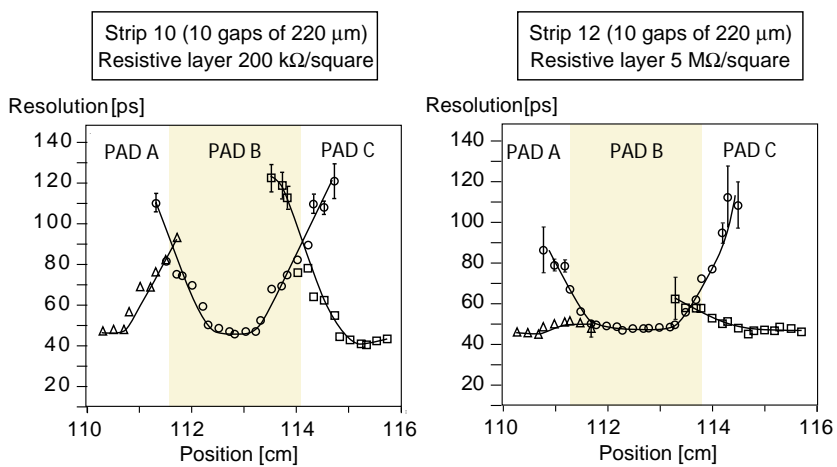


Figure 2.27: Time resolution as a function of the beam position along the strip, for strips 10 and 12.

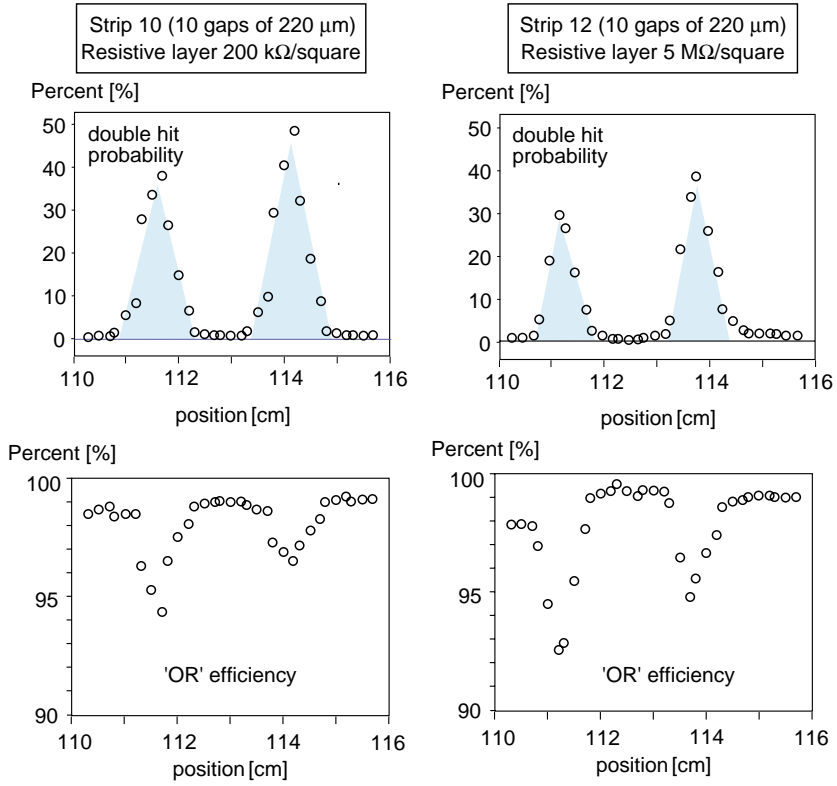


Figure 2.28: Double hit probability and global efficiency (OR of neighbouring pads) as a function of the beam position along the strip, for strips 10 and 12.

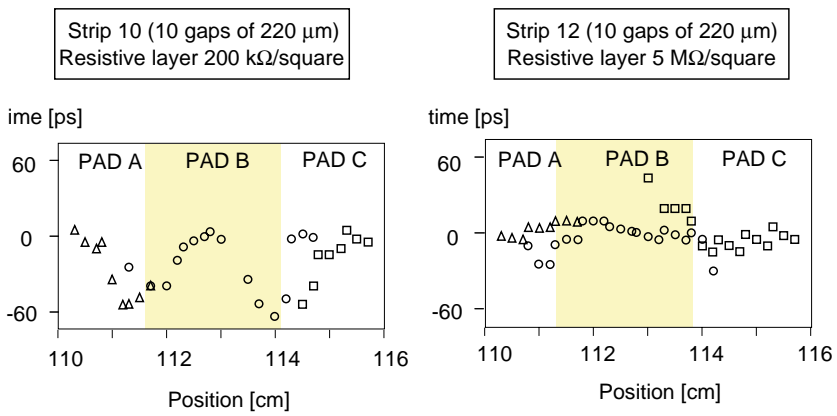


Figure 2.29: Time walk as a function of the beam position along the strip, for strips 10 and 12.

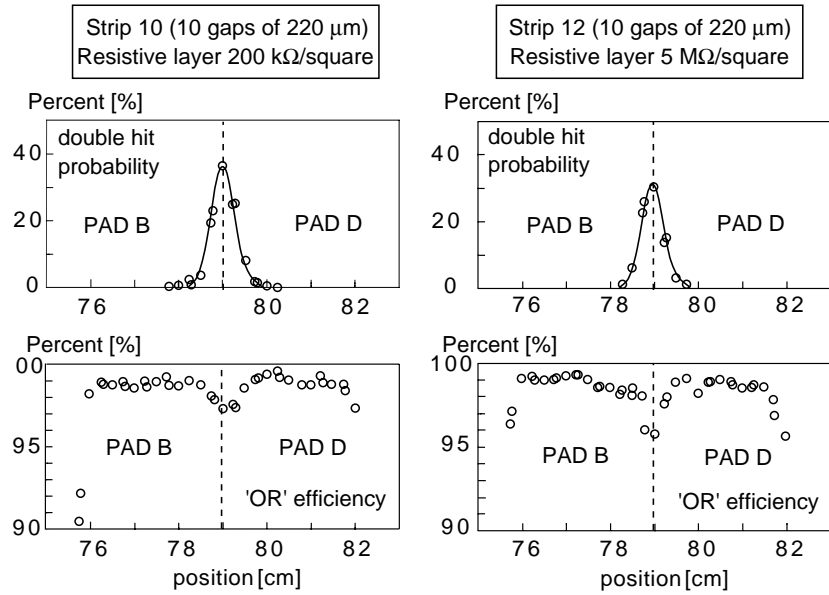


Figure 2.30: Double hit probability and global efficiency ('OR' of neighbouring pads) as a function of the beam position across the strip, for strips 10 and 12.

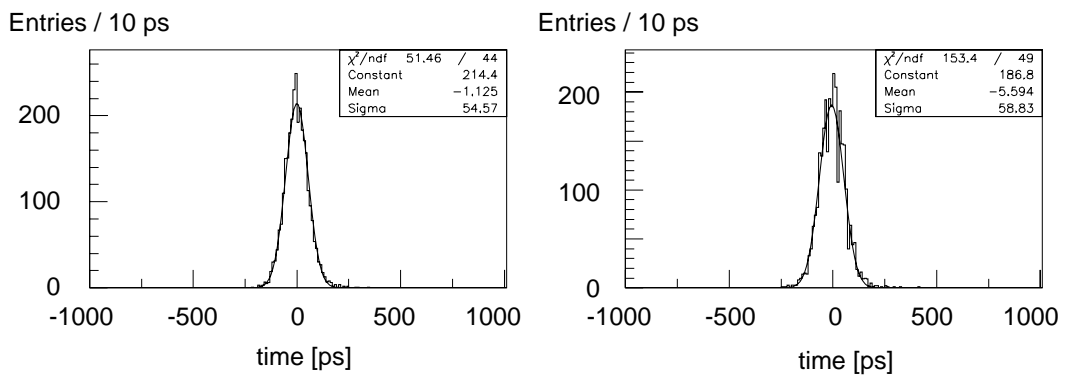


Figure 2.31: Left: time distribution after T(A) correction; right: time distribution after T(time width) correction for strip 10.

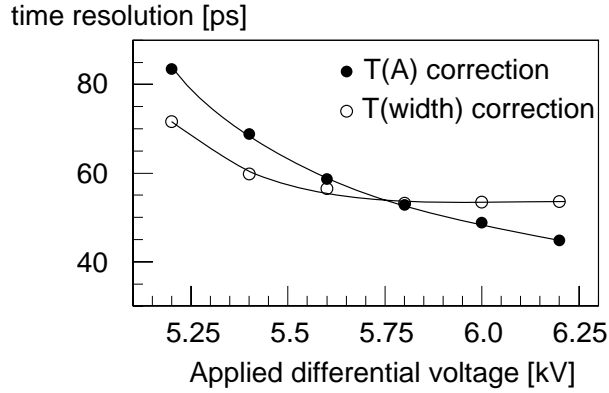


Figure 2.32: Time resolution (ps) using T(A) correction and T(time width) correction as a function of the differential high voltage for strip 10.

In Fig. 2.31 we show the time distribution after T(A) correction on the left-hand side and after T(time width) correction on the right-hand side. The values of the time resolution derived with the T(A) correction (46 ps) and the T(time width) correction (50.6 ps) are in good agreement. The data are from strip 10 and have been taken with differential high voltage of ± 6 kV.

In Fig. 2.32 we show the time resolution as a function of the differential high voltage for strip 10, using T(A) corrections and T(time width) corrections. There is good agreement.

These preliminary tests show that TOT can be used for slewing corrections, and give a time resolution in the 50 ps range.

2.3.6 Conclusion

The double stack MRPC was introduced in order to enhance the performance of the MRPC for the TOF system. The efficiency reached almost 100% and the time resolution 50 ps. However, to really exploit this performance, boundary effects have to be kept small.

For the chosen pad dimensions of 2.5×3.5 cm 2 , a 5 mm wide boundary drawn around each pad represents 30 % of the total area. We need to minimise the probability of double hits at the boundary, minimise the drop in efficiency and minimise the degradation of time resolution. Concerning the efficiency and double-hit probability, this depends on (a) the shape of the charge spectrum and (b) the size of ‘charge footprint’ on the pick-up pad. The shape of the charge spectrum was greatly enhanced by using 10 gaps rather than the 6 gaps originally proposed and this obliged us to continue with a double-stack design. We also found that the resistive coating used to apply the voltage to the stack increased the size of the charge footprint if the resistivity was below 1 M Ω /square. A large-sized charge footprint also led to a degradation of time resolution at the boundaries; while with resistivity above 1 M Ω /square the response was uniform right up to the boundary between pads. The 10 gap double stack MRPC that will be built for ALICE has a global double hit probability of ~ 15 % and a global loss in efficiency due to boundaries of less than 2 %.

2.4 Rate tests of double stack MRPC strips at the GIF

In the summer of 2001, the double stack MRPC strips 10 and 12, described in the previous section, were tested at the Gamma Irradiation Facility at CERN. The purpose of these tests at the GIF, presented in detail in [12], was to measure the change in performance of the MRPC as a function of source intensity; also to equate the source gamma intensity to a flux of through-going charged particles. The ultimate aim

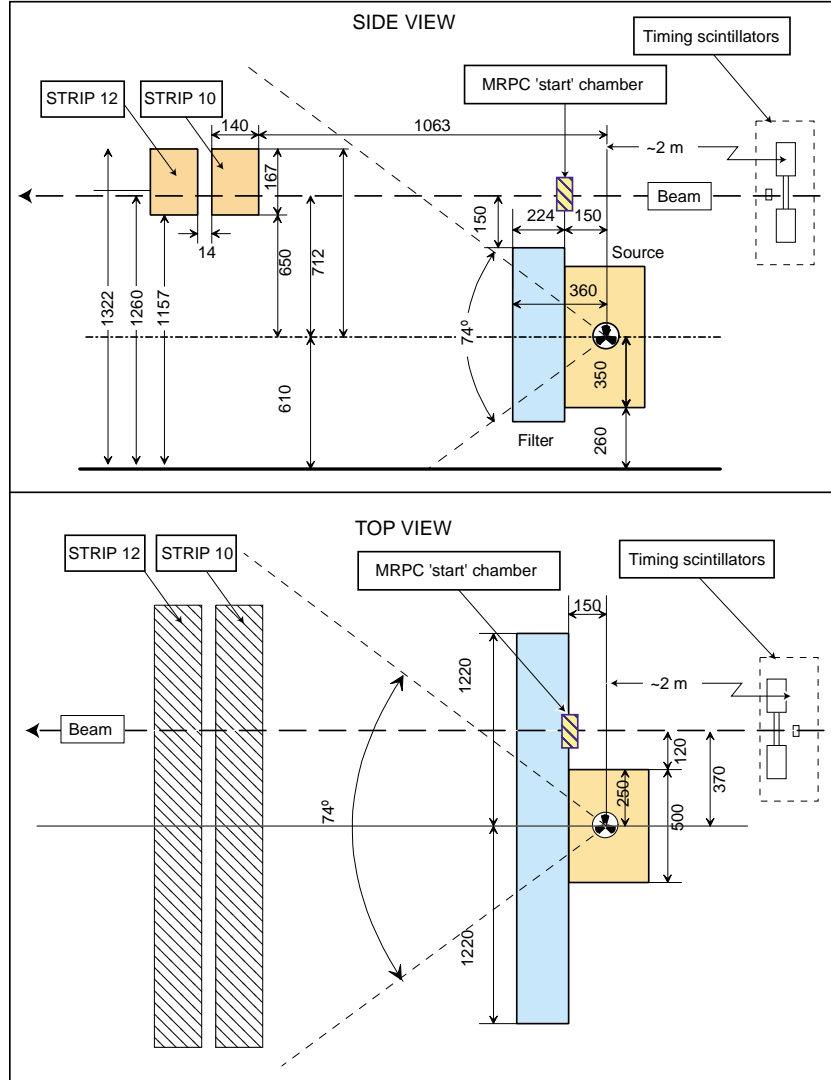


Figure 2.33: Location of the test chambers within the GIF zone at CERN.

is to verify that the performance of the MRPC will remain unchanged at the continuous rate of charged particles expected at LHC.

2.4.1 Description of the GIF and the experimental set-up

The Gamma Irradiation Facility (GIF) [13] at CERN allows a device to be irradiated by 662 keV photons from a 740 GBq ^{137}Cs source; at the same time its performance can be studied using a 150 GeV/c muon beam. This facility is located in the X5 beam in the West Hall at CERN. The two test chambers were mounted in gas boxes made of aluminium with external dimensions of $14 \times 16.7 \times 125 \text{ cm}^3$. The positions of the test chambers within the GIF zone are shown in Fig. 2.33. Strip 10 was at a distance of 116 cm from the source, while strip 12 was at 130 cm. Various filters can be placed in front of the source to vary the intensity of the gamma flux. These filters are specially shaped to give a uniform flux over a planar surface; the filter numbers refer to the attenuation with filter 1 corresponding to full source intensity, while filter 2 corresponds to 50 % of the full source intensity (i.e. flux from source $\sim 1/\text{filter number}$).

Data were taken triggering on through-going muons while the test chambers were exposed to a back-

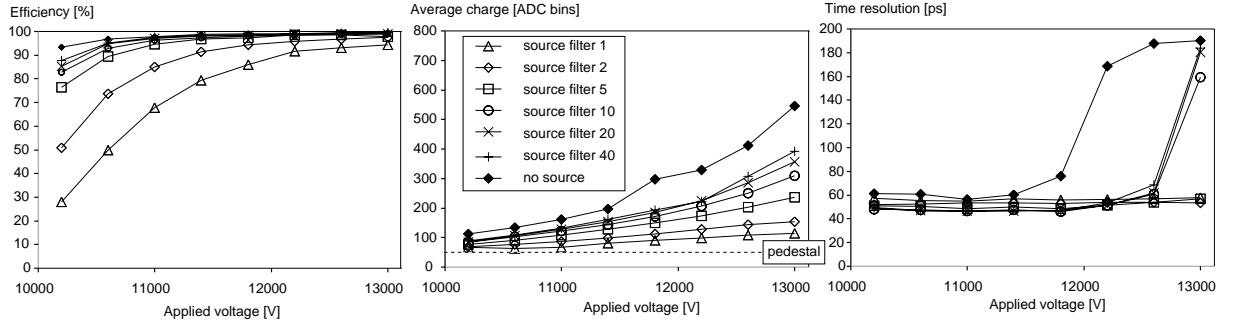


Figure 2.34: The efficiency, average charge and time resolution versus applied voltage for strip 10 with various source intensities.

ground flux of gammas. The experimental set-up was quite similar to that used at the T10 test beam, described in Sec.2.2.1. However, due to the very limited space at the GIF, no tracking chambers were used and no special trigger scintillators. The muon trigger was generated by two scintillators of dimensions $2 \times 2 \times 10 \text{ cm}^3$ arranged in a cross so that an area of $2 \times 2 \text{ cm}^2$ was selected. These two scintillator bars were read out by four photomultipliers; the signals were discriminated by constant fraction discriminators and the average used as the time reference for time resolution studies of the chambers. The time jitter of this averaged signal was estimated to be 30 ps. Another large scintillator (area of $20 \times 20 \text{ cm}^2$) was located downstream of the concrete wall surrounding the GIF zone; thus the trigger was unaffected by the intensity of gammas. In addition a ‘start’ pretrigger was generated by a small MRPC chamber (active area $4 \times 4 \text{ cm}^2$) located just above the GIF source. The reason for this pretrigger system is explained in Sec.2.2.1. We had to use 30 m of twisted-pair flat cable to sufficiently delay the TDC signals. The beam spot was larger than a readout pad ($2.5 \times 3.5 \text{ cm}^2$), thus we carefully aligned the two test chambers so that the pads of one chamber were aligned with the other. Thus we could use an offline selection where we demanded a valid ‘hit’ in strip 10 when we were studying strip 12 and vice-versa.

2.4.2 Some results of the measurements

We show in Fig. 2.34 the efficiency, the average charge and the time resolution as a function of applied voltage for various source intensities for strip 10. As mentioned the purpose of these tests at the GIF is to measure the change in performance of the MRPC as a function of source intensity . Since the MRPC is a parallel plate chamber with resistive plates, the performance of the device will depend on the current drawn by the device, since this will generate a voltage drop across the resistive plates that will lead to a reduction of the electric field within the gas gap. The reduction in voltage is the current drawn by the MRPC (a quantity we measure) multiplied by the resistance of the two stacks (in parallel). Previously we have measured the volume resistivity of the glass to be $\sim 10^{13} \Omega\text{cm}$, however we found that the MRPC had a performance better than expected using this value of resistivity. We have therefore deduced a value of the resistivity of the glass while the MRPC was in operation. Since the performance of the MRPC should depend solely on the electric field within each gas gap, there should be a unique curve for a variable such as efficiency when plotted against the effective voltage (where the effective voltage is the applied voltage minus the voltage dropped across the resistive plates). By varying the assumed resistivity of the glass plates we can change the effective voltage for a given set of measurements. We followed this procedure changing resistivity until we find that the data does follow a single curve. This is shown in Fig. 2.35 for strip 10 where the efficiency is plotted against effective voltage. The central plot is for a value of resistivity of $2.6 \times 10^{12} \Omega\text{cm}$. The top plot in Fig. 2.35 is for a value of resistivity 20 % lower, while the bottom plot is for a value 20 % higher. A similar exercise was carried out for strip 12 resulting in the same value of resistivity for the glass plates.

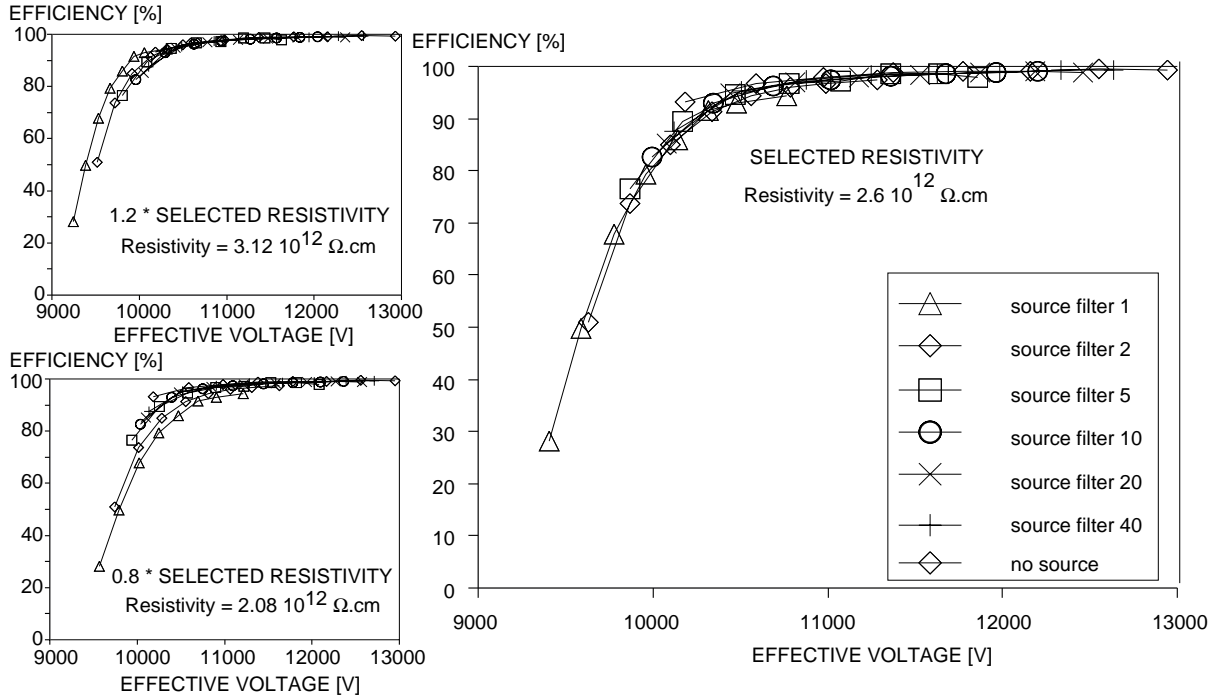


Figure 2.35: The efficiency of strip 10 for various source intensities. The effective voltage is the voltage across the gas gap; thus it is the applied voltage minus voltage dropped across the resistive plates. The voltage dropped across the resistive plates is calculated from the measured current and the resistivity of the glass plates. This resistivity is varied to make the efficiency plot shown above to follow a single curve. The resistivity of $2.6 \times 10^{12} \Omega \cdot \text{cm}$ gave the best result. The effect of changing this resistivity by 20 % is shown in the top-left and bottom-left plot.

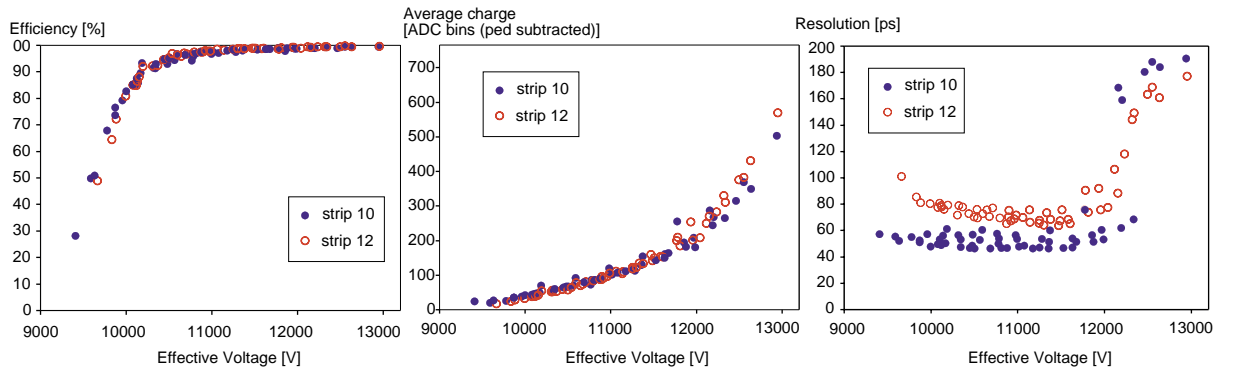


Figure 2.36: Efficiency, average charge measured in ADC bins and time resolution versus effective voltage for various source intensities.

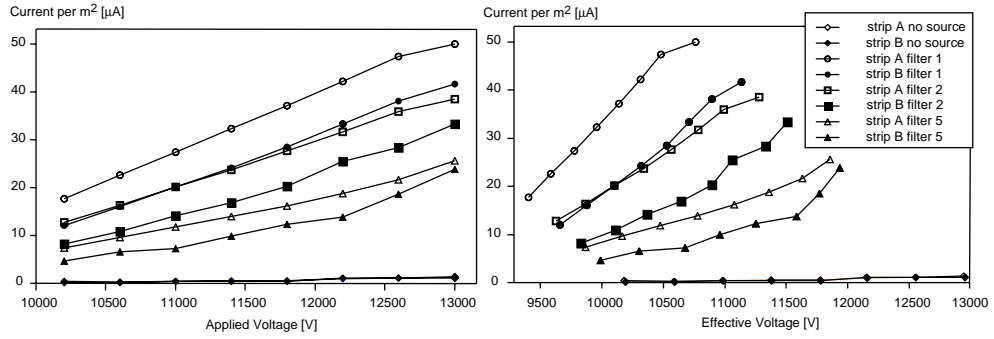


Figure 2.37: Current drawn by the MRPC strips (normalised for 1 m² area) versus voltage for various source filters. The left plot shows the current versus the applied voltage across a 5 gap stack, while the right plot shows the current versus the effective voltage. Details are given in the text concerning the meaning of effective high voltage.

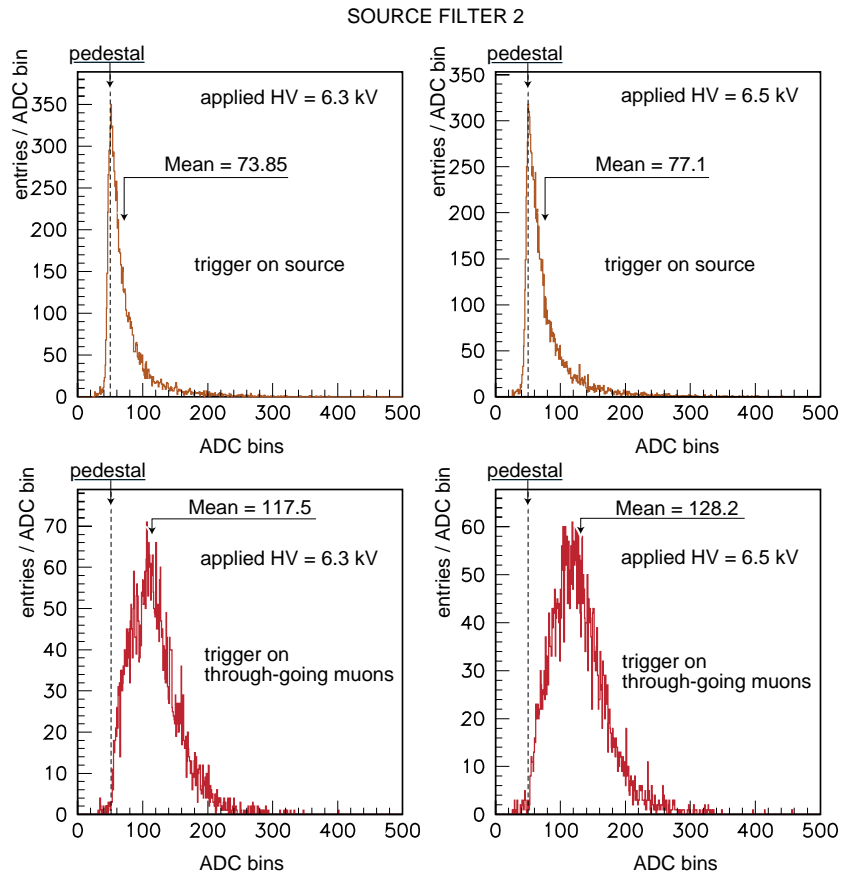


Figure 2.38: Pulse height spectra of MRPC when irradiated by gammas (filter 2). The top two spectra correspond to triggering on ‘hits’ on a given pad; the lower two spectra correspond to the same pad but triggering on through-going muons.

The results for efficiency, average charge and time resolution are presented in Fig. 2.36 for both strips 10 and 12 for all the data taken at various source intensities. The time resolution is somewhat different for the two strips with ~ 50 ps for strip 10 and ~ 65 ps for strip 12. Since this corresponds to illumination of a large fraction of the $2.5 \times 3.5 \text{ cm}^2$ pad, both these time resolutions are very good.

In Fig. 2.37 we show the current drawn by the strips plotted against applied voltage across the 5 gap stack, and also plotted against the effective voltage (as defined above).

We are interested in the performance of the MRPC strip in a background flux of charged particles; thus we need a way of equating this flux of gammas to a flux of charged particles. One way to do this is to use the measured current. We have measured that the average charge of the signal is ~ 300 fC at the knee of the efficiency plateau for a through-going charged particle. However this is only the fast component and the majority of the charge is generated by the drift of the positive ions towards the cathode. We have not measured the ratio of (fast charge)/(total charge) for this configuration of MRPC, but a value of 1:10 could be expected (see ref. [3] for a measurement of this ratio for a 2 mm gap RPC). Thus we would expect every through-going minimum ionizing particle to produce an average of 3 pC of charge. Therefore the current of $50 \mu\text{A}/\text{m}^2$ corresponds to a flux of charged particles of $1.7 \text{ kHz}/\text{cm}^2$.

Another way to evaluate the equivalent flux of charged particles is to measure the rate of interacting gammas for a given area; this rate has to be corrected since an interacting gamma does not produce the same amount of charge as a through-going charged particle. We measure the ‘fast’ charge of interacting gammas and compare these with the measured charge spectrum when triggering on through-going muons. With the source on and filter 2 in place, the measured spectra for applied voltage of ± 6.3 kV and ± 6.5 kV are shown in Fig. 2.38 for two cases (triggering on through-going muons and triggering on ‘hits’ on a given pad). By comparing the means of these distributions, one finds that the average ‘fast’ charge generated by through-going muons is 2.85 times larger than the charge produced by an interacting gamma. However the distributions shown for the gamma source trigger in Fig. 2.38 are the charge measured on a given pad when there is a hit on the same pad. Many of these interacting gammas will be near the boundary between two pads and the total induced charge will be given by the sum of two or more pads. Unfortunately the measurement of the interacting gamma spectra was performed with only one pad read out and we do not have data corresponding to the total induced charge. We assume that this will increase the mean pulse height of the interacting gamma spectra by 50 %; thus the ratio of average fast charge generated by through-going muons is 1.9 rather than 2.85 as stated above. We therefore divide the measured counting rate by 1.9 to get the equivalent flux of through-going muons. For full source intensity with applied high voltage of 13 kV we measure a counting rate of $3.1 \text{ kHz}/\text{cm}^2$ for strip 10. Using the correction factor discussed above indicates that the effective rate of through-going muons is $1.63 \text{ kHz}/\text{cm}^2$. Since these two techniques of evaluating the equivalent flux of through-going muons give very similar results, we have confidence in the values that we quote. We will use the technique based on the counting rate plus correction factor in the following evaluation of the rate capability.

We show the efficiency and resolution versus the equivalent flux of through-going particles in Fig. 2.39 for both a fixed applied voltage of 11.4 kV and for an effective voltage of 11.4 kV. It is clear that the efficiency remains high until a flux of $\sim 1 \text{ kHz}/\text{cm}^2$ for a fixed applied voltage of 11.4 kV, but if one has the freedom of increasing the voltage depending on the drawn current, then it is clear that the MRPC has high efficiency at the highest measured flux close to $2 \text{ kHz}/\text{cm}^2$. There is a noticeable degradation in time resolution at very low particle flux. A possible cause is that the internal resistive glass plates are floating. The voltage on these plates is stabilised to the ‘correct’ voltage by the flow of electrons and positive ions created in the avalanche process. At very low particle flux there are too few avalanches to ‘lock’ the voltages on these internal plates. One should recall that the MRPC has extremely low dark current (below $0.5 \mu\text{A}$ for 1 m^2 active area) so that the resistance between anode and cathode is greater than $10^{10} \Omega$; thus the voltage on an internal plate will slowly change depending on very small leakage currents to the voltage planes at the anode and cathode electrodes. The MRPCs discussed here were not constructed in a very clean environment; it is probable that this degradation in time resolution at low particle fluxes will become less when a clean environment is used.

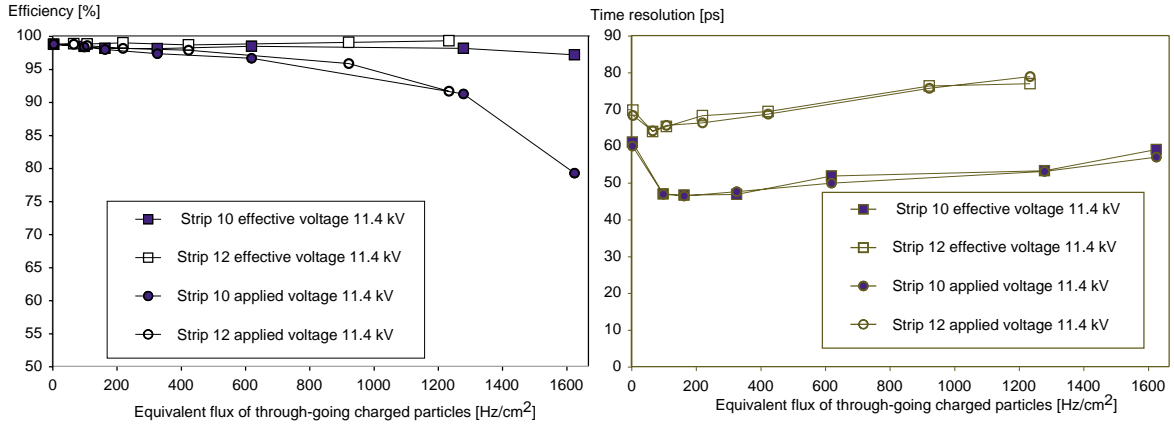


Figure 2.39: Efficiency and time resolution for strip 10 and strip 12 for a voltage of 11.4 kV versus equivalent rate of through-going charged particles. Details are given in the text concerning the meaning of applied and effective high voltage.

2.4.3 Rate capability

The maximum expected flux of particles at the TOF array located at 3.7 m radius in the ALICE experiment is 50 Hz/cm². We are clearly working with a device that has a rate capability far in excess of this value. We found that the bulk resistivity of the glass is $2.6 \times 10^{12} \Omega\text{cm}$ when the glass is in operation inside the MRPC, instead of the higher resistivity of $10^{13} \Omega\text{cm}$ that we had measured in the lab. This reduction of resistivity by a factor 4 translates into an increase in the rate capability by a factor 4 compared to what was expected using the lab measurement of the resistivity. We have considered possible causes for this change in resistivity and discuss them extensively in [12].

2.4.4 Power dissipation

We have shown that our device operates at a flux of 1 kHz/cm²; a major reason for this is that the charge of the signal is small and the charge spectrum is almost gaussian shaped. The good shape of the charge spectrum allows us to work at relatively high threshold (50 fC) but still have a long streamer-free plateau with close to 100 % efficiency. The small signal also means that the power dissipated by the MRPC is small. For example the MRPC operating at an effective voltage of 11.4 kV (applied voltage = 12.6 kV) with an equivalent flux of 1.6 kHz/cm² draws a current of 50 $\mu\text{A}/\text{m}^2$. Thus 570 mW/m² is dissipated in the gas and 60 mW/m² into the glass plates.

2.4.5 Conclusion

The GIF tests of the MRPC strip clearly show that this device can operate far in excess of the 50 Hz/cm², which is the maximum rate expected at the ALICE TOF array. The reason for this excellent behaviour is due to (a) the modification of the bulk resistivity of the glass sheets and (b) the small amount of charge produced for each through-going charged particle. The small charge produced in the MRPC equates to low power dissipation in the gas even at rates of 1.6 kHz/cm² (we measure 630 mW/m²).

2.5 Tests of first prototypes of a central module of the TOF system

In the autumn of 2001, two prototypes of the central module of the Time of Flight System were constructed, equipped with MRPC strips and tested with beam. The purpose of these tests was manyfold.

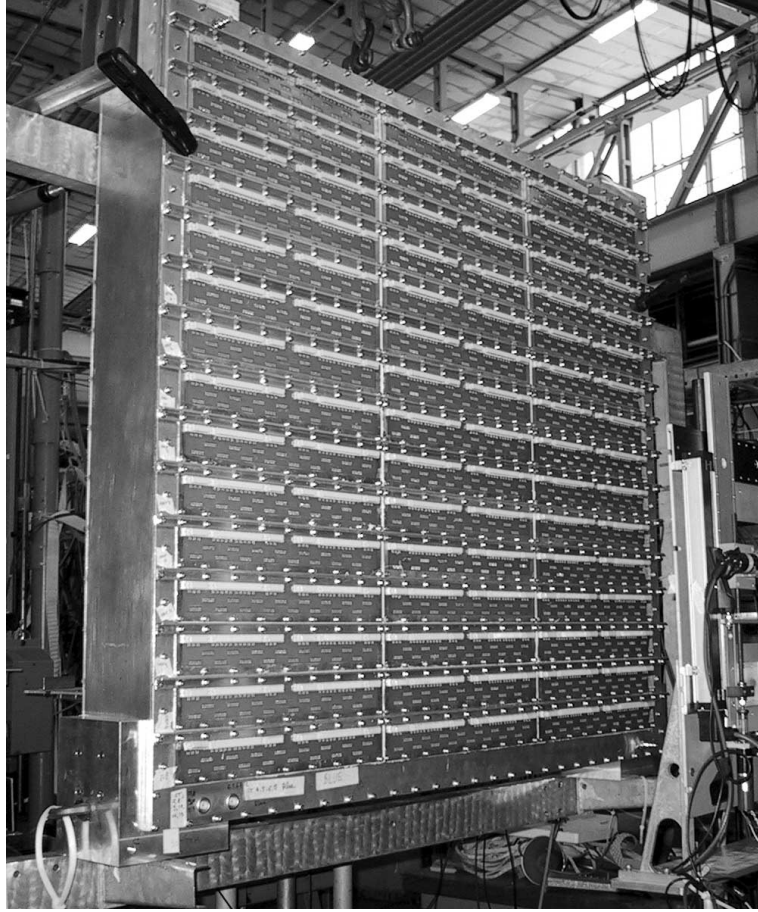


Figure 2.40: View of the prototype of the ALICE central module inside the T10 beam area. The surface seen contains the interface cards; the front-end electronics cards are plugged into the connectors on this surface.

- To study the various aspects of construction of the modules.
- To study the problems of installing the MRPC strips inside the module, the exact routing of cables, the interface between readout pads and front end electronics, the system of high voltage distribution etc.
- To establish that the performance of the strips is the same when they are inside the modules as when individually tested.
- To study mass production problems for the MRPC strips (18 such strips were produced).
- To study the uniformity of performance of the MRPC strips.

2.5.1 The prototype modules and the MRPC strips

Two prototype modules were constructed, both with the dimensions of the central TOF module. One was designed and constructed in Bologna and the other at CERN. Fig. 2.40 shows the CERN module installed in the T10 beam area at CERN. It is an aluminium box with dimensions 125 cm x 114 cm x 16 cm, designed to contain 15 MRPC strips. These are placed in two layers with an overlap so that there are no dead areas. This is shown in the cross section of the module in Fig. 2.41. One surface of this module is covered by interface cards. The front-end electronics are plugged into the outer side of the

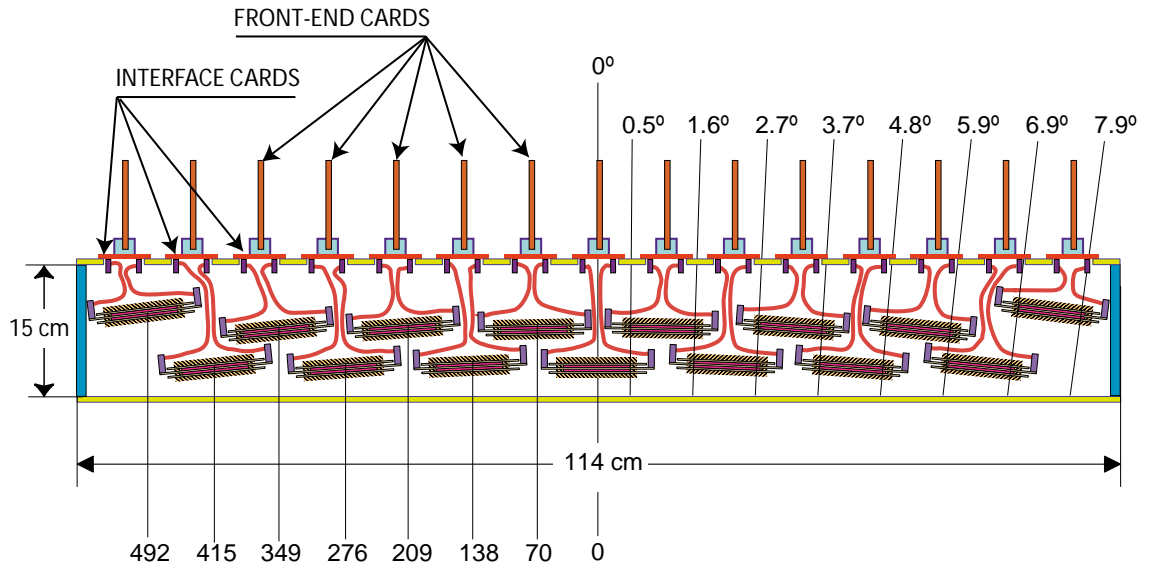


Figure 2.41: Cross section of prototype module with MRPC strips.

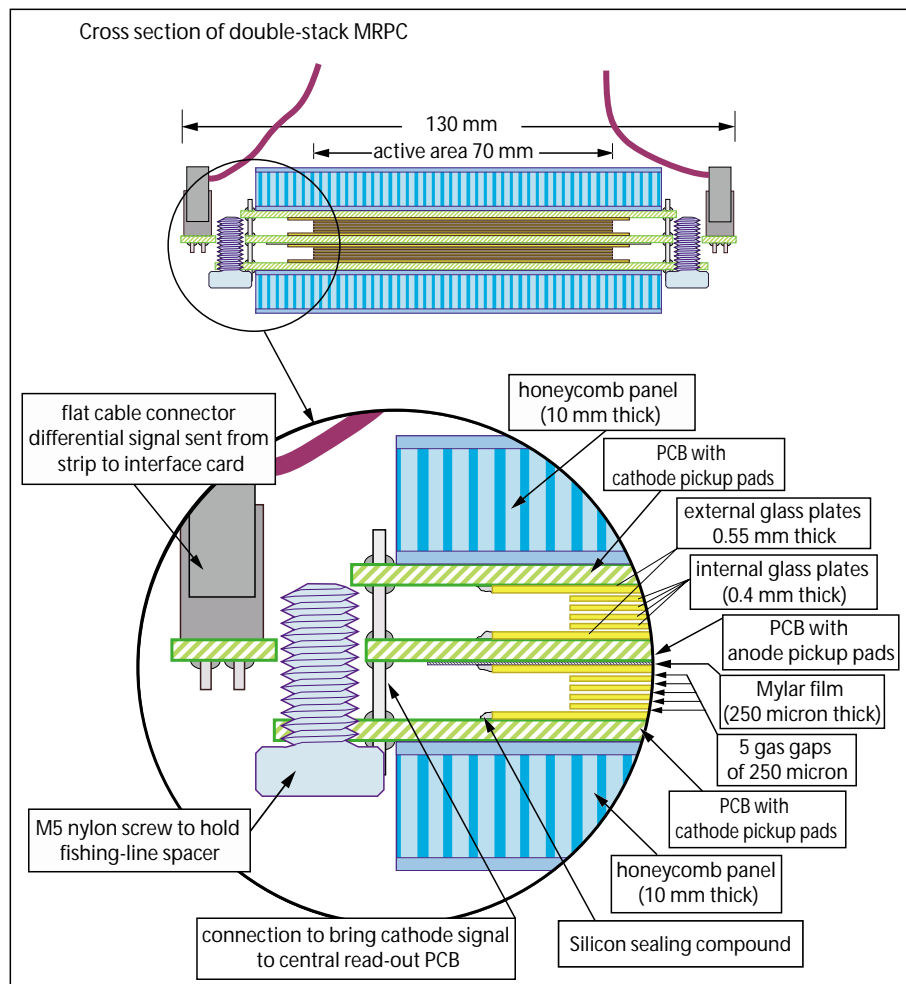


Figure 2.42: Schematic cross section of double stack MRPC strip.

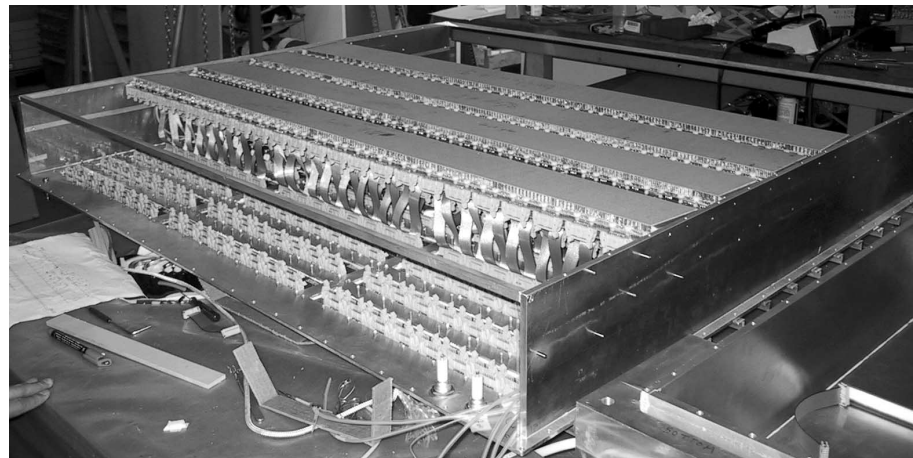


Figure 2.43: Photograph of prototype module with MRPC strips during assembly.

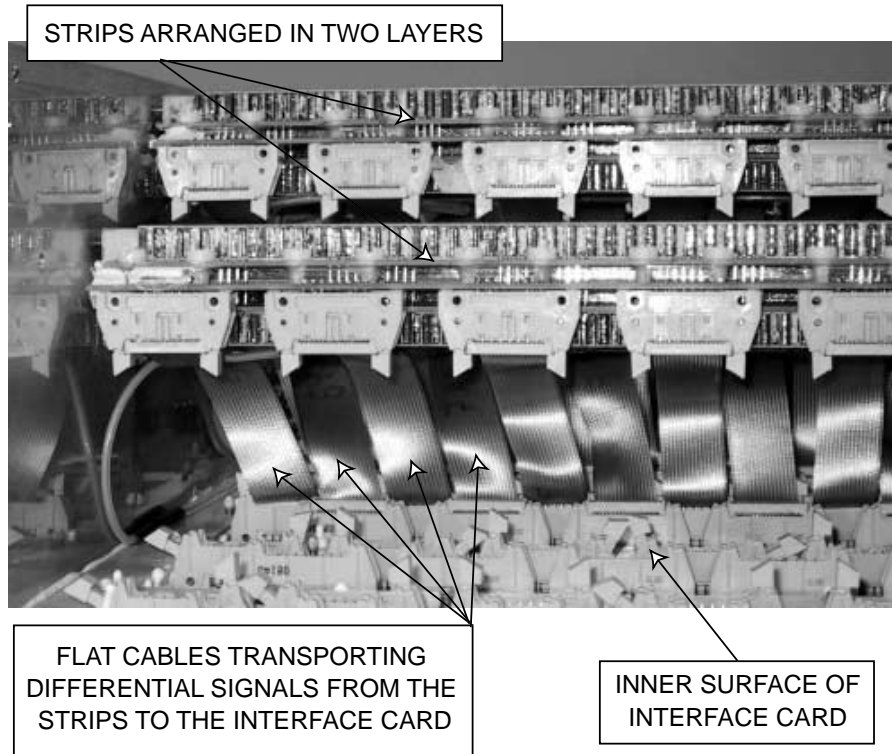


Figure 2.44: Details of the cables bringing the differential signals from the pick-up pads on the MRPC strips to the interface cards.

interface cards, as seen in the photograph of Fig. 2.40. Short flat cables bring the signals from the pickup pads of the MRPC strips into connectors mounted on the inner side of the interface cards. This is shown schematically in Fig. 2.41. There were three interface cards per strip, each serving 32 pickup pads (2 FE cards). Four high voltage connectors are used for the HV for this prototype module with the MRPC strips separated in two groups, each taking HV(positive and negative) from different channels of the HV power supplies.

The MRPC strips which were constructed and inserted in the two modules had the design shown in Fig. 2.42. They were of the double-stack type and had a total of 10 gas gaps of $250\text{ }\mu\text{m}$ each. To complete the R&D study concerning material, there were some slight variations between strips. The resistive coating for the high voltage electrodes had a value of $1\text{ M}\Omega/\text{square}$ for most strips, however one strip had $5\text{ M}\Omega/\text{square}$ and another had $18\text{--}20\text{ M}\Omega/\text{square}$. The internal glass sheets were $400\text{ }\mu\text{m}$ thick for most strips, with two strips built with slightly thicker glass of $550\text{ }\mu\text{m}$. Finally the PCB board with the anode and cathode pickup pads was 1.6 mm thick for most strips, with three strips built with 0.8 mm thick PCBs.

18 such MRPC strips were built in a period of 4 weeks. Each completed strip was first tested for holding HV in air. Once it had passed this test, it was installed in a test box designed for investigating individual strips and put under gas flow. After change of 5 volumes its performance was tested in the beam. 60% of the MRPC strips were tested in this way.

After being tested individually, the strips were mounted inside the modules. The CERN module was equipped with a total of 10 strips; the Bologna module with a total of 8 strips. Fig. 2.43 shows photographs of one module open with the strips inside and detail of the routing of the cables. Each cable brings the signal from 2 readout pads to the FE electronics. Fig. 2.44 shows the details of the flat cables carrying the differential signals from the strips to the interface cards. The modules were closed, tested for gas leaks and installed inside the T10 experimental area under gas flow of 7 l/h .

2.5.2 Test beam results

The modules were mounted on moving frames, so that it was possible to illuminate with the beam any strip inside them. After adequate volume changes (roughly 7) the full high voltage was applied. We systematically studied the high voltage plateau for all 18 strips. Here we present some of the results.

Fig. 2.45 shows the dark current of the MRPC strips as a function of the high voltage. This measurement was done with all 10 strips of the CERN module under HV. Four values of the current were being measured, corresponding to the four HV power supplies used for each module; the values shown are: the average of the sums (of the positive and negative high voltage power supply) normalised to the active area. Each curve corresponds to measurement of the dark current when that strip was in the beam. The curves are not smooth as the current would vary according to the temperature and atmospheric pressure. Also the dark current was still decreasing with time changing from $\sim 1\text{ }\mu\text{A/m}^2$ to $\sim 0.5\text{ }\mu\text{A/m}^2$ several days later. This is the first time we have measured a sufficiently large active area to make an accurate measurement of the dark current for the MRPC. We now know that the final value for the TOF system will be below $0.5\text{ }\mu\text{A/m}^2$.

Fig. 2.46 shows the efficiency and time resolution σ as a function of the applied differential high voltage for strip 7 of the CERN module, measured individually (Sept. 2001) and inside the module (Oct. 2001). It should be noted that different interface cards and different front-end electronics were used for the two tests; however the performance is very similar. Similar behaviour was shown by all individually tested strips. Therefore the strips mounted inside the module and surrounded by other strips perform as well as when mounted in the individual box.

Fig. 2.47 shows the efficiency and time resolution σ as a function of the applied differential high voltage for all good strips of the two modules (some strips were removed from this comparison for known problems, e.g. one strip was built with one gap missing). Although we can state that all strips are at full efficiency at $\pm 6.25\text{ kV}$ there are observable differences at voltages below the ‘knee’ voltage. We

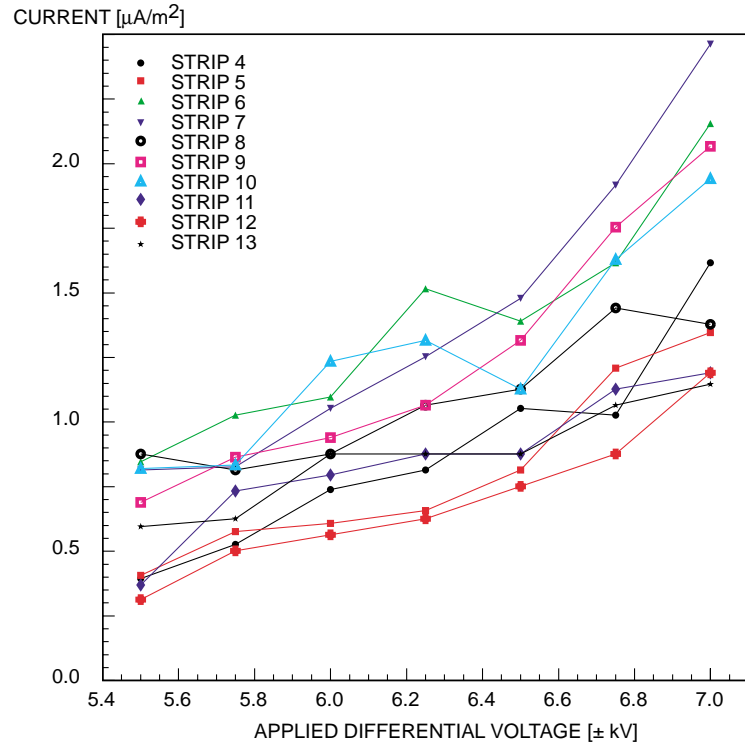


Figure 2.45: Dark current of MRPC strips ($\mu\text{A}/\text{m}^2$) versus differential high voltage.

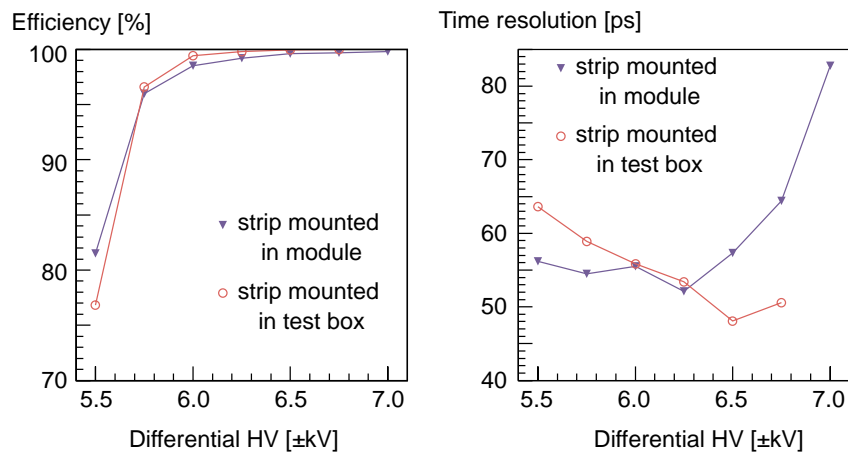


Figure 2.46: Efficiency and time resolution σ as a function of the applied differential high voltage, measured in individual box and inside module.

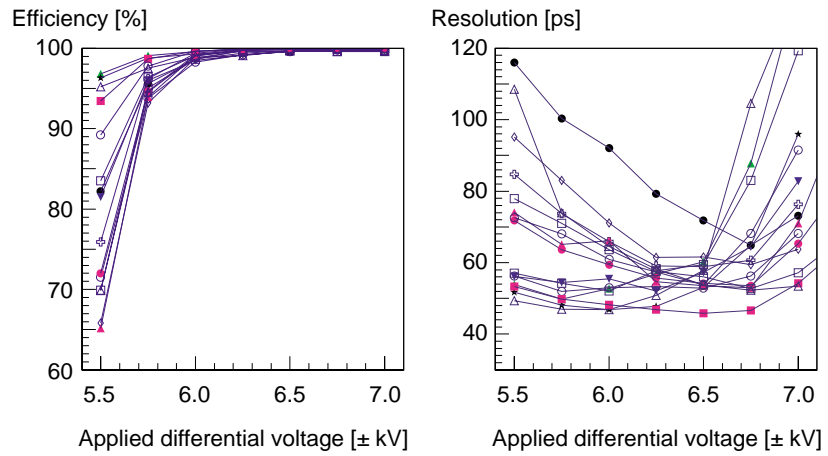


Figure 2.47: Efficiency and time resolution σ as a function of the applied differential high voltage for 15 MRPC strips.

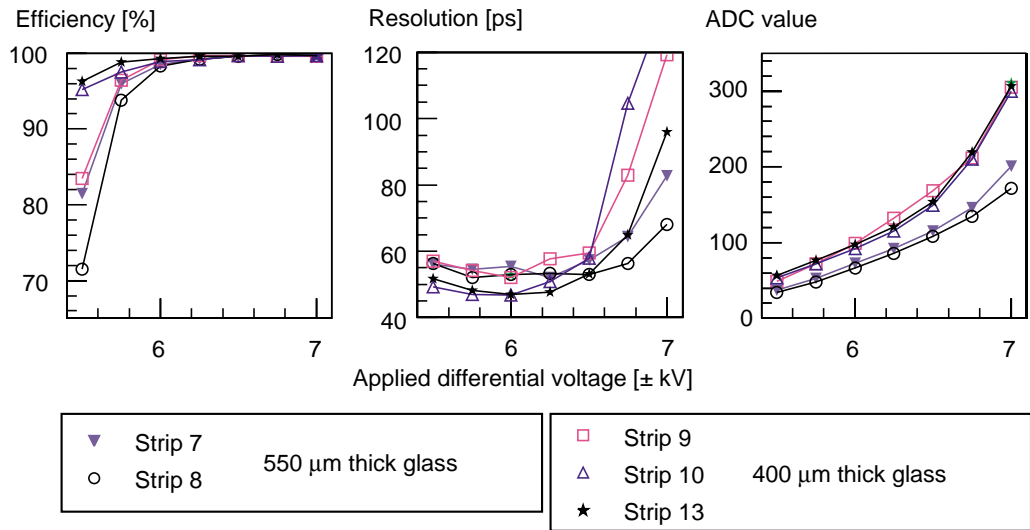


Figure 2.48: Efficiency, time resolution σ and average charge as a function of the applied differential high voltage for 5 MRPC strips with 400 μm and 550 μm thick internal plates.

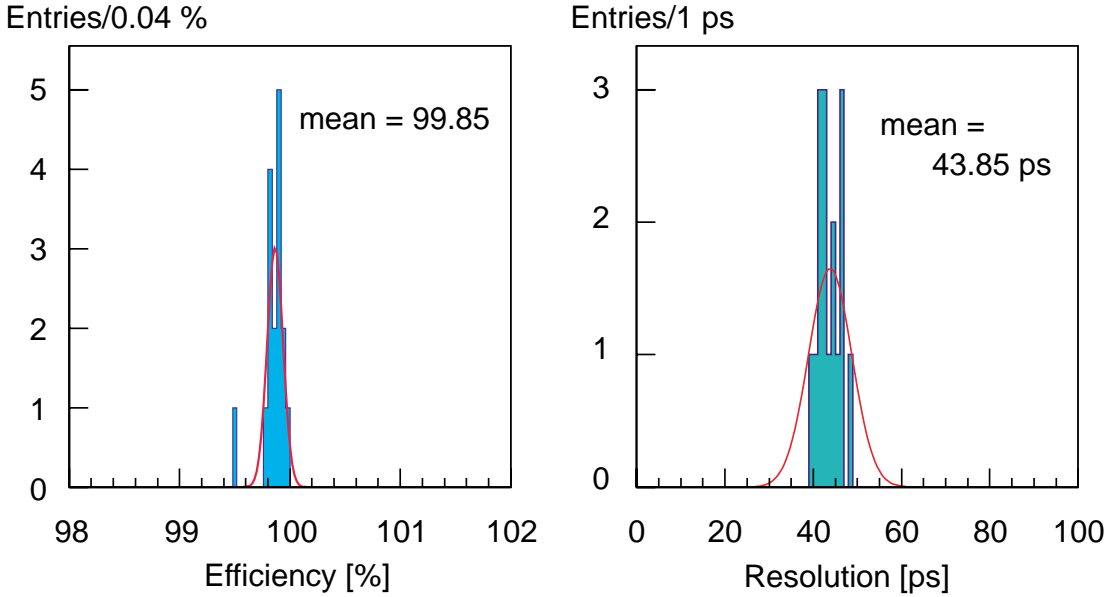


Figure 2.49: Distribution of efficiency and time resolution σ for 16 neighbouring pads (corresponding to the 16 electronic channels of a front end card) of a strip produced in Bologna.

attribute this to slight variations in the exact gap width, since different methods of applying pressure onto the stack of glass plates were used during the production of the strips. We have since defined the stacking procedure. At the nominal working voltage of ± 6.25 kV most strips have a time resolution between 45 and 65 ps; there is one strip that has a substantially worse time resolution of 80 ps at ± 6.25 kV. Although such performance would be usable for the TOF detector, we would like to have better uniformity among the strips. We also prefer the long plateau of good time resolution seen for some strips, since this increases the allowed range of applied voltage. We believe that a possible cause is the distortion of the gap as shown in fig. 2.12 possibly generated by misaligning the fishing-line spacer in some gaps. We are adjusting the routing of the fishing line to reduce such periodic distortions (as shown in fig. 2.12) and are confident that the next batch of strips produced will not have this problem.

From the CERN strips we selected and plotted, in Fig. 2.48, the efficiency, time resolution σ and average charge (in ADC bins) as a function of the applied differential high voltage for five comparable strips. These strips are comparable since the only difference is the thickness of the internal glass, with two of these strips having internal glass sheets of 550 μm thickness. We observe a lower value of the average charge for these two strips as compared with those with 400 μm thick internal plates, probably due to a shift in the working voltage to higher values. This indicates that there may be a slight voltage drop across the thicker plates. However, the important conclusion is that there is no degradation in performance (efficiency or resolution) when using thinner glass; thus the thinner glass will be used since it reduces the material budget.

Fig. 2.49 shows the distribution of efficiency and time resolution σ (ps) measured by 16 neighbouring pads read out by the 16 channels of a front-end electronics card. These measurements were taken with a strip produced in Bologna. The performance is excellent (99.85% efficiency, 44 ps resolution) as well as the uniformity.

2.5.3 Conclusion

The tests of the two prototype modules were successful; the performance of the detector is as expected from previous tests; the uniformity of time resolution of the strips was not as good as it should be, but

the reasons are understood. All in all, many things were learnt from the production of the strips and the assembling them inside the modules themselves. This will be discussed in the next chapter, where the detailed design of the modules will be presented.

2.6 Summary and proposed design

2.6.1 Summary of the R&D Program

In this chapter we have presented the R&D program that has led us to the final design of the TOF MRPC strip. We give here a brief summary of the key issues addressed by this R&D program.

Our very first goal was to scale up the small test MRPC to the full size MRPC strips ($7 \times 120 \text{ cm}^2$ active area) proposed for the TOF array. We found it was necessary to support the glass sheets with spacers across the width of the strip and chose nylon fishing line as this spacer. The easiest way to construct a MRPC strip using such spacers was to have the edge of the internal glass sheets defining the edge of the active area.

We also tested the dependence on the actual size of the gas gap by building MRPC strips with gap sizes between 200 and 280 μm . Somewhat surprisingly changing the gap size did not change the voltage needed to reach the efficiency plateau; it appears that, opting for smaller gaps, the increase in gas gain due to the field is balanced by the decrease in gas gain due to the smaller distance for the avalanche. The non-critical tolerance of the actual gap dimension indicates that strips can be built with relaxed mechanical tolerances.

In order to maximise the performance of the TOF elements and keep boundary effects small, we introduced the double-stack design. By using 10 gaps rather than the 6 gaps originally proposed the shape of the charge spectrum was greatly enhanced. We also found that the resistive coating used to apply the voltage to the stack increased the size of the charge footprint if the resistivity was below 1 $\text{M}\Omega/\text{square}$. We need to minimise the probability of double hits at the boundary, minimise the drop in efficiency and minimise the degradation of time resolution. Therefore we chose the 10 gap double stack MRPC; the resistive coating used to apply the voltage to the stack will have a resistivity $> 1 \text{ M}\Omega/\text{square}$.

One concern we originally had was whether commercial glass could be used or whether it would compromise the detector performance with rate. Commercial ‘soda-lime’ glass, with bulk resistivity of $\sim 10^{13} \Omega\text{cm}$, was used to construct 10 gap MRPC strips; these were tested at the GIF at CERN and the results showed that they can operate at a flux in excess of 1 kHz/cm^2 with no deterioration in their performance; this is to be compared with the maximum expected flux of 50 Hz/cm^2 at the ALICE TOF array.

At the end of 2001, we built 18 strips at CERN and Bologna as a test to show up possible problems in mass production. The result of this test was positive in that basically identical strips were built in these two centres. There are some small details that will be changed before starting the production line such as: the PCB board with the readout pads will be 122 cm in length instead of two PCBs of 61 cm; the positions of the connectors and the pins connecting the anode and cathode readout PCBs will be changed to facilitate the soldering and other details of this type. However, the bottom line is that we have arrived at a design of MRPC that has a performance ideally suited for the ALICE TOF, and we are confident that such MRPC strips can be mass produced without a degradation in performance.

2.6.2 Proposed design for the detector element for the TOF

As a consequence of the above, the proposed design for the detector element for the TOF system is as follows:

- A double stack MRPC strip - each strip having an active area of $7 \times 120 \text{ cm}^2$.
- Each stack will have 5 gaps with a gap size of $250 \mu\text{m}$ thus the MRPC strip will have 10 gaps.

- The outer glass sheets of the stack will be $550 \mu\text{m}$ thick; the internal glass sheets will be $400 \mu\text{m}$ thick.
- The resistive coating used to apply the high voltage will be with a specially developed acrylic paint with a surface resistivity of $5 \text{ M}\Omega/\text{square}$.
- The PCB board with the pickup pads will be 0.8 mm thick; the centres of the pads will be on a $2.5 \text{ cm} \times 3.5 \text{ cm}$ grid with 3 mm space at all boundaries.

3 Detector engineering design

3.1 Introduction

The TOF detector will surround the central interaction region of ALICE, covering a cylindrical surface of polar acceptance $|\theta - 90^\circ| < 45^\circ$ and full coverage in ϕ . The internal radius of the cylinder is 3.70 m from the beam axis. The total system consists of 90 modules attached to the outer cylindrical part of the ALICE space frame [1].

The detector is divided into 18 azimuthal sectors (Fig. 3.1). Five modules of three different types are grouped in a line to form one sector (Fig. 3.2). The different types of module have the same structure and transverse cross section but are different in length. The actual dimensions are defined in such a way that the joining areas of the modules are aligned with the dead areas of the space frame and of the other detectors (TRD, HMPID, PHOS) as projected from the interaction point, thus creating a configuration of minimal disturbance for the external detectors.

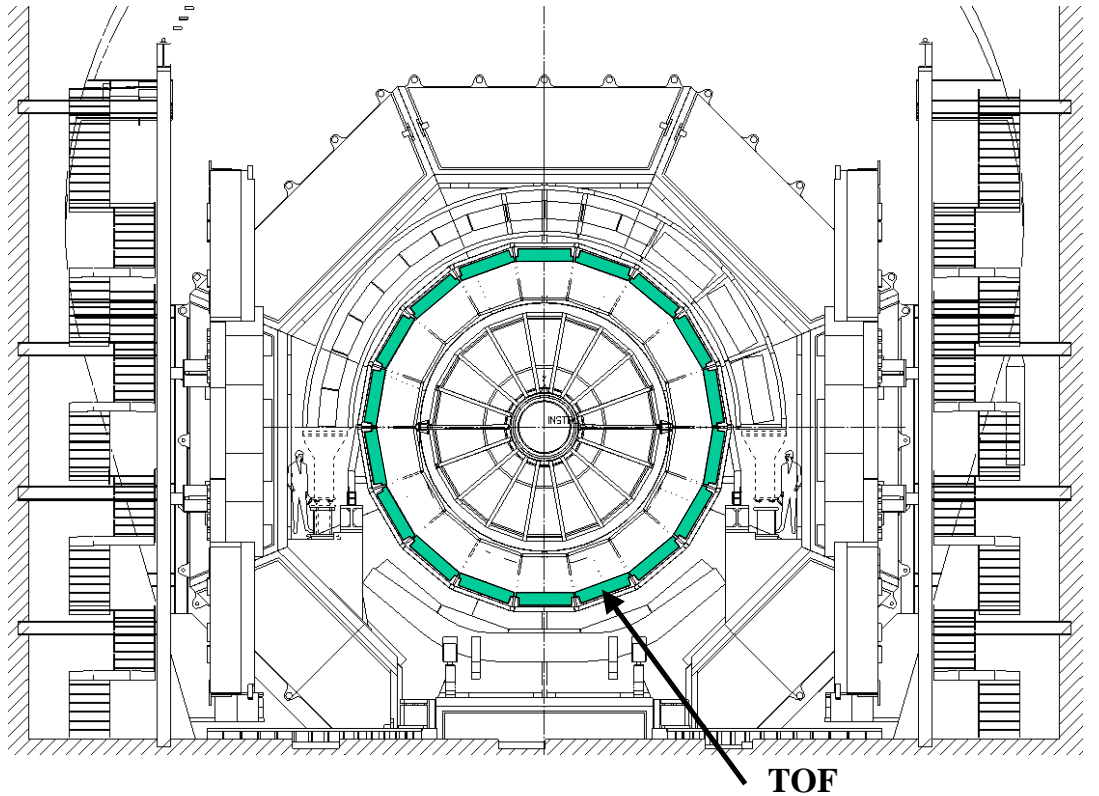


Figure 3.1: Front view of the ALICE detector, where the 18 sectors of the TOF system can be seen.

At both ends of each sector special crates will contain the readout electronic (TDCs and controllers) as well as the slow control modules. These crates will be assembled into a unique frame of dimensions

Table 3.1: Main parameters of the TOF modules.

Module	Central	Intermediate	External
Number of strips	15	20	19
Number of pads	1440	1920	1824
Total sensitive area in m ²	1.28	1.76	2.00
MRPC tilt angles in degrees	(-7.43, +7.43)	± (8.73, 27.8)	± (28.7, 43.9)

98×40×30 cm³, attached to extension rails connected to the space frame structure.

Each module consists of two separate volumes: an inner gas-tight region that will contain the MRPCs and an outer one containing the Front End Analogue cards (FEA) with amplifiers and discriminators. The MRPC strips will be placed transversely with respect to the beam direction and tilted in such a way as to be normal to the particles from the interaction point in the r-z plane. This will reduce the number of very oblique transversal paths that can create a sharing effect of the signal among adjacent pads and thus would increase the occupancy and the time jitter of the detected signals.

The three types of module have different length and will contain a different number of strips. The main parameters of the modules are listed in Table 3.1.

3.2 General module description

Each TOF module consists of a gas region which contains the MRPCs and an outer part with the front end electronics. The MRPCs have been described in detail in Chapter 2; a cross section with the external dimensions is shown in Fig. 3.3.

The inner gas tight box containing the MRPCs is made of glass fiber 3.0 mm thick covered inside with a 0.3 mm thick aluminum layer to ensure electrical shielding. The MRPCs are positioned inside the modules as shown in Fig. 3.4, Fig. 3.5, and Fig. 3.6. As mentioned in the introduction, a special positioning of the strips has been envisaged to minimise oblique traversal path of the particles in the detectors. Their angle with respect to the axis of the cylinder will be progressively increased from 0° in the central part ($\theta = 90^\circ$) of the detector to 45° in the extreme part of the external module ($\theta = 45^\circ$).

Adjacent strips will be positioned inside the modules in such a way as to create an overlap of about 4 mm between two adjacent strips, at the edge of the active area: this will ensure the inter-calibration of the strips via tracks traversing both of them.

The modules have been designed in such a way as to minimise losses of the sensitive area along the z axis. Special care has been taken in designing the overlapping region between two modules. The solutions proposed in Fig. 3.7 and Fig. 3.8 ensure a very limited dead region at the price of a different tilting angle of the strips near the corner.

For the inner and outer modules the gas box will be attached to the honeycomb aluminum plate (see below) with an O-ring ensuring the gas tightness of this volume. For the intermediate modules this is not possible because of the strips in the corner. The present solution foresees to glue the side parts of the gas box to the central support plane and then add a cover with a sealing O-ring.

A side view of the TOF central module is shown in Fig. 3.9. Both the gas volume with the strips and the electronics with the Front End Analogue (FEA) cards are visible. Fig. 3.10 shows the various parts of the electronics side: the aluminum honeycomb with the holes to bring the MRPCs signals to the Interface Cards, where the FEAs will be plugged into and the FEAs themselves.

The gas volume is separated from the electronics by means of an aluminum honeycomb plane 1.3 cm thick with two 1 mm aluminum skins. This plane is the structural part of a module and all around has a

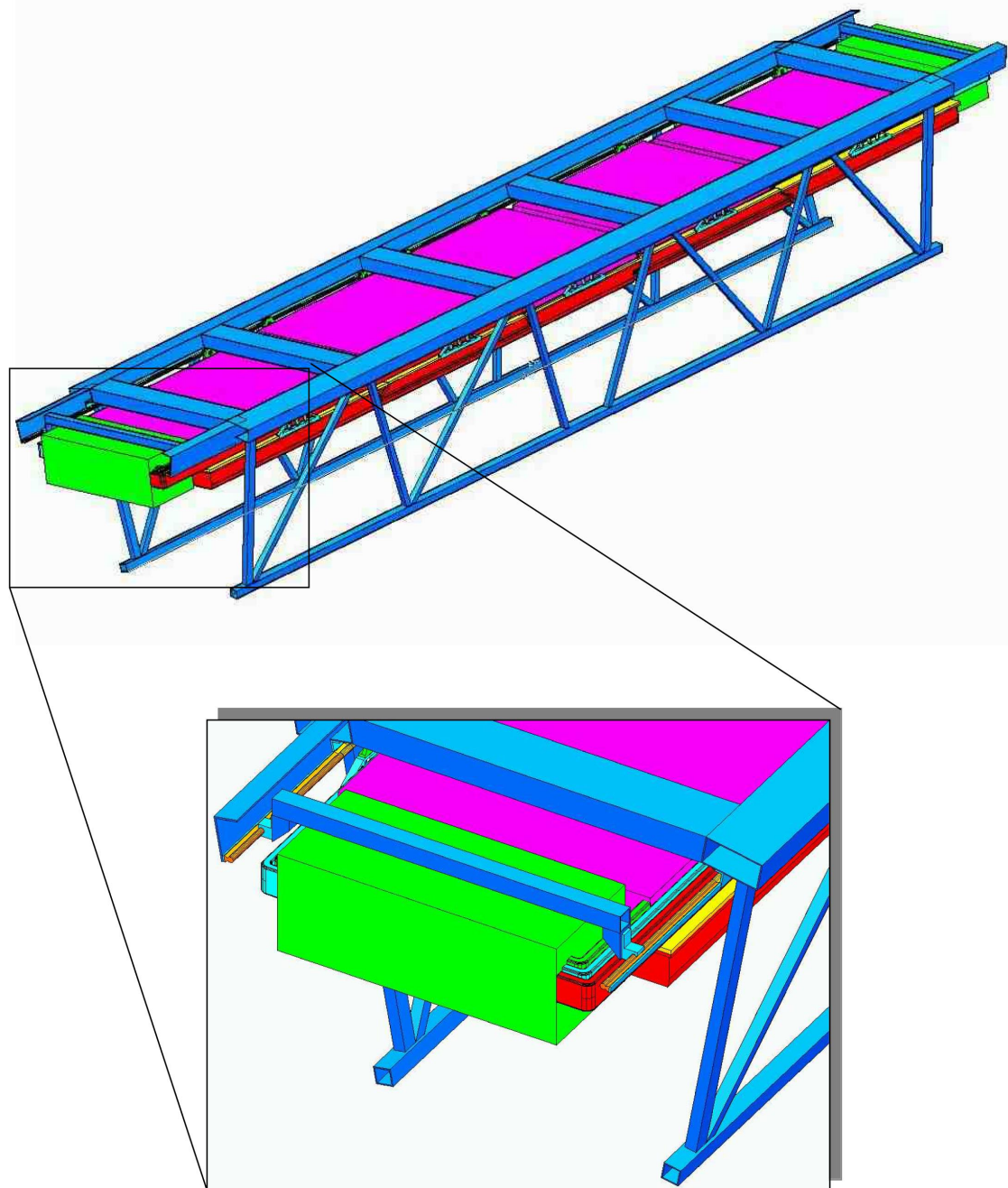


Figure 3.2: One TOF sector with 5 modules.

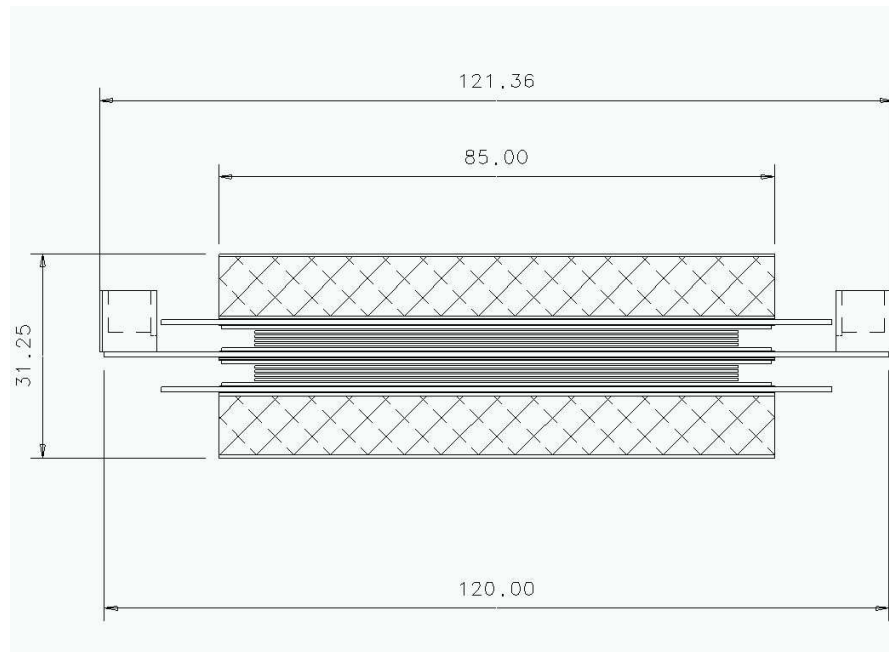


Figure 3.3: Cross section of a MRPC with the external dimensions.

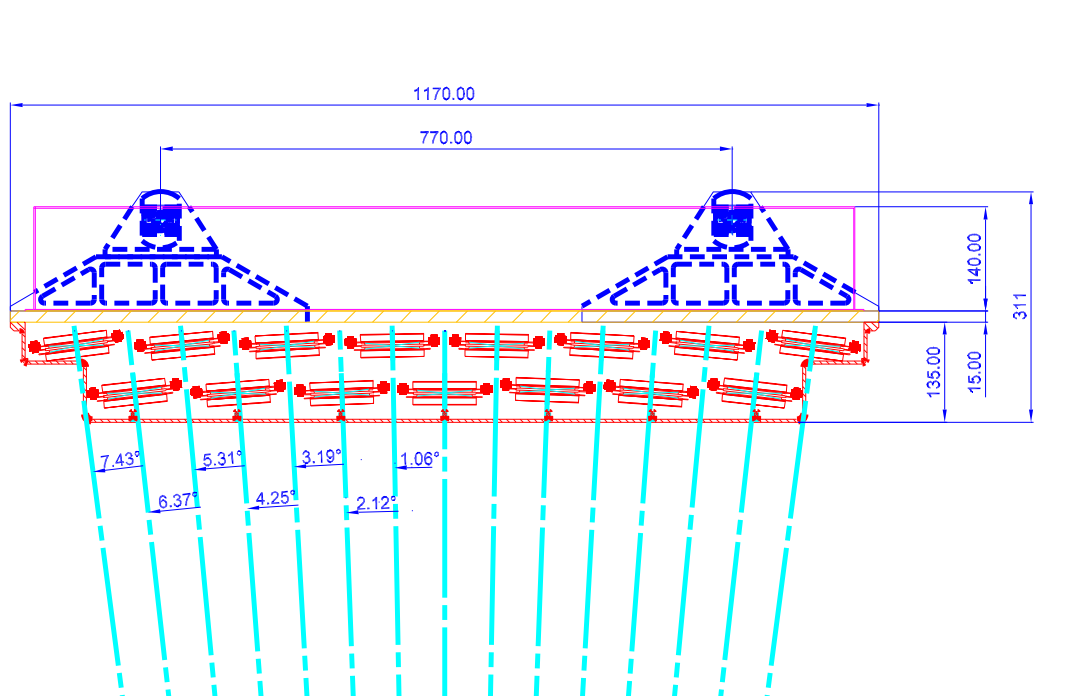


Figure 3.4: Central TOF module showing the positions and tilt angles of the MRPC strips.

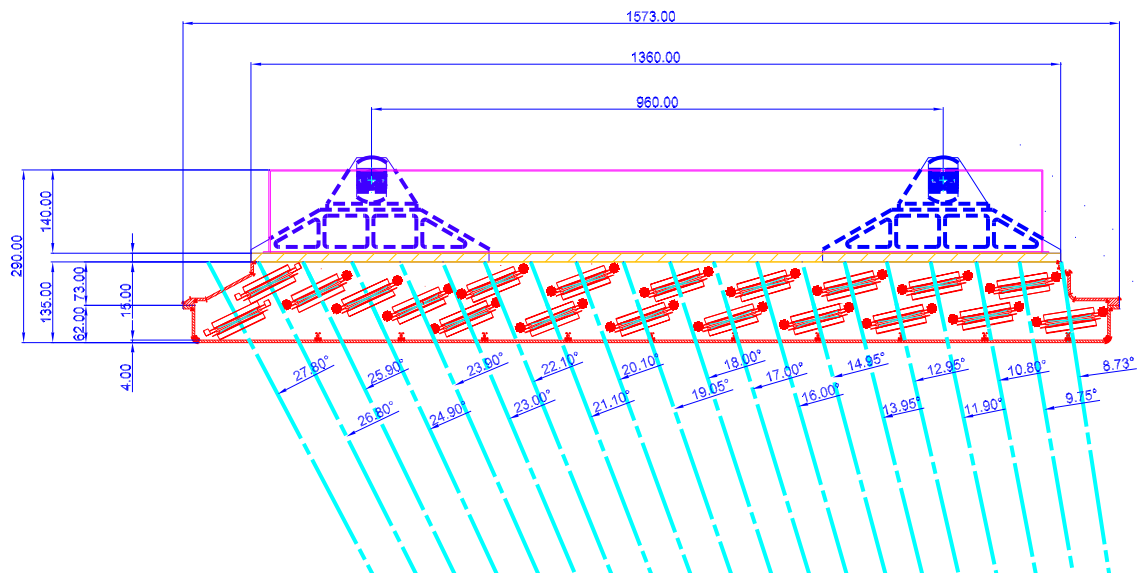


Figure 3.5: Intermediate TOF module showing the positions and tilt angles of the MRPC strips.

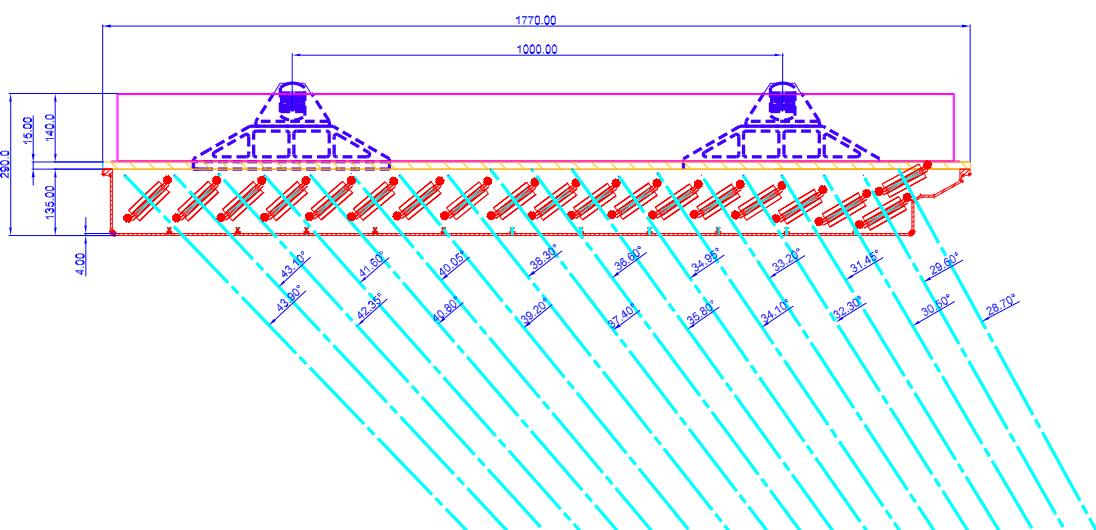


Figure 3.6: External TOF module showing the positions and tilt angles of the MRPC strips.

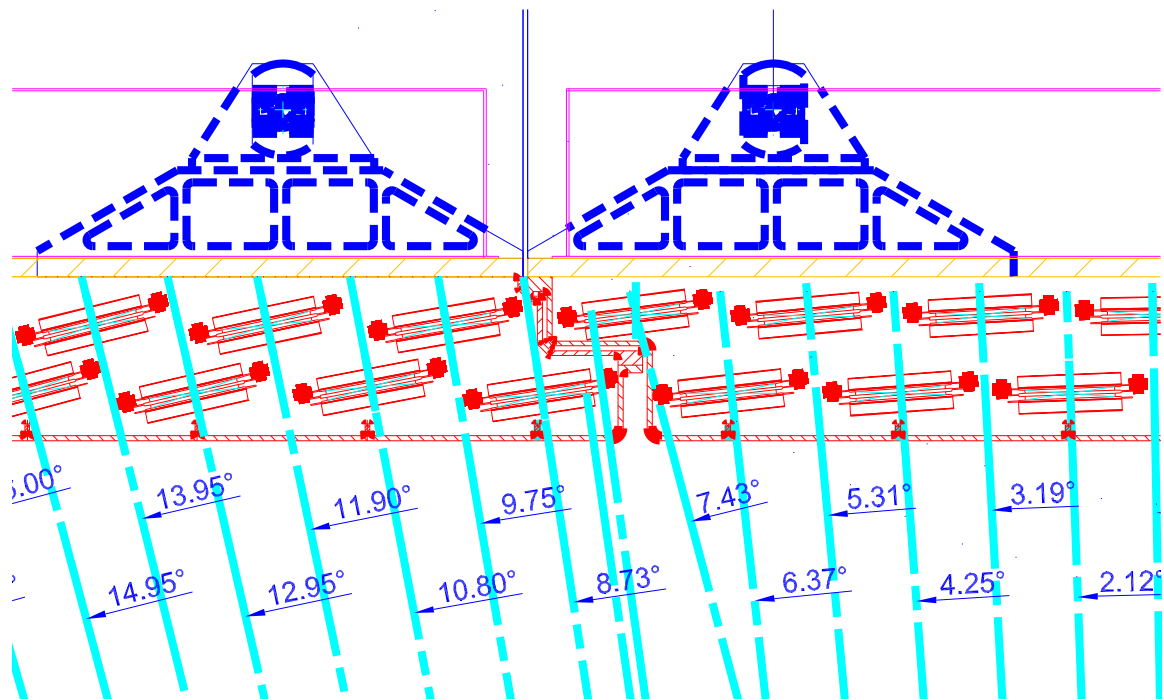


Figure 3.7: Detail of the overlap region between the central and intermediate TOF modules.

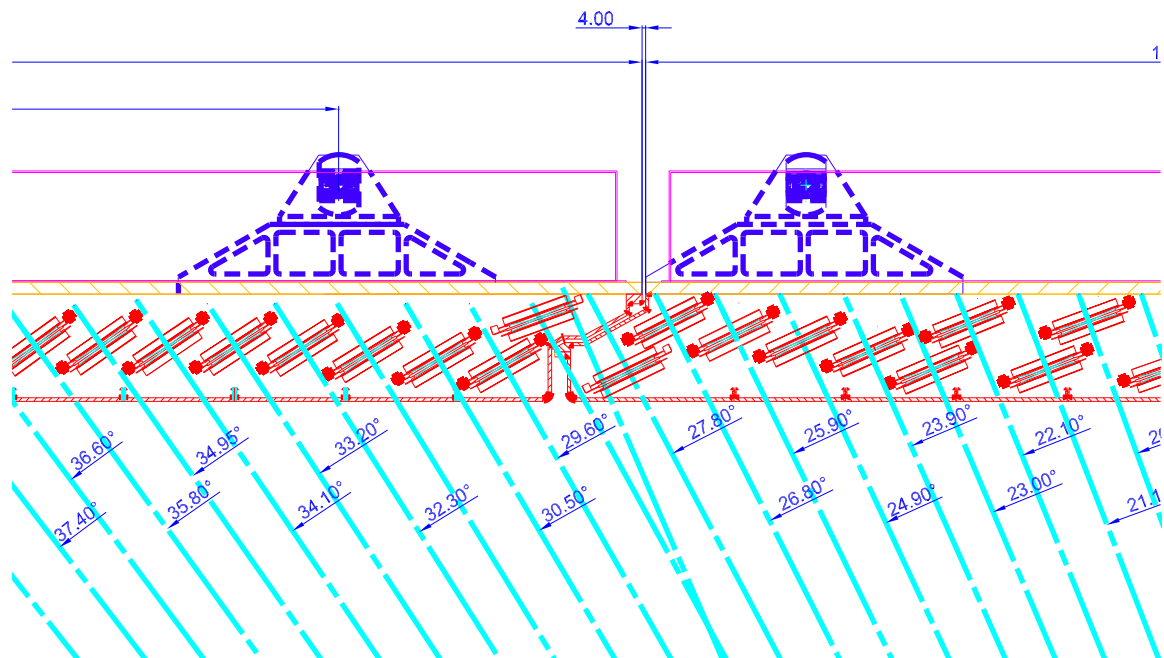


Figure 3.8: Detail of the overlap region between the intermediate and external TOF modules.

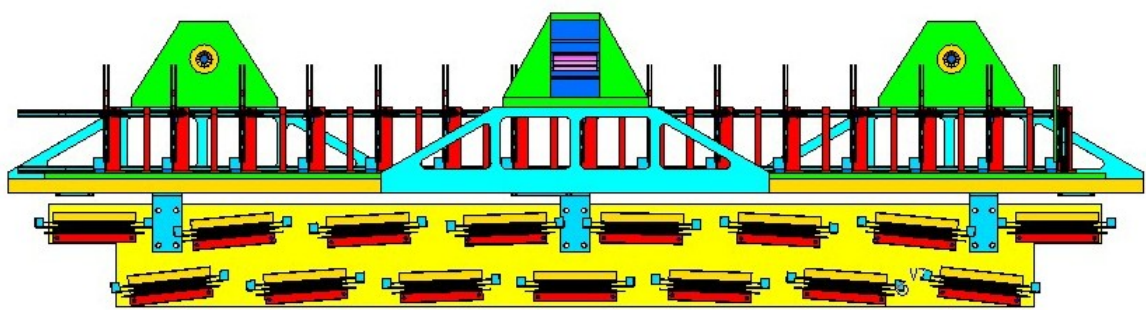


Figure 3.9: Side view of the TOF central module showing also the Front End Analogue cards.

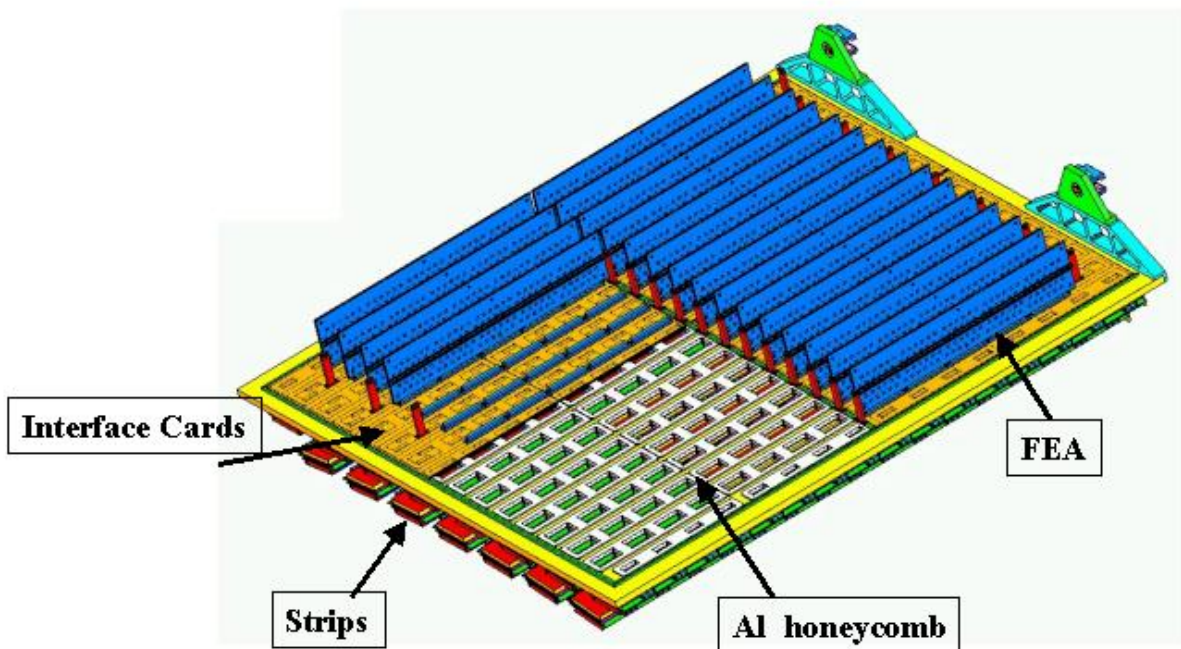


Figure 3.10: The central TOF module with details of the aluminum honeycomb plane, the ICs and the FEAs.

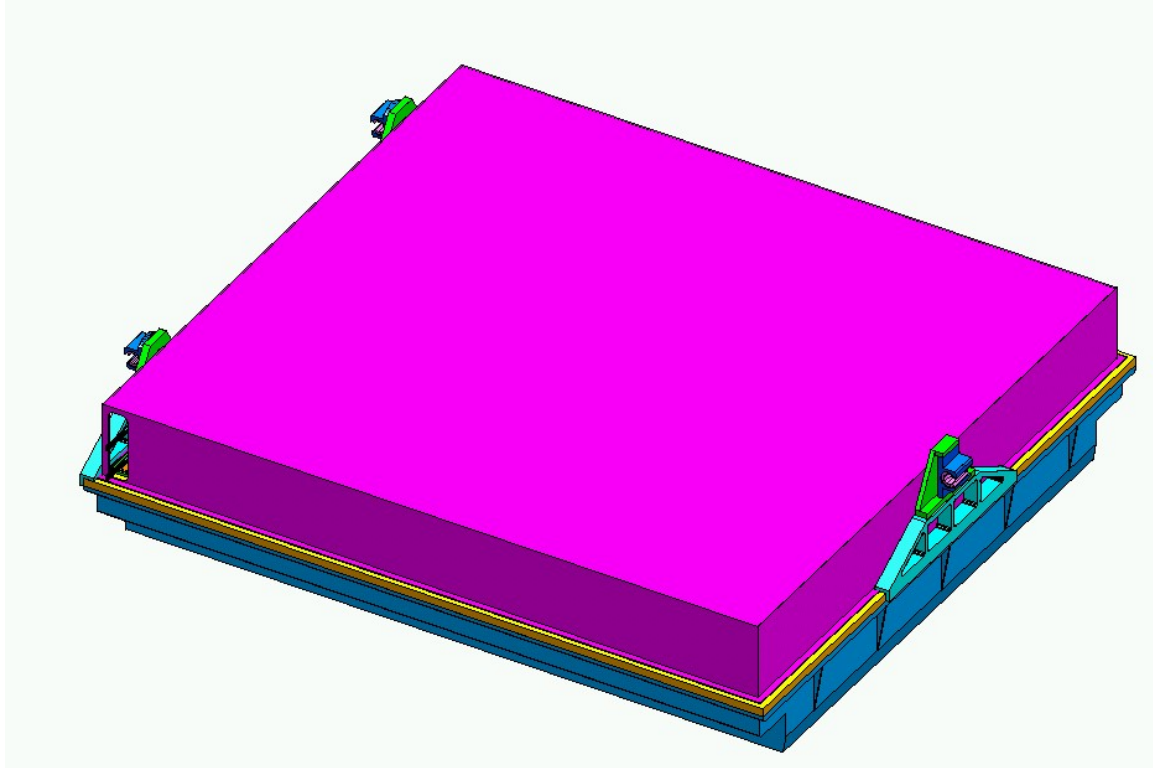


Figure 3.11: The central TOF module with its closing aluminum cover.

reinforcing structure to keep the required rigidity of the module under i) the stresses induced by its own weight whatever mounting orientation is applied and ii) an inner gas overpressure of 1 to 2 mb.

The signals from the pick-up pads on the MRPC strips are brought to the front end analogue electronics (FEA) via Interface Cards (ICs). The ICs are made of large PCBs covering 7 or 8 half strips and will be glued and fixed to the honeycomb plane closing in this way the gas volume. Each IC will have on one side the connectors facing the strips, and, on the other side, the connectors for the FEAs. These ICs are glued to a piece of polycarbonate with a special shape that ensures a good gas tightness. To add safety to the system a second glued gasket is placed around the perimeter of the IC providing a second sealing. All the soldered pins passing through the IC from the gas volume to the electronics side will be tightened with a silicon layer on the inner surface.

The FEAs, containing 48 channels each, are plugged into the connectors mounted on the ICs. The cables taking the signals to the TDC readout modules (see Chapter 4) will be routed to the edges of the module and from there to the readout crates placed at both ends of each sector. A space of 10 cm is foreseen to this scope at both sides of the module. This space will also be used for all other services to the modules.

A box made of a 0.5 mm thick aluminum layer with a reinforcing structure will cover and protect the electronics region (Fig. 3.11).

3.3 The module cooling system

The power consumption foreseen for the Front End Analogue card (FEA) is of ~ 400 mW per channel, for a total of 0.6-0.8 kW per module (see Table 4.1). To keep the temperature within the ALICE specifications, a water cooling system is envisaged.

Heat will be taken directly from each FEA by means of an aluminum board 1 mm thick. A thermal filler will be placed between the FEA and the aluminum board in order to provide the necessary electrical

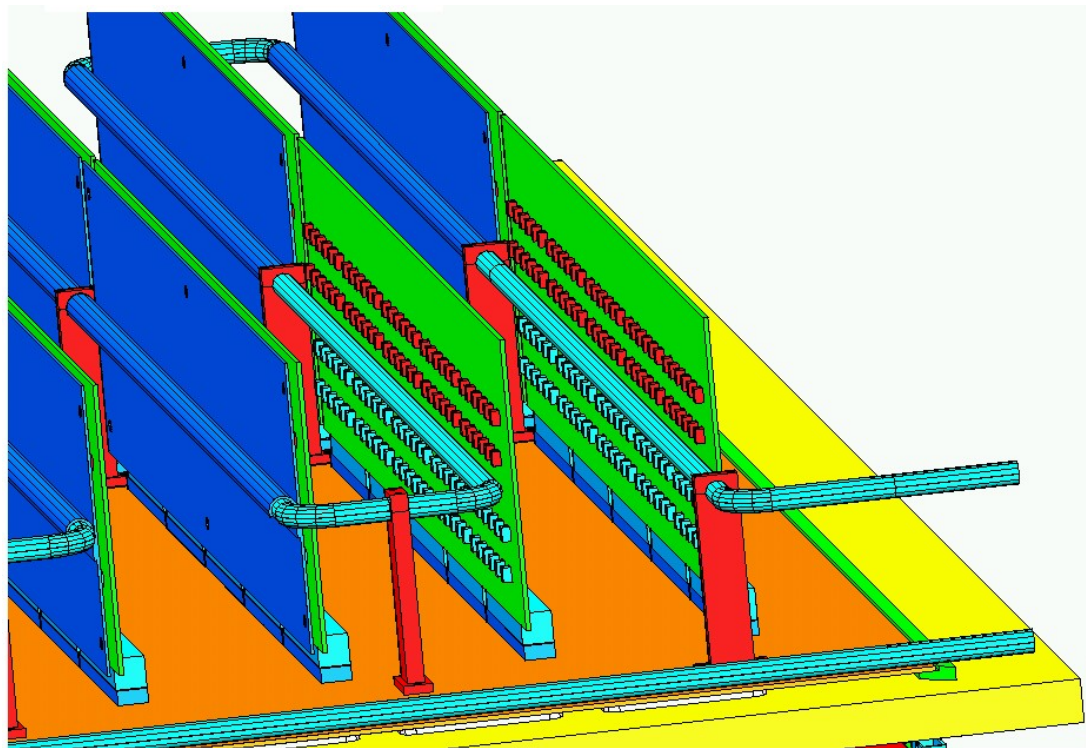


Figure 3.12: Detail of a TOF module with the FEA, the aluminum board and the cooling pipes.

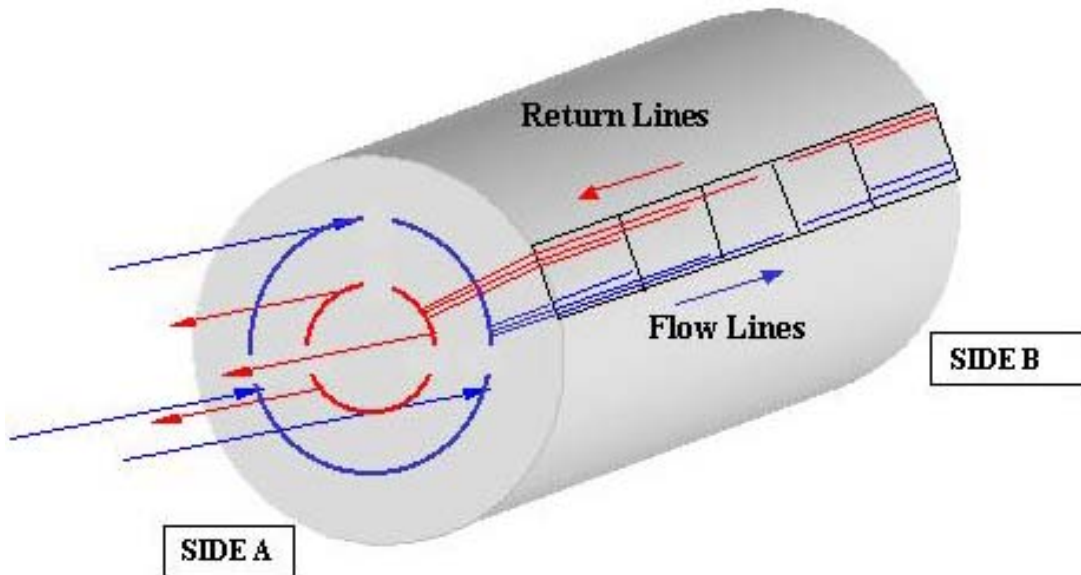


Figure 3.13: Sketch of the TOF cooling system.

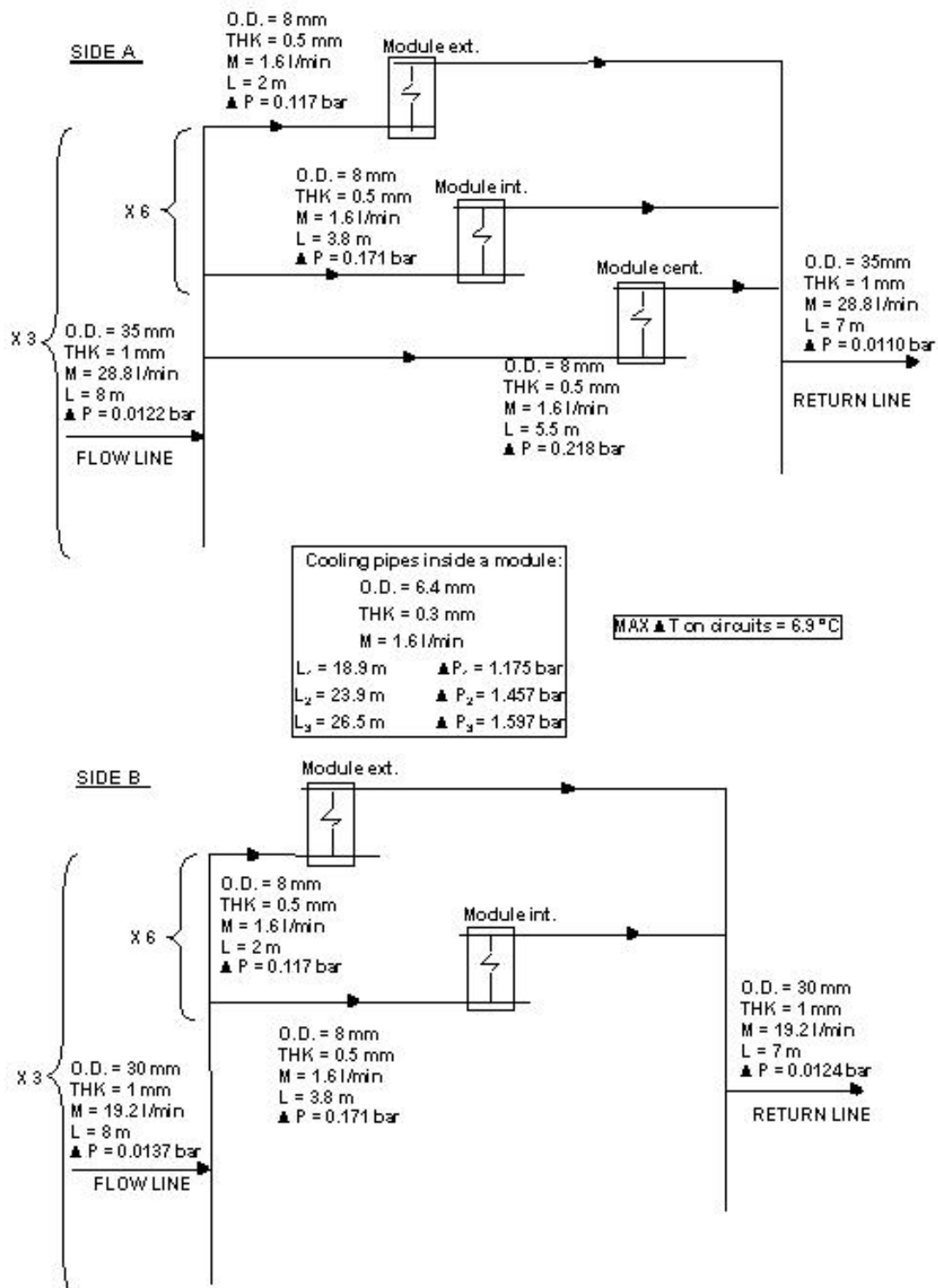


Figure 3.14: Hydraulic scheme for the TOF cooling system inside the modules, with details on pipe dimensions, water flow, pressure.

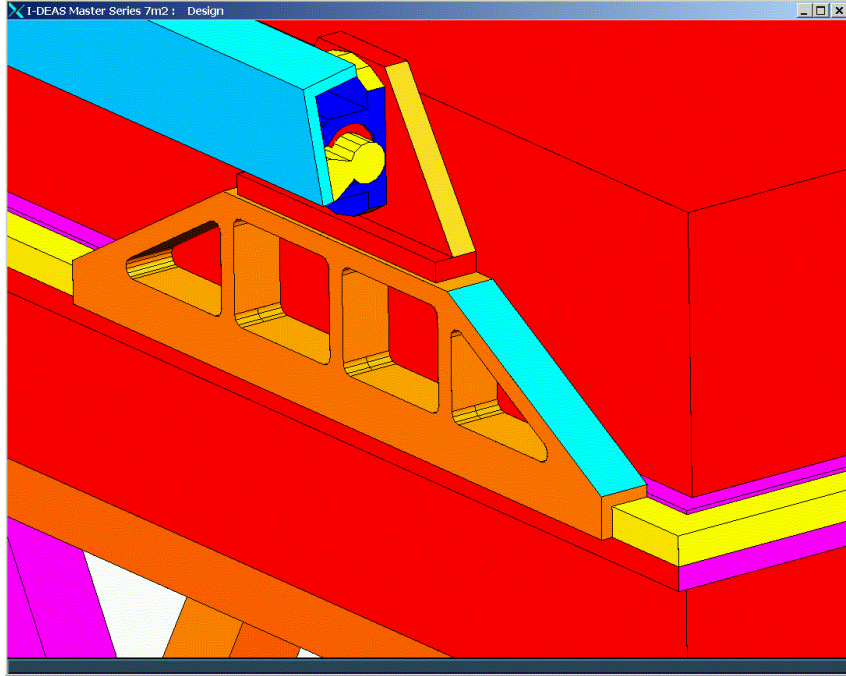


Figure 3.15: Detail of the bushes supporting the TOF module from the rails.

insulation and at the same time the requested thermal coupling. The FEA with its aluminum board will be attached to a copper pipe which runs through all the FEAs. (Fig. 3.12).

A global scheme of the cooling system is shown in Fig. 3.13. Water will be supplied from both ends of the space frame, each side with three independent lines. Each line will serve 6 TOF sectors. Each of the five modules of a sector will have an independent in and out water line.

In Fig. 3.14 the hydraulic scheme is presented, together with the diameter of the pipes , the water flow required and the pressure drops. The calculation [2] assumes a safe maximum temperature on the FEAs of 45 degrees and a temperature constraint of 21 degrees at the boundaries of a module, as requested by the Collaboration.

3.4 Installation procedure and services to the modules

The five TOF modules located inside each of the 18 sectors will be kept in position by two rails fixed to the space frame (Fig. 3.15). Three bushes are attached to the honeycomb reinforcing structure of the module; they allow the sliding of the module along the rails suspended from the space frame. The bushes are located along the edges of the modules, parallel to the beam axis, two of them on one side and the third on the other side. The mounting of the sliding system to the module has been studied in such a way as to allow the compensation of the changing distances and orientation induced onto the supporting rails by the progressive deformation of the space frame under the loads applied by the installation of different detectors. To allow this every bush will be attached to the module by means of a system having the appropriate degrees of freedom, translational and rotational. The system will allow to compensate for a maximum difference of 5 mm and a few degrees.

The installation will be done once the space frame will be in the parking position in the experimental hall. The modules will be inserted in their position one by one. This will be done by means of a rigid support structure able to contain any of the three different types of TOF modules. The structure is equipped with a pair of adjustable rails of the same kind used inside the space frame. To insert a module inside the space frame it is enough to suspend the structure with the hall crane in front of the chosen

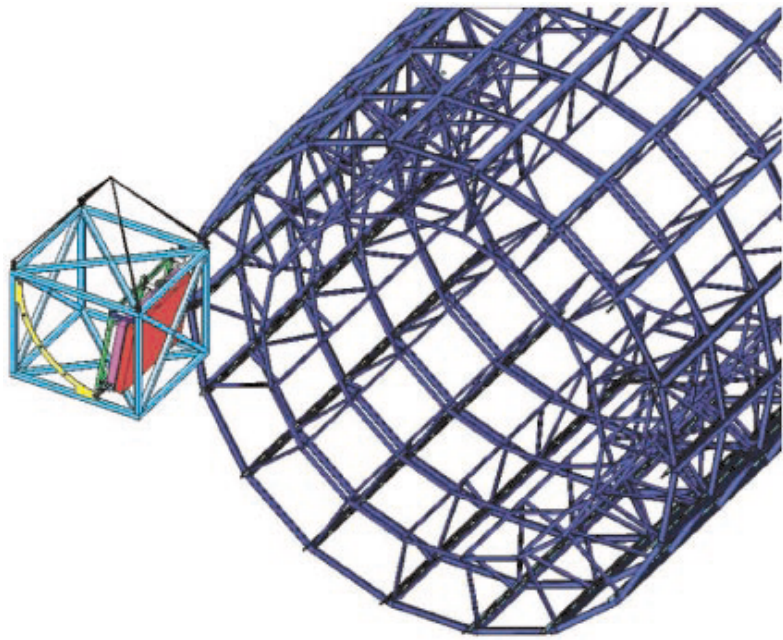


Figure 3.16: Schematic view of the installation procedure of a TOF module: the installation frame, supported by the crane, is placed in front of the space frame sector where the module will be inserted.

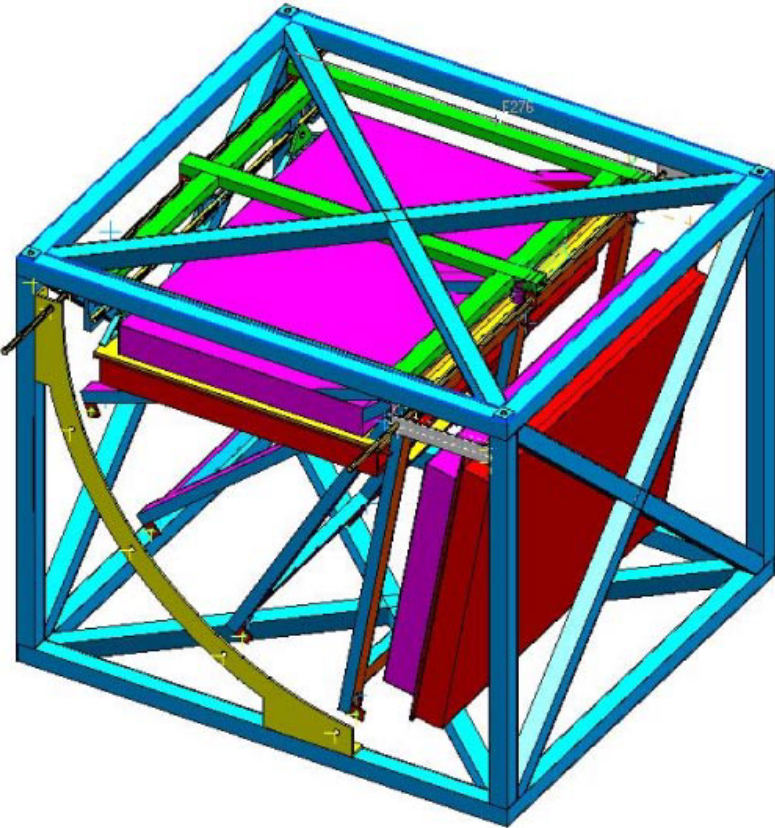


Figure 3.17: The installation frame in a 3D view. The module can be positioned at different angles depending on the sector orientation.

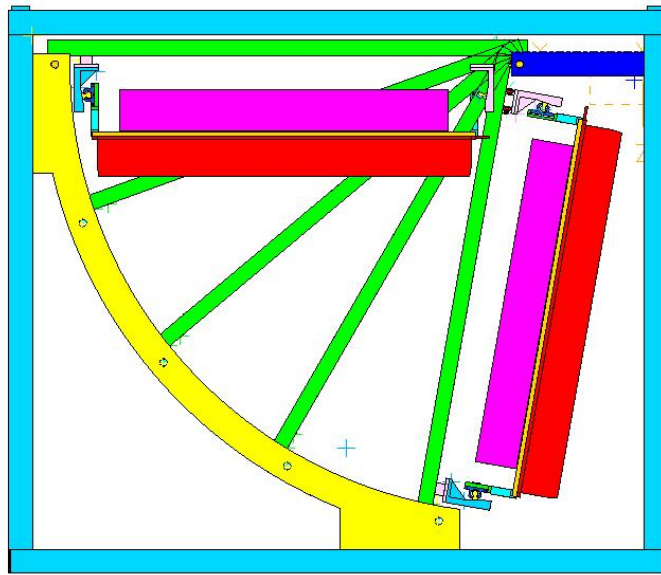


Figure 3.18: The installation frame in a projection.

sector and connect the rails together to form a unique sliding line that will allow to push the module in the right position (see Fig. 3.16). The supporting structure is designed in such a way as to allow the positioning of the module at the different angles corresponding to the ones of the sectors (see Fig. 3.17 and Fig. 3.18). The system will work equally well when the space frame will be in the parking position, with access at both sides, and when it is in the final position, in which case the module will slide only from one side. In the latter case a prolongation of the rail will run through the baby space frame to allow the mounting structure to be located outside the magnet in a region where a crane can be operated.

The requested positioning precision is not high (of the order of a millimeter), so a simple mechanical reference is sufficient to define the position.

In the future, as a consequence of discussions with the Collaboration, it is possible to envisage, if required, a different installation procedure. Instead of mounting the modules individually one after the other, an entire sector (with 5 modules) could be preassembled and mounted at one time.

All cables and pipes reaching or leaving the modules will run on the sides of the modules, to reduce the material in the central active area. A possible solution is sketched in Fig. 3.19 and Fig. 3.20. A space of about 10 cm will be available on each side of a module. This space will be divided into 3 regions, each one reserved for the cables/pipes for one module.

3.5 Assembly procedure

3.5.1 Assembly of the MRPC strips

We include here a summary of the construction process of the MRPC strips to reinforce the notion that, indeed, this detector does not rely on complex assembly techniques.

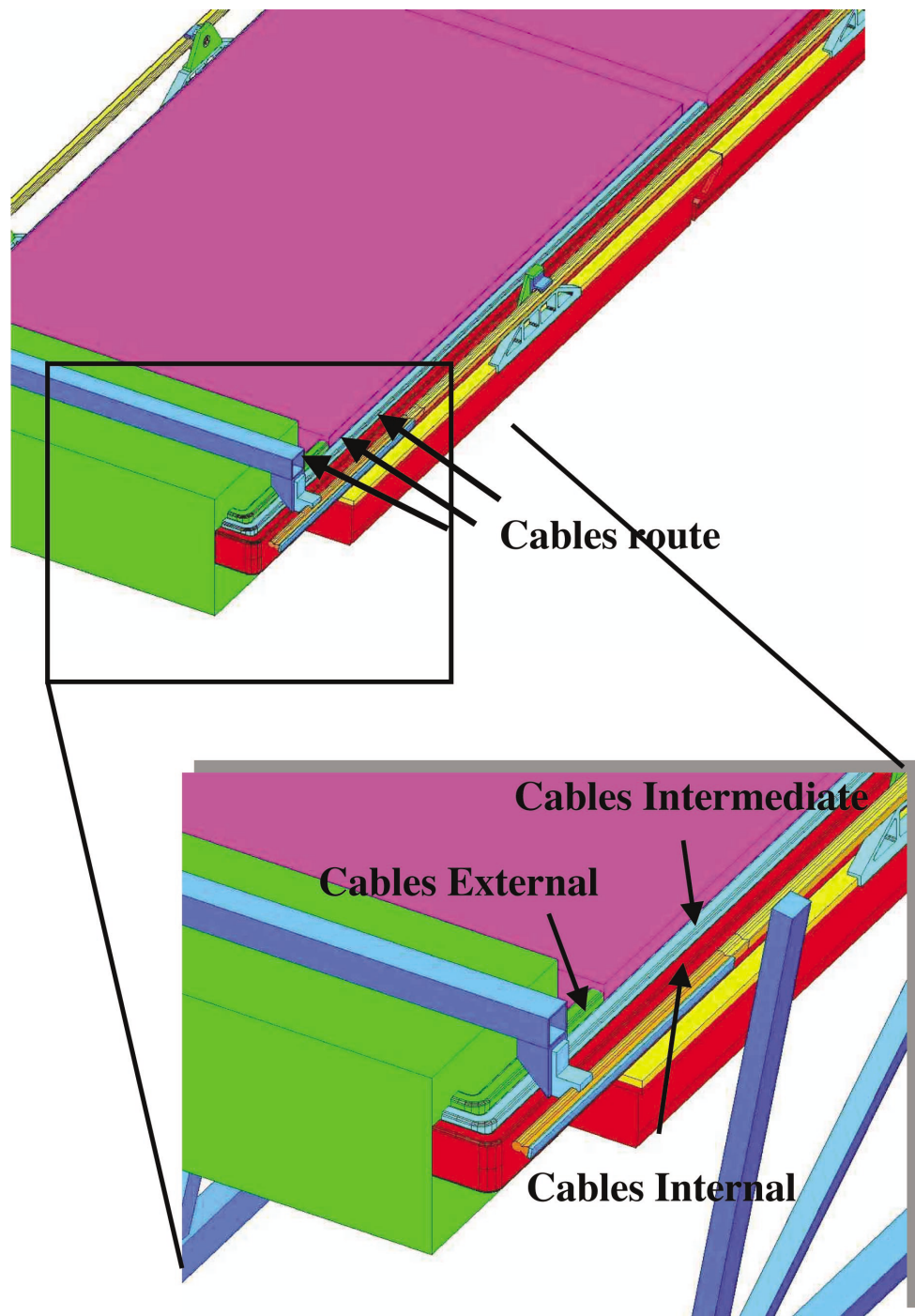


Figure 3.19: Sketch of the routing of the cables and pipes in a TOF module.

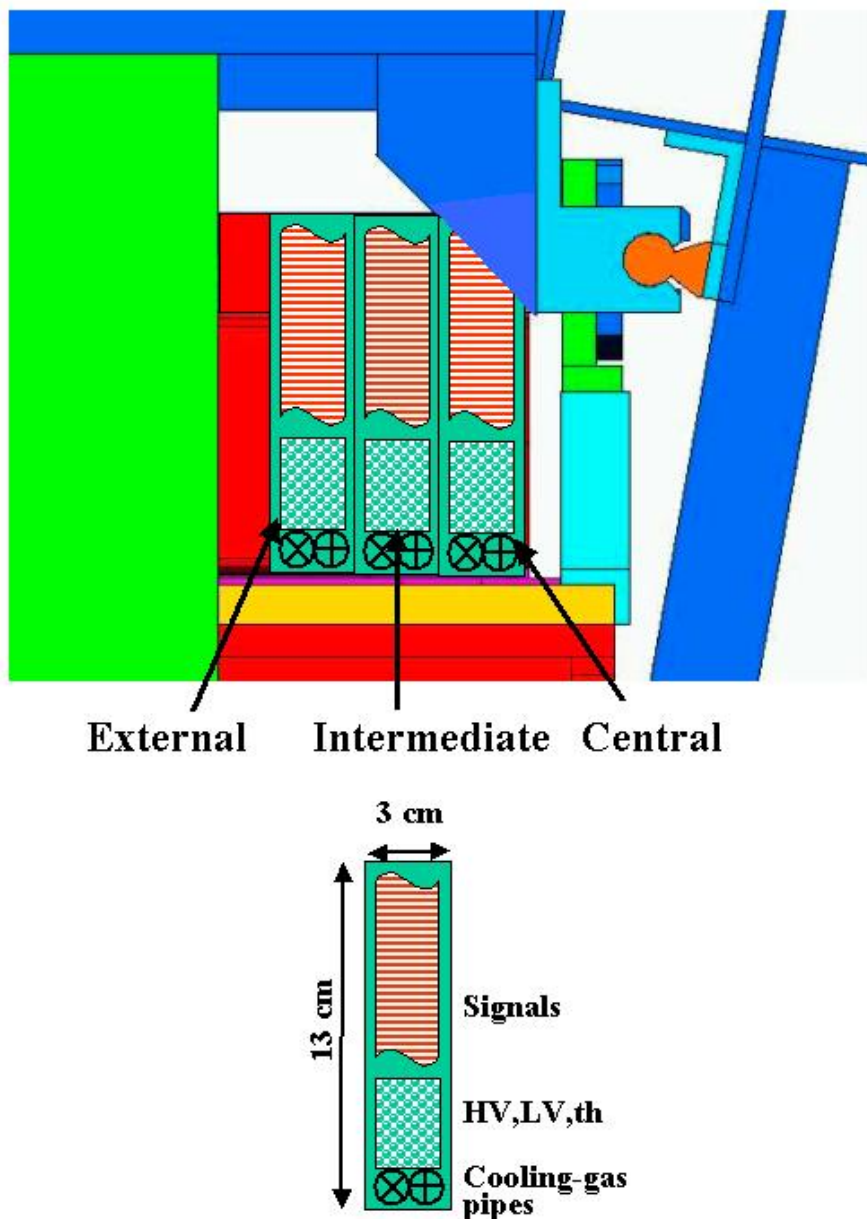


Figure 3.20: Cross section of a module with the spaces reserved for cables and pipes.

The MRPC strip is built starting from the lower honeycomb; this honeycomb first has to be equipped with a location block. A block is embedded into each end of the honeycomb strip; each location block contains two precise holes, 8 cm apart and 4 mm in diameter. A jig will be used when these location blocks are glued into the honeycomb strip, so that the distance between the blocks and the relative position between all four location holes will be precise. When the assembled strips are mounted inside the modules, screws will pass through the side plates of the module into these location holes to define the position and tilt angle of the strip.

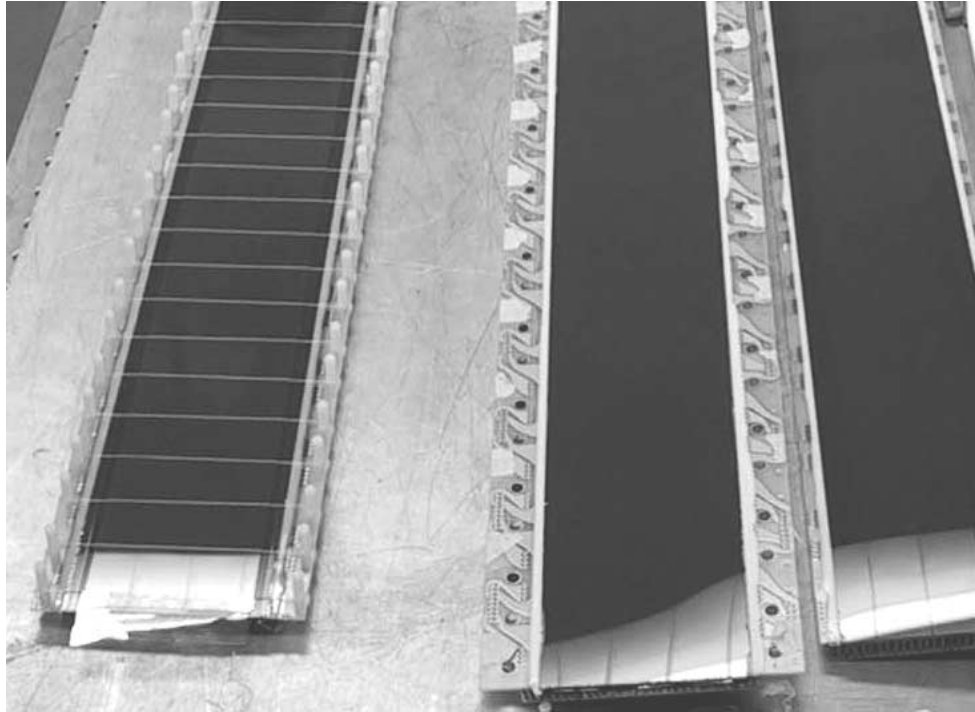


Figure 3.21: Photograph of strip during assembly. The white lines running across the strip on the left are the fishing-line spacers. The dark colour of the glass sheet is caused by the resistive paint (dark red) used to create the high voltage electrode.

Once the honeycomb strip is prepared the lower PCB is glued to it using double-sided pressure-sensitive adhesive tape; the pick-up pads are on the surface facing the honeycomb. The external glass sheet is glued to the PCB, the surface painted with the resistive paint facing the PCB; thus the PCB, with a thickness of 0.8 mm, insulates the pick-up pads from the high voltage resistive layer. The voltage connection to the resistive layer is made by having a trace on the surface of the PCB and using a conductive adhesive to connect this trace to the painted high voltage layer. A high voltage connection is made in this way at both ends of the strip. Plastic screws (M5) are positioned in pre-drilled holes in the PCB along the two sides of the glass plate. The fishing-line spacer (250 μm diameter) is run across the surface of the glass plate and around these screws. Fig. 3.21 is a photograph taken during the construction of a strip. The white lines that cross the left-hand strip are these fishing-line spacers. An internal sheet of glass is then placed on top of the fishing line. It is held in place at the two ends using a spacer made from mylar film (50 μm thick) and two layers of double-sided pressure-sensitive adhesive tape. These steps of placing the fishing line followed by the stacking of the internal glass plate is repeated until the stack contains four sheets of internal glass and five layers of fishing line spacer. Quick drying epoxy glue is applied to the fishing line where it passes around the plastic screw so that in the unlikely event that this fishing line breaks the degradation in performance (if there is a degradation at all) will remain local.

At this point the central PCB plane is assembled and added to the stack. An additional layer of insulation has to be added to this PCB on the side that has the pick-up pads; we use a 250 μm thick

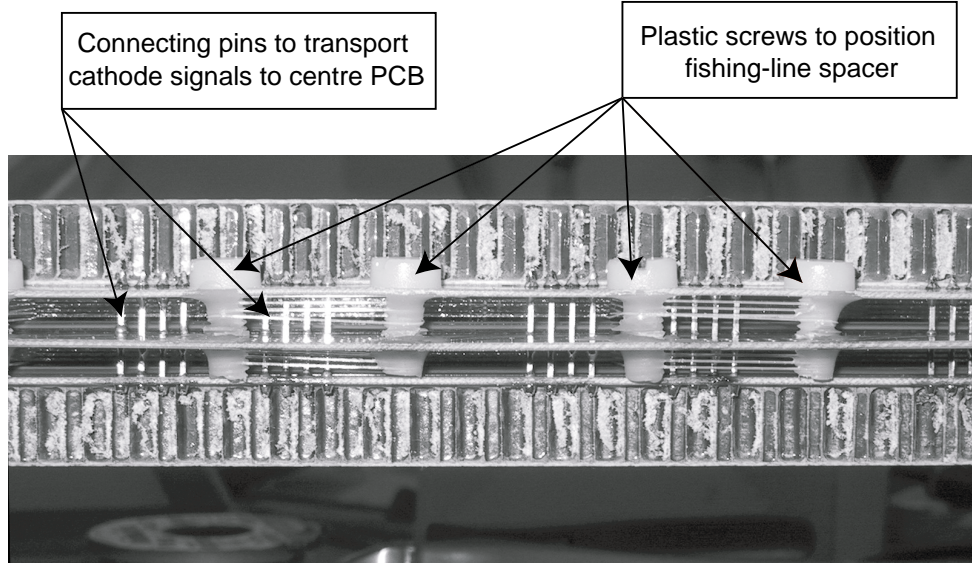


Figure 3.22: Photograph of strip after assembly.

layer of mylar for this. Glass is then glued to both sides of this PCB. This central PCB is wider than the other two PCBs, since the connectors used to transmit the differential signals are on this card. Clearance holes allow the screws, used for the routing of the fishing line, to pass through the central PCB; thus this assembly of PCB and glass sheets is simply just added to the stack. The assembling of fishing-line spacer and the internal glass plates is repeated in the same fashion as for the lower stack. Finally the top PCB is added; this top PCB has a glass sheet and honeycomb panel glued to it in a similar manner as for the bottom PCB. We include a photograph of the assembled strip; this is shown in Fig. 3.22.

At this time the whole stack is compressed by loading it with four lead bricks (~ 40 kg). Connecting pins (a group of four pins on 2.54 mm spacing) are soldered along each side of the double stack assembly. These connecting pins are used to bring the anode signals from the top and bottom PCBs to the central PCB (the central PCB reads out the cathode signals); thus the output signal is truly differential. These pins also fix the distance between the three PCBs and thus keep the stacks in the compressed state when the lead bricks are removed at the end of the soldering. An automatic machine to solder the pins from the anode to the cathode PCBs is under evaluation.

3.5.2 Assembly of the modules

All the mechanical parts of the modules will be produced and assembled by industry. External firms will also mount and seal the Interface Card PCBs to the central honeycomb plane, already equipped with the signal connectors. The final assembly of the MRPCs and the FEA cards inside the modules will be done in Bologna and CERN in clean rooms (see Chapter 6). The assembly areas will be equipped with cranes and special tools for the handling of the modules.

3.6 Quality assurance and test facilities

The production quality tests will consist of different steps, both at the strip and module level.

Each produced strip will have to pass a voltage test in air or vacuum. The pad connections will be checked by pulsing the anode/cathode pad and looking for the induced signal. A sample of strips will be tested with the final gas mixture and checked with cosmic rays or beam: the Time over Threshold signal, arrival time spectra and efficiency of each pad will be monitored. The time resolution tests would

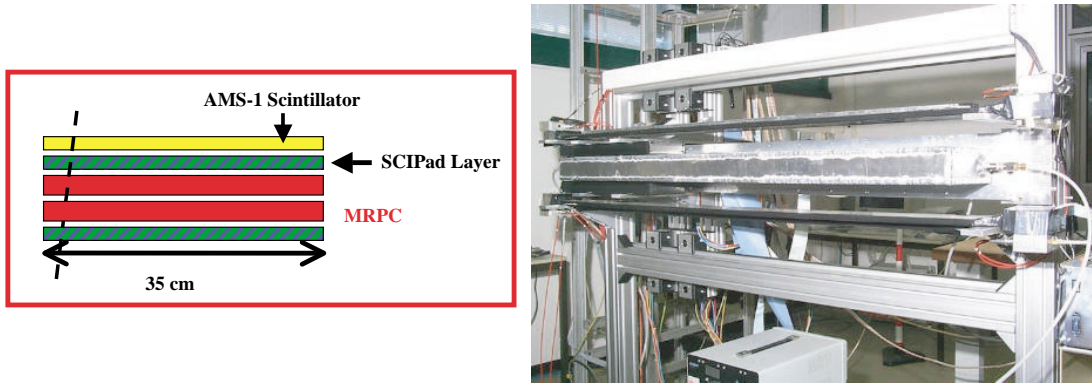


Figure 3.23: Cosmic ray station in Bologna. Left: the telescope layout; right: photograph of the telescope (see text for details).

probably be possible only with beam since with cosmic rays it would require too much time to collect a meaningful statistical sample.

One of the cosmic rays stations is already in operation in Bologna (Fig. 3.23). The telescope consists of two MRPCs, one AMS TOF scintillator counter [3] and two scintillator pads detectors (SCIPAD)¹ for tracking purposes. Data collected with this set-up give results which are compatible with the test beam results. The final test station will consist of a stack of 4 MRPCs, fully read out. A second station for tests with cosmic rays is being completed in Bologna.

Each assembled module will be tested immediately after production for gas tightness and HV in air. The tightness of the water cooling pipes will also be checked. After being transported to CERN, all modules will be tested in a cosmic rays test facility made of 4 piled-up modules: this facility should be equipped as much as possible with the final read-out system. We foresee 4 weeks in total to test one 4-module stack, with two weeks reserved for setting up and HV conditioning and 2 weeks of data taking. This should be enough to test the basic features of the TOF detector (efficiency and time spectra of each pad), but probably not enough for a precise time resolution measurement. As a consequence we also plan to test at the CERN PS test beam (T10) a small sample of modules. We intend to test 3 modules per year (about 10% of the TOF modules), and have requested 15 days of test beam per year. This allows us to test about 1% of the total read-out channels of the TOF system, assuming that in 5 days we can complete a test of 10% of the read-out channels of all strips of a module. This will allow the complete monitoring of the modules performance during the production, at least for this small sample.

After transportation of the modules to the experimental hall, all modules will undergo again HV, electronics and water sealing tests before being mounted on the experiment.

3.7 Weights of the TOF modules

Details of the evaluation of the module weights are given in Table 3.2. The total weight of the full TOF (90 modules) is thus 22500 Kg. Considering in addition ~ 2500 Kg for the read-out crates placed at the end of each sector, the total TOF weight on the space frame is ~ 25000 Kg.

3.8 Material budget for the TOF modules.

Table 3.3 gives the TOF material budget in terms of radiation length percentage, as seen by particles hitting perpendicularly the MRPC. The geometrical overlap of the MRPC strips inside a module has been

¹The SCIPAD system consists of an array of small scintillator counters read out via WLS fibers with a multianode Hamamatsu H6568 (4×4 channels). A total of 28 regions of 2.5×3.0 cm 2 are defined, each one covering one of the MRPC pads.

Table 3.2: Weights of the TOF modules (Kg).

Module	Central	Intermediate	External
Strips	(3.0× 15) 45.0	(3.0× 20) 60.0	(3.0× 19) 57.0
Top cover	14.0	25.0	21.0
Gas box	21.0	33.0	28.0
Support rails	35.0	45.0	40.0
Support plate	10.0	14.0	13.0
Electronics	23.0	30.0	29.0
Cooling pipes	8.0	10.0	9.0
Cables and connectors	50.0	50.0	32.0
Contingency	8.0	12.0	10.0
Total	214.0	279.0	239.0

Table 3.3: TOF material budget.

Material	Radiation Length X/X ₀ (%)
Gas box	1.9
2 plates Phenolic fiberglass honeycomb	1.6
3 PC board	1.9
3 Copper layer	0.6
MRPC glass plates	6.0
Central support plate	2.4
Cooling	2.6
Electronics	1.9
Top Cover	0.7
Cables	0.4
Total	20.0

taken into account for items 2 to 5. For the electronics cards and the cooling, which consist of discrete components, the total amount of material has been uniformly distributed over the module surface.

4 The readout system

4.1 Introduction

The TOF detector surrounds the central interaction region of ALICE with a total of 18 azimuthal sectors. Each sector will contain 5 modules of three different types. Each module will be filled with MRPC strips (see Table 3.1) which are read out by 96 pads each. Each sector will have 8928 readout channels, giving a total number of 160704 channels for the 18 sectors.

The signal from each pad will be amplified and discriminated by a ‘front end analogue’ card (FEA) mounted on the TOF module (Fig. 4.1). The discriminated signal will be shaped to provide a time over threshold (TOT) information; thus the leading edge of this signal gives the time of the hit and the width of the signal is equivalent to a measurement of its amplitude. Slewing corrections will then be made using the width of the TOT signal. This TOT signal will be transmitted via a 5 to 8 m long cable to the TDC Readout Modules (TRM) placed in custom crates positioned at the end of the sector (Fig. 4.1). Each TRM will be based on the HPTDC multi-event TDC presently being developed at CERN [1] and capable, in the very high resolution mode, of 25 ps bin size. The TRM modules will be read out by the Data Readout Module (DRM) placed in the same crate. This module will also provide the Detector Data Link (DDL) connection to the central DAQ of ALICE.

The readout crates at one sector edge should be able to handle signals coming from 2.5 TOF modules. This means 4464 readout channels per side, for a total of 24 TRMs with 192 channels each.

One Local Trigger Module (LTM) and a TRM for trigger readout complete the module requirements on each side of a sector. Two crates per side with 14 slots each will be enough to host the readout, trigger and control modules. These crates will be custom made, 9 U high and with a standard VME backplane. The required power will be provided by the low voltage distribution system (see Chapter 6). The crates will be installed in a box structure with an appropriate cooling system to avoid any heat dispersion towards the nearby detectors. In the following sections a detailed description of the readout hardware components is presented.

4.2 The Front End Analogue card: FEA

As discussed in Chapter 2, a very fast amplifier and discriminator must be mounted as close to the MRPC strips as possible. Initially we used a fast discrete components amplifier; however for the last 18 months we have been using a commercially available transimpedance amplifier MAXIM 3760. The output of this device is fed into a fast ECL comparator to generate a logic signal. The circuit diagram of the present test cards is shown in Fig. 4.2. The key components are the MAXIM 3760 amplifier and the MAXIM 9691 comparator. The circuit shown in this figure has an analogue output so that the pulse height can be measured by an ADC; in addition there are ECL outputs for both the time-over-threshold and trailing edge measurement. These outputs are needed since we are using CAMAC TDCs that can register only a single hit. The HPTDC chip that will be used to digitize the data for the TOF system will be fed with the signal directly from the output of the discriminator and use time-over-threshold for slewing correction; thus all this extra circuitry will be removed.

The best time resolution is obtained after making a correction that depends on the pulse height of the signal; this improves the time resolution from around 90 ps to about 50 ps. Pulse height information can also give indications that the ‘hit’ is noise (very small pulse height) or more than one particle passing through a cell (very large pulse height); thus the pulse height information is important but it is not crucial to measure it with high precision. For example, if the ADC spectrum is all contained in 20 bins, the

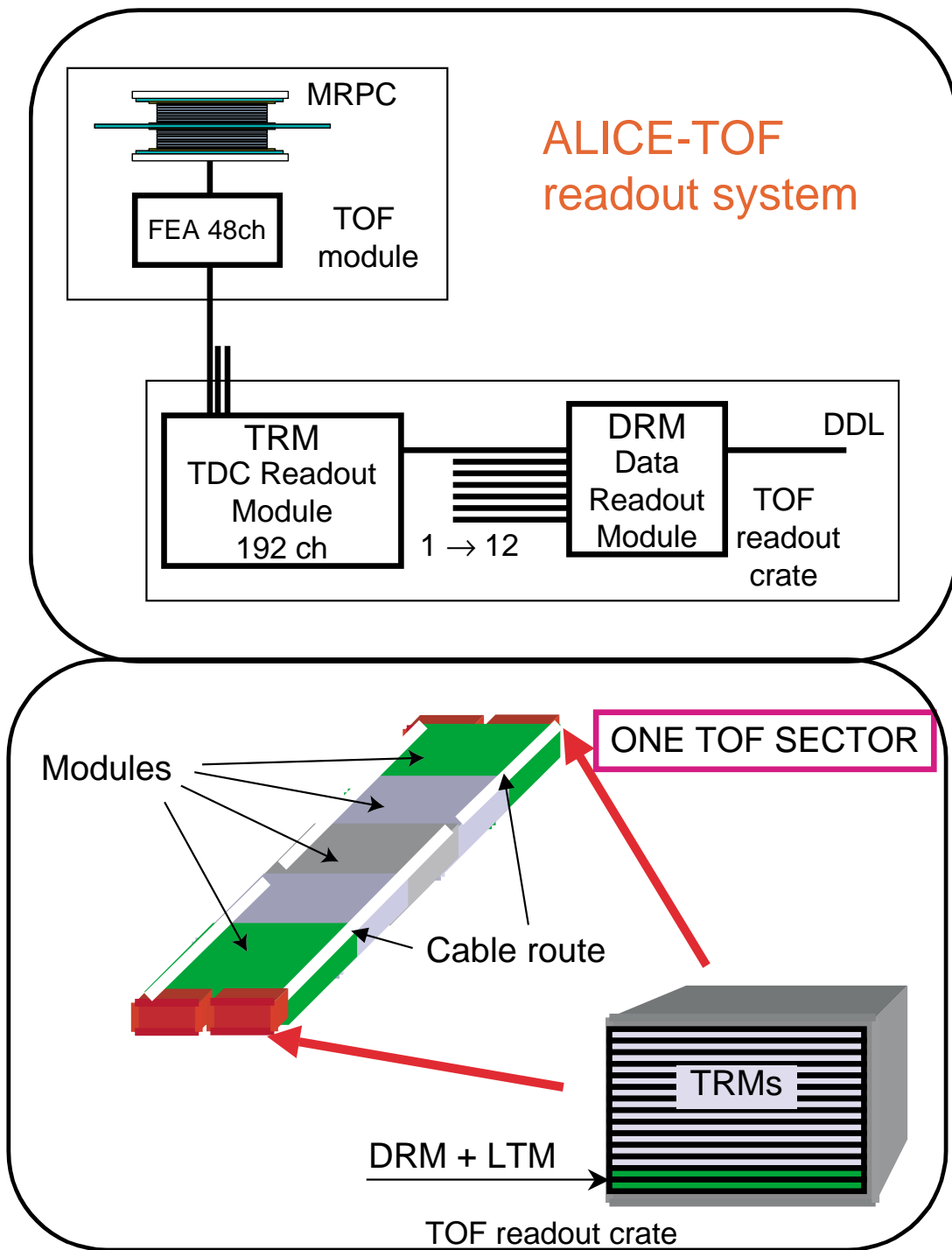


Figure 4.1: ALICE TOF readout general scheme.

resultant corrected time spectrum still has a resolution of 50 ps. The HPTDCs will be used in a mode where the time of both leading edge and trailing edge are measured in the same channel; however the input signal has to have a width greater than 8 ns, otherwise the time of the trailing edge is not measured. Therefore the front end analogue card has to produce a logic signal that has a width dependent on the pulse height with a minimum width of 10 ns.

Tests during the R&D phase showed that time-over-threshold (TOT) can be used for correcting the time producing the expected 50 ps time resolution (see Chapter 2). The baseline solution will be the MAXIM 3760 amplifier followed by the MAXIM 9691 comparator, although we will test other comparators which dissipate less power. Typically the output pulse width of this combination is ~ 5 ns, therefore an integration stage will be added. On the test card shown in Fig. 4.2 the differential output of the amplifier is connected to the differential input of the comparator; however tests have shown that comparable performance can be obtained with a single-ended connection. Thus we could use one of the outputs of the MAXIM amplifier directly connected to the comparator to ensure the best possible leading-edge timing, while an integration stage will be added to the other output. A possible circuit is shown in Fig. 4.3. Fig. 4.4 shows the simulated performance of this circuit (the time of the direct signal fed into one input of the comparator, the time of the signal after the integration stage fed into the other input and the differential sum of the two).

Fig. 4.3 shows the circuit diagram for a single channel; 48 such channels will be mounted on a 4 layer PCB of size 10 cm \times 50 cm (see the sketch in Fig. 4.5). Four 96-pin connectors will be used to connect this Front-End Analogue (FEA) card to the interface card. These connectors will be used to transport the input signals (3 pins for each anode and cathode signal). Additionally there will be a ‘CONTROL’ input connector on the outer edge of the card that will be used for the threshold settings (two thresholds per card), the ‘OR’ output (two LVDS ORs of 24 channels each for trigger purposes), the voltage sense lines and control lines to switch off the power on a complete card in case of problems. Power will be connected to each card from the power bus running along each edge of the module. The output signals from the comparator will be ECL; two standard flat cable 50-pin connectors will be used for this purpose; the cable will first be routed towards the sides of the module, and then along the sides to the end regions where the TDCs will be mounted in crates. These cables are in an area that is in the shadow of various space frame support structures and services for the TRD.

The FEA design presented here is the basic choice for the TOF detector. A possible further improvement based on the development of an ASIC chip is being actively pursued in conjunction with the LAA project.

4.3 The TDC readout module: TRM

4.3.1 The HPTDC - a summary

The readout scheme presented here is based on the HPTDC chip [1], [2]. This ASIC has been developed in the microelectronics group at CERN and designed as a general purpose TDC for LHC experiments.

Its main characteristics are summarised here (for a full description see [1]). The HPTDC works using a 40 MHz clock as a time reference to synchronize the acquisition of detector signals to bunch crossing. Different working mode resolutions are obtained from the 40 MHz clock through a Phase Locked Loop (able to generate clock frequencies up to a 320 MHz) feeding a Delay Locked Loop (DLL). The chip has several working modes: Low Resolution Mode (LRM: 800 ps LSB), Medium Resolution Mode (MRM: 200 ps LSB) and High Resolution Mode (HRM: 100 ps LSB). Finally an improved time resolution (Very High Resolution Mode VHRM: 25 ps LSB) can be obtained using a programmable R-C delay chain to control the sampling of the timing signals from the DLL. A specific set of calibration constants for each chip is needed in VHRM. This is the mode the TOF detector will use. In VHRM each chip hosts 8 separate channels (in the other modes it can handle up to 32 readout channels).

Every hit is encoded in 32 bit information (word). The HPTDC has multi-hit functionalities. Every

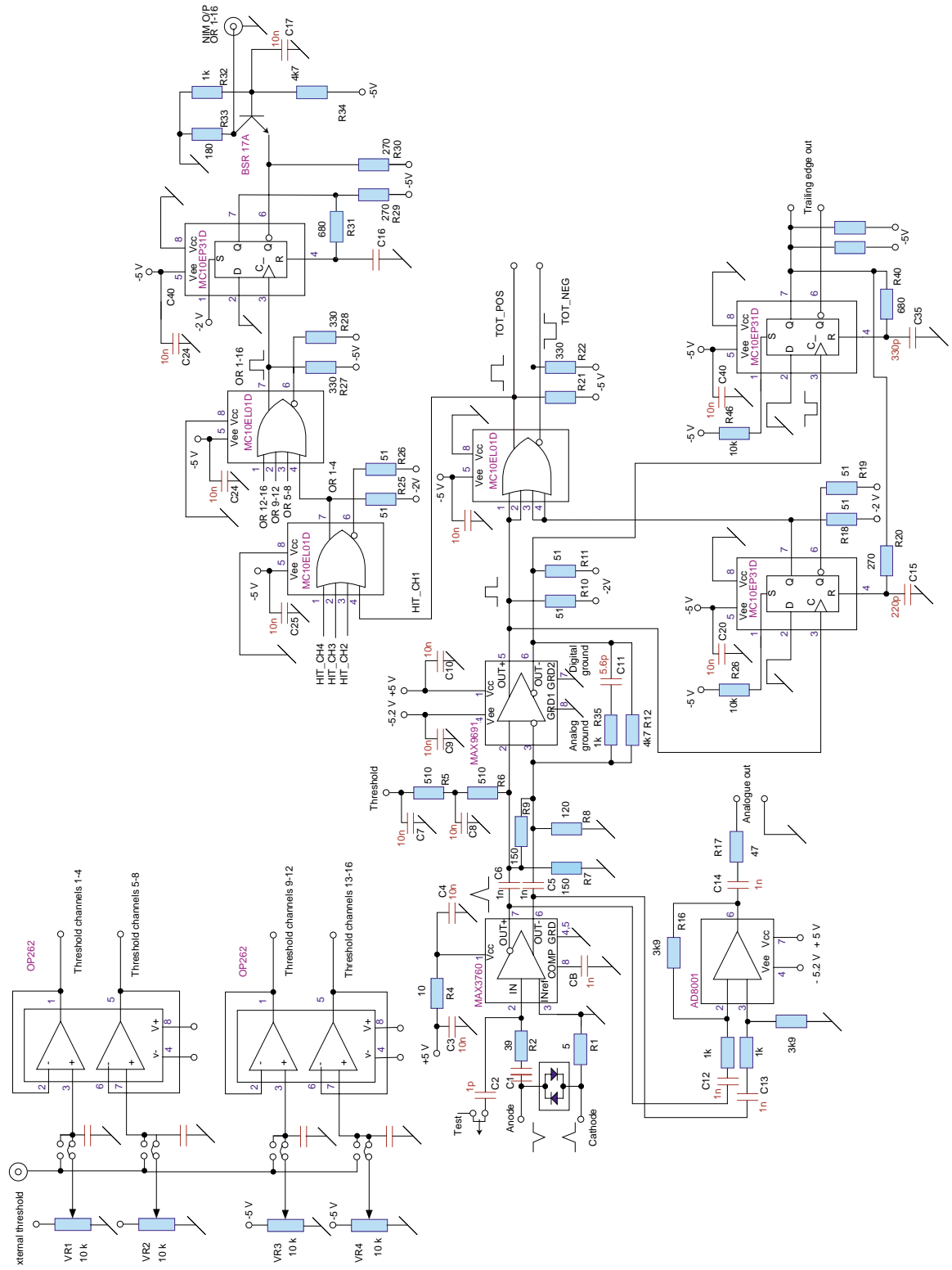


Figure 4.2: Circuit diagram of 16-channel Front-End Analogue card used for the tests.

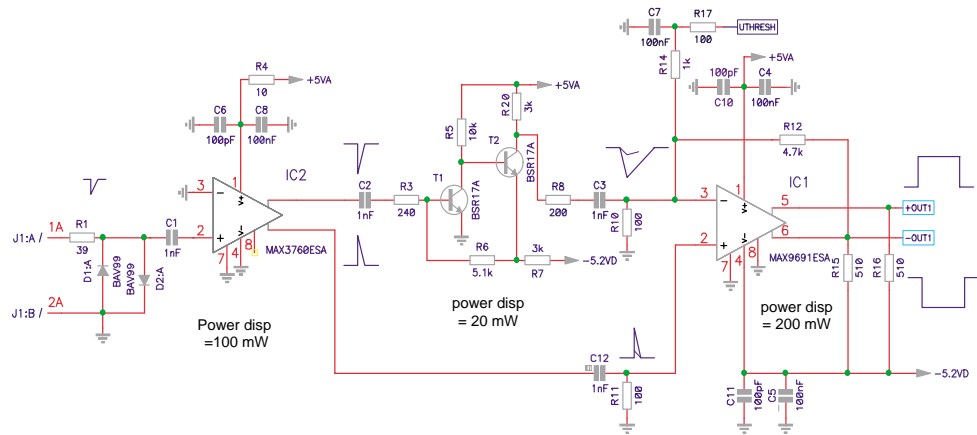


Figure 4.3: Front-end analogue card circuit diagram (one channel).

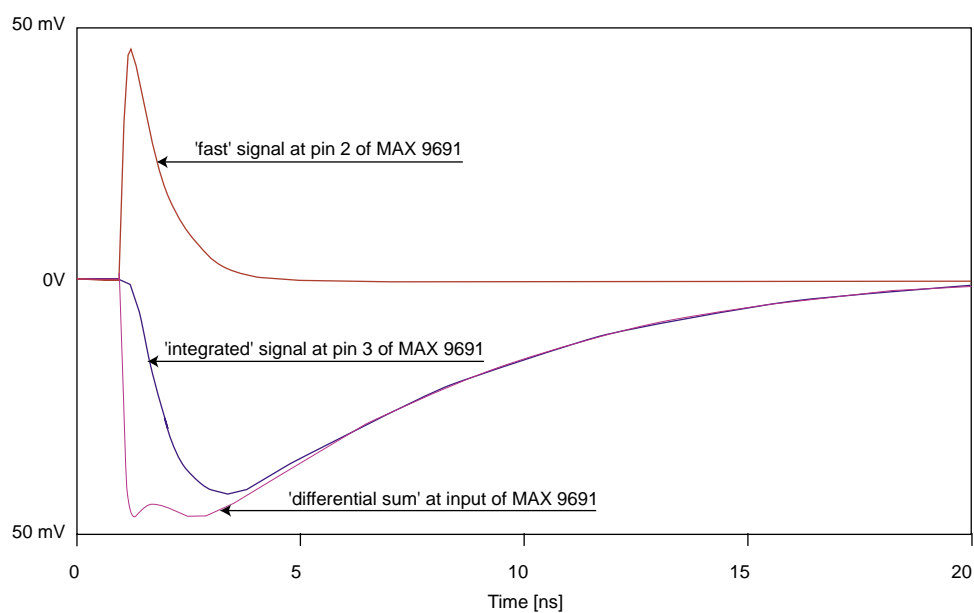


Figure 4.4: Simulated performance of integration circuit.

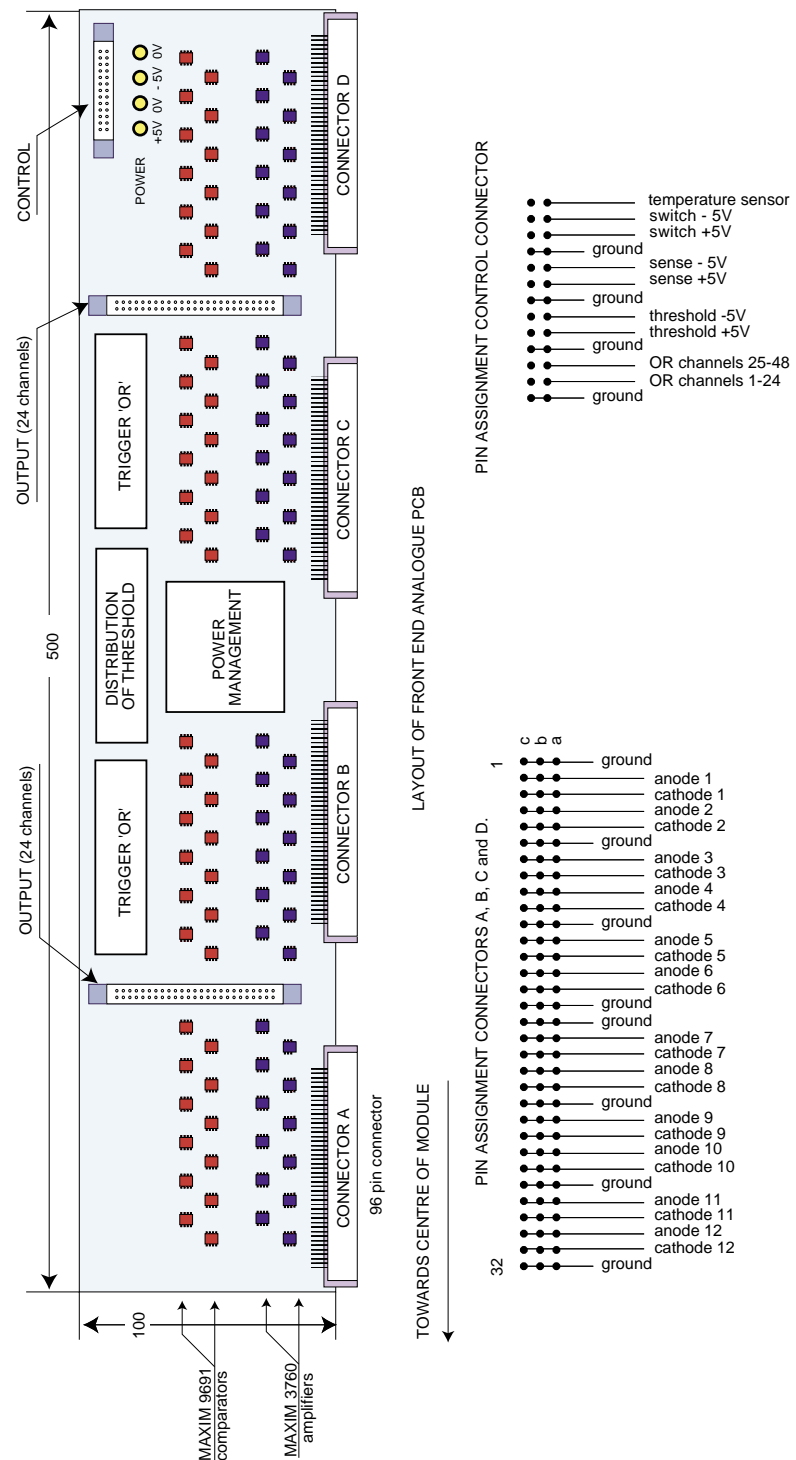


Figure 4.5: Sketch of Front End Analogue card.

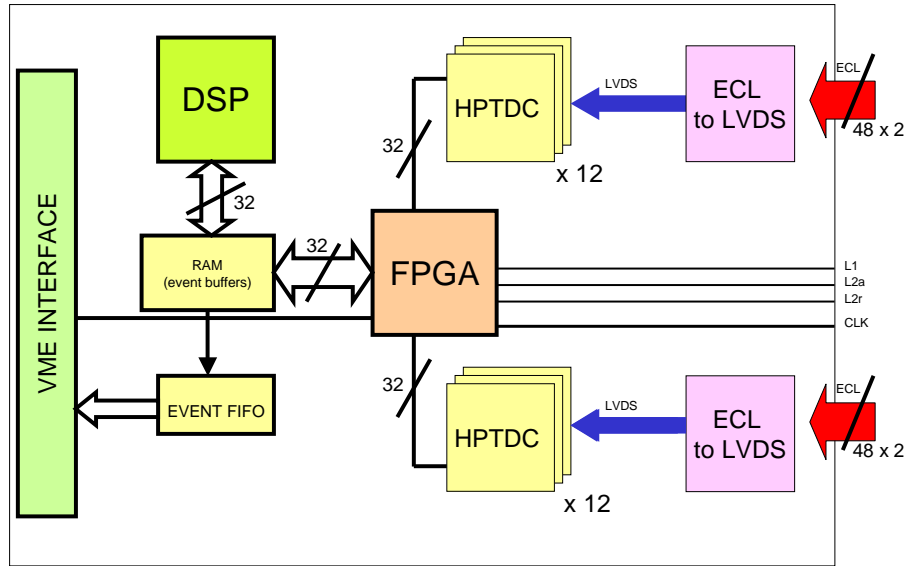


Figure 4.6: Block diagram of one TRM module with 192 channels.

group of two channels has a 256 words deep buffer attached to it. A trigger matching is then performed between a trigger time tag and the time measurements themselves at a given offset, within a user programmable time window. Hits matching a trigger are passed to a common readout FIFO (again 256 words deep) shared by each four-channel group.

4.3.2 The TRM

A block diagram of the TRM is shown in Fig. 4.6. This module receives 192 ECL shaped signals from the FEAs: these signals internally converted to LVDS standard, are sent to the 24 HPTDCs. An FPGA will then perform the readout of the HPTDCs. To ensure high bandwidth the FPGA will act as an external readout controller of two separate chains consisting of 12 HPTDC slaves (in token-base parallel-readout configuration). The use of an Altera APEX family FPGA is foreseen. A Digital Signal Processor (DSP) will control various setup operations (including R-C delay chain calibration) and data packaging. The use of a Analog Devices Shark family DSP is foreseen. Memory (RAM and SRAM) is provided for event buffering and program hosting.

Program loading and general control of the TRM will be managed through a VME interface. Initialisation and setup of the HPTDC chips will be normally performed through the DSP.

At reception of a L1 signal from the ALICE Central Trigger Processor (CTP) the HPTDCs will look for hits with a time offset of $\approx 6.2 \mu\text{s}$ (the exact value will be determined by the L1 decision time, still to be specified [3]) and a programmable time window (of the order of 100 ns), moving them to the internal readout FIFO. This operation does not cause dead time to the acquisition of data by the HPTDC.

Immediately after the L1 signal, the FPGA looks at the HPTDC readout FIFO and performs the readout of one event (the HPTDC provides event separation between hits with event header and trailer for each received trigger). The FPGA will then send the data to the DSP for further processing (data

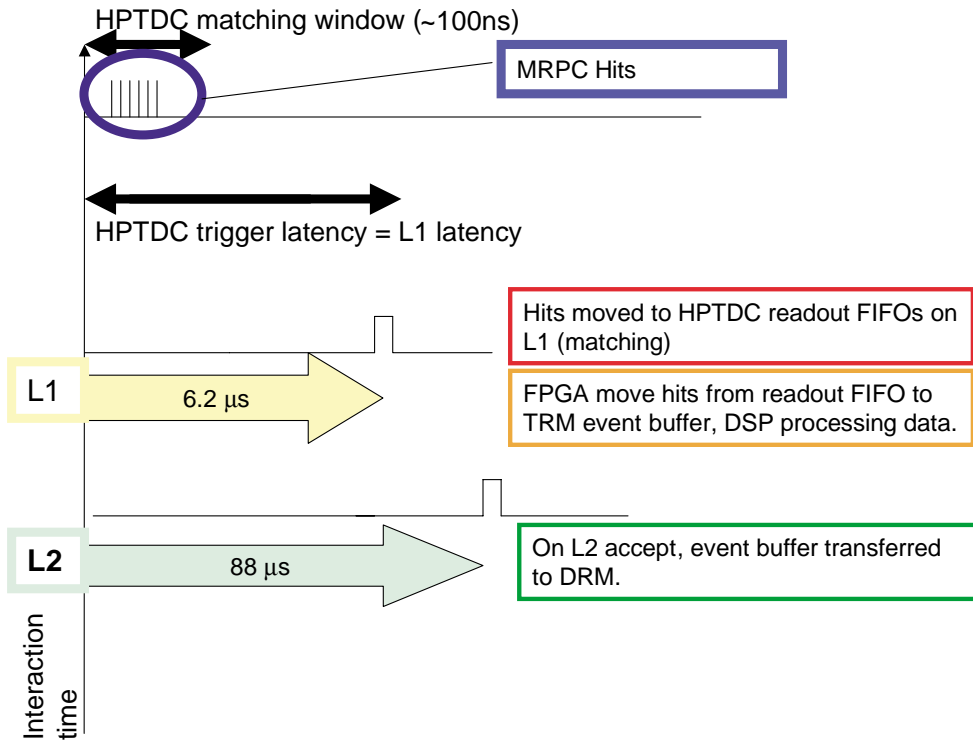


Figure 4.7: ALICE triggers and HPTDC readout scheme. On L1 hits will be removed from HPTDC readout FIFOs; on L2 reject corresponding event buffer will be cleared.

reordering and packaging) and final storing to RAM event buffers (capable to contain up to 16 events). A cyclic redundancy checking (CRC) of data is also foreseen implemented through a look-up table. All these operations are also performed with no dead time for the HPTDC.

A L2 reject message from the CTP clears (through the DRM) the corresponding event buffer on the TRM. A L2 accept starts the data transfer through the VME64 bus and clears the event buffer. The readout logic and timing is summarised in Fig. 4.7.

It is worthwhile to note that in VHRM the HPTDC cannot provide “paired” measurements (e.g. packing in a single 32 bit word the leading edge and the width measurement of the pulse, through detection of the trailing edge). We therefore need, for this HPTDC application, to enable simultaneous measurement of leading and trailing edges; these are then flagged inside the data, allowing time over threshold measurement. Each TOF hit will therefore account for 64 bit (one 32 bit word for the leading and one 32 bit word for the trailing). Consistently HPTDC buffers (the internal one, shared by 2 channels and the readout buffer) will be 128 hit deep. A custom packing of the two resulting measurements in a single word (leading edge and width) will be performed by the DSP (12 bits will be assigned to the leading edge and 9 bits to the width measurement). This reduces the required bandwidth by a factor of 2.

An important task of the DSP will also be to reorder the hits. Due to the HPTDC architecture, hits are digitised inside the internal buffer using a simple arbitration scheme. Leading and trailing edges of the same pulse could be separated by signals coming from other channels and sharing the same internal buffer. The DSP will control this reordering, as well the monitoring of errors and of noisy channels.

4.3.3 Tests of the HPTDC

During 2001 a HPTDC Test Board (TB1 with 16 channels) containing two HPTDC-1.0 chips has been built. A photograph of this test board is shown in Fig. 4.8.

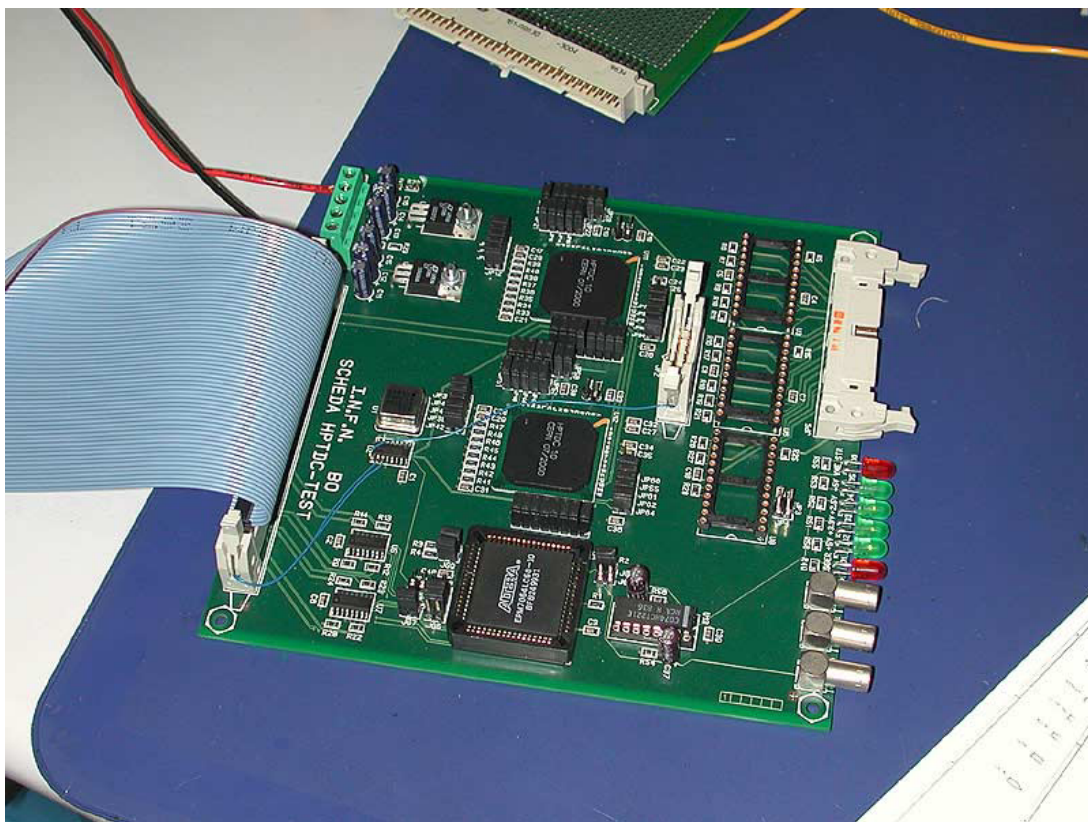


Figure 4.8: The HPTDC TB1 test board.

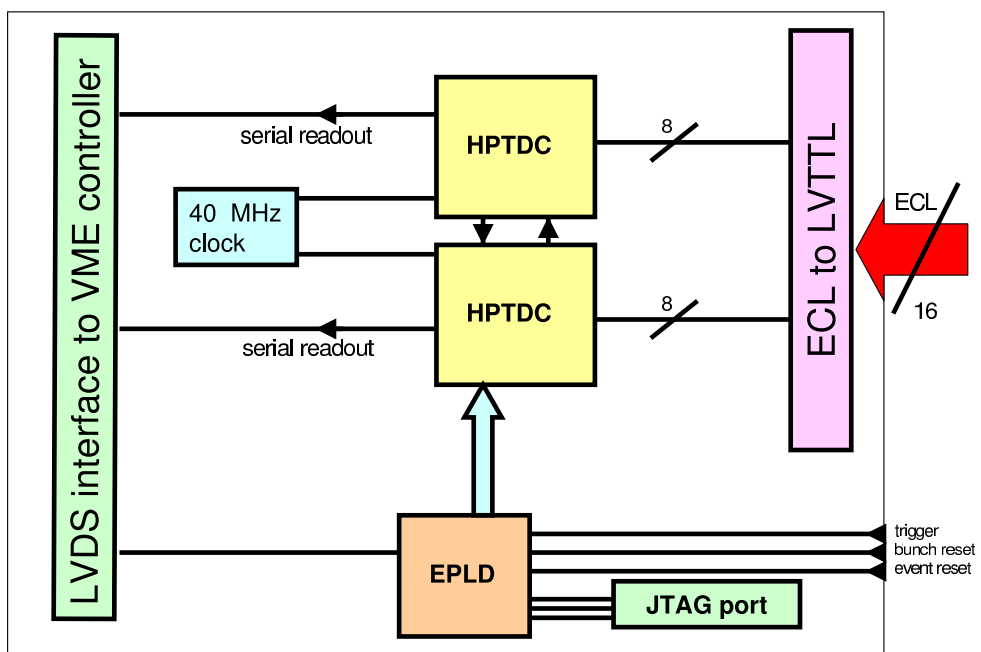


Figure 4.9: Logic block diagram of HPTDC TB1.

It was designed mainly as a tool to learn and check the HPTDC functionalities. A block diagram is shown in Fig. 4.9. A 40 MHz clock is provided on board (the clock source is a commercial crystal oscillator) where the ECL inputs have been selected to match the current FEA cards. The two HPTDC chips have been mounted in token ring master/slave configuration. The communication with the card is done by means of a private LVDS bus (driven by a 6U VME controller) and a JTAG port. A 68-pins Altera EPM7064 CPLD completes the test board, providing the needed handling of logic signals. Three TTL inputs reserved for trigger, event reset and bunch reset are also available and have been used to check the HPTDC trigger logic.

All the basic features of the HPTDC have been successfully tested following the procedure outlined in [2]. The resolutions measured in VHRM have been found to be compatible with the ones obtained by the CERN microelectronics group.

With the latest packaging (version 1.2) available since January 2002, the CERN microelectronics group has shown that the HPTDC 1.2 still has some crosstalk, in its high resolution modes, between the logic part of the chip and the time measurement part affecting in particular the integral non linearity (INL) of the converter. This limits the time resolution of the HPTDC to 50 - 60 ps RMS. Using a compensation table to take into account the integral non linearity dependence along the 25 ns period [2], a value of 19 ps has been obtained [4].

During the first months of 2002, the HPTDC-TB1 has been also equipped with HPTDC 1.2 chips and the resolution has been measured for different delay lines after applying a compensation table. Fig. 4.10 shows the measurement of differential non linearity (DNL)¹ and integral non linearity (INL)² for two channels in VHRM belonging to two different chips done with this board, from which the need to apply a correction becomes clear. The pattern observed for the INL is similar to the one observed by the CERN group. Fig. 4.11 shows the measurement of a 12 ns cable delay line by means of the same two channels, before and after applying the compensation table correction. To obtain the resolution per channel the RMS of these distributions has to be divided by a factor $\sqrt{2}$. In Fig. 4.12 the resolutions obtained per single channel before and after compensation for different delay lines are shown. Resolutions below 20 ps have been obtained after compensation.

During 2002 other intermediate test cards (32 channels) will be implemented towards the final TRM design. FPGA and DSP code will be implemented and thoroughly tested together with clock distribution within the card. The new release of the HPTDC foreseen during 2002 would make a better isolation of the power supply for the time measurement part with the potential to reduce the observed crosstalk [4] and the need to apply a compensation table.

The minimum time between two consecutive time measurements is a critical parameter of the HPTDC. This value - according to the HPTDC manual is “typically 5 ns (guaranteed 10 ns)” - has been carefully investigated. The result presented in Fig. 4.13 shows the fraction of “complete” pulses (that is when both leading and trailing edges have been detected) registered by the HPTDC for different pulse widths. Data have been collected in VHRM with both leading and trailing edges enabled. Therefore the FEA will provide the TOT signal with a minimum width of 10 ns. The resulting dead time of each TDC channel will depend on the TOT value and will be between 20 and 30 ns.

4.4 The Data Readout Module: DRM

Each crate will be equipped with a Data Readout Module (DRM) card that will act as main interface between the Central Alice DAQ, the CTP and the TOF electronics.

A functional block diagram of the DRM is shown in Fig. 4.14.

¹Differential Non-Linearity (DNL) is the deviation of the output bin size from its ideal value of one least significant bit (LSB) [2]

²Integral Non-Linearity (INL) is the deviation of the input/output characteristic and a straight line of ideal gain (slope) that best fits the curve, obtained by adding an offset to the ideal transfer characteristic [2]

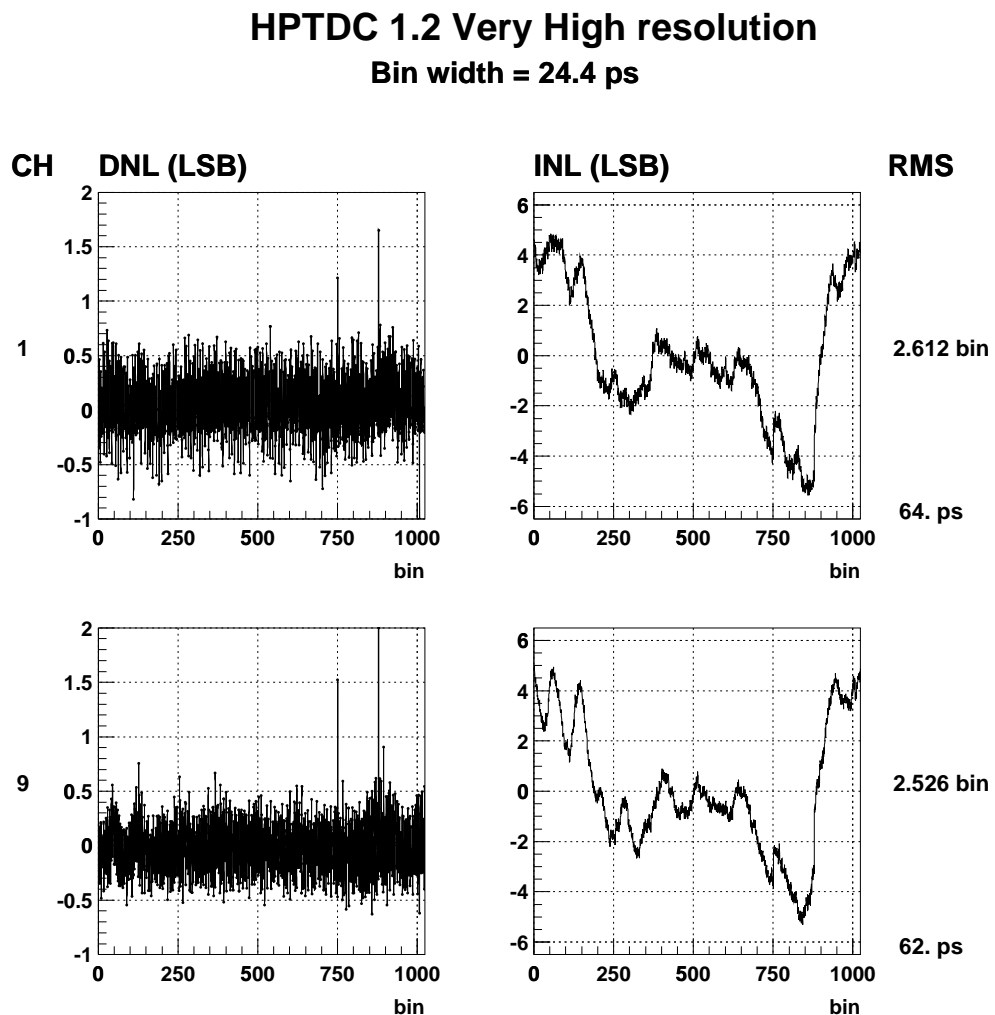


Figure 4.10: HPTDC differential non linearity (left side plots) and integral non linearity (right side plots) for two different channels. The estimated RMS is obtained from the RMS of the INL distribution along the 25 ns period.

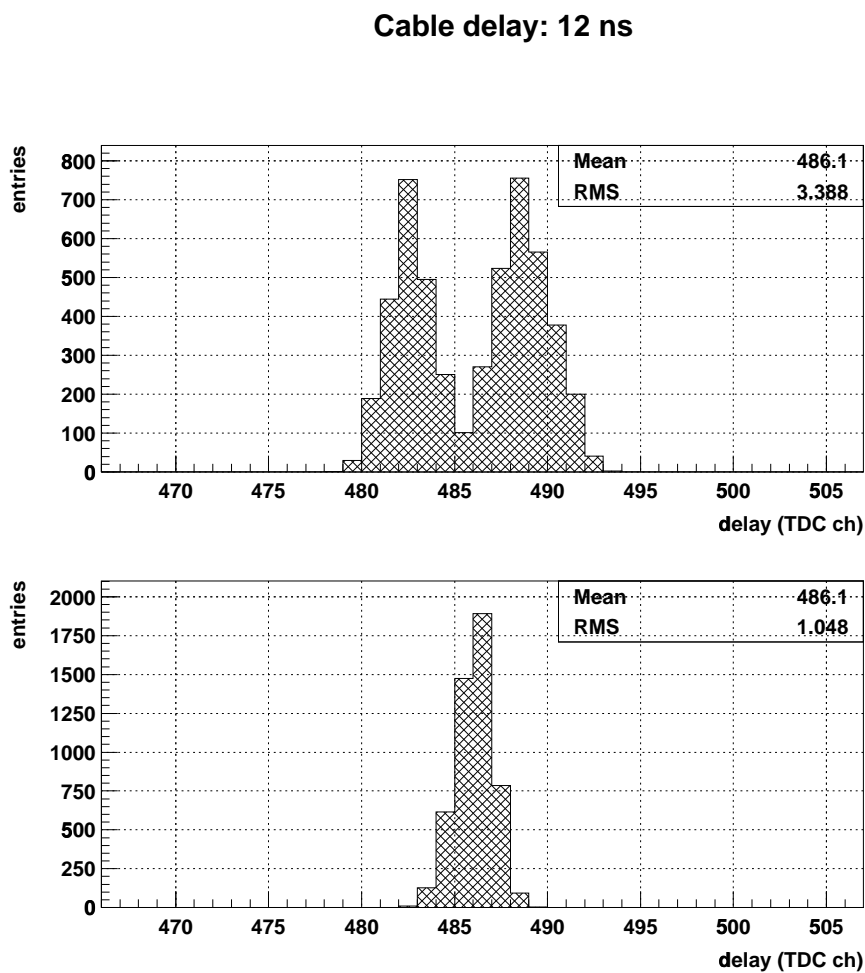


Figure 4.11: Measurement of a cable delay line of 12 ns with the HPTDC-TB1 in VHRM mode without compensation (upper plot) and with compensation (lower plot). The TDC bin width is 24.4 ps.

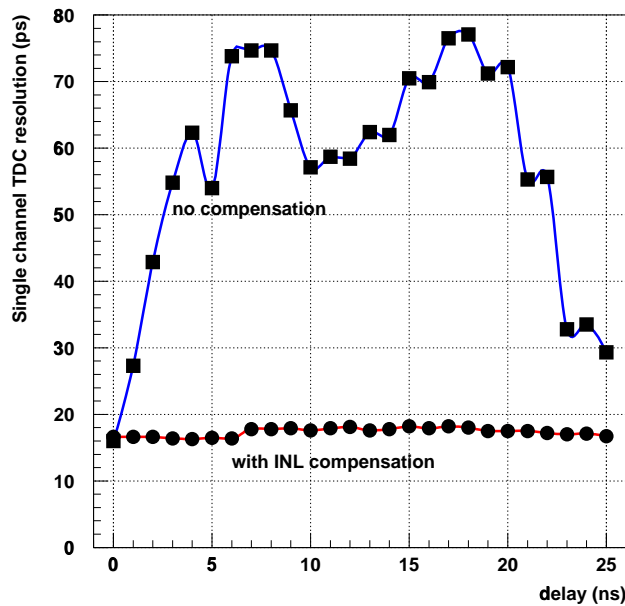


Figure 4.12: TDC single channel resolutions obtained with HPTDC in VHRM mode without compensation and after applying a compensation table.

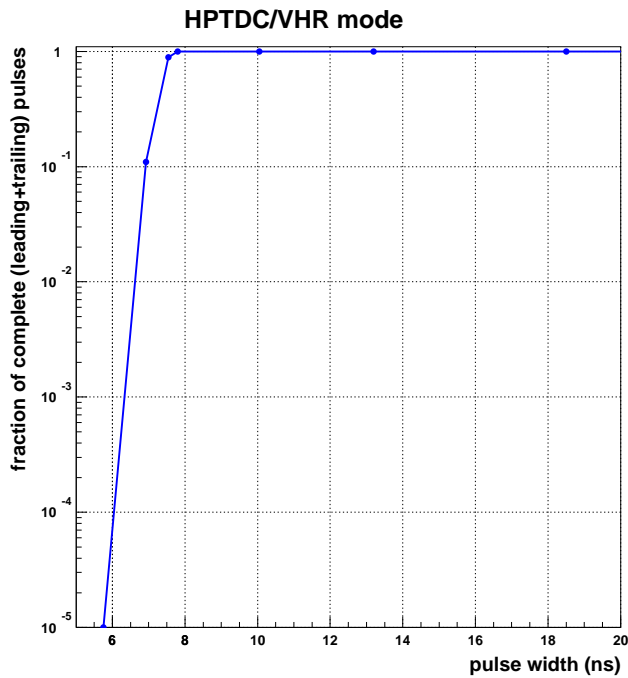


Figure 4.13: Fraction of complete pulses (leading and trailing) detected by the HPTDC as a function of the pulse width.

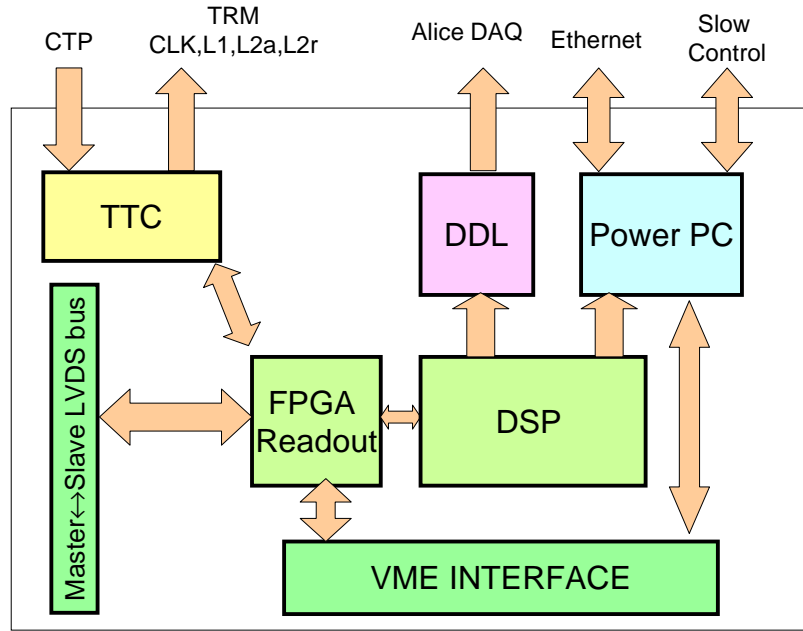


Figure 4.14: Block diagram of one DRM Master module (the Slave one is not equipped with the DDL interface).

The DRM will receive and distribute the 40 MHz clock and the trigger signals (L1, L2) to the TRMs. The clock will be received through an optical fiber, while the other signals will be derived from a TTCrx. The clock will be distributed to the TRMs via ECL connections. The control signals (L1, L2 accept and L2 reject) will be distributed with a LVDS bus to the TRMs through an external flat cable.

The DRM will read the data from the TRM modules. If a L2 reject is received the corresponding event buffer will be cleared on the TRMs, otherwise on L2 accept data will be transferred from all the TRMs to the DRM via the VME64 backplane. This data transfer is performed by the FPGA.

The data will be further processed and encoded by a DSP on board and sent through a standard ALICE DDL interface to the central DAQ.

A Power PC will allow monitoring of the data and will host the slow controls of the TOF system (threshold setting, ...). All these I/O devices (TTC and DDL interfaces and PowerPC card) will be developed as piggy-back card in standard PMC format applied to a VME card.

In the present scheme, one of the two crates at the sector edge will contain a DRM equipped with the DDL (DRM Master); the second crate will contain a reduced version without the DDL (DRM Slave): the DRM master will first read and transfer the data from its crate and then take and transfer the data from the DRM slave. The data communication between Master and Slave is obtained by means of a private LVDS bus. The block diagram shown in Fig. 4.14 corresponds to the DRM master.

A first prototype of the DRM is presently under design, it will have the possibility to receive and distribute the clock and the control signals and to read the data from the prototype TRM.

4.5 Expected readout bandwidth

Concerning the required bandwidth of the readout system, an average multiplicity per TRM of about 58 hits per event (corresponding to a conservative 30% occupancy: the expected average occupancy is about 15%, see Chapter 5) produces:

- 58 hits per event per TRM → 58 words (leading+trailing packaged in one word by the DSP).
- Since each word consists of 32 bits = 4 Bytes and considering about 40 Bytes for controls (HPTDC identification), each TRM will have on average 272 Bytes per event.
- Considering at maximum 12 TRMs per crate, we obtain 3.2 KByte of information per crate and per event.
- Requiring about $200 \mu\text{s}$ for a crate readout (ALICE DAQ impose a maximum readout time of 1 ms, including DDL encoding), the required bandwidth should amount to about 16 MB/s per crate. This does not pose a problem for a VME readout.

The connection through a private LVDS bus between the two DRMs is expected to have at least 10 MB/s bandwidth. Data transfer from Slave to Master will occur while the Master is already sending its own data through the DDL.

4.6 Timing and the T0 array

All timing of the TOF array will be done with respect to the LHCC signal defining the bunch crossing time; this is discussed in the following paragraph. Since the beams have a finite size there is a time interval during which the interaction may happen; this introduces a time uncertainty with a σ of 170 ps. If the time of the interaction is not measured this uncertainty would be the dominant contribution to the time-of-flight measurement. The T0 counter arrays, discussed below, will measure the time of the interaction with a precision of 50 ps (or better).

4.6.1 LHC timing

The timing of the LHC bunch crossing is controlled in the LHC main control room and is obviously very precise (otherwise there would be no colliding beams). The LHC clock will be distributed to all LHC experiments using optical fibres using the TTC system [5]. The jitter on this clock will be about 80 ps; however this jitter can be eliminated by the TTCmi module which employs a phase-locked loop controlling a ‘pulled’ crystal oscillator to generate the 40.079 MHz clock with a 10 ps jitter. This clock can be fanned out locally using an optical fanout and commercial optical receivers such as the AMP 269052-1. Tests performed by Bruce Taylor using 100 m optical fibre between TTCmi module and the optical receiver give a clock with 15 ps jitter. There will be 72 of these optical receivers (one per crate, two at each end of each sector) plus one mounted in the T0 TDC readout crate (see below). This is shown in Fig. 4.15.

The HPTDC used by the TOF system discussed before relies on having a stable clock. The time of each hit is measured with respect to this clock and stored in a buffer. Internally the HPTDCs have phase-locked loops locked onto the input clock, thus jitter on the input clock is filtered out. Simulations by Jorgen Christiansen and Manuel Mota show that (a) a 20 ps input jitter translates into a 12 ps jitter on the internal clock within the HPTDC; (b) a shift of 100 ps for one clock cycle at the input would be completely filtered out; (c) a permanent shift of 100 ps would cause the internal PLL to shift by 100 ps, but it would take about 100 clock cycles to follow such a shift. Thus although the jitter of this clock is an important parameter, we believe that this is well under control. A more important variable is the shift in phase between different parts of the TOF system. That is why the 73 optical fibres connecting the optical fanout in the ALICE control room to the crates containing the TDCs will follow a common path to the centre of the ALICE magnet and then divide into two, one for each end of the TOF system.

There will be changes in the phase between this clock and the time of the LHC interaction following a daily or seasonal cycle; however we should (a) be able to monitor this with the continuous calibration of the TOF array (see Section 4.8) and (b) these changes should cancel because we use the T0 array to measure the time of the interaction and the T0 will be measured with respect to the same clock signal.

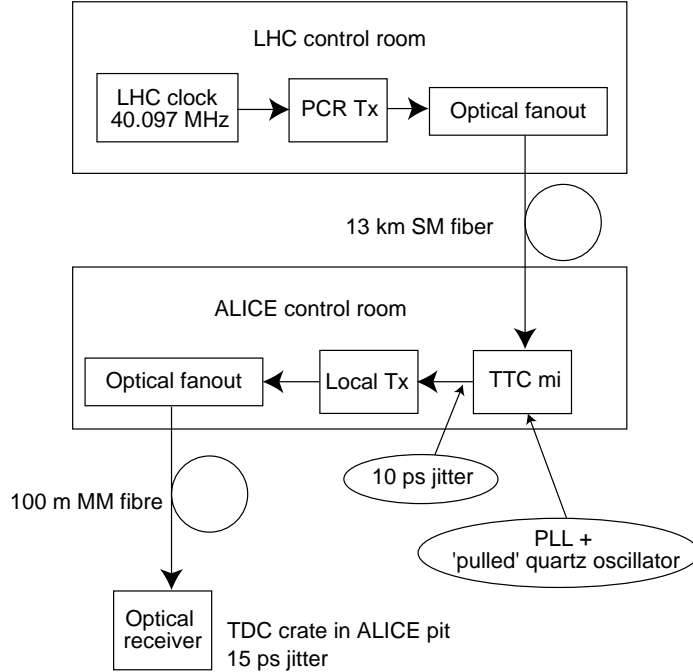


Figure 4.15: Diagram showing fan out of LHC clock from the LHC control room to the TDC crates mounted inside the ALICE magnet

4.6.2 T0 array

Two arrays, each containing 12 quartz radiators read out with mesh photomultipliers [6] will be mounted around the beam pipe. $T0_R$ is ~ 70 cm from the interaction point with its position constrained by the muon filter and all the other detectors and services that have to be fitted in. $T0_L$ is much less constrained since there is no muon filter; this array will be mounted 3.5 m from the interaction point. The layout is shown in Fig. 4.16. Each array of 12 detectors is connected to an electronic summing circuit that will select the earliest hit; the average of the time measured by $T0_L$ and $T0_R$ will be computed by a mean-timer circuit and thus generate a T0 signal independent of the actual position of the interaction. From simulation one finds that T0 will have a σ of 50 ps. Of course this depends on getting all 12 elements of the array timed together better than the expected resolution of 50 ps and that the constant fraction discriminators work perfectly over a very wide dynamic range. Thus, even though we will use the T0 signal as created, we will monitor the time of all elements of the T0 array to check that the algorithm is perfectly tuned at all times.

Since we want to measure the T0 time with respect to the LHC clock fanned out to all the TOF readout crates, it simplifies everything if the time of T0 and all the elements of the T0 array are measured using the same HPTDC chip clocked by the same clock. However since the individual hit rate of each of the T0 elements is much higher than for the hits from the TOF array, there has to be a change in implementation of the HPTDC. A simple add-on card (applied to one or two TOF TRMs) to implement a de-multiplexing scheme of T0 channels is foreseen. This option is currently under study and will be presented in the TDR concerned with all the forward detectors in ALICE.

4.7 Cosmic and multiplicity TOF trigger

The requirements of the trigger derived from the ALICE TOF are two-fold. The first is to provide a cosmic ray trigger that can be used for calibration purposes by the TOF and other subdetectors. The second purpose is to provide fast topology information that can be used to aid more complex trigger

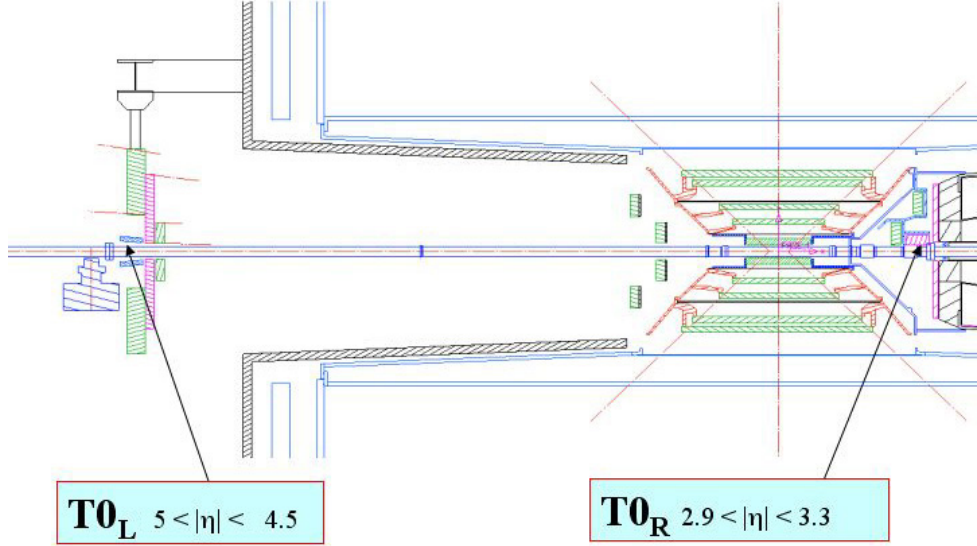


Figure 4.16: Section along the beam showing the location of the $T0_L$ and $T0_R$ arrays

algorithms.

4.7.1 Cosmic trigger

The cosmic trigger provided by the TOF will be given by two hits in the TOF barrel corresponding to a particle entering and leaving the central region of the ALICE experiment. Each of the 18 sectors will be subdivided into eight ‘areas’ making 144 areas for the total TOF barrel. Each of these areas we call a cosmic zone; the basic cosmic trigger will be a coincidence of ‘back-to-back’ cosmic zones; in this way the triggered cosmics will pass close to the interaction point. An ‘almost vertical’ cosmic in the centre of the TOF barrel will cross the diameter of the barrel (7.4 m); thus the two cosmic zones fired will be delayed by 25 ns with respect to each other. For cosmics at 45° to the vertical, firing cosmic zones located at opposite ends of the TOF barrel, the time difference will be 35 ns needing a different delay for the signals making the coincidence. The coincidence gate needs to be kept as short as possible to suppress random triggers caused by ‘dark’ noise in the MRPC strips. Additionally we will allow different cosmic triggers to be set up for other subdetectors (such as the HMPID) where cosmics that satisfy different geometrical constraints could be selected.

The FEA card provides 2 OR outputs, each corresponding to an OR of 24 channels. Thus for each of the 18 sectors there will be 372 of these OR signals. Half of these (186) will go to each endcap to a Local Trigger Module (LTM). The LTM will receive 186 inputs and output 4 OR signals corresponding to a group of 46 or 47 of the FEA OR signals (the OR of ~ 12 strips). Each of these outputs will correspond to a hit in a cosmic zone of $\sim 1 \text{ m}^2$. The LTM will also be able to inhibit any of the inputs in case there is a FEA OR counting at some very high rate for some reason. Also there will be programmable delays so that the FEA OR signals making a group can be timed in.

There will be a dedicated TRM associated with each LTM so that the 186 input signals can also be timed.

The 4 output signals provided by the LTM correspond to the cosmic zone discussed above; thus there will be 72 such cosmic-zone signals per endcap. These signals will be fed to a Cosmic Trigger Module (CTM) located in a crate close to the Central Trigger Processor (CTP) outside the ALICE magnet. A schematic diagram of the hardware implementation of the cosmic trigger is shown in figure 4.17. In the CTM there will be a coincidence formed between each ‘back-to-back’ cosmic zone with the appropriate timing. The CTM will assume that cosmics go downwards, since the rate of upward cosmics is so low. Additional circuitry within the CTM will be able to form the various ORs between a given number of

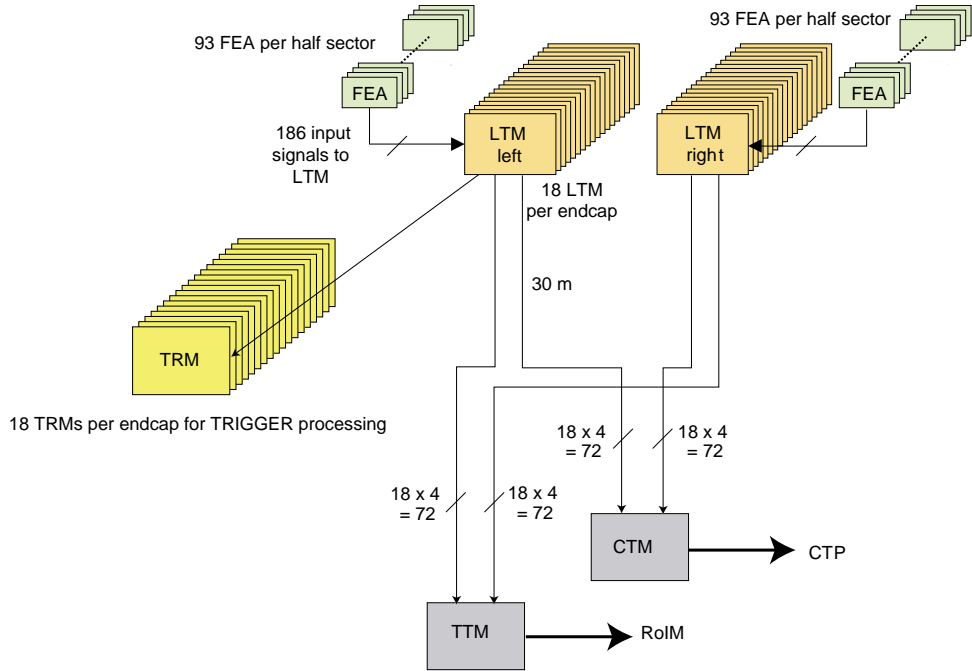


Figure 4.17: The TOF trigger system for cosmics.

cosmic zone signals and form a coincidence between such ORs, such that special purpose cosmic ray triggers could be set up to service other ALICE detectors.

In order for this cosmic trigger to be effective the ‘dark counting rate’ has to be 0.1 Hz/cm^2 or below. At present this counting rate is around 1 Hz/cm^2 ; however this was measured with our prototype strips, which were built in rather unclean conditions. We are confident that this noise rate will be reduced to the required level when the MRPC strips are built in clean conditions. Additionally if a further reduction in noise is required we could increase the discriminator threshold. A small increase in this threshold has a large effect on the noise counts, but only a small effect on the efficiency. Since the cosmic ray triggers will only be operative outside the normal data taking runs, such a threshold adjustment will have no effect on the physics. If a further reduction in the trigger rate is required the cosmic scintillator array could be added to the coincidence.

4.7.2 Topology trigger

As stated above the TOF will also be used to provide a topology trigger that can be used in conjunction with various L0 triggers to further define the event. At present the combination of information from various subdetectors of ALICE to create triggers is foreseen in the Region of Interest Module.

The LTM will thus have a second function besides creating the cosmic zones discussed above. The LTM will also count the number of FEA OR signals for each interaction. Such counting will be strobed by the LHC 40 MHz clock. This clock is available since it is used as the clock input to the TRM. Thus for each clock cycle the 186 OR signals to the LTM will be counted, and signals generated for four (programmable) thresholds (such thresholds could be set to 1, 5, 10 and 50 inputs firing). Each LTM will thus generate 4 bits that will be sent to the Topology Trigger Module (TTM) located near the Region of Interest Module in the main trigger crate located outside but near the ALICE magnet.

4.8 Monitoring and Calibration

Tests of the TOF system and long term monitoring of the system will be performed in dedicated calibration runs with a pulser. The pulse, synchronised with the 40 MHz clock, will be injected along a dedicated line placed on the MRPC lower cathode PCBs, on the face opposite to the pads. The induced signal will be recorded using the complete readout chain (FEA, TRM, DRM) allowing monitoring of the channel performance. This pulser system will be used throughout the assembly of the modules to verify that all connections between pads and front-end electronics are good. The same system will be used during the installation of the modules inside the magnet, to verify that the full electronics chain for all channels is in a good state.

A temperature sensor in each module is presently foreseen so that monitoring of the calibration constants with temperature will also be possible.

4.9 Grounding scheme

The baseline grounding system of the TOF system follows the prescription given for the ALICE experiment [7]. The HV, FEAs and the readout system will have their own return line to a well defined common grounding point. Each module is in fact a Faraday cage and it is not grounded to the space frame. Ground references will be available, should the necessity arise, at the space frame borders.

4.10 Power consumption estimates

The foreseen power consumption for the electronics placed inside the ALICE magnet is shown in Table 4.1. Including 10% contingency, the total power consumption of the TOF system is about 125 kW. In case the DC/DC converters option is chosen, this number will increase to about 165 kW due to the inefficiency of the conversion and some other losses.

An independent cooling system, similar to the one described for the FEA, will be used to cool the digital modules in the crates.

Table 4.1: Power consumption of the TOF electronics.

FEA	Power/ch.(W) 0.4	Power/module (kW) 0.58-0.77-0.73	Power/sector (kW) 3.58	Total (kW) 65
TRM	Power/Module(W) 50	Power/crate (kW) 0.63	Power/sector (kW) 2.5	Total (kW) 45
DRM	25	0.025	0.1	1.8
LTM	30	0.03	0.06	1.1
Total				113

4.11 Basic time resolution of the TOF detector and electronics

The time measurement system described above will have a total time jitter as described in Table 4.2. All contributions have been added in quadrature to obtain the total time jitter foreseen in ALICE TOF following the formula

$$\sigma_{Tot}^2 = \sigma_{T0}^2 + \sigma_{MRPC}^2 + 2\sigma_{TDC}^2 + 2\sigma_{CITRM}^2 + \sigma_{Clock}^2$$

Where σ_{T0} is the intrinsic T0 time jitter , σ_{MRPC} is the MRPC intrinsic time jitter, σ_{TDC} is the intrinsic time resolution of the HPTDC, σ_{Clock} is the clock distribution jitter via the TTC system and σ_{CITRM} is the jitter introduced when distributing the clock in the TRM. The third column makes more conservative assumptions on the MRPC and HPTDC time resolution.

Table 4.2: Time resolution estimation for the ALICE TOF system.

Description	Average time resolution (ps)	Maximum (ps)
σ_{T0}	50	50
σ_{MRPC}	50	80
σ_{TDC}	25	50
σ_{Clock}	15	15
σ_{CITRM}	10	10
Total	82	120

5 TOF Detector Performance

5.1 Introduction

As already pointed out [1], the particle identification (PID) power of a very large TOF system covering the central rapidity region ($|y| \lesssim 1$) is of crucial importance in the ALICE experiment. Pion/kaon/proton separation in the intermediate momentum range (from 0.2 to $2.5 \text{ GeV}/c$) will provide relevant observables in order to investigate the nature and the dynamical evolution of the hadronic system produced in ultra-relativistic heavy ion collisions, at LHC energies.

The basic physics motivations for the ALICE TOF detector have been outlined elsewhere [1, 2]. The large-coverage, powerful TOF detector we envisage building should operate efficiently in extreme multiplicity conditions. It should have an excellent intrinsic response and a low overall occupancy at the highest envisaged charged particle density ($dN_{ch}/dy \leq 8000$). This demands a design with more than 10^5 independent channels.

In this chapter we illustrate, by means of detailed Monte Carlo simulations, the performance of the TOF system, thus testing our assumptions and verifying its foreseen PID capability in a “real” heavy ion collision environment. We discuss the PID procedure in terms of inclusive acceptances, efficiencies and contaminations for different particle species and in different experimental scenarios.

5.2 Detector description

5.2.1 Software tools for detector description and particle tracking

The present Monte Carlo simulation studies have been performed using AliROOT 3.06-Rev02¹ [3], the latest release of the ALICE off-line code implemented in the ROOT [4] framework for event simulation, reconstruction and analysis. The AliROOT framework is interfaced with several event generators (JETSET [5], PYTHIA [6], HIJING [7], SHAKER [8], etc.) thus providing a complete set of instruments to simulate ion-ion collisions.

5.2.2 Detector layout for Monte Carlo simulation studies

The detector covers a cylindrical surface of polar acceptance $|\theta - 90^\circ| < 45^\circ$. It has a modular structure corresponding to 18 sectors in ϕ (the azimuthal angle) and to 5 segments in z (the longitudinal coordinate along the beam axis), as shown in Fig. 5.1.

Each module has an overall thickness of 29 cm and an internal structure organised in planar strips equipped with sensitive pads. The whole device is inscribed in a cylindrical shell with an internal radius of 370 cm and an external one of 399 cm. In terms of material, the whole device thickness corresponds to $\sim 20\%$ of a radiation length.

Along z , we have a central module, two intermediate modules placed on both sides of the central one and two outer modules. All modules have the same width (125 cm) and increasing lengths, adding up to an overall TOF barrel length of 750 cm.

Inside each module the strips are tilted, as illustrated in Chapter 3, in order to minimise the traversal path through the strips for particles coming from the interaction vertex. In the Monte Carlo, this is achieved by introducing a strip tilting angle, progressively increasing with the z -position of the strip, in such a way that, in the median side view of each of the 18 sectors, the strip face is perpendicular to the

¹This version is currently used in the ongoing studies for the ALICE Physics Performance Report (PPR) preparation.

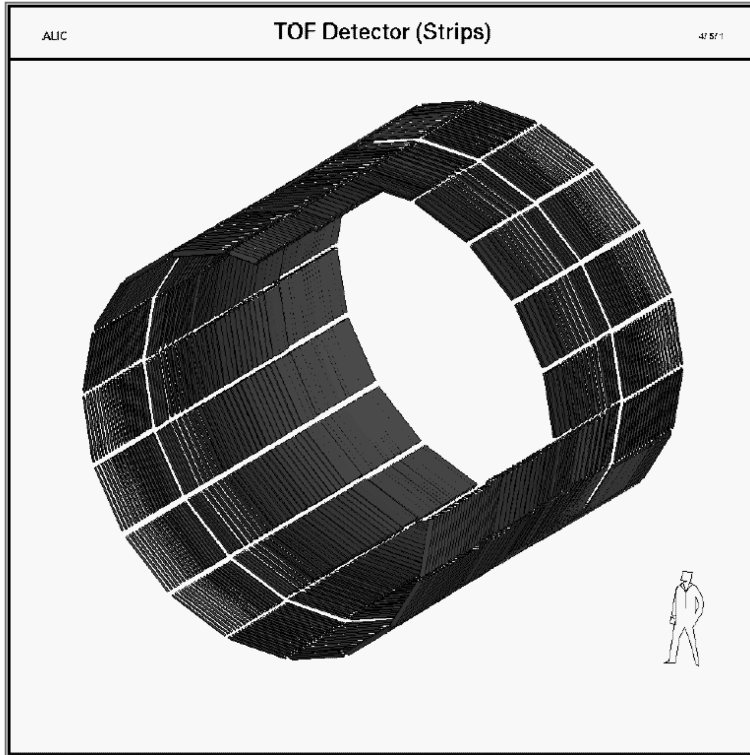


Figure 5.1: Time-Of-Flight (TOF) detector layout in AliROOT (full-coverage TOF version).

straight line connecting its centre to the vertex. In order to minimise the dead area, the strip arrangement inside the modules is such that the frame of each strip (transverse to the beam axis) is overlapped with the pick-up pad rows of the neighbouring strips. This tilted-strip detector meets the requirement for incident tracks to be as perpendicular as possible to the TOF pads in the longitudinal view, so as to reduce the number of very oblique traversals, in particular in the outer modules at both ends of the TOF barrel. This minimises the undesired effect of signal sharing among adjacent pads (border effect), with increased time jitter.

The double stack-strip arrangement (see Chapter 2) has been described in the GEANT3 tracking package of AliROOT and all simulations have been done with this new type of strip. A sensitive strip is equipped with two rows of $3.5 \times 2.5 \text{ cm}^2$ pick-up copper pads. The pad rows, in all the modules, are always transverse with respect to the z axis (see Chapter 3). Each row contains 48 pads, so that we have an array of 96 sensitive pads per strip. The interpad area of the strip is sensitive since a particle passing between two pads will induce a signal on the closest pad (or sometimes on both). The total active surface of the detector is 141 m^2 and the total number of pads (i.e. detector channels) is ~ 161000 . The overall detector dead space, which has been minimised along ϕ and z in such a way as to match the structure of the ALICE space frame and inner detectors, corresponds to $\sim 5\%$ of the total TOF barrel area.

Let us point out that, apart from the redefinition of the internal strip structure, the geometrical features of the TOF detector are unchanged with respect to our previous document [2].

5.3 Monte Carlo event generators

Different event generators are available to simulate central Pb-Pb collisions at a center-of-mass energy of $5.5 \text{ TeV}/\text{nucleon}$ [9]. As in our previous studies [1, 2], we have essentially used two of them, SHAKER [8] and HIJING [7], to simulate the global features of the event relevant for detector design. These event

generators have been used as an input for the GEANT3 tracking package of AliROOT, in the following way:

- HIJING alone, for the central rapidity region, i.e. $|\theta - 90^\circ| < 45^\circ$ (250 events²). In HIJING the average charged particle density is $dN_{ch}/dy = 6700$ for $-1.5 \leq y \leq 1.5$ ($dN_{ch}/dy = 7200$ for $-1 \leq y \leq 1$). The total multiplicity of primary particles per event is ~ 78000 while the total charged multiplicity is ~ 44000 .
- SHAKER for the central rapidity region, i.e. $|\theta - 90^\circ| < 45^\circ$ (100 events), coupled to AliGenHIJINGPara [10] (the internal HIJING generator of AliROOT, which is an appropriate parametrization) for the forward and backward regions, in order to estimate the background contribution from the $|\theta - 90^\circ| > 45^\circ$ outer region. In SHAKER a flat charged particle density has been used in the central rapidity region, with $dN_{ch}/dy = 8000$. Notice that the very high value of the charged particle density chosen for SHAKER events will be useful to test the TOF detector performance in a critical environment. We have also generated a sample of events with a modified inclusive p_t -spectrum for π^\pm , K^\pm , p and \bar{p} , according to recent RHIC results [11] (for more details see later on Section 5.6). This will be referred to in the following as the SHAKER “à la RHIC” event sample.

It is also worth recalling [1] what the particle ratios are in these event generators, namely: $K/\pi=0.13$ (0.20) and $p/\pi=0.08$ (0.07) in HIJING (SHAKER).

5.4 Detector acceptance studies

The present studies have been performed taking into account the presence of a solenoidal magnetic field along the beam axis, since the TOF barrel is internal to the ALICE magnet [9]. The reference value for the ALICE experiment is 0.2 T which is a good compromise among the several needs of the different detectors. The greater the magnetic field, the better would be the identification of high-momentum particles, but on the other hand, both the track finding process carried on by the TPC [12] and the ITS [13], and all the matching procedures are affected and their power lowered. A good solution can be to operate at different magnetic fields, 0.2 T and 0.4 T , so as to satisfy the different components. Hence, the need for a detailed simulation of the TOF performance at 0.4 T was straightforward. The various event samples (listed in Section 5.3) have therefore been tracked twice, i.e. at $B = 0.2\text{ T}$ and 0.4 T .

5.4.1 Momentum spectra and acceptances

Figures 5.2 and 5.3 show the distributions of various kinematical and geometrical variables for all charged primary particles generated with HIJING in the $|\theta - 90^\circ| < 45^\circ$ region and tracked with magnetic field values respectively equal to 0.2 T and 0.4 T . The corresponding distributions for charged primaries reaching the TOF barrel are superimposed in Figs. 5.2 and 5.3.

The occupation of the (p, y) plane by charged primary hadrons reaching the TOF is shown in Figs. 5.4 and 5.5 for HIJING events and for both magnetic field values. Different empty regions for pions, kaons and protons are due to magnetic field and polar angle acceptance. Particle decays are also taken into account. Hence the K/π and p/π ratios at the TOF detector level turn out to be lower than the original ones at the generator level [1].

The overall TOF acceptances for charged primaries produced in the $|\theta - 90^\circ| < 45^\circ$ region and, in particular, for different hadron species are given in Table 5.1 (where both HIJING and SHAKER event generators are considered) at $B = 0.2\text{ T}$ and in Table 5.2 for HIJING only at $B = 0.4\text{ T}$. The TOF acceptances for π , K and p decrease by the factors 0.78, 0.92 and 0.91, respectively, when the magnetic field is strengthened. This loss mostly concerns low-momentum pions.

²The impact parameter range for HIJING events is [0-3]fm.

Assuming that [1, 2] a charged primary particle produces a “trackable” track in the TPC if it has a hit in the last TPC pad row and a total number of hits in all TPC pad rows ≥ 30 , we can derive the different TPC and TOF acceptances relative to “trackable” π , K , p primaries. These are also reported in Tables 5.1 and 5.2 as “TPC” and “TPC & TOF” acceptances. In HIJING events, the overall (TPC & TOF)/TOF acceptance ratio equals to 0.97 for both magnetic field values.

Table 5.1: TPC and TOF acceptances (%) for charged primary particles produced in the $|\theta - 90^\circ| < 45^\circ$ region, taking into account “trackable” tracks in the TPC: for 250 HIJING events and, in brackets, for 100 SHAKER events, at $B = 0.2\text{ T}$.

Detector	π^\pm	K^\pm	$p(\bar{p})$	All
TPC	74 (76)	44 (47)	78 (82)	72 (73)
TPC & TOF	45	23	42	43
TOF	46 (48)	24 (27)	44 (48)	44.5 (45)

Table 5.2: Same as Table 5.1, only for HIJING (250 events) at $B = 0.4\text{ T}$.

Detector	π^\pm	K^\pm	$p(\bar{p})$	All
TPC	68.5	43	77	67
TPC & TOF	35	21	39	34
TOF	36	22	40	35

Table 5.3: TPC and TOF acceptances (%) for charged primary particles produced in the $|\theta - 90^\circ| < 45^\circ$ region, taking into account “trackable” tracks in the TPC: for 250 HIJING events and, in brackets, for 25 HIJING events without the TRD, at $B = 0.2\text{ T}$.

Detector	π^\pm	K^\pm	$p(\bar{p})$	All
TPC & TOF	45 (52)	23 (25)	42 (53)	43 (50)
TOF	46 (54)	24 (26)	44 (55)	44.5 (51.5)

A comparison with the TPC and TOF acceptance values derived in the past with HIJING at $B = 0.2\text{ T}$ (see *Tables 6.1 and 6.2* in [2]) with a different AliROOT version, shows that the TPC acceptance is unchanged while the TOF acceptance is slightly lower. The overall reduction factor is 0.95, but it is 0.85 in particular for protons. Since the TOF detector geometrical layout and MRPC strip arrangement are the same (as already said, only the MRPC internal structure has been updated), this indicates that, in the current AliROOT version, the intervening materials of the TRD [14] (detector and services) between the TPC and the TOF are now different. In Table 5.3 a comparison is made of the present TOF acceptance values when the TRD detector is included or excluded from the ALICE set-up description, using HIJING events at $B = 0.2\text{ T}$. At this level, i.e. for GEANT tracks, the TRD effect corresponds to an overall 0.86 reduction factor and, in particular, to the factors 0.85, 0.92 and 0.80 for π , K and p , respectively (the effect is less pronounced for kaons, due to decays). We will come back to this point later on in Section 5.5.2.

Figure 5.6 shows the time-of-flight distributions of all charged primaries reaching the TOF, at $B =$

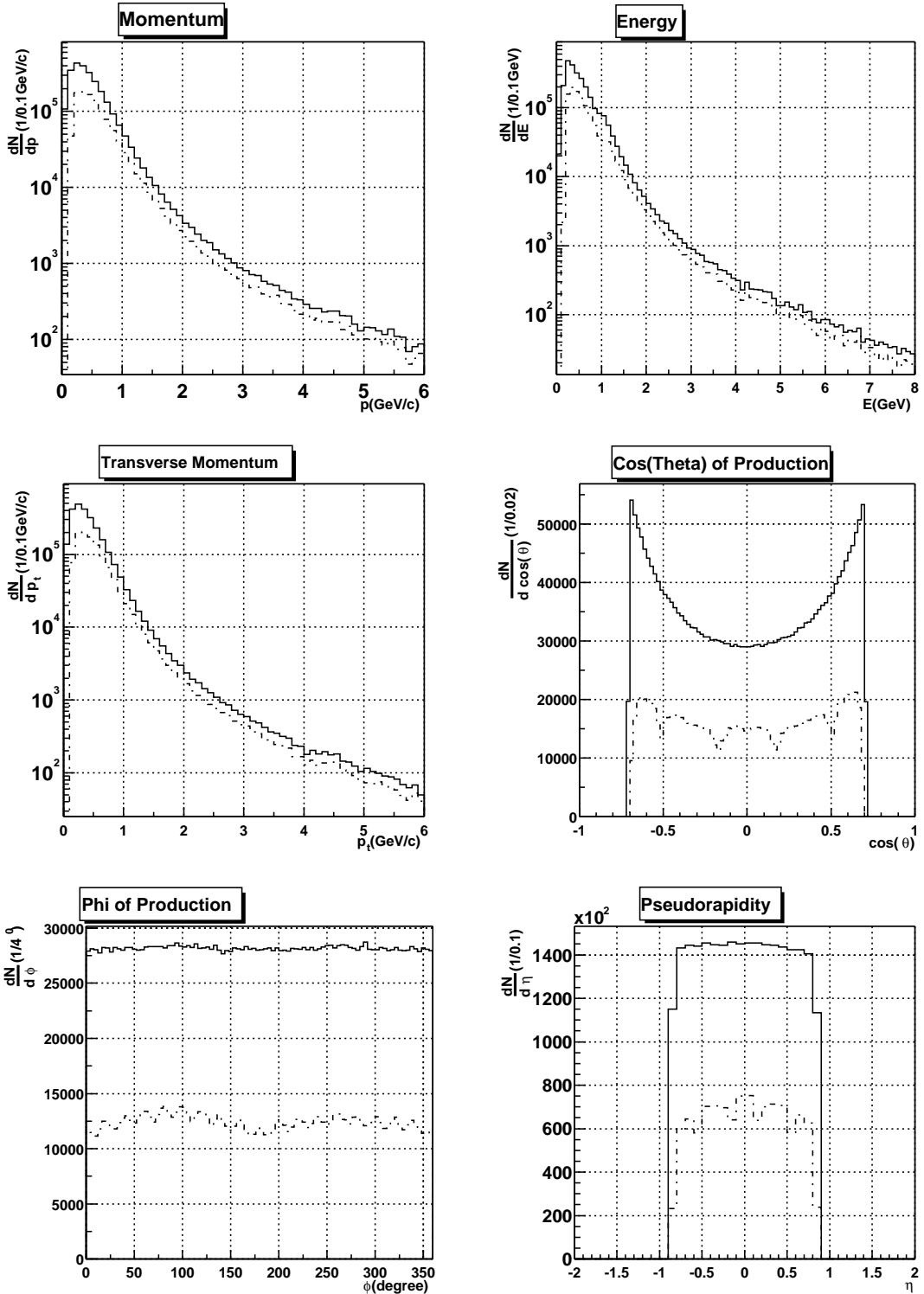


Figure 5.2: Kinematical and geometrical variables of all charged primary particles generated with HIJING (250 events) in the $|\theta - 90^\circ| < 45^\circ$ central region (solid-line histograms). Superimposed the same distributions for all charged primary particles reaching the TOF (dashed-line histograms). The magnetic field value is 0.2 T.

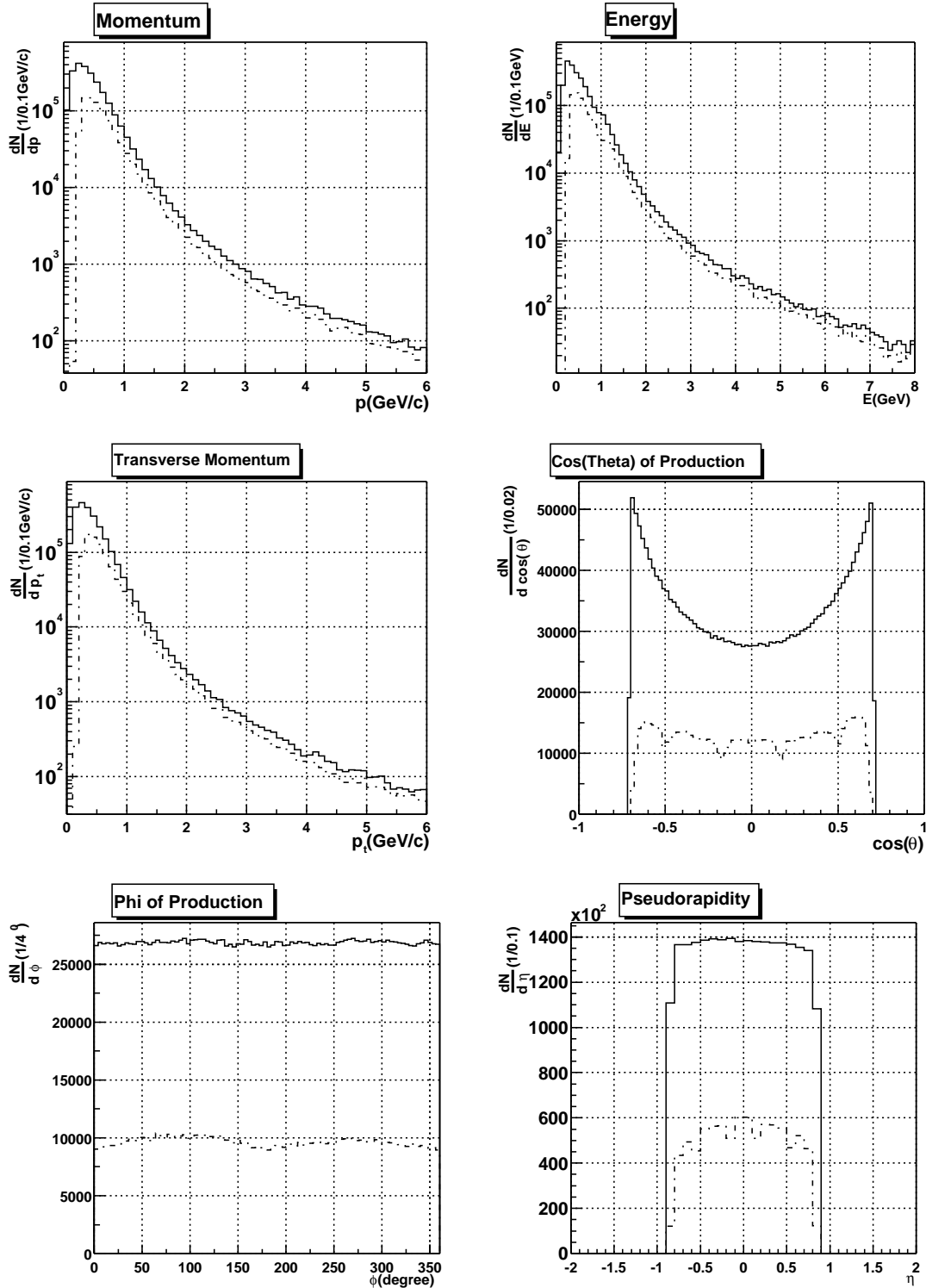


Figure 5.3: Same as Fig. 5.2, for $B = 0.4$ T (250 HIJING events).

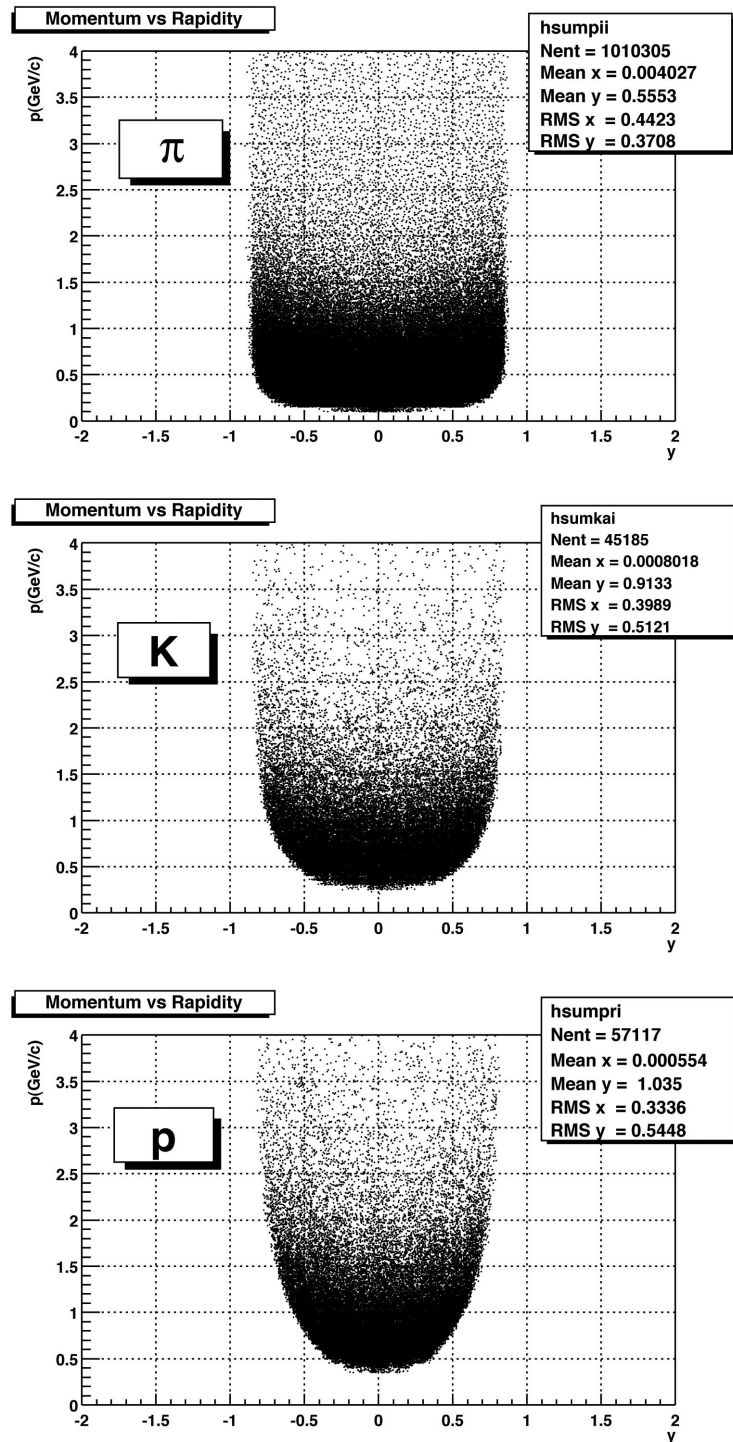


Figure 5.4: TOF acceptance regions for charged primary hadrons produced with $|\theta - 90^\circ| < 45^\circ$, tracked with a magnetic field value $B = 0.2\text{ T}$: from top to bottom, for pions, kaons and protons (250 HIJING events).

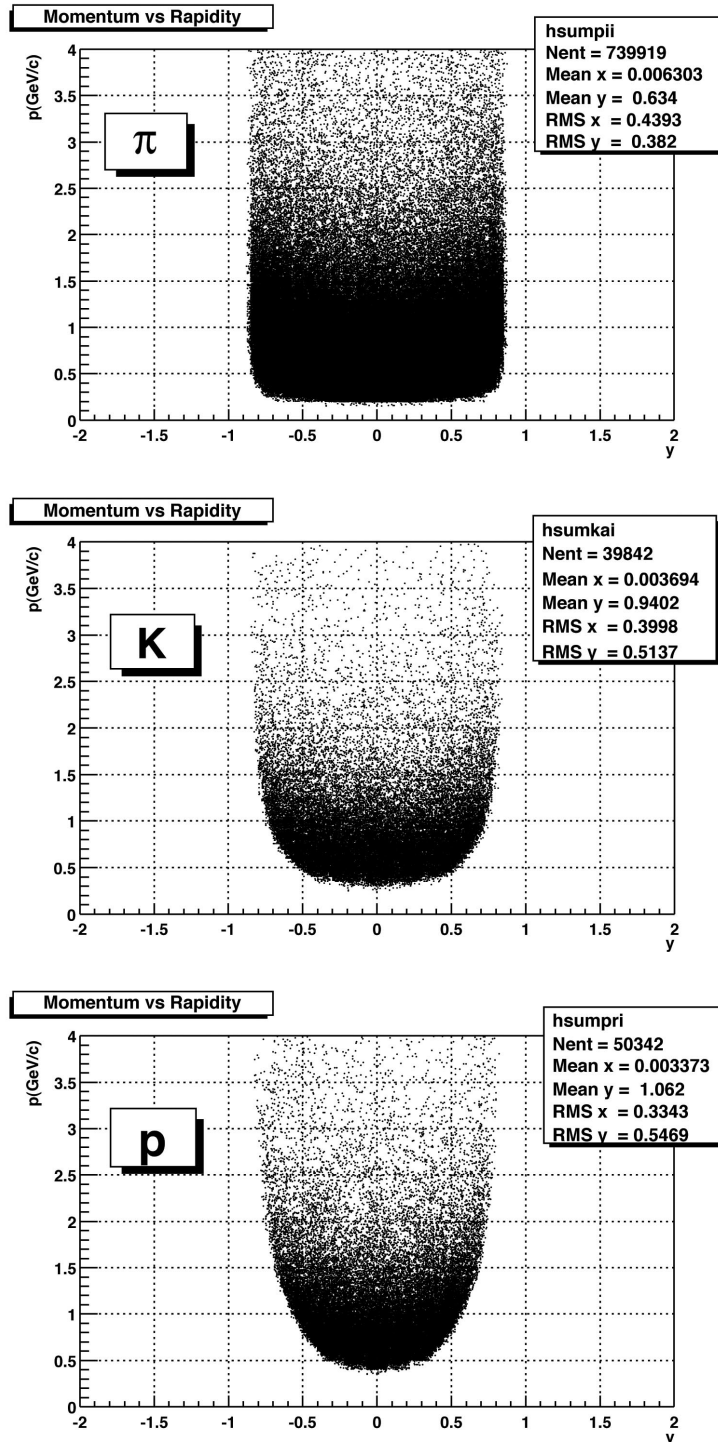


Figure 5.5: Same as Fig. 5.4, for $B = 0.4$ T (250 HIJING events).

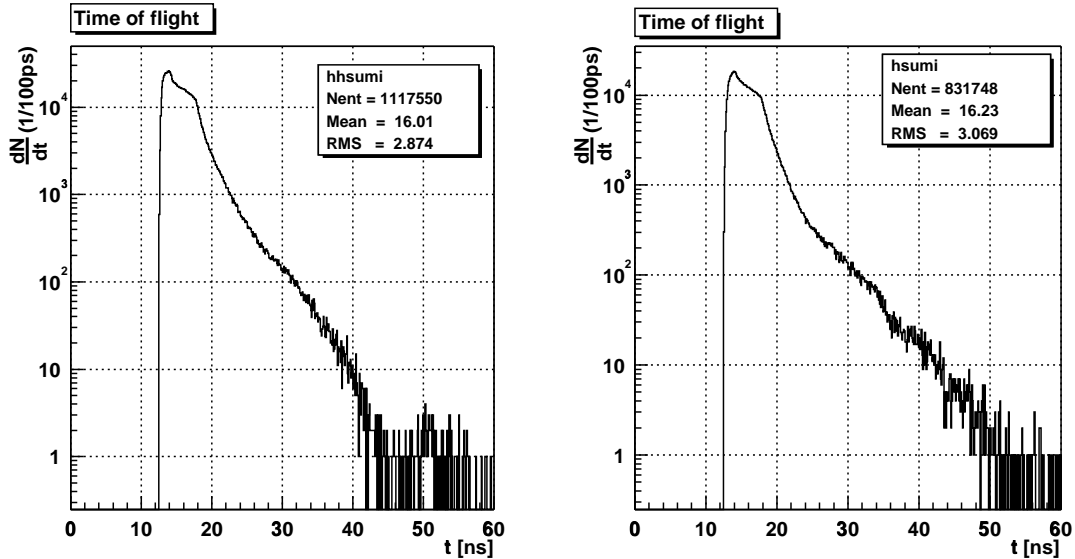


Figure 5.6: Time-of-flight distributions for primary particles from the $|\theta - 90^\circ| < 45^\circ$ region reaching the TOF with $B = 0.2\text{ T}$ (left) and $B = 0.4\text{ T}$ (right) magnetic field, as obtained with 250 HIJING events.

0.2 T and $B = 0.4\text{ T}$: the magnetic field strengthening corresponds to 200 ps shift of the mean value and 200 ps widening of the spectrum.

5.4.2 Incident angle studies

Due to the magnetic field, multiple scattering and energy loss, a charged primary track reaching the TOF surface at a given impact point deviates from a straight line connecting the vertex to the same impact point. We can consider the angular deviation, $\Delta\alpha$, of an incident track direction, at a given impact point, with respect to the normal to the TOF pad at the same point. Figure 5.7 shows the $\Delta\alpha$ distribution for $B = 0.2\text{ T}$ and $B = 0.4\text{ T}$. The average deviation obviously increases, as B increases, from $\langle \Delta\alpha \rangle = 17.1^\circ$ to $\langle \Delta\alpha \rangle = 27.6^\circ$. However, thanks to the strip tilting angle (see Section 5.2.2) $\langle \Delta\alpha \rangle$ does not depend on the z coordinate of the impact point [1, 2].

5.4.3 Occupancy

Let us first focus on the physical aspect of the occupancy, i.e. on the various kinds of particles impinging on the TOF. In a single SHAKER event there are on the average ~ 12000 primary charged particles in the $|\theta - 90^\circ| < 45^\circ$ central region. With a magnetic field value $B = 0.2\text{ T}$, about 9000 (75%) of them have tracks³ in the TPC. There are in addition ~ 2000 secondary charged particles (with $R_{vtx} < 50\text{ cm}$) which also have TPC tracks.

In the full-coverage, tilted-strip TOF detector there are ~ 25000 fired pads (with 99% efficiency) and we have a TOF occupancy of $25000/161000 = 16\%$ (including border effects, as described later on). Notice that this value corresponds to the extreme assumption $dN_{ch}/dy = 8000$ in SHAKER events. In HIJING events, this occupancy is in fact smaller (14%). Doubling the magnetic field intensity, the SHAKER (HIJING) occupancy slightly decreases to 15% (13%).

³Here and in the following, the previously defined “trackable” tracks in the TPC are simply referred to as tracks in the TPC.

⁴ $R_{vtx} = \sqrt{(x_{vtx}^2 + y_{vtx}^2)}$, where x_{vtx} and y_{vtx} are the coordinates of the particle production vertex in the (x, y) plane transverse to the beam line.

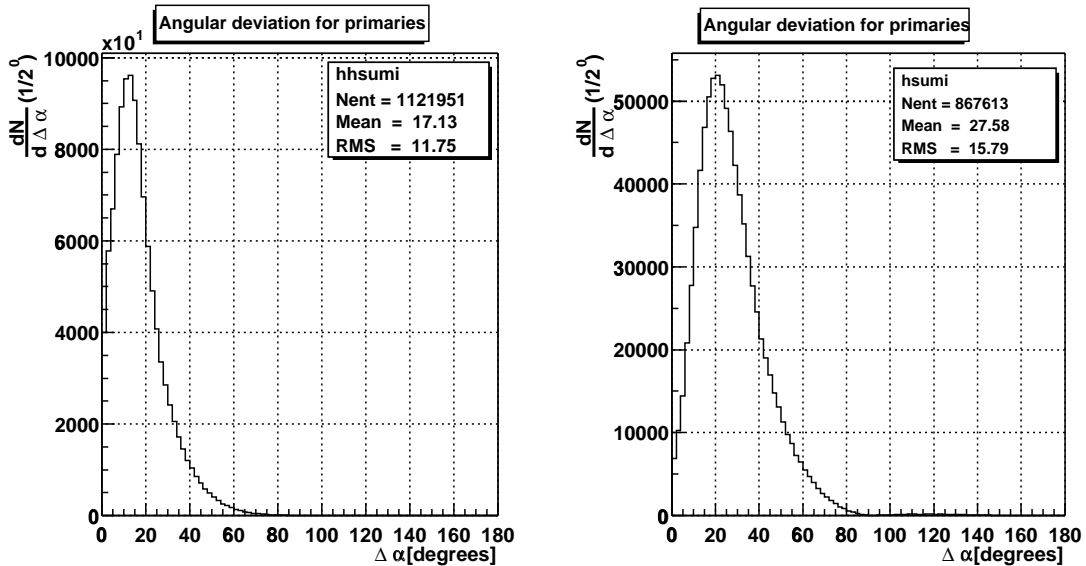


Figure 5.7: Distributions of $\Delta\alpha$ angular deviation for primary particles from the $|\theta - 90^\circ| < 45^\circ$ region reaching the TOF with $B = 0.2 \text{ T}$ (left) and $B = 0.4 \text{ T}$ (right) magnetic field, as obtained with 250 HIJING events.

Only 25% of the fired pads are hit by particles having TPC tracks, in their first crossing of the TOF-sensitive surface. A further 40% are hit by particles without TPC tracks (in one or more crossings) as well as by particles with TPC tracks in their second, third, etc. crossings. We define the latter percentage of hits as noise from the $|\theta - 90^\circ| < 45^\circ$ central region (collectively produced by charged and neutral primaries). The contributions to the noise hits according to particle species are as follows: 71% are e^\pm , 16% are μ^\pm , 10% are π^\pm , 3% are $p(\bar{p})$.

The rest of the fired pads, 35%, are hit by particles originating from the $|\theta - 90^\circ| > 45^\circ$ outer region. The number of TOF hits due to this outer region has been estimated as follows. A sample of charged and neutral primary particles has been generated in each of the forward and backward regions, using the HIJING generator and tracked with $B = 0.2 \text{ T}$. Additional TOF pads hit by the charged products (from decays, interactions, backscattering, etc.) of these primaries have been found, summing up to a total of ~ 9000 per event at $B = 0.2 \text{ T}$, and also taken into account.

The distributions of the production vertex radius in cylindrical coordinates for background tracks reaching the TOF from the outer region (5 HIJING events) are shown in Fig. 5.8, separately for $p(\bar{p})$, K^\pm , π^\pm , e^\pm , μ^\pm and altogether for all charged particles. Most of the e^\pm noise originates from the TPC and TOF walls and from the TRD. These are also important sources of hadron noise. For hadrons, the main production mechanism is due to hadronic interactions, for muons, to particle decays, for e^\pm , to photon conversions, δ -ray emissions and Compton scattering. The relative abundance of each particle type is reported in Table 5.4. From this outer region, 48% of the tracks reaching the TOF are produced in the forward region ($0^\circ \leq \theta \leq 45^\circ$) and 52% in the backward region ($135^\circ \leq \theta \leq 180^\circ$). Among mother-particles (charged or neutral), whose charged daughter-tracks hit the TOF, $\sim 70\%$ in the forward region and $\sim 60\%$ in the backward region are photons. For each event, the background pads are spread on the TOF surface according to parametrised distributions [1, 2], namely a uniform ϕ -distribution, in the transverse plane, and a polynomial z -distribution (reproducing the small forward/backward asymmetry), along the beam direction. The corresponding time spectrum has an exponential behaviour [1, 2], parametrised as $\exp[-t/20(ns)]$. Small differences in the background simulation, when going from 0.2 to 0.4 T , have been duly taken into account.

Let us now consider an additional contribution to the occupancy caused by the TOF detector itself,

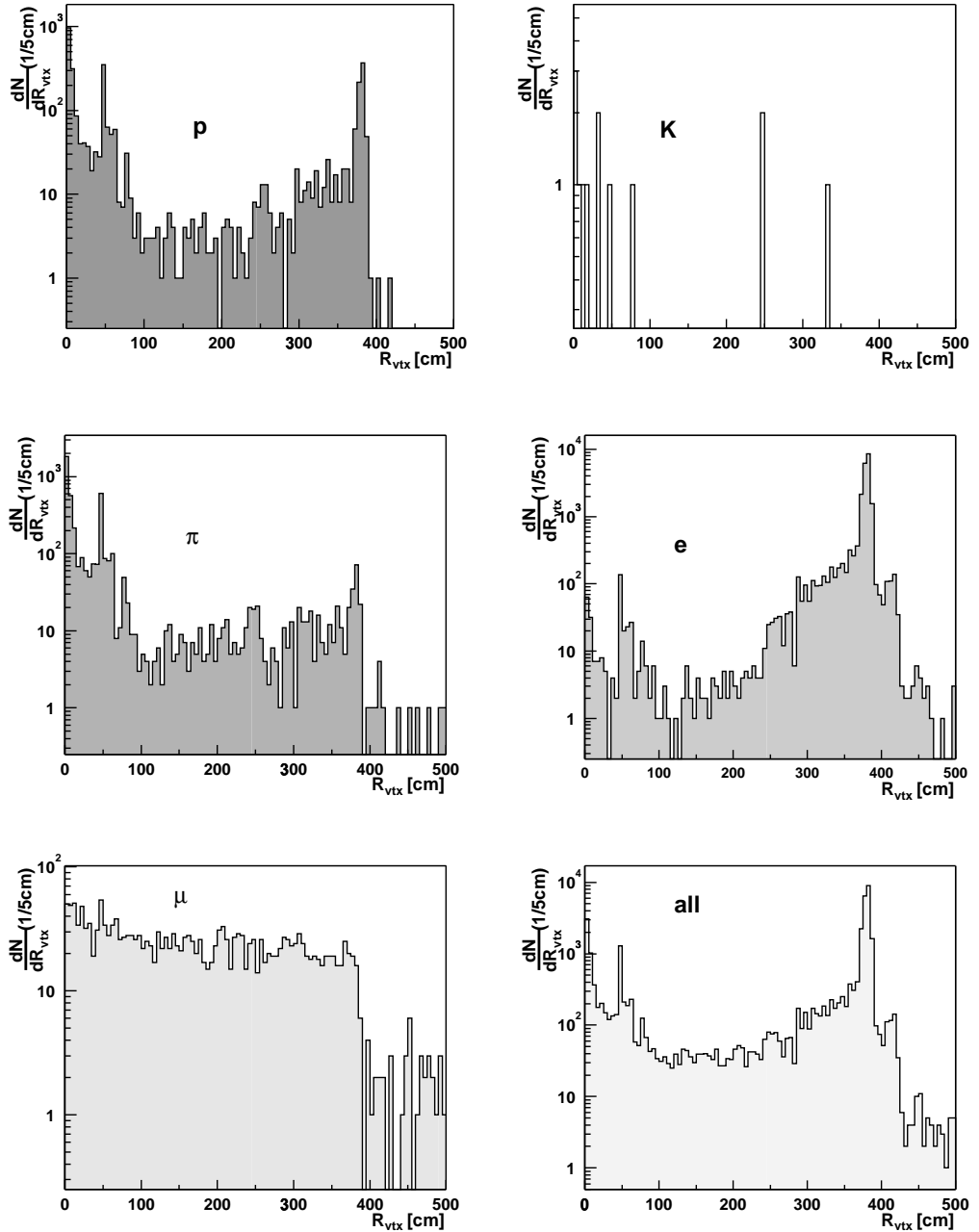


Figure 5.8: The distributions of the production vertex radius in cylindrical coordinates for background tracks hitting the TOF from the outer region of 5 HIJING events ($B = 0.2 \text{ T}$): for $p(\bar{p})$, K^\pm , π^\pm , e^\pm , μ^\pm and all charged particles.

Table 5.4: Percentages of background tracks hitting the TOF separately from the forward and backward regions (5 HIJING events, $B = 0.2\text{ T}$).

Outer region	e^+	e^-	μ^+	μ^-	π^+	π^-	K^+	K^-	p	\bar{p}	nuclear fragments
Forward	13.3	60.5	2.5	2.4	5.0	6.3	< 0.05	< 0.05	8.7	< 0.05	1.2
Backward	16.9	45.8	3.8	3.7	7.9	9.0	< 0.01	< 0.02	10.9	< 0.01	2.0

namely by secondary effects such as border effects between adjacent pads. Due to the readout structure of the MRPC strip, when a particle goes through the strip close to a pad border, ionizing the gas inside the gaps and inducing a certain amount of charge on the pad, sometimes a smaller amount of charge will be induced on the neighbouring pad(s). These signals, of course, will contribute to noise and occupancy.

Border effects between adjacent pads have been simulated [2] starting from the test beam results of the TOF detector prototypes (see Chapter 2) as far as the pad efficiency (ε_{eff}) and intrinsic time resolution (σ_{intr}) are concerned. The border between two pads is defined as a $\pm 5\text{ mm}$ wide region (centred on the border between two pads) where the efficiency of one pad decreases (from 99% to zero) according to the fitted curve of test beam results, while the efficiency of the nearby pad correspondingly increases (from zero up to 99%). This effect concerns three sides of each pad. Along the fourth side (which has no neighbouring pad) there is only a 5 mm wide region where the efficiency slightly decreases (dropping to zero at the strip edge). As already pointed out in Chapter 2, with the present double-stack MRPC, border effects are reduced to the 10-15% level.

In the border regions, the detector time resolution (σ_{intr}) increases from a minimum value of $\sim 50\text{ ps}$ up to a maximum of $\sim 110\text{ ps}$ (see Chapter 2). The overall TOF system resolution (σ_{TOT}) has been defined as $\sigma_{TOT}^2 = \sigma_{intr}^2 + \sigma_{add}^2$, where the additional contribution (σ_{add}) to the overall time resolution was assumed to be $\sim 100\text{ ps}$ [1, 2]. Keeping $\sigma_{add} = 100\text{ ps}$ (constant), σ_{intr} was allowed to vary as specified above depending on the impact point of the particle on the TOF pad. Therefore, for each track crossing a TOF pad, a cluster of (up to four) fired pads with different time jitters was considered.

Finally, from our test beam data on border effects, the correlation between the charge ratio of signal pairs from adjacent pads (q_2/q_1) and their relative delay ($t_2 - t_1$) has been determined. The index 1 refers to the pad actually hit by a particle, the index 2 to its neighbouring pad. A linear decrease of $\ln(q_2/q_1)$ vs. $(t_2 - t_1)$ has been found in the above defined border region, with a maximum delay of only $\sim 120\text{ ps}$. This effect has also been included in our simulations (see later on Section 5.5.1).

The border effect contribution to the overall TOF occupancy (13-16%) is only $\sim 2\%$, i.e. drastically lower than in the past [2] thanks to the new MRPC strip performance.

5.5 Track matching

As in [2], we shall use the following inputs for the average momentum and space errors at the outer wall of the TPC [12, 15]: $\sigma_\phi = 2 \text{ mrad}$, $\sigma_\theta = 2 \text{ mrad}$, $\sigma_p/p = 2.1\%$, $\sigma_z = 0.77 \text{ mm}$, $\sigma_{r_\phi} = 0.62 \text{ mm}$.

These values, except for σ_ϕ and σ_θ , are larger than those used in the TOF TDR [1]. The momentum dependence of the TPC tracking errors has been also included, according to the results obtained in [16] for σ_ϕ and σ_θ , in [17] for σ_p/p , in [18] for σ_z and σ_{r_ϕ} . It should be pointed out that all the errors decrease as the particle momentum p increases, but σ_p/p which first decreases then increases above $p \simeq 0.5 \text{ GeV}/c$.

5.5.1 Matching with TPC tracks

Let us recall the main features of the matching algorithm used in our simulation [1]. All TPC tracks are ordered according to their transverse momentum. Starting from the highest p_t track, for each track, a statistically significant sample of probe tracks is generated and tracked in the magnetic field from the TPC (i.e. from the hit in the last TPC pad row) to the TOF. These probe tracks deviate from our track in the last TPC hit point according to a Gaussian distribution with standard deviation given by $\theta_{\text{plane}}^{\text{rms}}$, the mean deflection angle due to multiple scattering in the outer wall of the TPC⁵. Every probe track can cross a TOF pad or a TOF dead region and be assigned a weighting contribution: $\text{weight}_1 = \epsilon_{\text{eff}}$ if the sensitive pad hit has fired (i.e. if the pad has given a time signal), $\text{weight}_1 = 1 - \epsilon_{\text{eff}}$ if the sensitive pad hit has not fired, 1 if an insensitive region is hit. Notice that $\epsilon_{\text{eff}} = 99\%$ was used in the present simulation. Accounting for the improved MRPC strip response, this value is higher than the one (95%) used in the past [1, 2].

As already seen in Section 5.4.3, a particle crossing a TOF pad can sometimes induce a signal on the neighbouring pad(s) and this signal can be slightly delayed (the lower the charge induced on the neighbouring pad, the longer the delay). Therefore, to each fired pad we assign an additional weighting factor [19], $\text{weight}_2 = q_{\text{induced}}^2$, where q_{induced} is the (normalised) charge induced on the pad, so that its resulting weight is: $\text{weight} = \text{weight}_1 \times \text{weight}_2$.

For a given TPC track, we have then a set of TOF pads and TOF dead regions crossed by the probe tracks. For each TOF element (sensitive pad or dead region) a weight is defined as the sum of the weighting contributions from all the probe tracks that cross it. The element with the largest weight is chosen to be the match for the TPC track. Notice that this match is a first crossing match on the TOF surface, for each track.

Although the TRD is foreseen as a detector with tracking capability, this has not yet been taken into account in the present matching algorithm. Moreover, the TPC efficiency for track finding and reconstruction has been assumed to be 100% throughout our simulation.

5.5.2 Matching efficiency and contamination

Let us recall now the definitions used in the matching analysis [1, 20, 21]. Given N tracks matched with the TOF system, these are subdivided into two sets: mismatched tracks, N_{mis} , and well matched ones, N_{match} , with $N = N_{\text{mis}} + N_{\text{match}}$.

A mismatched track is a track to which we cannot unambiguously attribute a time-of-flight. This set of tracks can be presented as follows: $N_{\text{mis}} = N_0 + N_2$, where N_0 includes the cases when the TOF pad corresponding to the track is not fired or when the track is matched with a TOF dead region; N_2 is the number of tracks for which the fired pad was matched to more than one track. Physical reasons for the presence of set N_0 are the intrinsic inefficiency of the pad (1%), the extension of the TOF dead region ($\sim 5\%$) and the possibility of particle decays between the TPC and the TOF.

For the well matched tracks, to which a time-of-flight can be unambiguously attributed, one can

⁵Here the pion mass is assumed for all tracks.

distinguish between those matched with true time, N_t , and those matched with wrong time, N_w , with $N_{match} = N_t + N_w$. The wrong time assignment corresponds to the matching of the extrapolated track with a pad fired by another particle, mostly due to noise from the central or outer regions (see Section 5.4.3). The true time assignment corresponds to the correct matching of the extrapolated track with the pad it has actually fired.

The relative abundance of the various sets for primary particles matched with the TOF is reported in Table 5.5, for different event generators and magnetic field values, with or without the TRD in front of the TOF in the ALICE detector description. As anticipated in Section 5.4.1, the effect of the TRD on the TPC-TOF track matching is more evident than in the past [1]: in particular, the ratio with/without for subset N_t is ~ 0.7 in Table 5.5, irrespective of the magnetic field value. This ratio was ~ 0.8 in our previous simulations (see *Tables 4.2, 4.3* and *Figs. 4.22, 4.23* in [1]).

Table 5.5: Subsets (%) of primary particles matched with the TOF, as specified in the text (Section 5.5.2), for: 100 SHAKER events at $B = 0.2\text{ T}$; 100 HIJING events at $B = 0.2\text{ T}$ (in brackets, without the TRD); 100 HIJING events at $B = 0.4\text{ T}$ (in brackets, with the TRD).

Generator	Magnetic field value (T)	N_0	N_2	N_t	N_w
SHAKER	0.2	26	7	37	30
HIJING	0.2	27 (20)	7 (6)	34 (47)	32 (27)
HIJING	0.4	31 (23)	5 (5)	33 (46)	31 (26)

The matching procedure can be evaluated in terms of efficiency and contamination. These are defined as follows:

$$\text{efficiency} = \frac{N_t}{N}, \quad \text{contamination} = \frac{N_w}{N_{match}}.$$

The momentum dependence of our matching results is presented in Fig. 5.9. To which extent these are affected by the presence of the TRD, in particular in the proton case, is shown in Figs. 5.10 and 5.11.

In Figs. 5.12 and 5.13, the acceptances relative to the various steps of the matching procedure, for primary particles of different species (e^6 , π , K, p), originally generated in the $|\theta - 90^\circ| < 45^\circ$ central region and tracked with $B = 0.2\text{ T}$, are reported as a function of momentum, together with the original particle momentum spectra. The acceptances shown (from top to bottom, dashed/dotted-line histograms) concern: i) the particle tracking in the TPC; ii) the extrapolation to the TOF surface; iii) the extrapolation to the TOF sensitive pads; iv) the extrapolation to the fired TOF pads; v) the correct matching with the fired TOF pads. In each figure, the solid-line histogram superimposed shows the acceptance of GEANT tracks really hitting the TOF sensitive pads and should be taken as a reference.

The corresponding acceptance losses are also summarised in Table 5.6 (with $B = 0.2\text{ T}$): the loss “without TPC tracks”, referring to particles not fulfilling the TPC track requirements, entering the TPC dead space or decaying before or inside the TPC; the loss “out of TOF geometry”, referring to extrapolated TPC tracks missing the TOF surface; the loss “TOF dead space”, referring to extrapolated TPC tracks ending up in the TOF dead space (between neighbouring strips, for instance); the loss “empty pads”, referring to extrapolated TPC tracks reaching TOF pads which are not fired⁷; the loss “wrong time”, referring to extrapolated TPC tracks matched with pads fired by other tracks ($N_2 + N_w$). Finally, the “true time” acceptance, referring to extrapolated TPC tracks matched with the pads they have actually fired (N_t), is also reported in Table 5.6. The corresponding numbers derived without the TRD are included in the table. Table 5.7 summarises the results of the same analysis repeated with $B = 0.4\text{ T}$.

By comparison with analogous studies performed in the past (see *Section 4.5.2* in [1] and *Sections*

⁶“Primary” electrons are those originated from the decays of primary neutral pions.

⁷“TOF dead space”+“empty pads” = N_0 .

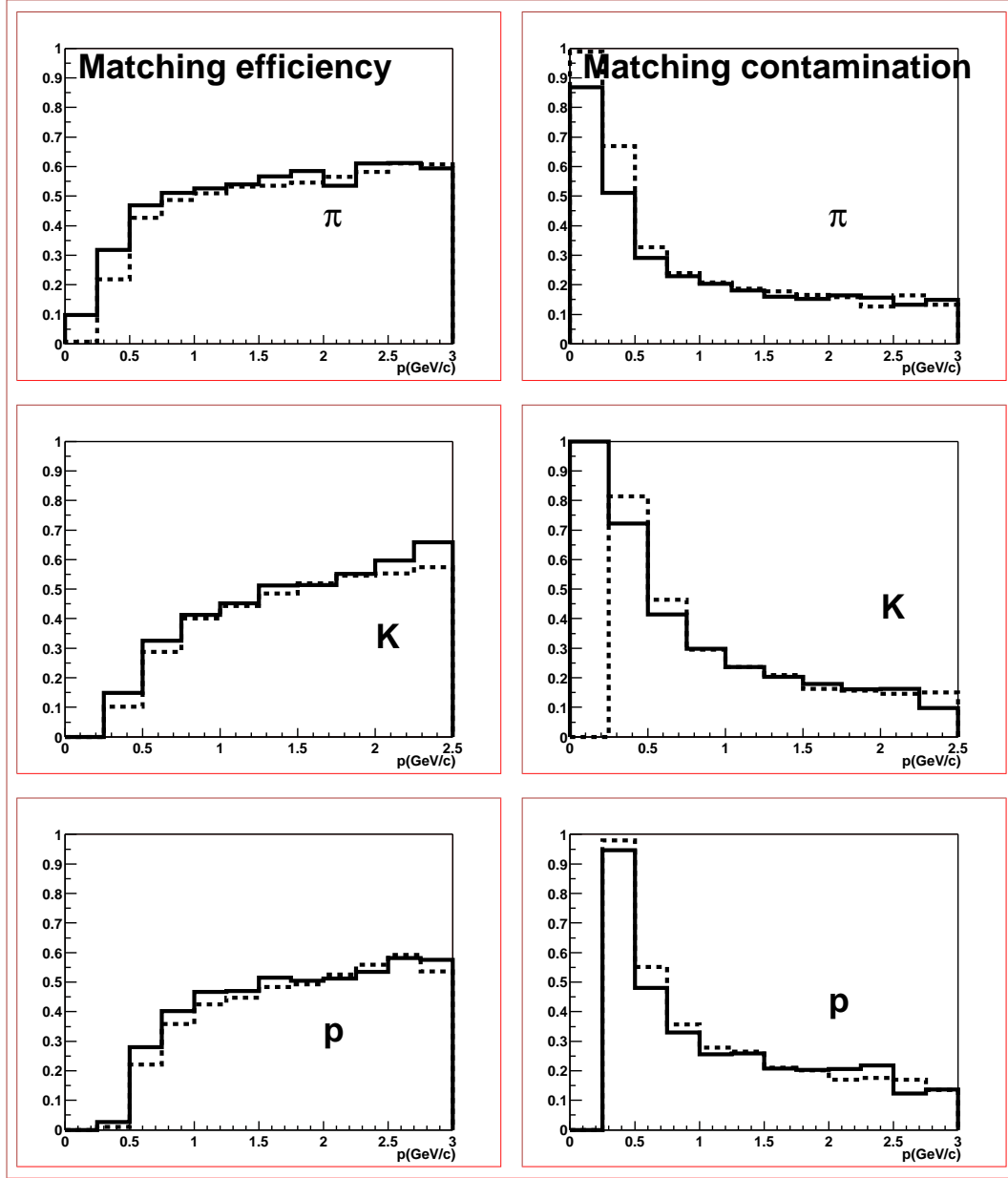


Figure 5.9: The momentum dependence of the efficiency (left column) and contamination (right column) of the TOF matching procedure (solid-line histograms: with $B = 0.2 \text{ T}$; dashed-line histograms: with $B = 0.4 \text{ T}$) for primary particles of different species originally generated in the $|\theta - 90^\circ| < 45^\circ$ region (100 HIJING events).

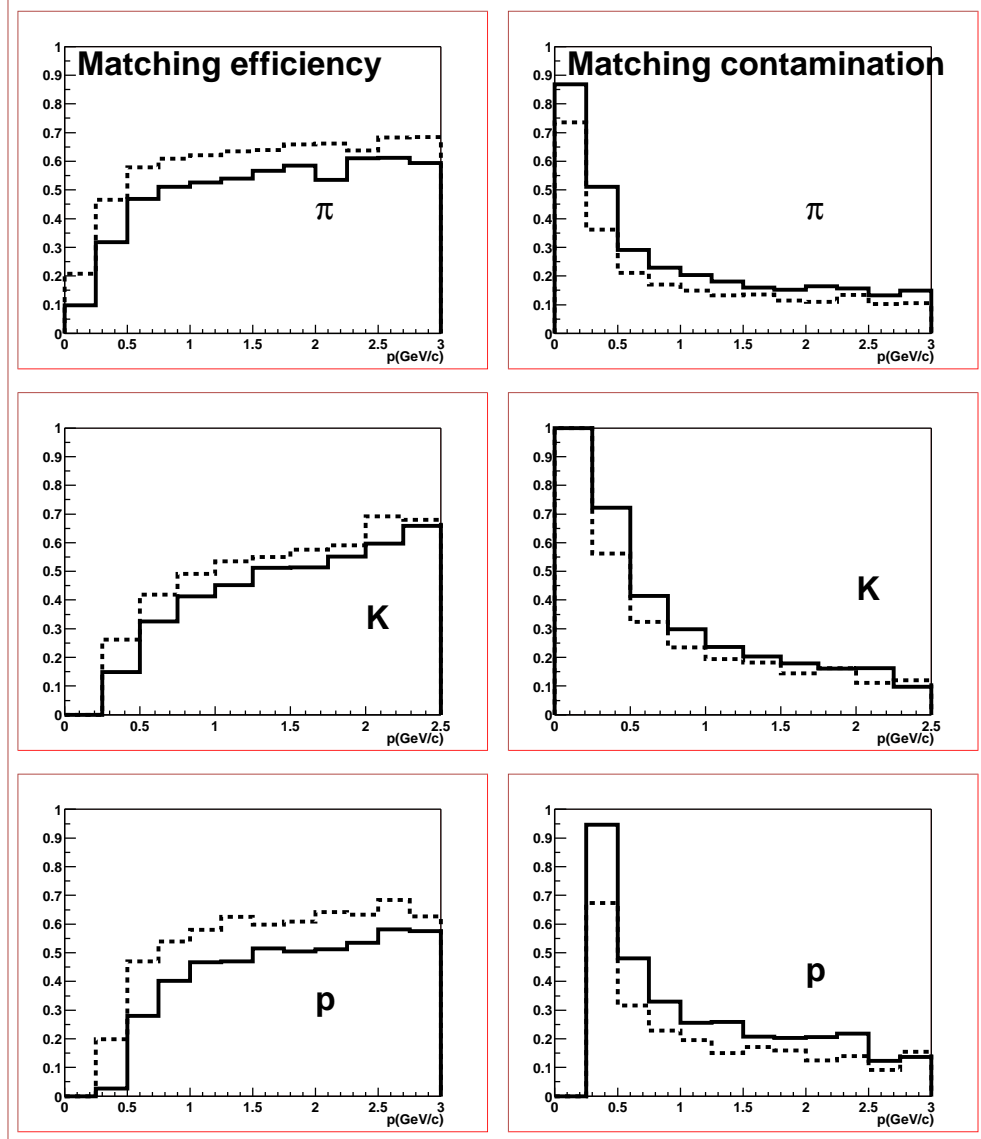


Figure 5.10: The momentum dependence of the efficiency (left column) and contamination (right column) of the TOF matching procedure (solid-line histograms: with the TRD; dashed-line histograms: without the TRD) for primary particles of different species originally generated in the $|\theta - 90^\circ| < 45^\circ$ region and tracked with $B = 0.2$ T (100 HIJING events).

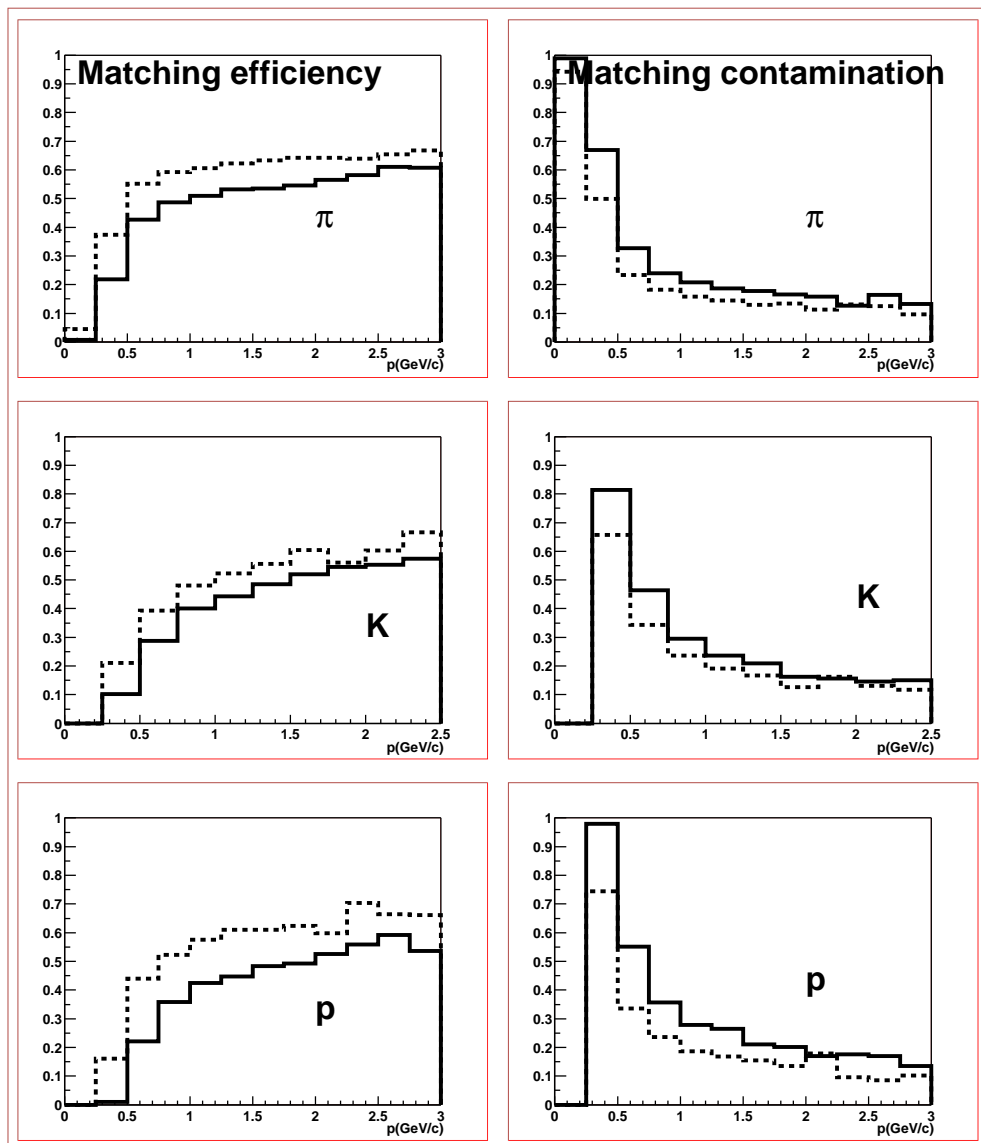


Figure 5.11: Same as Fig. 5.10, for 100 HIJING events at $B = 0.4$ T.

6.2, 6.3, 6.4 in [2]), it clearly appears that with a better TOF efficiency, reduced border effects among TOF pads and the same TOF geometrical layout, nevertheless the TPC-TOF matching results turn out to be 10-15% worse. Since we know that the matching quality is dominated by multiple scattering, this worsening is in fact due to the increase of materials along the TPC-TOF extrapolation path in the current ALICE detector description. Let us also recall that since the particle momentum spectra are softer in HIJING than in SHAKER, the effect is more evident for HIJING events. Detailed studies are presently being carried on in order to improve the TOF matching algorithm, in particular with the purpose to efficiently include the TRD detector tracking capabilities.

Table 5.6: Acceptance losses (%) in the TPC-TOF matching procedure and TOF acceptances (%) for primaries of different species matched with true time, as explained in the text (Section 5.5.2), for 100 HIJING events at $B = 0.2\text{ T}$. In brackets, the percentages relative to the last three rows, without the TRD, also for 100 HIJING events at $B = 0.2\text{ T}$.

Acceptance loss	π^\pm	K^\pm	$p(\bar{p})$	e^\pm
Without TPC tracks	26	56	22	66
Out of TOF geometry	4	1	2	11
TOF dead space	7	5	8	2
Empty pads	11 (7)	11 (9)	20 (12)	3 (2)
Wrong time	28 (23)	13 (11)	24 (20)	14 (12)
True time acceptance	24 (33)	14 (18)	24 (36)	4 (7)

Table 5.7: Same as Table 5.6, for 100 HIJING events at $B = 0.4\text{ T}$.

Acceptance loss	π^\pm	K^\pm	$p(\bar{p})$	e^\pm
Without TPC tracks	34	57	23	83
Out of TOF geometry	12	2	4	8
TOF dead space	6	5	8	1
Empty pads	10 (6)	11 (9)	22 (12)	2 (1)
Wrong time	18 (17)	12 (10)	22 (19)	4 (4)
True time acceptance	20 (25)	13 (17)	21 (34)	2 (3)

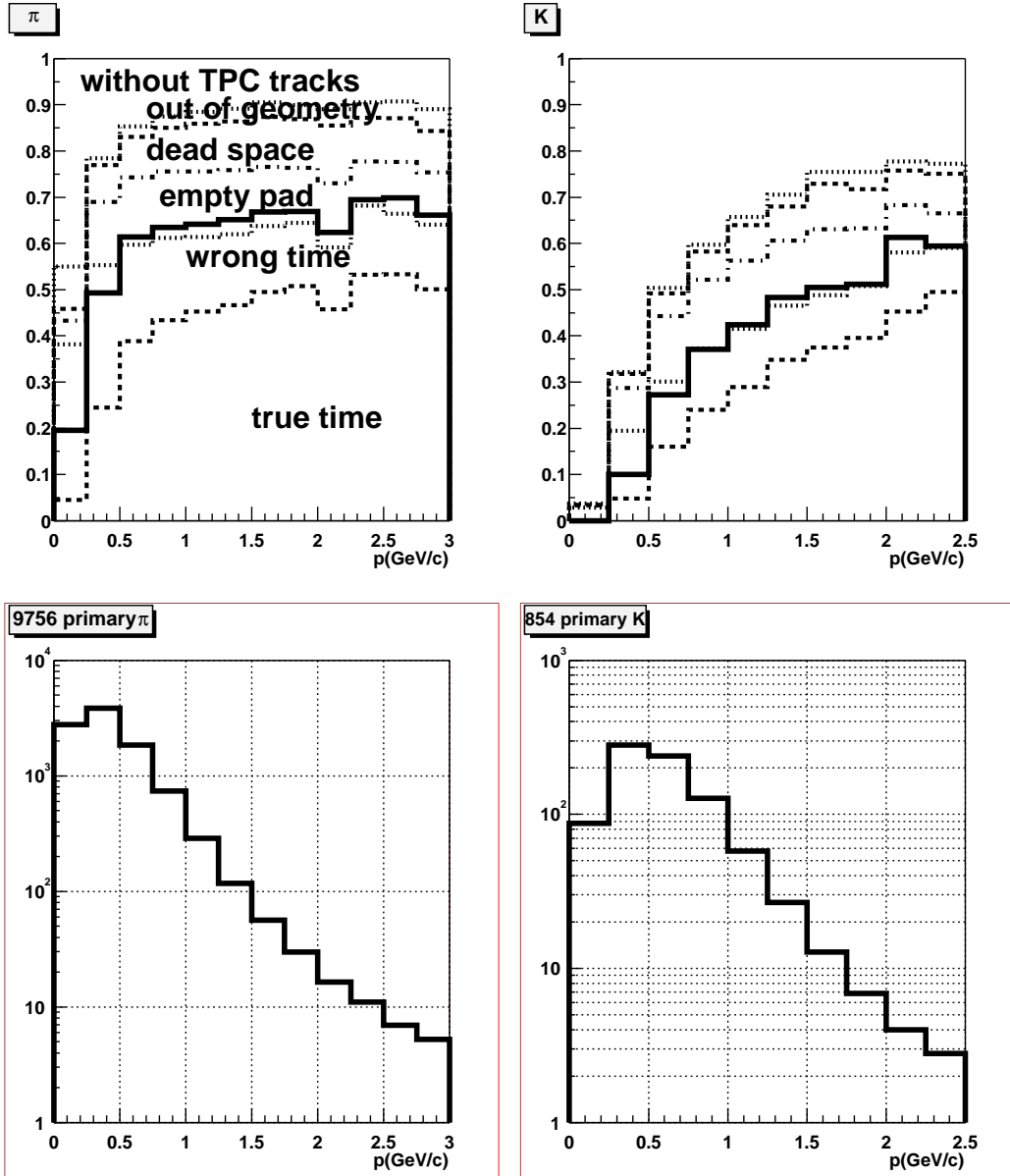


Figure 5.12: Acceptances vs. momentum (upper histograms), as specified in the text (Section 5.5.2), and single-event momentum spectra (lower histograms) referring to primary π^\pm (left column) and K^\pm (right column) originally generated in the $|\theta - 90^\circ| < 45^\circ$ region, for 100 HIJING events at $B = 0.2 \text{ T}$.

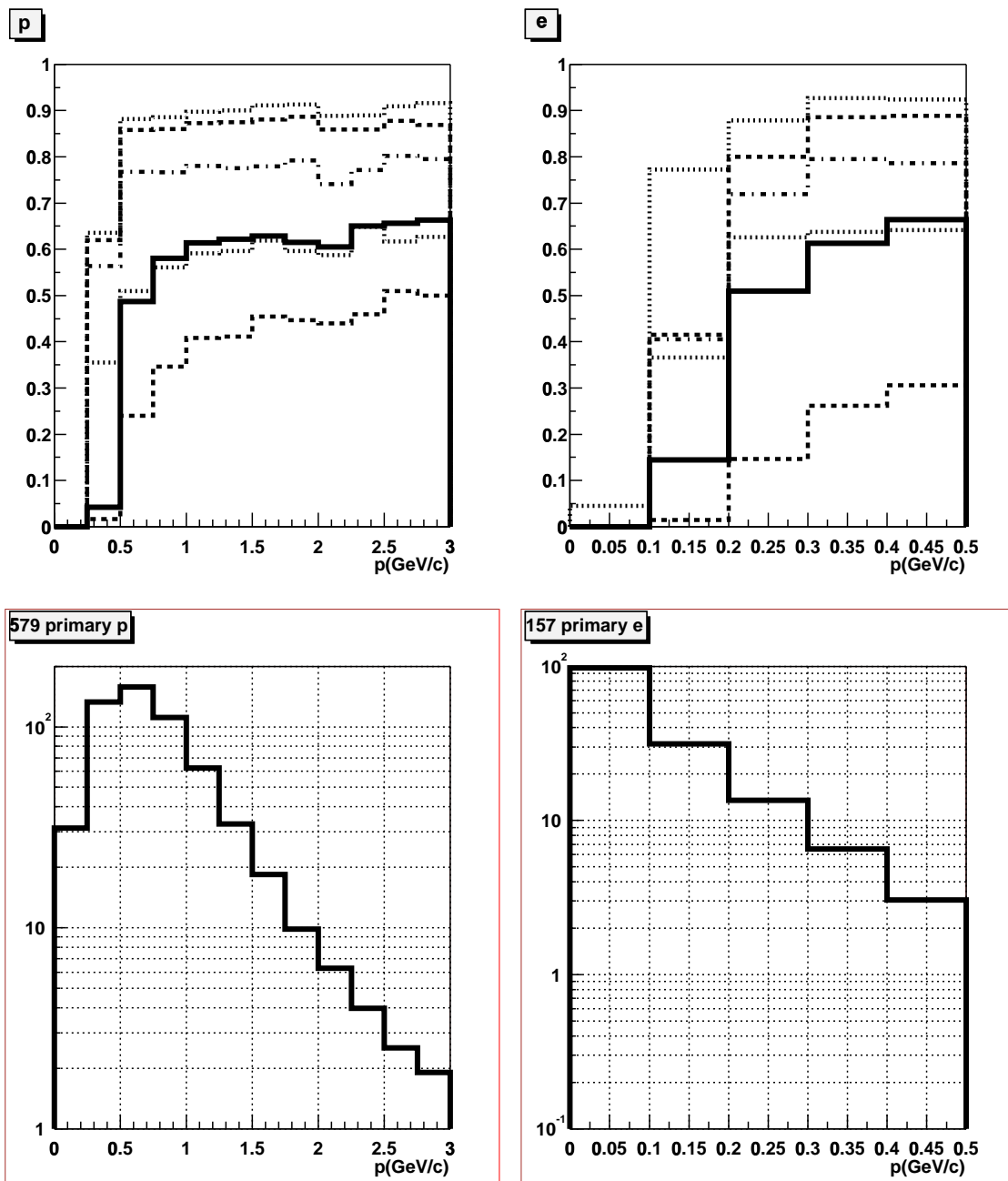


Figure 5.13: Same as Fig. 5.12, for primary $p(\bar{p})$ and e^\pm (100 HIJING events at $B = 0.2 \text{ T}$).

5.6 Particle identification (PID)

As already discussed in previous documents [1, 2], the performance of a TOF system for particle identification does not only depend on the intrinsic timing resolution of the detector, but on the whole system resolution. The particle mass resolution, at relatively high momenta, is predominantly affected by the errors in the time-of-flight and track length measurements, rather than by the error on the momentum determination. Other evident parameters influencing the mass resolution are related to the electronics (errors due to the TDC time digitisation, to the event start time, to the amplification/discrimination circuits, to the time signal distribution, etc.) and to the online/offline calibrations and corrections (pad-to-pad relative timing, time versus amplitude corrections, etc.).

In our simulations, the various sources of time uncertainty are: i) the intrinsic TOF detector resolution (see Chapter 2), including border effects; ii) the different contributions to the TOF system resolution reported in Table 4.2; iii) the track length error (corresponding to $\sim 30 \text{ ps}$) and the momentum error ($\sim 20 \text{ ps}$). We assume an overall system resolution of approximately 120 ps , as anticipated in Section 5.4.3. Thus we smear the time of each pad according to this number.

5.6.1 PID basic method

Let us recall the basic method used for particle identification. All TPC reconstructed and TOF matched primary particles are entered in a momentum versus mass plot as shown in Fig. 5.14 for SHAKER events. Negative mass values correspond to negative square root arguments in the mass determination formula, $m = p(t^2/l^2 - 1)^{1/2}$, p , t and l being the particle momentum, time-of-flight and track length. Let us recall that these primary particles have so far been analyzed in the presence of background from the central and outer regions producing spurious firing of pads in the detector.

Notice that in this plot we have all the particles belonging to set $N_{match} + N_2$, as defined in Section 5.5.2, i.e. all the particles associated with fired TOF pads. Set N_2 (tracks matched with multihit pads) has been included here in order to check the full particle identification power of the detector, as we will see later on. We observe distinct clusters corresponding to pions, kaons and protons as well as a horizontal broad band which corresponds to mismatched tracks, with pads giving wrong times (see Section 5.5.2). This leads to contamination, even in momentum regions where the time resolution is good. For the identification procedure we introduce specific contour cuts, shown in Fig. 5.14, for kaons and protons. The shape of the contours is dictated by the concern to extend the range of pure identification to the largest momenta, even at the expense of efficiency. Figure 5.14 shows two different choices of the kaon contour cut. Unless differently specified, the kaon contour cut corresponding to the narrower (m, p) region has been used as default cut in the following.

Besides these graphical cuts, in the PID procedure, different matching cuts were applied to different particle species. The strongest matching cuts were applied to kaons (because of the large pion contamination): only unambiguous correspondences between tracks and TOF pads were selected, i.e. only pads matched with single tracks (set N_{match} , as defined in Section 5.5.2). For protons, pads matched with more than one track were considered also (set $N_{match} + N_2$ in Section 5.5.2), since we expect one half of these tracks to have true time and the other half to be outside the PID contour cuts. Unless differently identified (as kaons or protons), all the other TPC reconstructed primaries, matched or mismatched with the TOF (set $N_{match} + N_{mis}$ in Section 5.5.2, with $N_{mis} = N_0 + N_2$), were regarded as pions. This does not lead to a very large contamination due to the overwhelming percentage of pions in the SHAKER and HIJING events [1, 2]. We do not consider any contour cut for attempting electron identification below $0.5 \text{ GeV}/c$ since the pion contamination is dominant in this case.

5.6.2 PID efficiency and contamination

Let us call $N_{id}(i)$, with $i = \pi, K, p$, the number of identified particles of different species according to the criteria specified in our previous Section 5.5.2. This number is obviously given by $N_{id}(i) =$

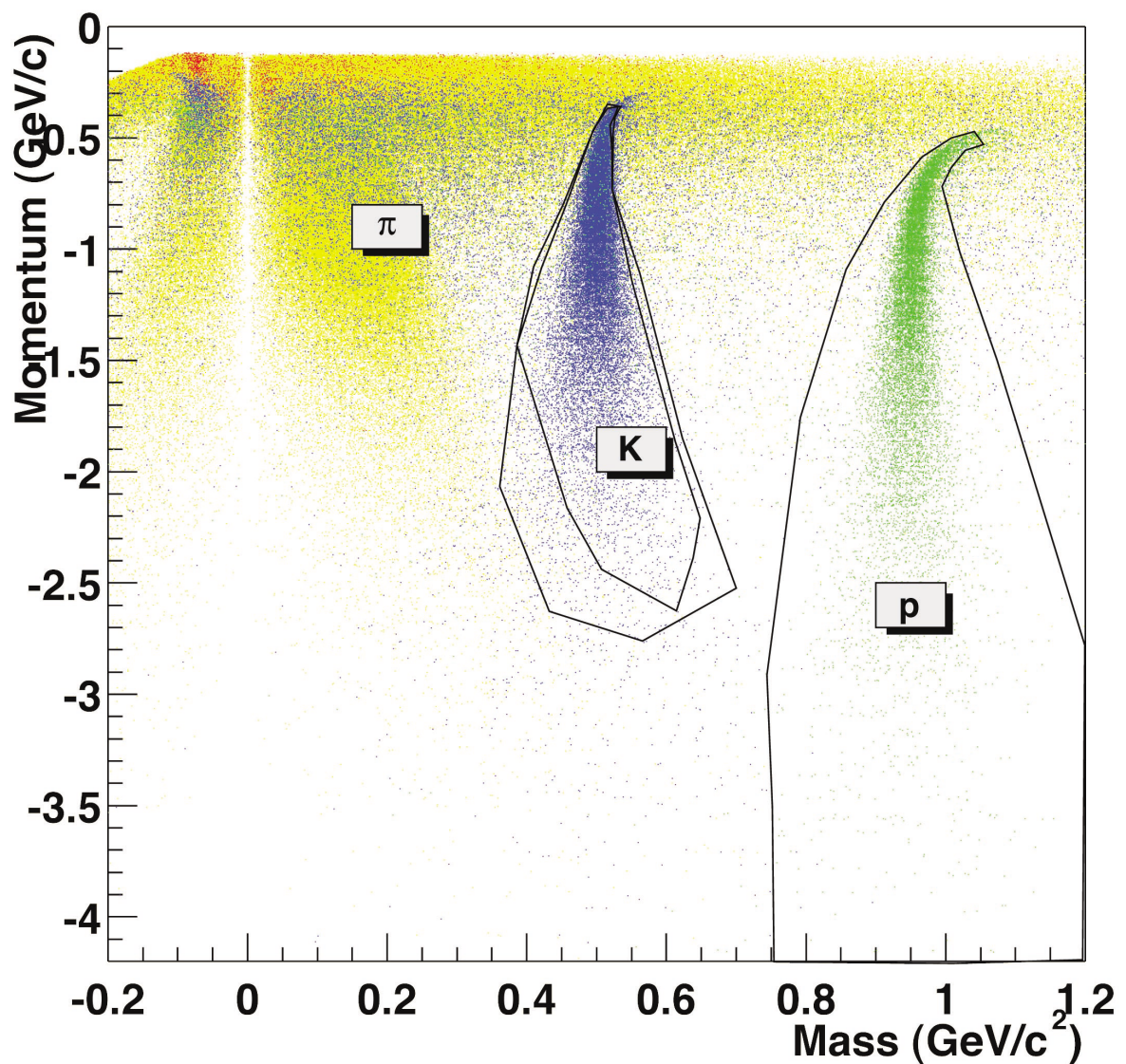


Figure 5.14: Mass separation with the TOF detector (time resolution: 120 ps) as a function of momentum for 25 SHAKER “à la RHIC” [11] events (see later on Section 5.6.2), with $B = 0.2 \text{ T}$.

$N_{id}^t(i) + N_{id}^w(i)$, where $N_{id}^t(i)$ is the number of well identified particles of type i and $N_{id}^w(i)$ the number of non-type i particles misidentified as particles of type i . The efficiency and contamination of the PID procedure, for each type of particle, are then:

$$\text{efficiency} = \frac{N_{id}^t(i)}{N(i)}, \quad \text{contamination} = \frac{N_{id}^w(i)}{N_{id}(i)}$$

where $N(i)$ is the total sample of particles of type i matched with TOF system and, due to the different matching selections adopted, $N(\pi) = N_{match}(\pi) + N_{mis}(\pi)$, $N(K) = N_{match}(K)$ and $N(p) = N_{match}(p) + N_2(p)$. The momentum dependence of the results relative to the last step of our PID procedure (i.e. once the TPC-TOF track matching is achieved) is presented in Fig. 5.15 for 100 HIJING events at $B = 0.2\text{ }T$ and at $B = 0.4\text{ }T$, separately for π , K and p .

In Fig. 5.16 we show the overall PID efficiency, i.e. the PID power of the TOF detector, as a function of momentum, for π , K and p primary particles produced in the $|\theta - 90^\circ| < 45^\circ$ central region, and the overall contamination (which is obviously the same as in Fig. 5.15); here again the results refer to HIJING and to the two magnetic field values adopted so far. The overall PID efficiency, for each momentum bin, is equal to the fraction of primaries produced within the TOF geometrical acceptance which are actually identified. These results are also summarised in Table 5.8, integrating over the same momentum ranges as used in the past [1, 2]. The TOF PID capability for kaons and protons remains practically unchanged when the magnetic field intensity is doubled. In accordance with what anticipated in Section 5.4.1, a higher field has a sizeable influence only on low-momentum pions, below $0.5\text{ }GeV/c$. Figure 5.17 shows the reconstructed particle mass for TOF-identified primaries with momenta in the range $p = (0.5\text{--}2.5)\text{ }GeV/c$, where the achieved PID quality in terms of $\pi/K/p$ separation clearly shows up.

The same PID analysis has been repeated for SHAKER events. A comparison with HIJING results, at $B = 0.2\text{ }T$, is given in Fig. 5.18. The small, expected differences one can observe are a consequence of the different p - and p_t -slopes embedded in the two event generators.

Since it is obvious that the overall PID efficiency and contamination will indeed depend on the particle momentum spectra, we have made the exercise to modify the SHAKER p_t -generation parameters in order to approximately reproduce the recent experimental data on the inclusive π , K , p distributions from RHIC [11]. As shown in Fig. 5.19, the p_t -slope of pions has been steepened and the whole PID procedure applied to a new sample of SHAKER events generated “à la RHIC”. The results obtained are compared with standard SHAKER results in Fig. 5.20, as a function of momentum. Clearly for $p > 1\text{ }GeV/c$, the K and p contaminations are lower for SHAKER “à la RHIC”, while the π contamination is higher. The latter could be reduced by defining a PID contour cut in the (m, p) plane also for pions. In Fig. 5.21, two different contour cuts for kaons (see Fig. 5.14) have been applied to the SHAKER “à la RHIC” sample, thus showing how a better kaon efficiency is achievable, say for $p > 1.75\text{ }GeV/c$, at the cost of a limited contamination increase. However the differences between standard SHAKER and SHAKER “à la RHIC”, concerning the tails of the spectra (i.e. particles at relatively high momenta), disappear in Table 5.9 when summing up over the whole PID momentum interval. This table should also be compared with Table 5.8 relative to the HIJING event generator.

Finally, the sizeable effect of the TRD is shown for HIJING events at $B = 0.4\text{ }T$: in Fig. 5.22 for the last step of the PID procedure, in Fig. 5.23 and Table 5.10 for the overall PID. Clearly an improvement of the TPC-TOF matching procedure will be translated in a further increase of the present TOF PID power.

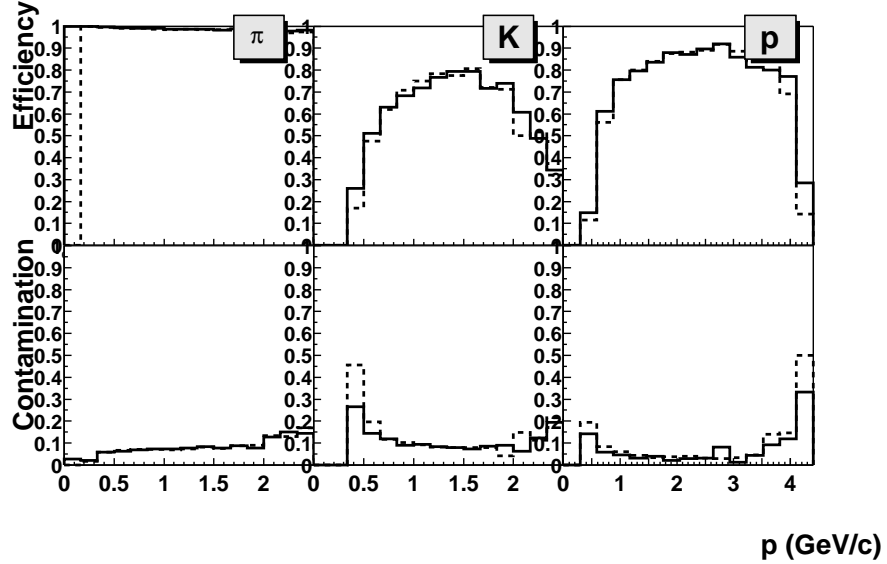


Figure 5.15: The momentum dependence of the efficiency and contamination of the last step of the PID procedure for primary charged particles of different species matched with the TOF (100 HIJING events), tracked with $B = 0.2\text{ T}$ (solid-line histograms) and $B = 0.4\text{ T}$ (dashed-line histograms).

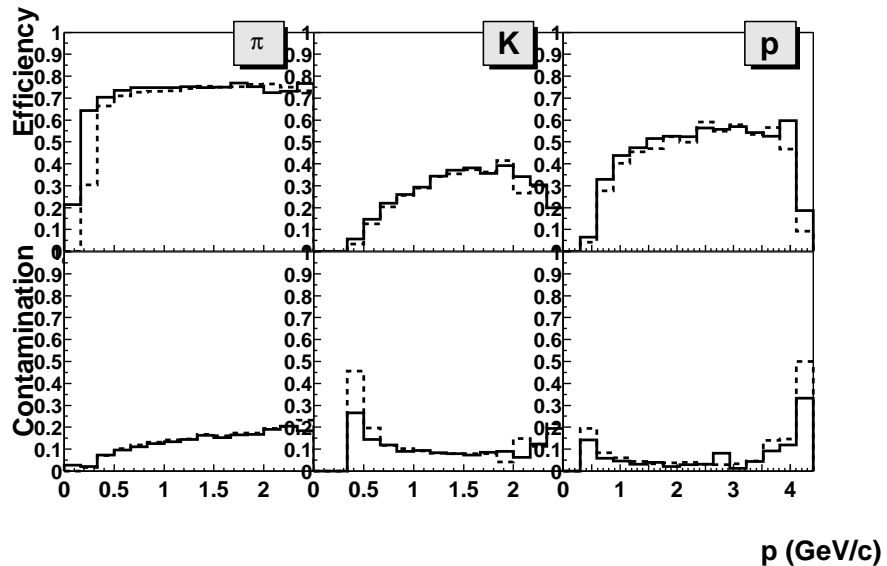


Figure 5.16: The momentum dependence of the overall PID efficiency and contamination for primary charged particles generated in the $|\theta - 90^\circ| < 45^\circ$ region (100 HIJING events), tracked with $B = 0.2\text{ T}$ (solid-line histograms) and $B = 0.4\text{ T}$ (dashed-line histograms).

Table 5.8: Overall PID efficiencies (%) and contaminations (%) in different momentum (GeV/c) ranges for primary hadrons generated in the $|\theta - 90^\circ| < 45^\circ$ region (100 HIJING events), tracked with $B = 0.2 T$ and, in brackets, with $B = 0.4 T$. (*) [Identified pions, kaons and protons have respectively: $p \gtrsim 0.15$ (0.2), 0.25 (0.3) and 0.35 (0.4) GeV/c , at $B = 0.2$ (0.4) T .]

Primary hadron	Momentum range	Efficiency	Contamination
π^\pm	(*) $p < 2.5$	63 (48)	7 (9)
K^\pm	(*) $p < 2.5$	14 (13)	13 (15)
$p(\bar{p})$	(*) $p < 4.5$	27 (24)	5 (7)
π^\pm	$0.5 < p < 2$	74 (72)	11 (12)
K^\pm	$0.5 < p < 2$	23 (21)	11 (12)
$p(\bar{p})$	$0.5 < p < 2$	37 (33)	5 (7)

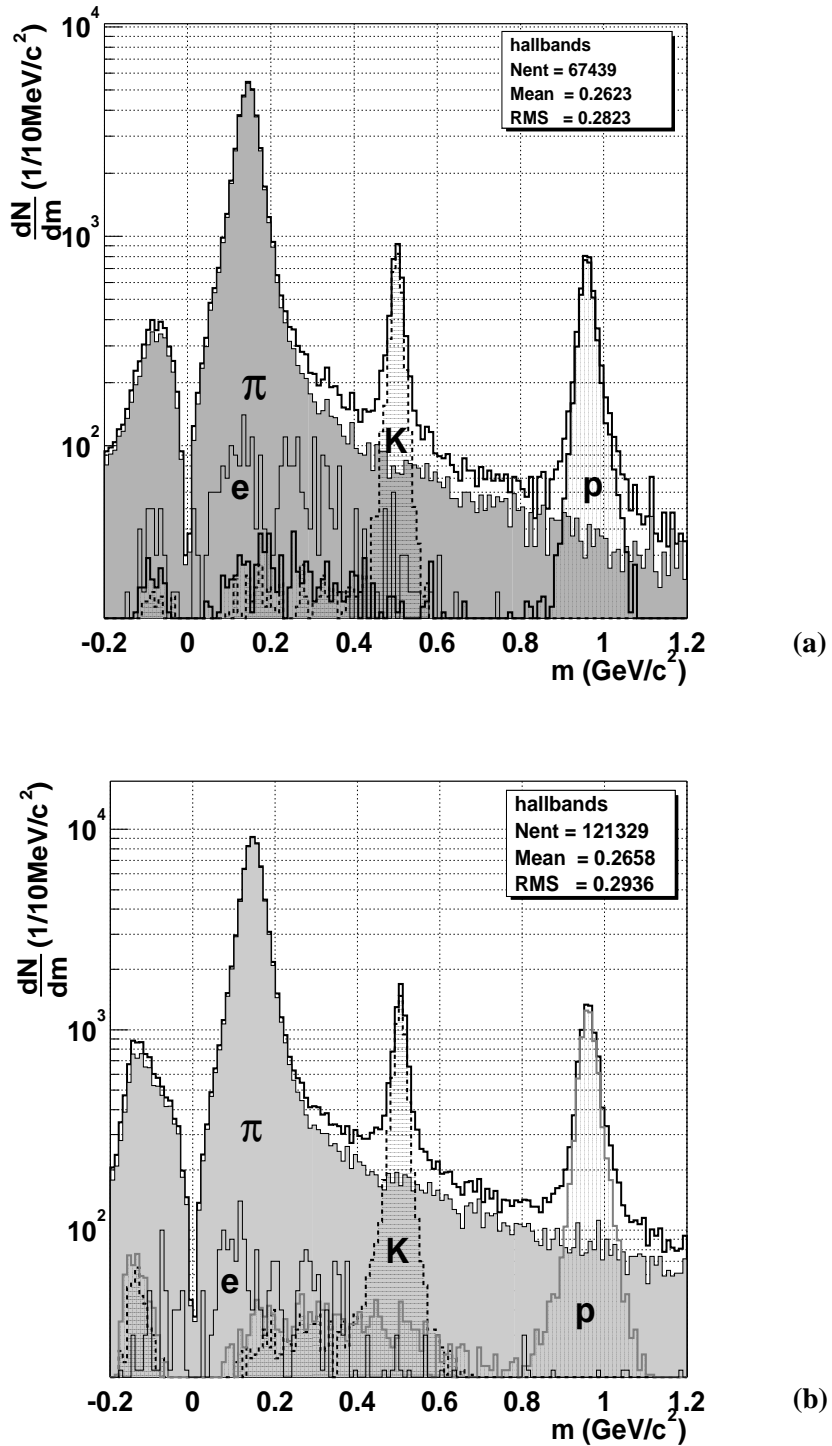


Figure 5.17: Reconstructed mass with the TOF detector (overall TOF system resolution: 120 ps) in the momentum range $0.5 \text{ GeV}/c \leq p \leq 2.5 \text{ GeV}/c$, for: a) 25 HIJING events at $B = 0.2 \text{ T}$; b) 50 HIJING events at $B = 0.4 \text{ T}$. The grey- and dashed-area histograms superimposed show the individual mass distributions of the true pions, kaons, protons and electrons associated with fired TOF pads; for electrons, this distribution has been multiplied by a factor 10.

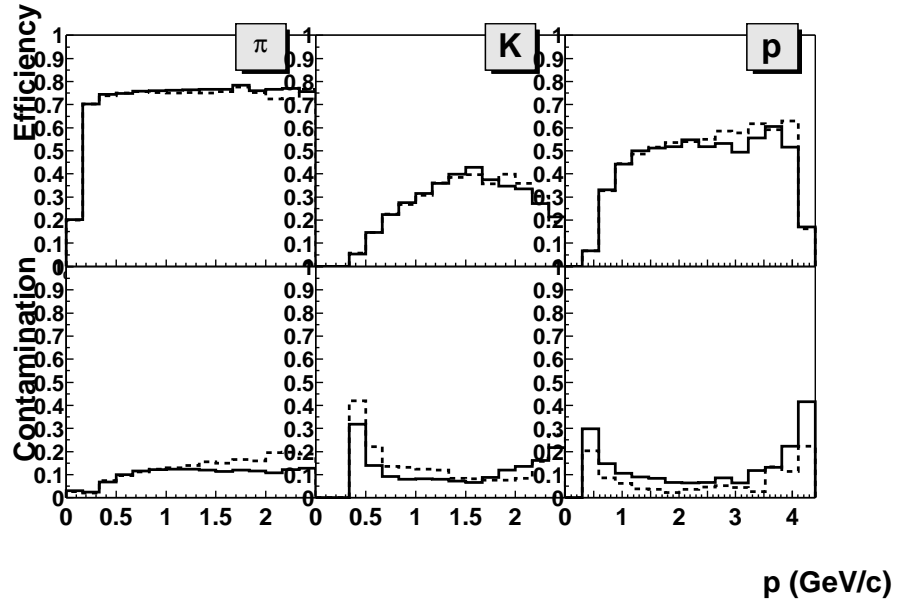


Figure 5.18: The momentum dependence of the overall PID efficiency and contamination for primary charged particles of different species generated in the $|\theta - 90^\circ| < 45^\circ$ region and tracked with $B = 0.2\text{ T}$: for 100 SHAKER events (solid-line histograms) and 100 HIJING events (dashed-line histograms).

Table 5.9: Overall PID efficiencies (%) and contaminations (%) in different momentum (GeV/c) ranges for primary hadrons generated in the $|\theta - 90^\circ| < 45^\circ$ region and tracked with $B = 0.2\text{ T}$ for 100 SHAKER events, and, in brackets, for 100 SHAKER “à la RHIC” events.

Primary hadron	Momentum range	Efficiency	Contamination
π^\pm	$p < 2.5$	65 (65)	8 (8)
K^\pm	$p < 2.5$	17 (17)	8 (8)
$p(\bar{p})$	$p < 4.5$	34 (34)	8 (7)
π^\pm	$0.5 < p < 2$	75 (74)	11 (12)
K^\pm	$0.5 < p < 2$	25 (25)	7 (7)
$p(\bar{p})$	$0.5 < p < 2$	41 (41)	8 (8)

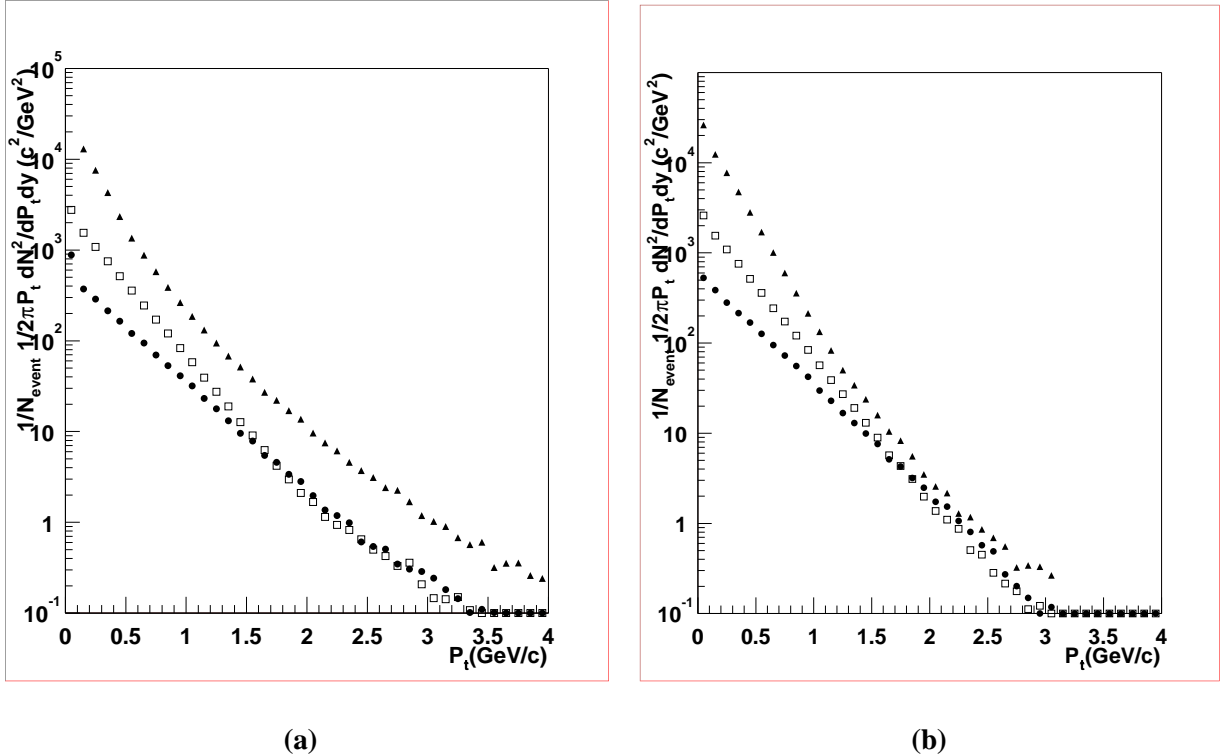


Figure 5.19: p_t -distributions for π^\pm (\blacktriangle), K^\pm (\square) and $p(\bar{p})$ (\bullet) using: a) the standard SHAKER event generator; b) the SHAKER event generator modified “à la RHIC” [11]. Each plot corresponds to 50 events.

5.6.3 PID in p-p interactions

Proton-proton collisions are characterised by a much lower multiplicity and a consequently much lower background with respect to typical heavy-ion collisions, thus allowing us to be confident that a good particle identification will be achieved with the TOF detector during the LHC p-p running periods.

Let us present some preliminary results obtained with a sample of 6000 PYTHIA [6] events, corresponding to minimum bias p-p interactions at a centre-of-mass energy $\sqrt{s} = 14 \text{ TeV}$. As in the Pb-Pb case, the events have been tracked with GEANT, using a magnetic field value $B = 0.2 \text{ T}$. The same TPC-TOF matching procedure (see Section 5.5) and PID method (see Section 5.6.1) have been applied to charged particles.

As already done for Pb-Pb collisions (see Fig. 5.14 in Section 5.6.1), all TPC reconstructed and TOF matched primary particles are entered in a momentum versus mass plot as shown in Fig. 5.24, where distinct clusters corresponding to electrons, pions, kaons and protons can be clearly seen. In Pb-Pb collisions, the identification of electrons was not considered because of an exceedingly high background level. In the present p-p analysis, we gain a significant PID efficiency for electrons in the $0.1 \text{ GeV}/c \leq p \leq 0.5 \text{ GeV}/c$ range.

In Fig. 5.25 we show the overall PID efficiency, i.e. the PID power of the TOF detector, as a function of momentum, for e, π , K and p primary particles produced in the $|\theta - 90^\circ| < 45^\circ$ central region. This figure should be compared with Fig. 5.18, obtained using Pb-Pb data (with both SHAKER and HIJING event generators). The contour cuts defined for e, K and p in p-p events are drawn in Fig. 5.24. These cuts differ from those previously adopted in the Pb-Pb case. The resulting PID performance of the TOF detector is summarised in Table 5.11 (to be compared with Tables 5.8 and 5.9).

Figure 5.26 shows the p_t -distributions of different particle species, as obtained with PYTHIA p-p events at LHC energy, to be compared with Fig. 5.19, relative to SHAKER Pb-Pb events.

Table 5.10: Overall PID efficiencies (%) and contaminations (%) in different momentum (GeV/c) ranges for primary hadrons generated in the $|\theta - 90^\circ| < 45^\circ$ region and tracked with $B = 0.4 T$ for 100 HIJING events with the TRD (as in Table 5.8), and, in brackets, without the TRD.

Primary hadron	Momentum range	Efficiency	Contamination
π^\pm	$p < 2.5$	48 (63)	9 (6)
K^\pm	$p < 2.5$	13 (17)	15 (8)
$p(\bar{p})$	$p < 4.5$	24 (36)	7 (3)
π^\pm	$0.5 < p < 2$	72 (74)	12 (9)
K^\pm	$0.5 < p < 2$	21 (27)	12 (7)
$p(\bar{p})$	$0.5 < p < 2$	33 (50)	7 (3)

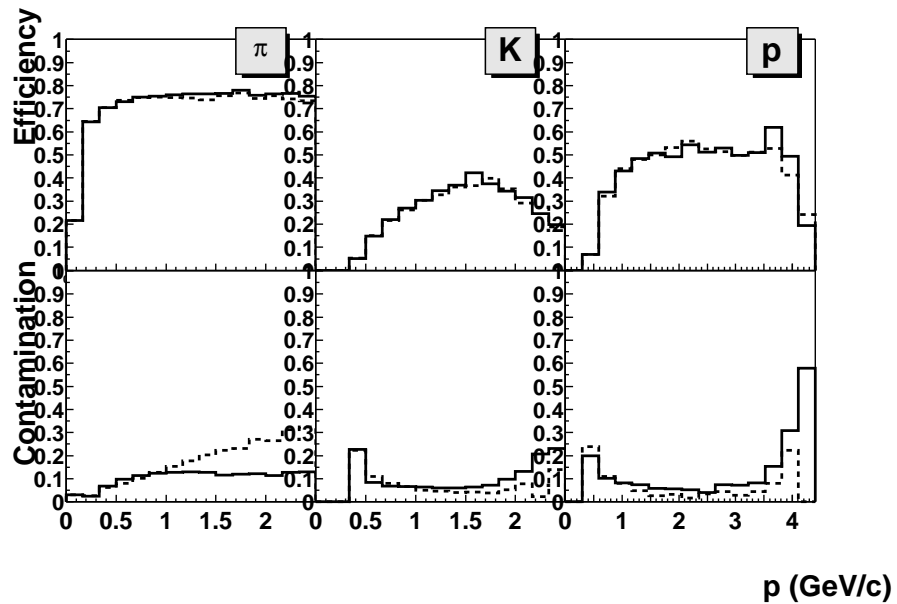


Figure 5.20: The momentum dependence of the overall PID efficiency and contamination for primary charged particles of different species generated in the $|\theta - 90^\circ| < 45^\circ$ region and tracked with $B = 0.2 T$: for 100 SHAKER events (solid-line histograms) and 100 SHAKER “à la RHIC” events (dashed-line histograms).

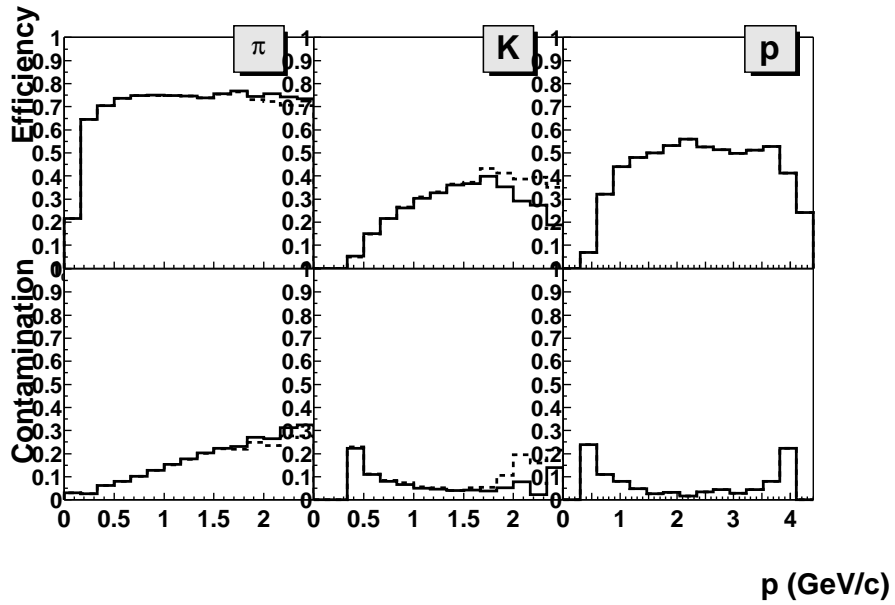


Figure 5.21: The momentum dependence of the overall PID efficiency and contamination for primary charged particles of different species generated in the $|\theta - 90^\circ| < 45^\circ$ region and tracked with $B = 0.2$ T (100 SHAKER “à la RHIC” events): applying the narrower (solid-line histograms) and wider (dashed-line histograms) contour cuts shown in Fig. 5.14 for kaon identification.

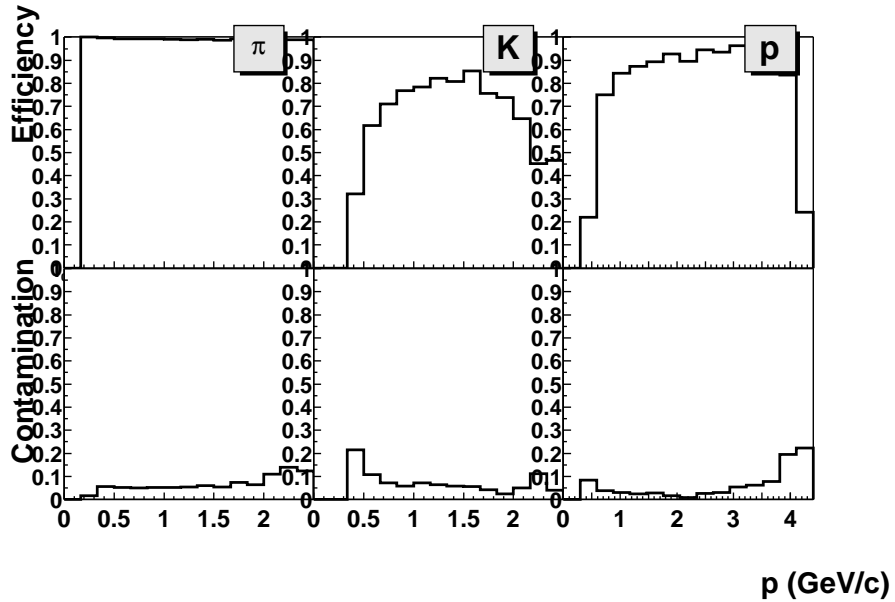


Figure 5.22: The momentum dependence of the efficiency and contamination of the last step of the PID procedure for primary charged particles of different species matched with the TOF and tracked with $B = 0.4$ T (100 HIJING events) without the TRD.

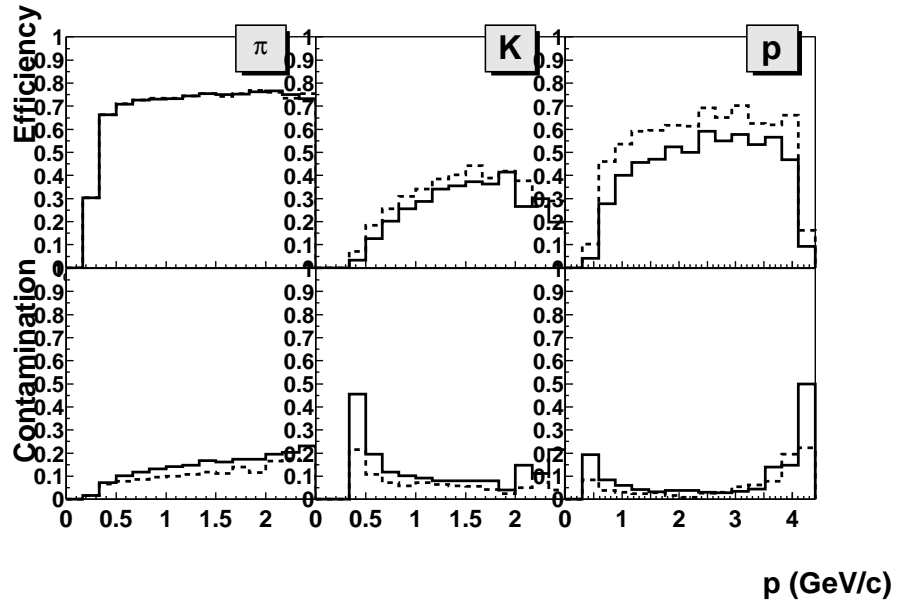


Figure 5.23: The momentum dependence of the overall PID efficiency and contamination for primary charged particles of different species generated in the $|\theta - 90^\circ| < 45^\circ$ region and tracked with $B = 0.4$ T (100 HIJING events): with the TRD (solid-line histograms) and without the TRD (dashed-line histograms).

Table 5.11: Overall PID efficiencies (%) and contaminations (%) in different momentum (GeV/c) ranges for primary particles generated in the $|\theta - 90^\circ| < 45^\circ$ region and tracked with $B = 0.2$ T (6000 p-p PYTHIA events).

Primary particle	Momentum range	Efficiency	Contamination
π^\pm	$p < 2.5$	61	6
K^\pm	$p < 2.5$	22	1
$p(\bar{p})$	$p < 4.5$	40	1
e^\pm	$0.1 < p < 0.5$	23	8
π^\pm	$0.5 < p < 2$	73	8
K^\pm	$0.5 < p < 2$	29	1
$p(\bar{p})$	$0.5 < p < 2$	45	0

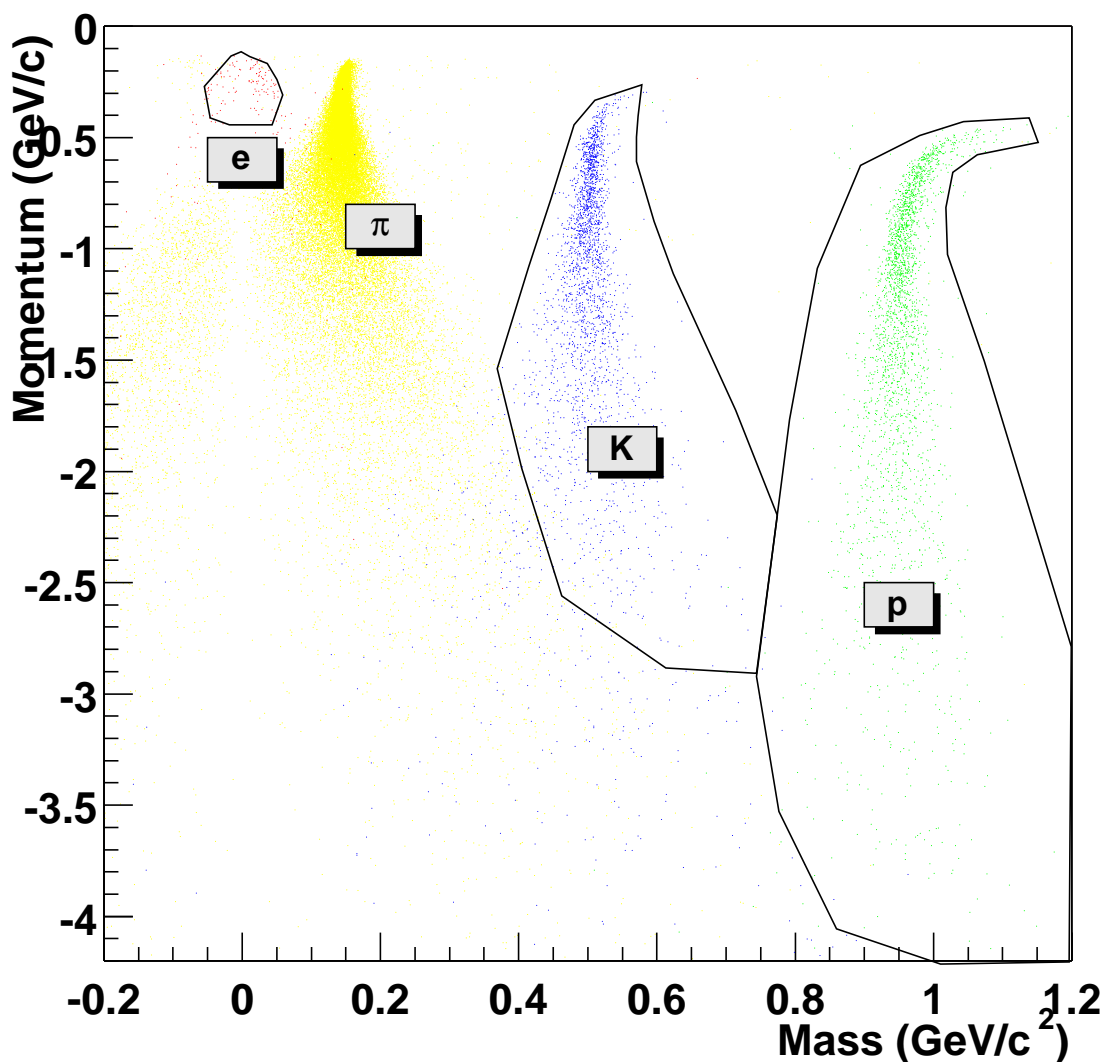


Figure 5.24: Mass separation with the TOF detector (time resolution: 120 μs) as a function of momentum for 6000 p-p PYTHIA events, with $B = 0.2 \text{ T}$.

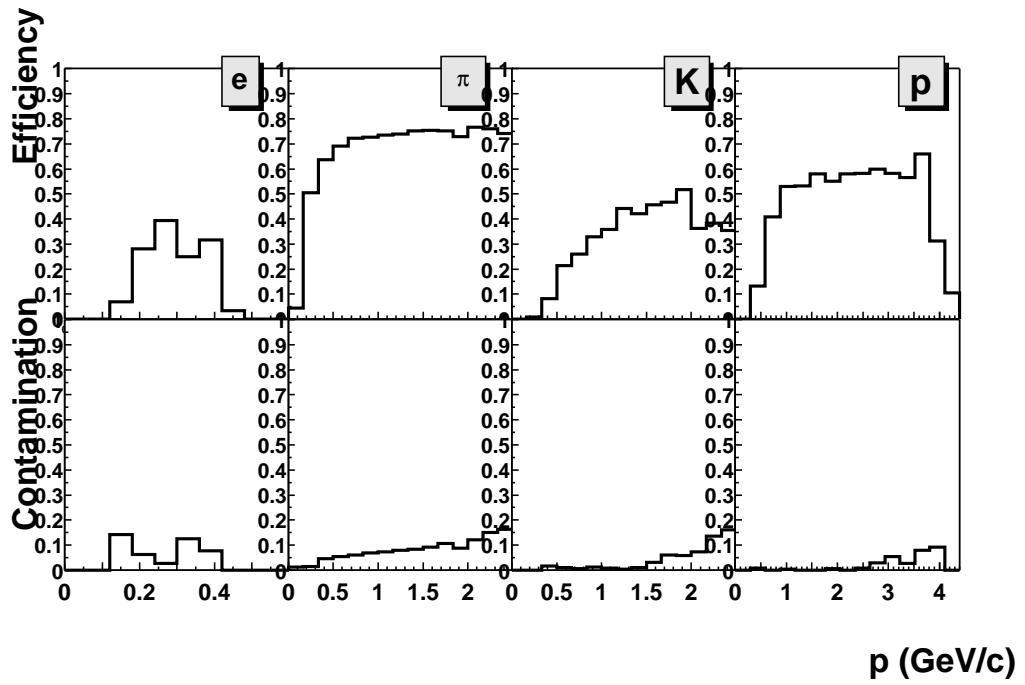


Figure 5.25: The momentum dependence of the overall PID efficiency and contamination obtained with the TOF detector for primary charged particles of different species generated in the $|\theta - 90^\circ| < 45^\circ$ region and tracked with $B = 0.2$ T (6000 p-p PYTHIA events).

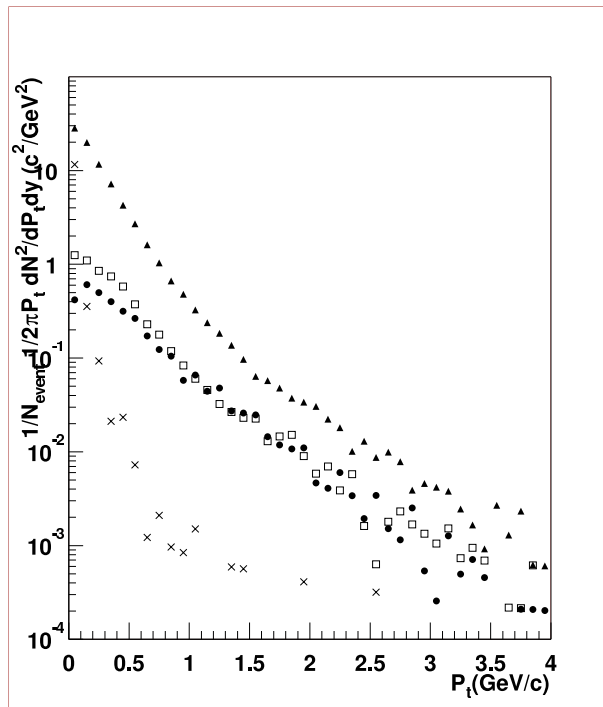


Figure 5.26: p_t -distributions for π^\pm (\blacktriangle), K^\pm (\square), $p(\bar{p})$ (\bullet) and e^\pm (\times) in 1000 PYTHIA p-p events at LHC energy.

5.6.4 Conclusion on PID

Let us first consider Pb-Pb interactions. A comparison of the TOF PID results obtained herein (Fig. 5.20) with our previous results (*Fig. 6.8* in [2]) is straightforward when referring to SHAKER events at $B = 0.2\text{ T}$. Notwithstanding the worsening of the TPC-TOF matching step, the overall PID now achieved is better than previously obtained owing to the much improved TOF detector performance, in particular in terms of time resolution. As visible in Fig. 5.20, for kaons the contamination vs. momentum remains below 10% from 0.5 to $2\text{ GeV}/c$ and below 25% up to $2.5\text{ GeV}/c$. In [2], this was true from 0.5 to $1.75\text{ GeV}/c$ and the contamination rose up to 45% at $2.5\text{ GeV}/c$. For protons, in Fig. 5.20, the contamination stays below 10% in the $(0.5\text{-}3.5)\text{ GeV}/c$ interval and below 30% up to $4\text{ GeV}/c$. In [2] this happened in the $(0.5\text{-}3.25)\text{ GeV}/c$ interval and a 60% contamination level was reached at $4\text{ GeV}/c$. As far as the PID efficiency vs. momentum is concerned, this is essentially unchanged with respect to [2]. When folding in the inclusive particle momentum spectra, the overall PID efficiencies and contaminations (Table 5.9), integrated over identical momentum intervals with respect to the past (*Table 6.2* in [2]), are the same.

When referring to HIJING events, the results are slightly different (because of the different generator structures) but perfectly consistent (Fig. 5.18). Kaon identification (Figs. 5.16 and 5.18) can be achieved in a comparably wide momentum range, reaching and even exceeding $2\text{ GeV}/c$, with a contamination at the 10% level. For protons (Figs. 5.16 and 5.18) the momentum range is wider, reaching $4\text{ GeV}/c$, and the contamination well below 10%. However the integration over differently shaped (with respect to SHAKER) particle momentum spectra shows up in Table 5.8, when compared with Table 5.9 (relative to SHAKER events).

As far as the magnetic field is concerned, an increase from 0.2 to 0.4 T does hardly affect the K and p identification, as shown in Fig. 5.16, and only marginally the π identification (below $0.5\text{ GeV}/c$).

The conclusion from our present simulations is that, once the different event generator parameters (dN_{ch}/dy density, p_t spectra, K/π and p/π particle ratios) and magnetic field values are accounted for, in a single Pb-Pb interaction the TOF detector will be able to identify 5000-7000 pions, 100-250 kaons and 150-200 protons with 10% or less contamination, in the momentum range extending up to $2.3\text{ GeV}/c$ for pions and kaons, and up to $4\text{ GeV}/c$ for protons.

Turning now to the p-p case, the TOF PID is even better, thanks to the reduced background conditions. In the momentum ranges mentioned above the π , K, p PID efficiencies are higher and the contaminations lower, almost negligible for kaons and protons (see Fig. 5.25). Moreover, electrons can be identified in the $(0.1\text{-}0.5)\text{ GeV}/c$ momentum range, with a contamination level below 10%.

5.7 Measurement of the t_0 event time with TOF

In a Pb-Pb or p-p event, all primary particles are generated at the same time (the so called “zero-time”, t_0). No matter if this time is equal to zero: it is a constant for all primary particles in the event. Moreover, event-by-event, it will correspond to a different constant. This t_0 information is propagated to the TOF detector as the flight times of primary tracks are recorded by the TDCs. In the following we will describe how to come back to the initial information (just the t_0) using only the TOF data. For the time being the algorithm [22] has been applied to Pb-Pb simulated events.

5.7.1 The statistical method

Let us consider a Pb-Pb event at LHC and a very small subset of primary charged tracks (say n tracks) produced in this event and reaching the TOF detector⁸.

Let l_1, l_2, \dots, l_n be the lengths of the particle trajectories from the common interaction vertex, p_1, p_2, \dots, p_n the corresponding particle momenta (all these quantities will be given by track reconstruction in the TPC and extrapolation to the TOF) and t_1, t_2, \dots, t_n the corresponding flight times (given by the TOF). If we require that the velocity of each particle is not a continuous variable but can assume only three values, $\beta(\pi), \beta(K), \beta(p)$, as obtained by attributing to the particle either the pion, the kaon, or the proton mass, then, by assigning a mass configuration to the n selected tracks in the event, we can require a best fit condition thus deriving the most probable mass configuration for the n tracks, out of the possible $N = 3^n$ cases, and the corresponding most probable t_0 for the event.

Given a mass configuration $C(m_1, m_2, \dots, m_n)$ we can derive a zero-time value $t_i^0(m_i)$ relative to each primary track i

$$t_i^0(m_i) = \frac{l_i}{c\beta_i(m_i)} - t_i$$

and therefore compute the weighted average over the n primary tracks

$$\langle t^0 \rangle(C) = \frac{\sum_{i=1}^n \frac{t_i^0(m_i)}{e_i^2(m_i)}}{\sum_{i=1}^n \frac{1}{e_i^2(m_i)}}$$

where

$$e_i(m_i) = \left[e_{t_i}^2 + \left(\frac{l_i}{c\beta_i^2(m_i)} \right)^2 e_{\beta_i}^2 + \left(\frac{1}{c\beta_i(m_i)} \right)^2 e_{l_i}^2 \right]^{\frac{1}{2}}$$

is the error on $t_i^0(m_i)$ determination by means of track i , which is a function of the errors on t_i , β_i and l_i . Notice that the error on β_i is in fact the error on the momentum p_i . Obviously a wrong mass assumption for primary track i will result in a large deviation of $t_i^0(m_i)$ with respect to the zero-time.

We can compute the $\chi^2(C)$ of each mass configuration C as follows:

$$\chi^2(C) = \sum_{i=1}^n \frac{[t_i^0(C) - \langle t^0 \rangle(C)]^2}{e_i^2(m_i)}$$

and identify the configuration C_{best} giving the minimum $\chi^2(C)$ as the one corresponding to the best mass assignment for the selected set of n primary tracks, with $\chi_{MIN}^2 = \min\{\chi^2(C_1), \chi^2(C_2), \dots, \chi^2(C_{3^n})\}$.

Finally we can determine the zero-time for the current event by taking the mean (over the n selected primary tracks) $\langle t^0 \rangle(C)$ corresponding to the best configuration, i.e. $\langle t^0 \rangle(C_{best})$. We will also consider the confidence level of this χ_{MIN}^2 with $(n-1)$ degrees of freedom, i.e. $P(\chi_{MIN}^2) = Prob(\chi_{MIN}^2, n-1)$, acting as a monitor of the uncertainties introduced in the Monte Carlo simulation. This quantity will

⁸As we will see in the following, this method needs only $\sim 5\%$ of the total number of primary charged particles reaching the TOF in the $B = 0.4$ T case.

actually play the same rôle in the analysis of real events.

From the point of view of particle identification, we can derive a natural definition of the probability w for a certain track i to be a pion, a kaon, or a proton. This is given by

$$w_i(\pi) = \frac{\sum_{C^*} P_{C^*}(m_i = m_\pi)}{\sum_C P_C}$$

where P_C is the confidence level of $\chi^2(C)$ (with $(n - 1)$ degrees of freedom) and C^* is the set of mass configurations in which particle i is assumed to be a pion. Analogous expressions hold true for $w_i(K)$ and $w_i(p)$. From the definition, we obviously obtain:

$$w_i(\pi) + w_i(K) + w_i(p) = 1.$$

5.7.2 t_0 determination in Monte Carlo events

We have performed a preliminary test of the t_0 determination algorithm described in the previous section, using 250 HIJING Pb-Pb events and a magnetic field value of 0.4 T. In each event we select n primary tracks reaching the TOF detector, in the momentum range $1.25 \text{ GeV}/c < p < 1.75 \text{ GeV}/c$ which is the best range for TPC-TOF track matching and $\pi/K/p$ PID in the TOF. For each track extrapolated to the TOF surface, the time-of-flight uncertainty is obtained by Gaussian smearing, using the global TOF-system resolution σ_t (see Section 5.6). The track-length uncertainty (converted to ps) is already included in σ_t . The momentum uncertainty is also derived by Gaussian smearing, using $\frac{\sigma_p}{p} = 2.5\%$ for any momentum value. For the time being no border effects between adjacent TOF pads (see Section 5.4.3) have been included in the simulation.

The best zero-time, $\langle t^0 \rangle(C_{best})$, is then computed for each event. By assuming that in all Monte Carlo events this zero-time is actually equal to zero (i.e. $t_0 = 0$), from the $\langle t^0 \rangle(C_{best})$ distribution around zero, as obtained for many events, the uncertainty on t_0 determination can be estimated. In the present exercise, in order to enlarge the statistics, more than one uncorrelated set of n primary tracks reaching the TOF detector in the specified momentum range has been considered for each event.

The $\langle t^0 \rangle(C_{best})$ distributions have been derived for different set sizes ($n = 10$ and $n = 15$) and TOF resolutions ($\sigma_t = 120 \text{ ps}$ and $\sigma_t = 150 \text{ ps}$). We obviously expect a better resolution on t_0 determination when n increases and σ_t decreases. Figures 5.27 and 5.28 show the comparison between the global TOF resolutions $\sigma_t = 120 \text{ ps}$ and $\sigma_t = 150 \text{ ps}$, separately for $n = 15$ and $n = 10$. The different distributions obtained for $\langle t^0 \rangle(C_{best})$ confirm the expected behaviour. Also notice that for normally distributed measurements (i.e. if the so-called “normality assumption” is verified) the confidence level distribution must have a uniform distribution over the interval $[0, 1]$ [23]. Figure 5.29 shows that this is indeed true and that no bias has been introduced in the present analysis.

Table 5.12 summarises the results⁹: a t_0 resolution below 50 ps can be reached in any case (as required, see Section 5.6) and, in particular, for $\sigma_t = 120 \text{ ps}$ and $n = 15$, the result is $\sigma_{t_0} = (32 \pm 1) \text{ ps}$. Considering the combinatorial character of the algorithm, the CPU computing time¹⁰ for the $\langle t^0 \rangle(C_{best})$ determination is also given in Table 5.12, as a function of the number n of selected tracks per set. Since the n tracks of each set, with $1.25 \text{ GeV}/c < p < 1.75 \text{ GeV}/c$, are actually identified as π , K or p by means of t_0 determination, the percentual contaminations of the whole samples of analyzed particles and sets (a set being misidentified when containing at least one misidentified particle) are included in Table 5.12.

The procedure described herein allows to derive the event zero-time with very good precision, using only the TOF TDC information of a limited sample of tracks as time input. Since the charged particle

⁹The C++ code for this simulation is available on the CVS Repository. For the time being the analysis with $n = 15$ tracks per set is done via a ROOT macro while that with $n = 10$ tracks per set is done via the “ad hoc” class *AliTOFT0*. The documentation and the use case are available on the implementation file.

¹⁰Referring to a typical PIII 800 MHz machine.

Table 5.12: Summary of the results on t_0 determination, relative to 250 HIJING events with $B = 0.4 T$.

Global time resolution	Number of tracks per set (total number of sets per event)	Gaussian fit σ_{t_0}	% of misidentified particles (sets)
120 ps	10 (5) CPU computing time per set: 5''	(41±1) ps	0.6% (4%)
	15 (3) CPU computing time per set: 10'	(32±1) ps	0.2% (3%)
150 ps	10 (5)	(51±1) ps	1.3% (10%)
	15 (3)	(42±1) ps	1.1% (14%)

mass is allowed to vary among m_π , m_K , m_p values, no systematic effect depending on the K/ π or p/ π ratios (which are unknown for real Pb-Pb events) is foreseen, as it would be the case if the pion mass was assumed for all tracks. Moreover, by iteration, the t_0 algorithm could be likely used to improve the overall TOF PID. This method is also promising for p-p events, where the multiplicity will be lower by orders of magnitude.

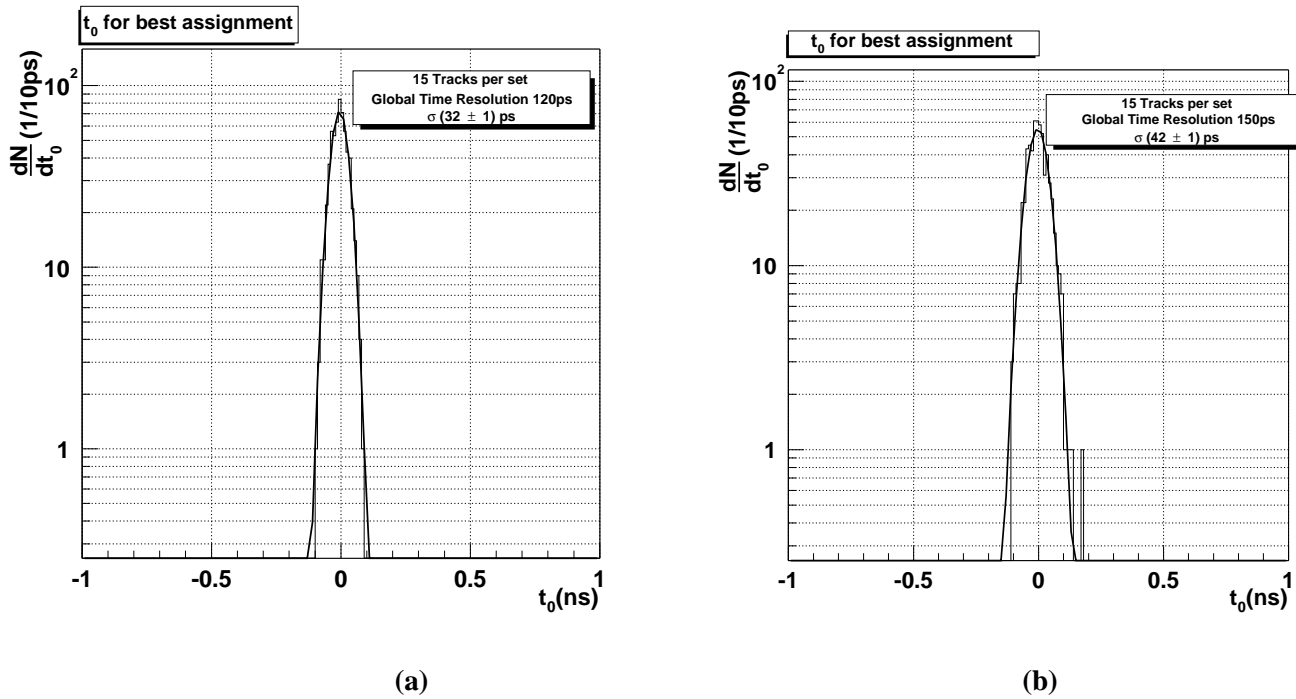


Figure 5.27: $\langle t^0 \rangle(C_{best})$ distributions for $n = 15$ with a TOF global resolution: a) $\sigma_t = 120 \text{ ps}$; b) $\sigma_t = 150 \text{ ps}$.

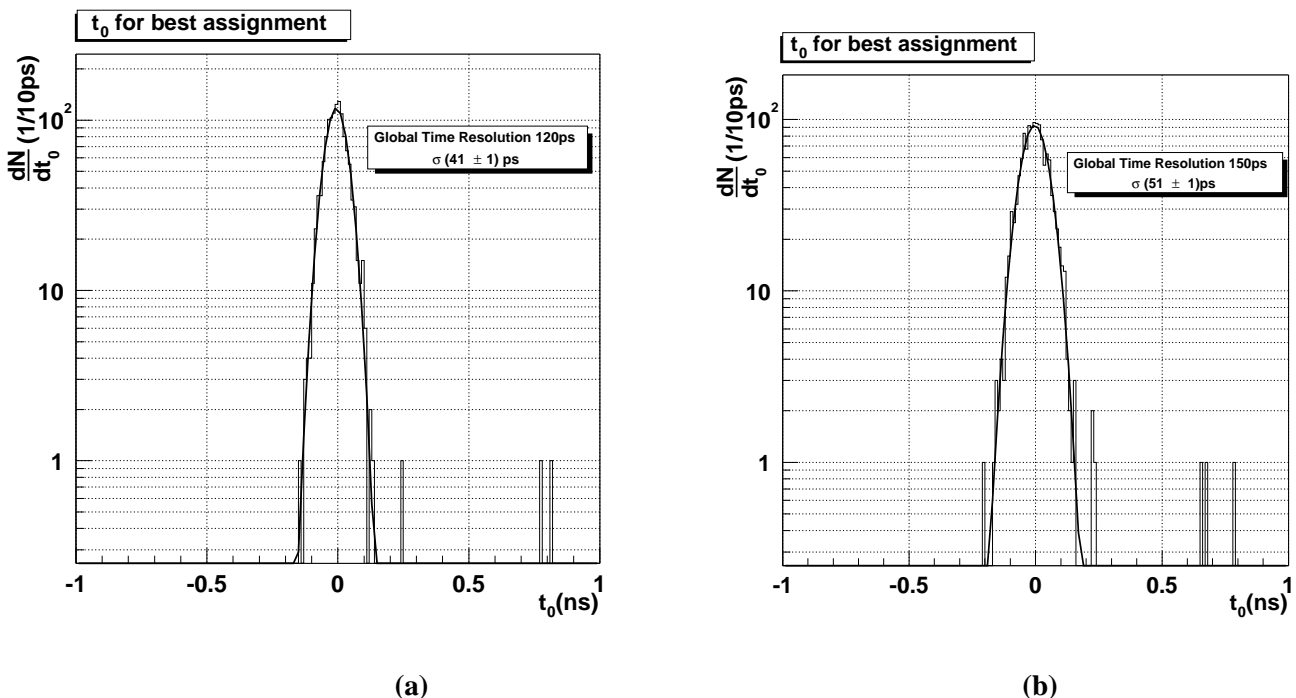


Figure 5.28: Same as 5.27 for $n = 10$.

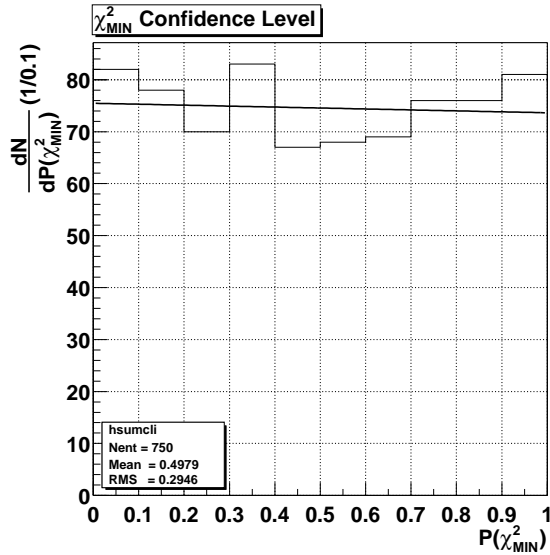


Figure 5.29: Distribution of the confidence level $P(\chi^2_{\text{MIN}})$ for $n = 15$ and $\sigma_t = 120 \text{ ps}$.

5.8 Monte Carlo event production in the framework of ALICE-GRID

For the Monte Carlo simulation studies presented in this document, the first tests in the GRID framework [24], [25], [26], [27] were performed in Bologna by the TOF Group using the *quantum grid* nodes. The INFN-GRID project has financed a basic setup for participating sites of 3 dual-processor PIII nodes. These nodes in Bologna are equipped with PIII 800 *Mhz* CPUs and 30 *GB* disks with 512 *MB* RAM.

The software currently required by the distributed computing environment has been installed on these nodes and the most relevant packages (and the corresponding tasks) are:

- *Globus* (user authentication and authorization);
- *Condor* (job scheduling and submission);
- *Condor Bypass* (log file and data retrieving);
- *MRTG* (monitoring of the node resources);
- *MySQL* (bookkeeping).

The first ALICE-GRID test in Bologna was performed in April 2001 using *Globus* and the standard Unix *fork* for job submission. Bologna site managers installed the operating system, *Globus* and *MRTG*. A minimal set of users was created. As such users were already certified by the INFN-CA (INFN Certification Authority), the site managers mapped their GRID certificates. The standard - for all sites - version of the ALICE software was distributed by the Torino Group. The data produced in this test were used, after a quality check, both in Bologna and Salerno, for offline analysis. All files were stored on Bologna mass storage and CPU activity was remotely monitored using *MRTG*.

In July-August 2001 further tests were made of the existing GRID tools focusing on bookkeeping facilities with *MySQL*: this activity led to the mirroring in Bologna of the Catania production status databases, with network monitoring and dynamically created web pages in order to display database entries and AliROOT log files on the geographically distributed nodes.

In January 2002 a new small farm with 5 nodes and a disk server was installed in Bologna. The various services like network setup and minimal user authorization at Linux level were configured and the

farm is currently up and running; a total amount of 10^3 Pb-Pb events plus 10^5 p-p events were simulated for Monte Carlo analysis.

Finally, the INFN has financed a prototype Tier1 [28] site in Bologna at CNAF¹¹. A TOF Group member is also member of the ALICE Coordination Group for INFN Tier1 activities. The Tier1 Management Board is active and monthly meetings are scheduled. ALICE requirements are prepared and presented to the Tier1 Management. We foresee that in short time the first tests will start to evaluate and customise Tier1 activities in response to the ALICE requests.

This activity is in a fast expansion phase, according to the ever growing needs of computing power for the ALICE Collaboration, and in particular for the TOF Group.

¹¹Historically, “Centro Nazionale Analisi Fotogrammi”; now, “Centro Nazionale per la Ricerca e lo Sviluppo nelle Tecnologie Informatiche e Telematiche”.

6 Services

6.1 Low Voltage Power Distribution

The TOF detector electronics will be located in two different areas: (1) the front end analogue electronics will be placed inside the single detector modules (these regions could be accessed only during very long shutdown), (2) the TDC and readout cards will be hosted in crates placed on the space frame in correspondence to the TOF sectors, two at each end of each sector (these could be accessed during short shutdown periods).

Low voltage has to be distributed to both areas, keeping the power delivered to digital and analogue electronics separated for noise reduction.

Two options have been considered to supply LV power to the electronics:

- Power supplies located immediately outside the ALICE magnet, in the experimental hall, delivering the needed voltage and current directly to the load.

Considering the amount of power (> 100 kW) to be distributed to the TOF electronics, this solution has a strong impact on the power cable cross section since we want to limit, as much as possible, the voltage drop along the distribution lines. Cable size and weight represent, therefore, an important concern.

- DC-to-DC converter placed inside the magnet as close as possible to the load. Such converters must operate in a high magnetic field (possibly up to 0.5 T) and substantial radiation environment. These devices are presently being developed and extensive tests on the final prototype are scheduled starting April 2002.

The total power consumption of the TOF is 165 kW. Assuming the use of three voltages ± 5 V and 3.3 V, more than ~ 20 kA will be circulating through the TOF electronics. In both options the main low voltage power supplies will be located as close to the detector as possible, but outside the magnetic field region, i.e. outside the ALICE magnet (UX25 cavern) in an area not accessible during LHC operation. From these power supplies onward the distribution will depend on the option chosen, as explained in what follows.

6.1.1 Distribution schemes

6.1.1.1 Standard solution

We consider now the first of the two LV system options mentioned above. The closest location for the power supplies is at ~ 25 m on each side of the space frame (RB24 and RB26 areas). The detector is subdivided in 18+18 half sectors. Each half sector needs ~ 1.8 kW for the analogue electronics and ~ 1.6 kW for the digital electronics. We will then use three cable lines for the analogue and two cable lines for the digital circuitry of half a sector and their respective return lines. The cables will pass through the ALICE magnet doors, at about half height of the detector. Each cable line will draw a current of more than 100 A. The use of copper bus bar of an appropriate cross section is needed for such a distribution. A compromise between the voltage drop and the power dissipation determines the cross section. Allowing a 0.5/0.6 V voltage drop through the 25 m line, the cross section of each bus bar turns out to be of the order of 100 mm^2 . 360 copper bus bars, 100 mm^2 thick, are needed and the total surface occupied by the bare cables is of about 360 cm^2 . The total weight of such copper bus bar is of ~ 10 tons. In addition

to the bare bus bar space some more space has to be considered for isolation and water cooling of the cables, since the total dissipated power on the cables can reach 25 kW.

The design of the cables can be further optimised considering the limitation in space in the region inside the ALICE magnet: a bigger bus bar cross section can be used in the cable part which is outside the ALICE magnet in order to minimise the voltage drop, then we can reduce the bus bar cross section inside the ALICE magnet in order to limit the occupied space. This low voltage system has disadvantages in terms of cable cost, heat loss in the cables, substantial voltage drop, together with high circulating currents, big weight and space occupied by the bus bar cables.

6.1.1.2 DC-to-DC converters solution

To circumvent the previous problems, the most promising alternative is based on delivering the power at higher voltage (48 V or more), using LV power supplies located outside the ALICE magnet and converting it, using DC-to-DC converters, to the required voltages in a region very close to the electronic cards. The main concern in this choice is that the region where the DC-to-DC converters should be located is irradiated and with a significant magnetic field (up to 0.5 T). Commercially available DC-to-DC converters are not able to operate in magnetic field higher than 0.05 T. Several companies are developing DC-to-DC converters with characteristics that would be suitable to the ALICE environment. Among them, CAEN has proposed a technique based on the use of toroidal coils. During 2001 two prototypes have been tested: the first one showed a good behaviour up to 0.185 T using a small test magnet provided by the CERN electronic pool, proving that the technique is promising. A second, more extensive test, in a magnetic field up to 1 T has been performed during July 2001: the device, a DC-to-DC converter with 48 V input and 4 V output voltage and 30 A maximum current, has shown an excellent behaviour according to our specifications, up to 0.5 T. The performance was still good up to 0.8 T and started to degrade approaching 1 T, with the failure of some components. Following these results the TOF group has commissioned CAEN for a prototype, with the appropriate power to cope with the segmentation of the TOF detector. A DC-to-DC converter prototype, with 48 V input and 7 V output and 50 A maximum current (350 W), will be delivered to the TOF group during April 2002.

Extensive tests are ongoing to prove the capability of such a device to fulfill all the specifications of our LV system. With the use of DC-to-DC converters the layout of the LV system is significantly simplified (Fig. 6.1): we can use only one commercial power supply (48 V, 200 A) located outside the ALICE magnet and only one bus bar (cross section of $\sim 100 \text{ mm}^2$) to supply the LV power to the DC-to-DC converters of two contiguous half sectors. The converters will be housed in dedicated crates located at the edges of each sector and 10 modules of the type described above will be required per each half sector. Therefore, to power the whole TOF detector, a total number of 360 DC-to-DC converters is needed. The DC-to-DC converters include also remotely controlled distributors to fan out and monitor the low voltage power delivered to the front end, TDC and readout cards. The final dimensions of one of these devices will be approximately $12 \times 6 \times 20 \text{ cm}^3$.

6.2 High Voltage Distribution

6.2.1 HV power consumption

The detector element of the TOF system, the MRPC strip, will be operated with a differential voltage of about $\pm 6 \text{ kV}$, i.e. $\sim 12 \text{ kV}$ across each of the two 5 gap stacks.

Taking into account that the maximum expected rate at the ALICE experiment will be of the order of 50 Hz/cm² and assuming that the average charge induced on a hit pad is $\sim 3 \text{ pC}$ (see Sec. 2.4.2), the current and the power consumption of the TOF detector can be evaluated as shown in Table 6.1.

The measured power consumption [1] and the values quoted in Table 6.1 confirm that the MRPCs are low power devices with respect to the standard RPCs.

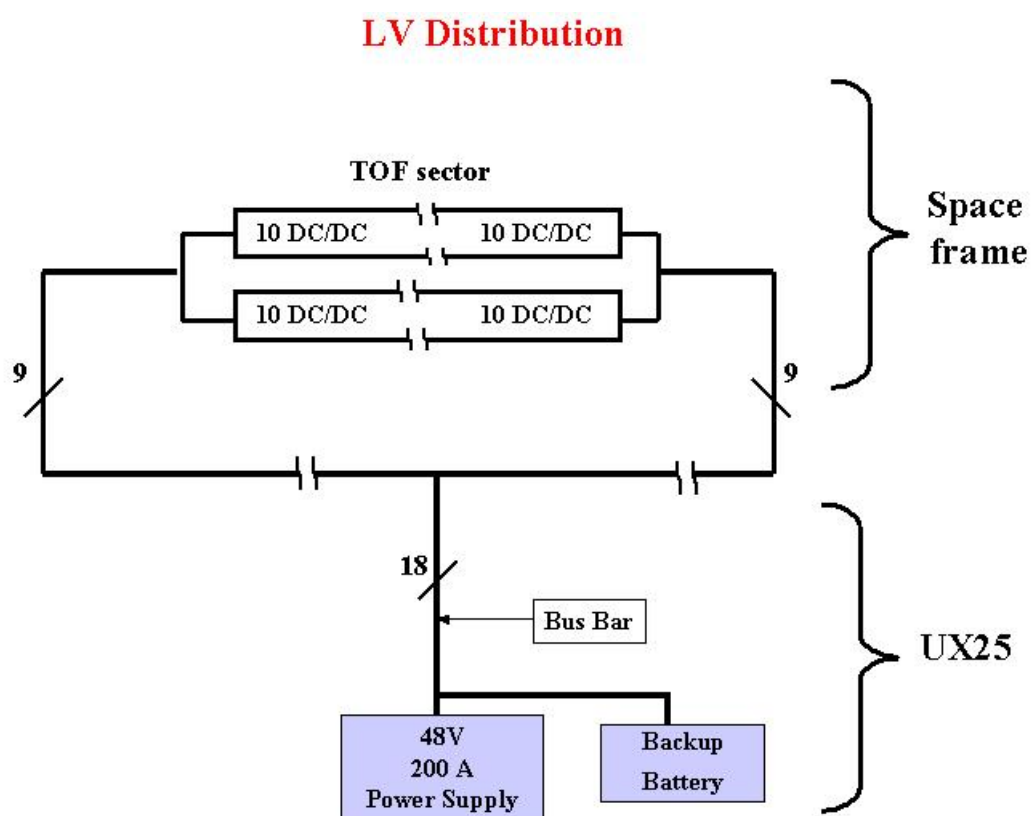


Figure 6.1: DC-to-DC converter distribution scheme.

Table 6.1: Estimates of the current and power for the HV system.

	Current (double stack)	Power (double stack)
Strip (96 pads)	130 nA	1.6 mW
Module (20 strips)	2.6 μ A	31.2 mW
Sector (5 modules)	13 μ A	156 mW
Whole TOF detector	234 μ A	2.8 W

6.2.2 Distribution system

The detector will be inaccessible during LHC operation; hence a remote control is mandatory to switch on/off eventual malfunctioning strips, while keeping the rest of the detector operational. We will use 2 power supply channels (a positive and a negative one) per module, 180 power supply channels are therefore needed to deliver the HV power to the 90 TOF modules. The CAEN module A1526, providing up to 15 kV and 0.1 mA, in groups of 8 channels, is currently under consideration. The power supply channels will be housed in 4 multichannel mainframes (CAEN 1527 with 48 channels); this will allow accurate remote control and monitoring of single channel parameters (trip, limits, current, etc.). We will use 2 mainframes for the positive and 2 mainframes for the negative voltage channels. Fig. 6.2 shows the HV distribution scheme for half of the TOF system.

Each channel will be connected to a 20 output passive distributor (see Fig. 6.2), located very close to the multichannel mainframes. A pair of positive and negative lines from a positive and a negative voltage distributor will feed a strip. An entire module will require 2 distributors and 40 supply lines; the whole detector will need 180 distributors and $20 \times 2 \times 90 = 3600$ supply lines. The outputs of the distributors will be equipped with bistable relays, which can be remotely driven to switch the strip on or off. A strip failure, typically resulting in a short-circuit, will be signaled by the mainframe channel control, with straight tracing of the module affected by the malfunctioning strip; powering off all the strips of that module and then progressively turning them on will allow to pin down the damaged strip. Standard CERN 50 Ω cables can be used to connect each supply channel to a distributor (length of a few meters). Then a multiwire-shielded cable (23 wires) will connect a distributor to the module. 180 multiwire cables will be used, with a total section of about 300 cm². The cable bundle will be connected to the detector passing through the ALICE magnet doors (RB24 and RB26). Each multiwire cable requires 4 multipin connectors, 2 for the connection to the distributor and 2 for the connection to the module.

6.3 TOF gas system

6.3.1 Introduction

The design of the TOF gas system essentially remains the same as described in the Technical Design Report [2], however the integration of the various components is now better defined. Although the gas volume of the detector remains relatively small, the high cost of the gas mixture still makes a closed loop circulation system necessary.

It is still envisaged to install 90 modules, comprising a total gas volume of approximately 16 m³, and operated with a non-flammable freon rich gas mixture containing C₂H₂F₄, i-C₄H₁₀ and SF₆ (90%/5%/5%). The design parameters of the system can be seen in Table 6.2.

The mixing unit, purifier, and the optional gas recovery plant, will be located in the gas building on the surface (SGX2). The circulating rack will be located on the shielding plug in the pit (PX24). The final distribution manifold will be located in the experimental cavern. An overview of the gas system can

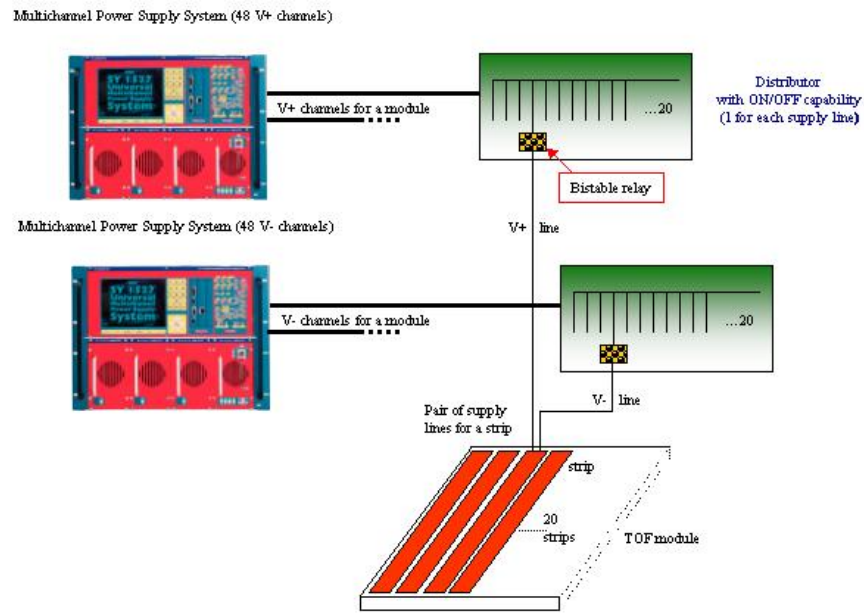


Figure 6.2: HV distribution scheme for half of the TOF system.

be seen in Fig. 6.3.

Primary gases are supplied to the mixing rooms and are available at standard distribution panels. The gas mixing unit, purifier and eventual gas recovery unit are located in the mixing room. An overall view of the gas building at Point 2 can be seen in Fig. 6.4.

6.3.2 The Closed Loop Distribution System

The 90 detector modules are supplied with gas from a manifold in groups of five. Internal module pressures due to hydrostatic height of the detector will be minimised by splitting the distribution system into two distinct height zones. Each zone will have its own pressure control and protection system. This arrangement results in 18 gas segments. The gas is circulated in a closed loop system (see Fig. 6.5) with an expected regeneration rate of 95%. A gas exchange rate of one volume every 6 hours is foreseen for the detector. The expected circulation flow rate will be $2.7\text{m}^3/\text{h}$, and with a fresh gas injection of 1% the entire gas volume will be renewed once every 25 days. During the initial outgassing of the chambers this fresh gas flow rate might have to be higher. A detailed description of the system is given in the Technical Design Report [2].

The gas mixing and purifier units will be located in the mixing room of the gas building, a layout of this room can be seen in Fig. 6.6.

Gas flow from the surface building will be split into two sections at the Plug level (PX24). Each of the two sections has its own pressure regulation and protection system. The pressure in each section is adjusted to account for hydrostatic pressure differences of the two height zones. The mechanical stability of the modules must, however, be sufficient to support the full hydrostatic pressure of about 3 mbar for correct filling or purging.

The hydrostatic pressure over the half height of the ALICE magnet is ~ 1.2 mbar. The centre of each

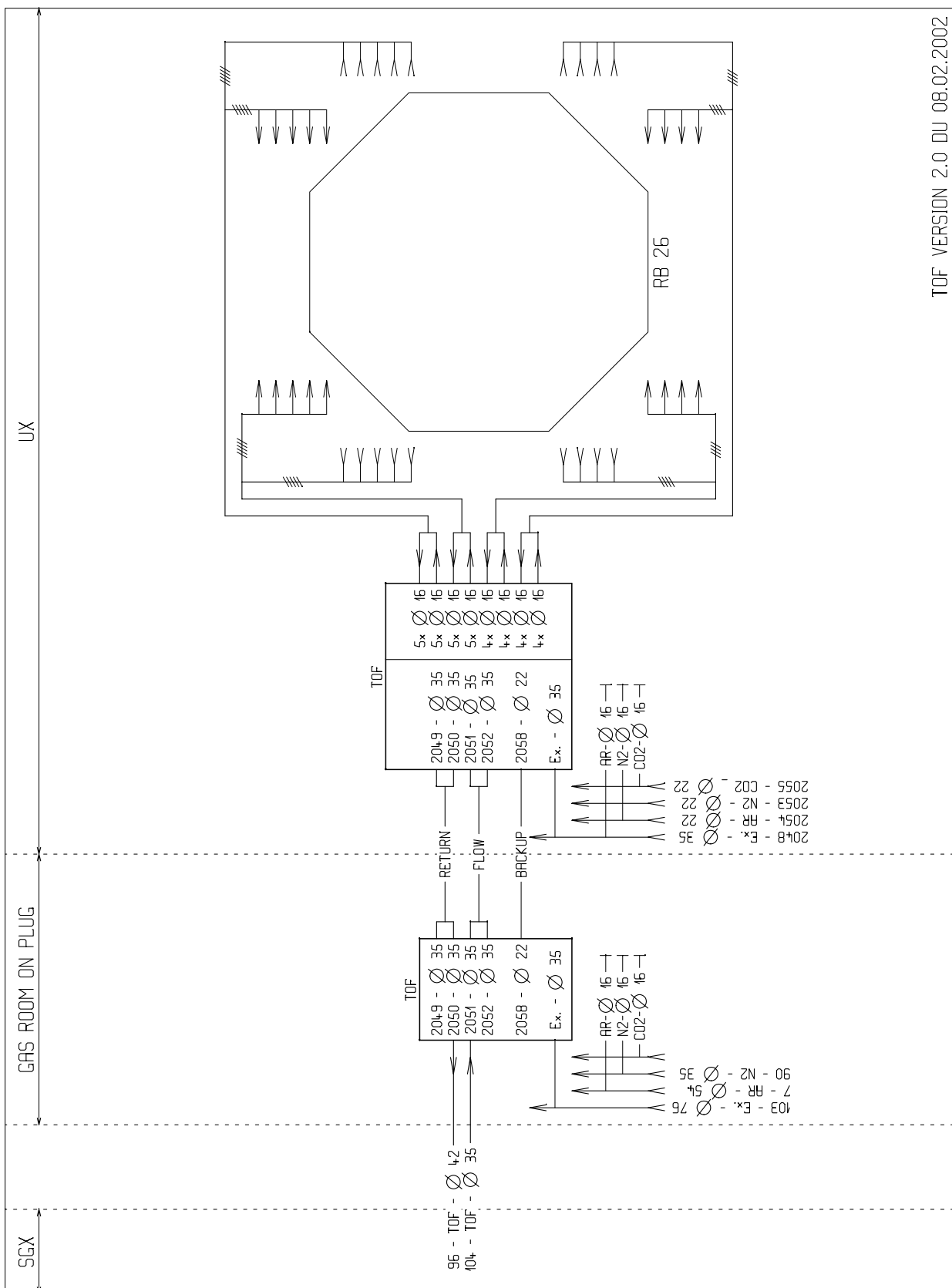


Figure 6.3: Overview of the TOF gas system.

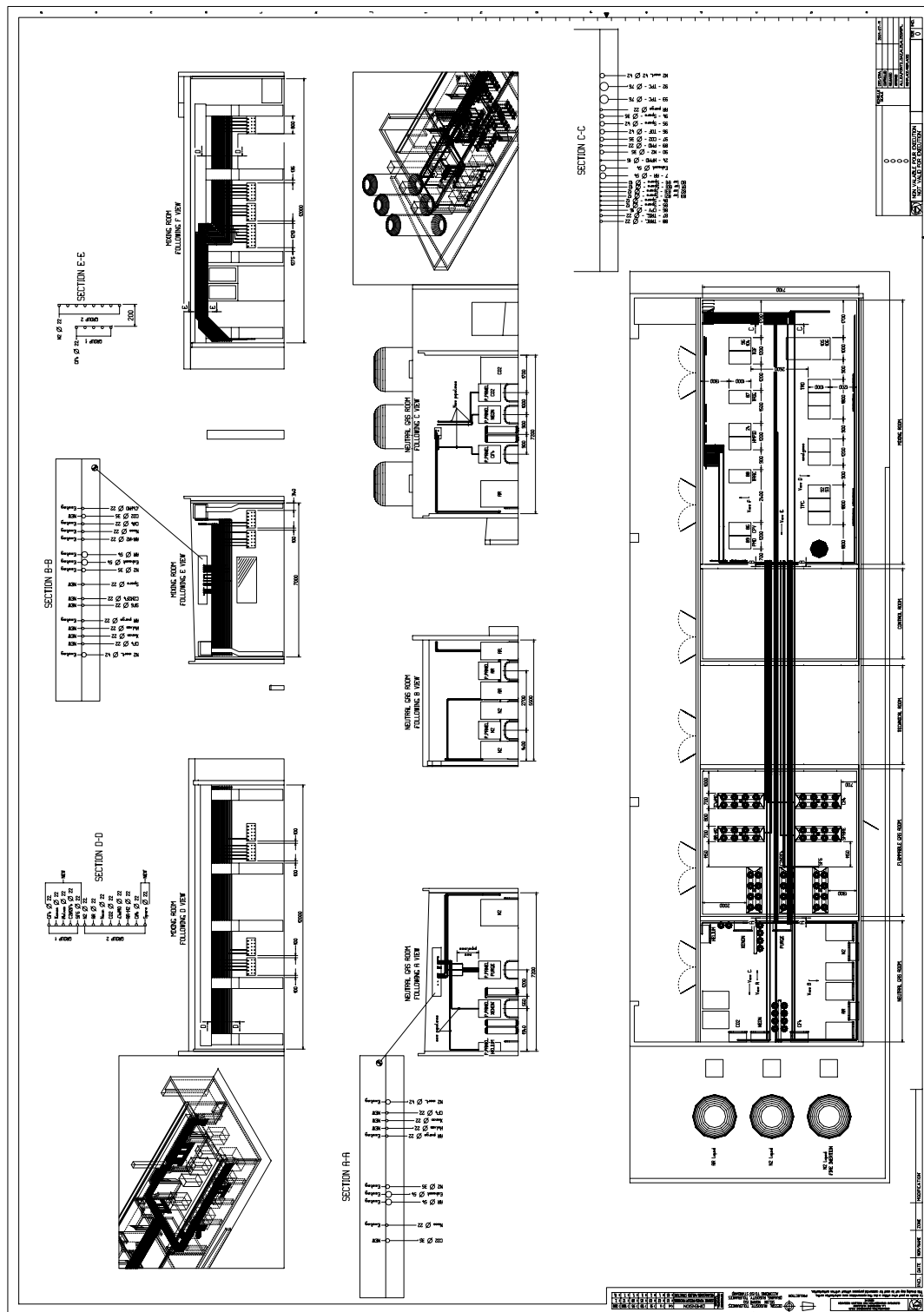


Figure 6.4: Overview of the gas building at Point 2.

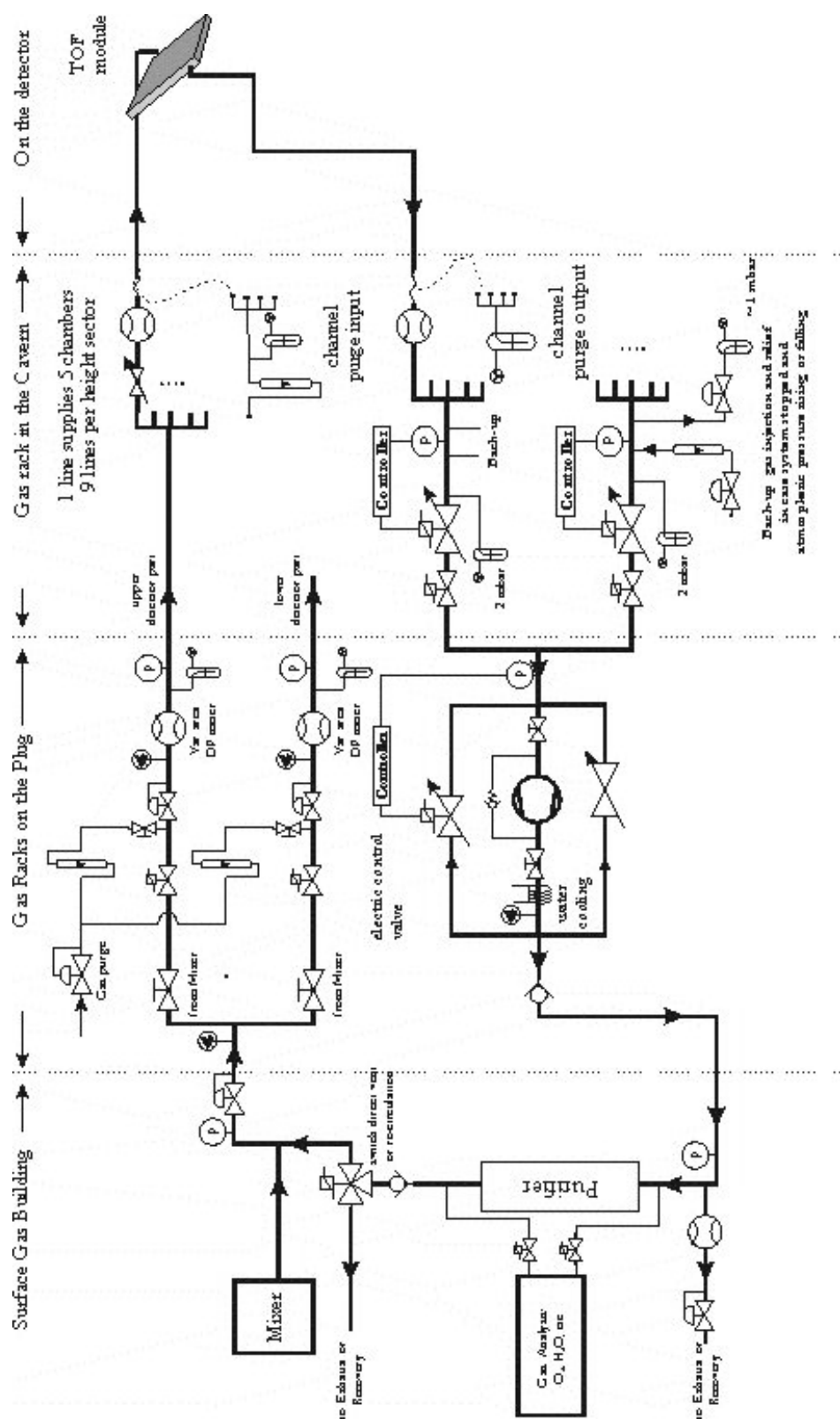


Figure 6.5: Layout of the closed loop distribution system.

Table 6.2: Design parameters of the TOF gas system.

Total volume	16 m^3
No of modules (max)	90
Gas mixture	$\text{C}_2\text{H}_2\text{F}_4$, - i- C_4H_{10} - SF_6 (90%/5%/5%).
Volume exchange/day	4
Total flow rate	$2.7 \text{ m}^3/\text{h}$
Working pressure	< 3 mbar
Fresh gas flow rate	$0.027 \text{ m}^3/\text{h}$
Tolerable O_2 content	< 1000 ppm
Tolerable H_2O content	< 100 ppm

height band will be kept at atmospheric pressure which implies that there will be 0.6 mb overpressure for the modules at the bottom of the height band and -0.6 mbar (under)pressure at the top of the height band. This 0.0 mb pressure can be controlled to ± 0.2 mb; thus the chambers have to operate with a pressure of ± 0.8 mb. This pressure regulation can only be achieved by placing the control rack at mid-height of the ALICE magnet.

A pump, located at the Plug level, compresses the return gas from the modules to approximately 200 mbar necessary for return to the surface gas building, and recycling through the purifier. A regulator valve, in parallel with the pump, controls the compressor input pressure to between -5 and -10 mbar. This under pressure will allow to lift the gas the 20 meters to Plug level whilst maintaining the module gas pressure at 1 mbar. In case of power failure or during a long shutdown, a back-up cylinder will provide gas to compensate for fluctuations in atmospheric pressure. A layout showing the gas circulation racks and modifications to the pipework are seen in Fig. 6.7.

Each of the two sections is then split, in the cavern UX25, into 9 segments. Each of these segments will be equipped with a differential flow measurement, and then split into 5 subsegments feeding the chambers of each height zone. These 5 subsegments will be equipped with manual flow regulator and on-off switch. Each individual gas segment can be separately disconnected, if necessary, and connected to a local purge system using flexible pipes and self-sealing couplings. The location of the distribution racks can be seen in Fig. 6.8.

A projected layout of the gas pipes around the detector can be seen in Fig 6.9. Each segment supplies gas to 5 modules, which are connected in parallel along the length of the Space Frame. Pipe diameters are sized to ensure that each module will have the same gas flow.

6.3.3 Distribution Pipework

All tubes and fittings within the systems will be made of stainless steel. Existing pipes at point 2 will be re-used as far as possible. Table 6.3 shows an overall view of the main piping parameters. The tubes (at the shielding plug end) will be modified to link up with the new position of the distribution rack. In the experimental cavern (UX25) they will be extended into the ALICE solenoid magnet and up to the detector modules. A flow sheet indicating the pipe allocations for the TOF detector can be seen in Fig. 6.9.

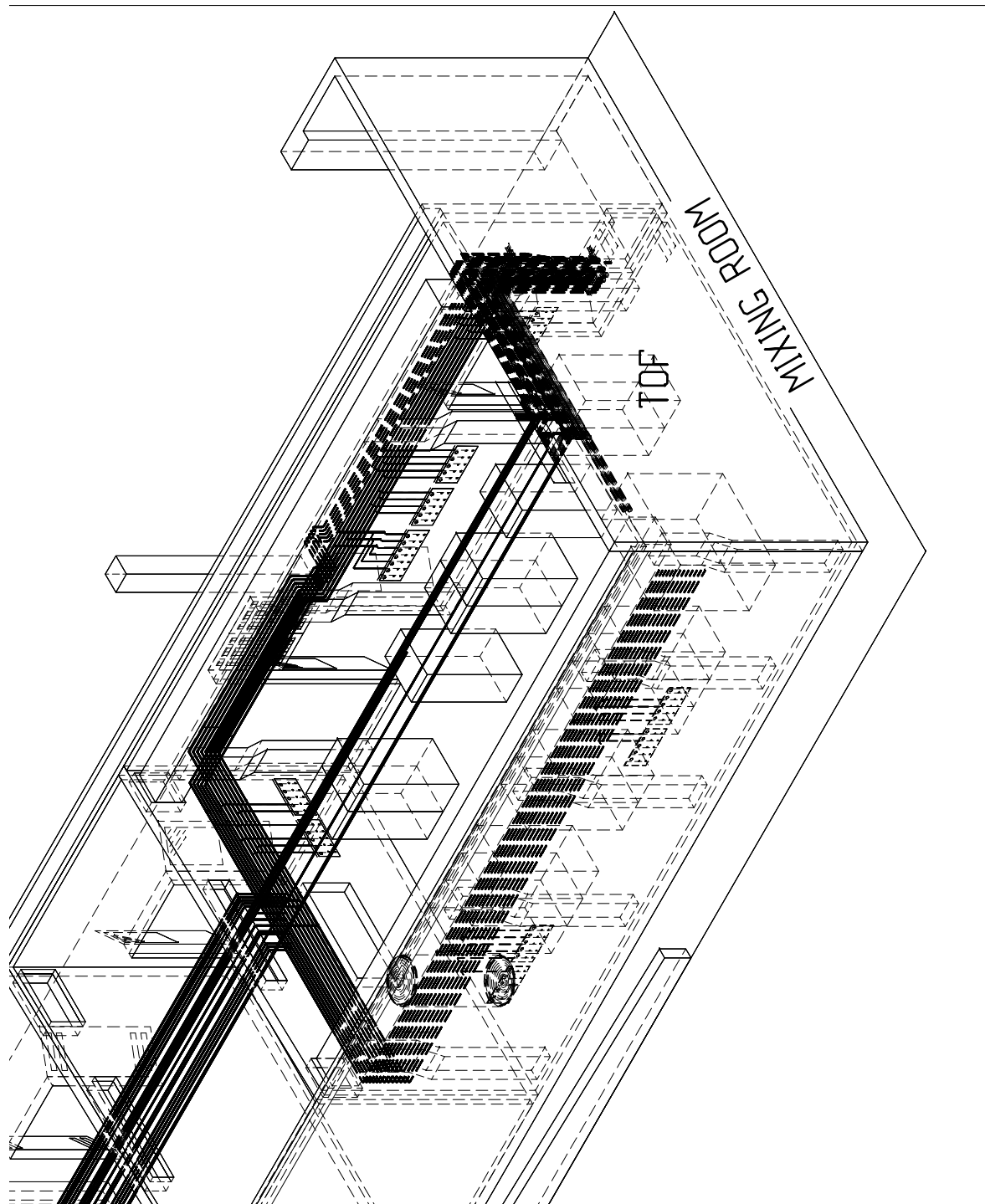


Figure 6.6: Layout of the gas mixing room.

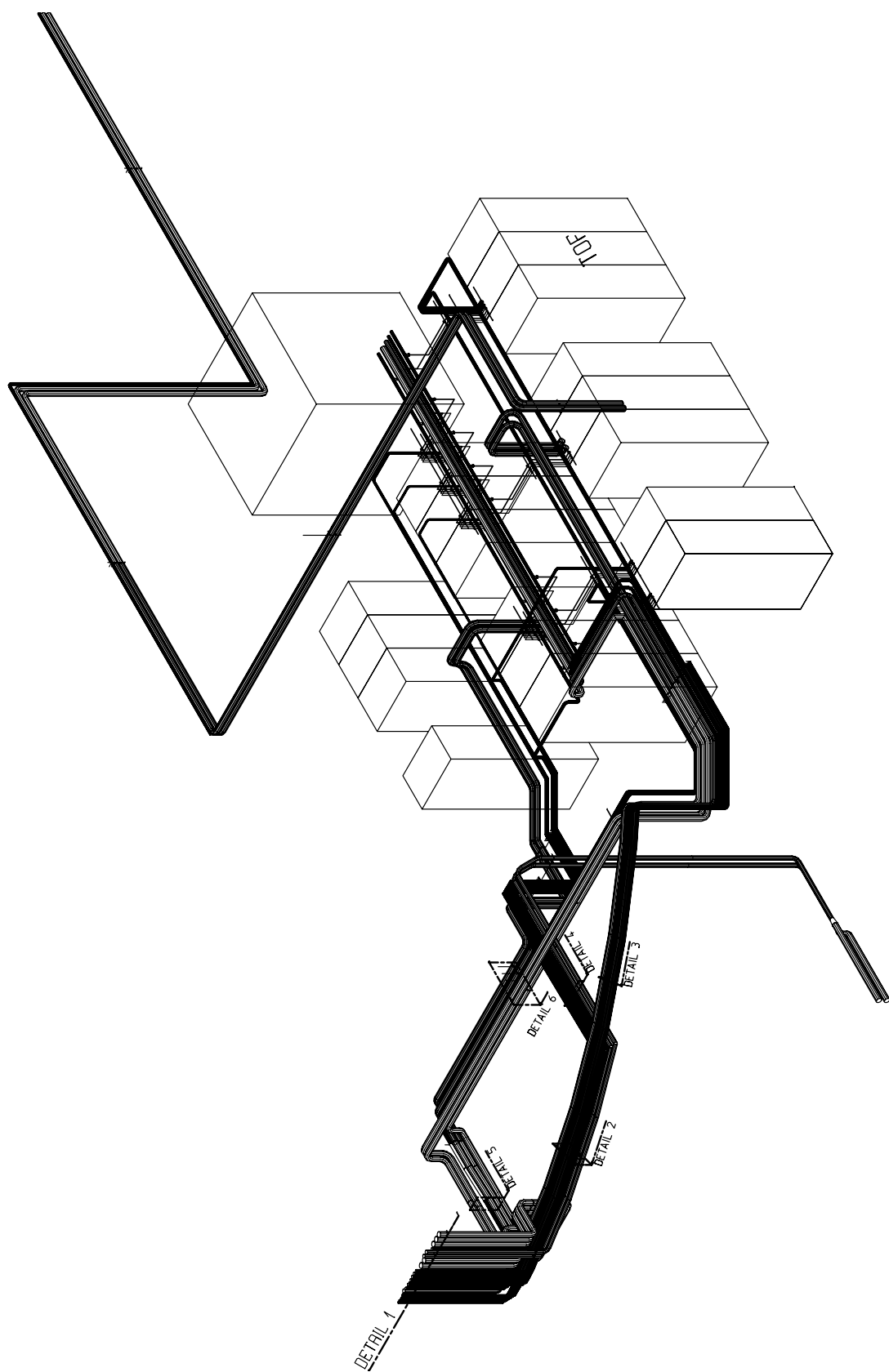


Figure 6.7: Layout of the gas circulation racks on the Plug (PX 24).

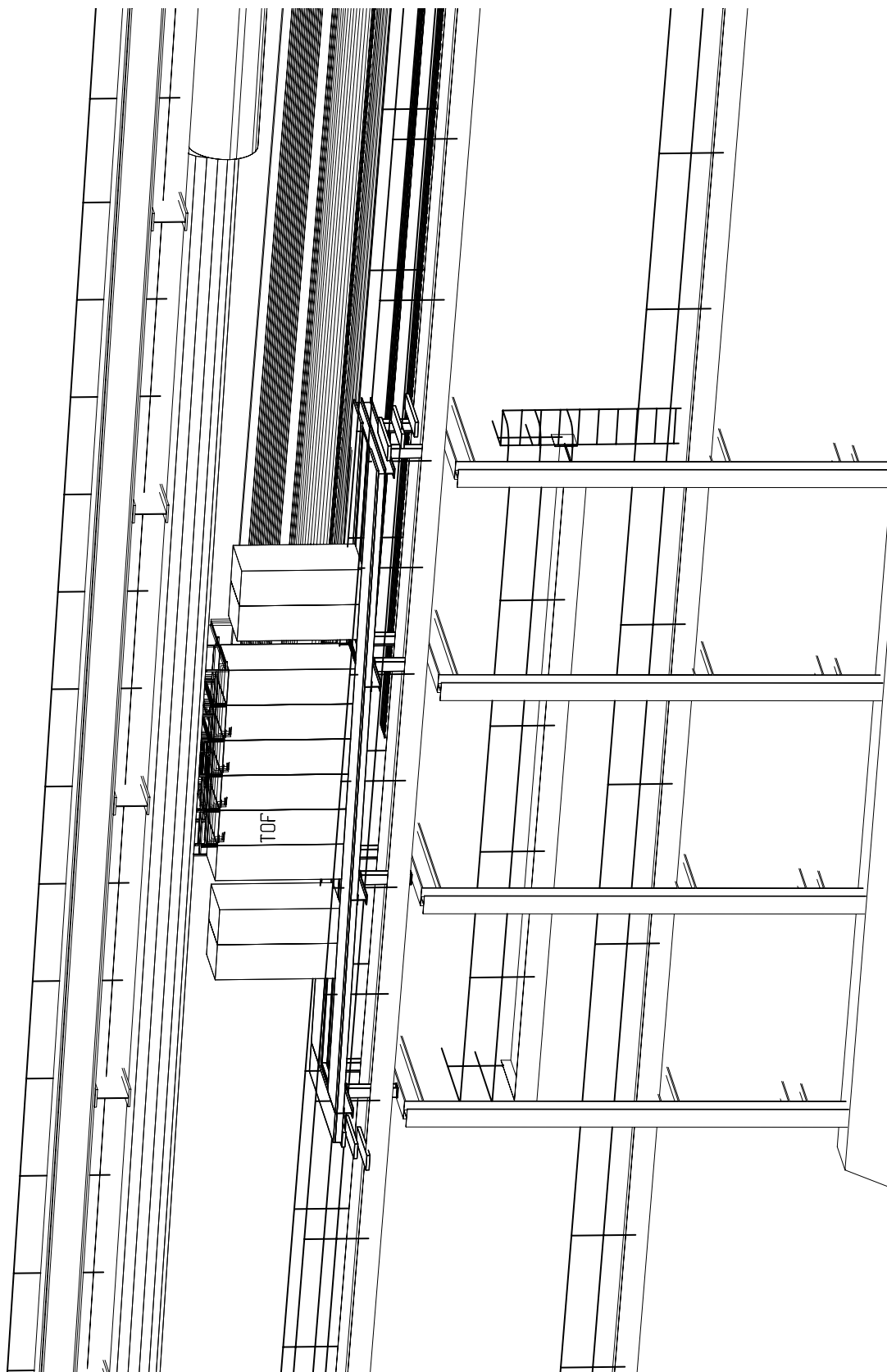


Figure 6.8: Location for the gas distribution racks in the UX25 cavern.

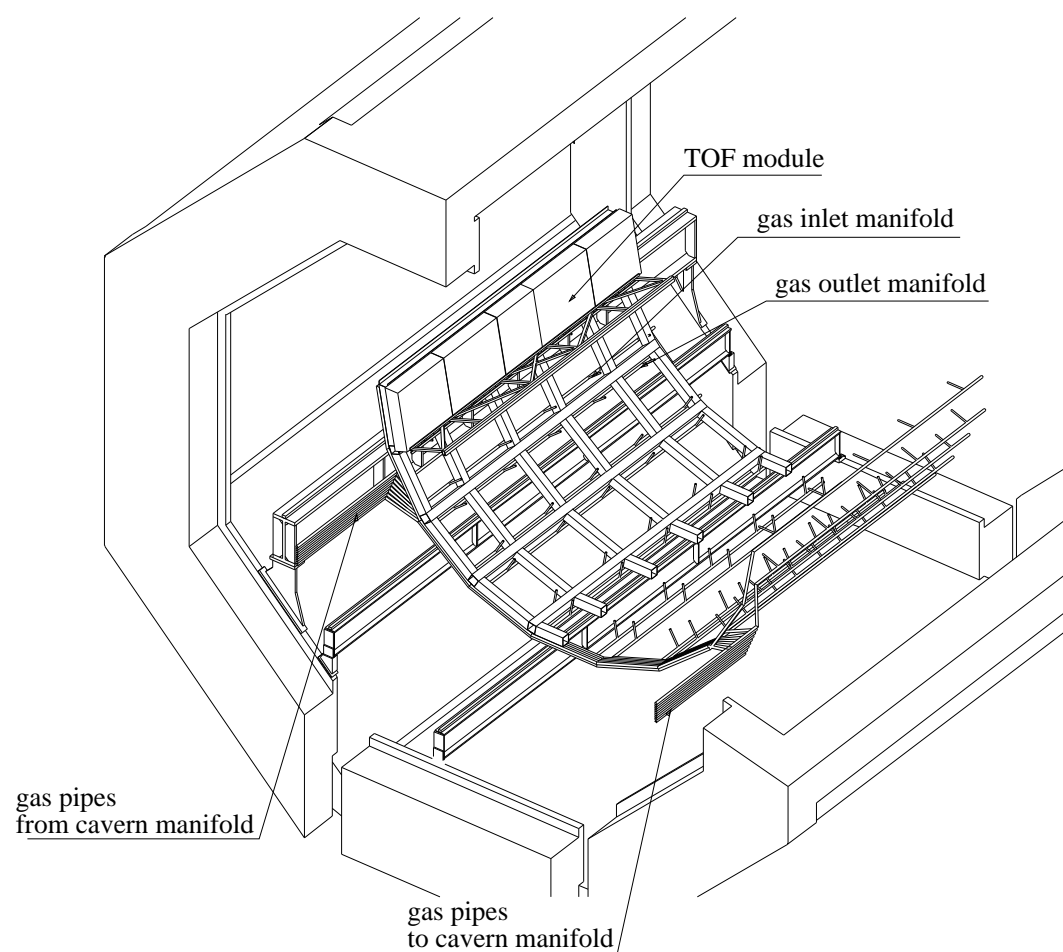


Figure 6.9: Layout of gas pipes around the detector.

Table 6.3: Main piping parameters. Max. flow includes a safety factor of 3.

	N ⁰ of pipes	Length (m)	Inner Pipe Dia (mm)	Max. Flow (m ³ /h)	Pressure Drop (mbar)
SGX-Plug	1	90	33	8.00	9.30
Plug-Cavern	2	100	26	4.00	9.50
Cavern-Detector	18	30	14	0.44	0.80
Detector-Cavern	18	30	14	0.44	0.80
Cavern-Plug	2	100	26	4.00	9.50
Plug-SGX	1	90	33	8.00	9.30

6.4 Space requirements

The construction and test of the ALICE TOF MRPCs and modules will require adequate space both at CERN and Bologna. Certain areas should be equipped with a clean room. In Bologna the required areas are already available and being prepared, at CERN a clean room is under construction in building 167. Table 6.4 and Table 6.5 summarise the space requirements.

Table 6.4: Space required for construction/test - Bologna.

Type of space required	Space needed m ²
Glass and pads cleaning	40
Clean room Class 100000 for strip assembly and strip storage	130
Clean room Class 100000 for module assembly strip test area (2 stations)	60
Storage area	80
Electronic and DAQ test laboratory	60-80
	60

Table 6.5: Space required for construction/test - CERN.

Type of space required	Space needed m ²
Glass and pads cleaning	40
Clean room Class 100000 for strip assembly, strip storage and module assembly/repair	60
strip/module test area	120
Storage area and last minute tests	100
Electronic and DAQ test laboratory	60

7 Schedule, costs and responsibilities

7.1 Schedule and milestones

Figure 7.1 shows the foreseen design, production and test schedule for the TOF components. The installation schedule, not presented, will be subdivided into several periods between autumn 2005 and summer 2006 and will be discussed in details with the Collaboration. Table 7.1 shows a list of the milestones of the Project.

7.2 Budget

The expected budget for the TOF detector is shown in Table 7.2.

7.3 Responsibilities

The Bologna - Salerno group is fully responsible for the design, construction and commissioning of the TOF detector of ALICE.

At present two other groups are interested in this project. The group from ITEP Moscow (Russia) is presently participating in the strip construction and tests, in electronics development and Monte Carlo simulation. The group from the Department of Physics, Kangnung National University (Korea) is presently involved in ageing tests of the MRPCs at the 2 GeV electron linac at the Pohang Accelerator Laboratory (Korea). Discussions are underway to define the terms of a possible future collaboration.

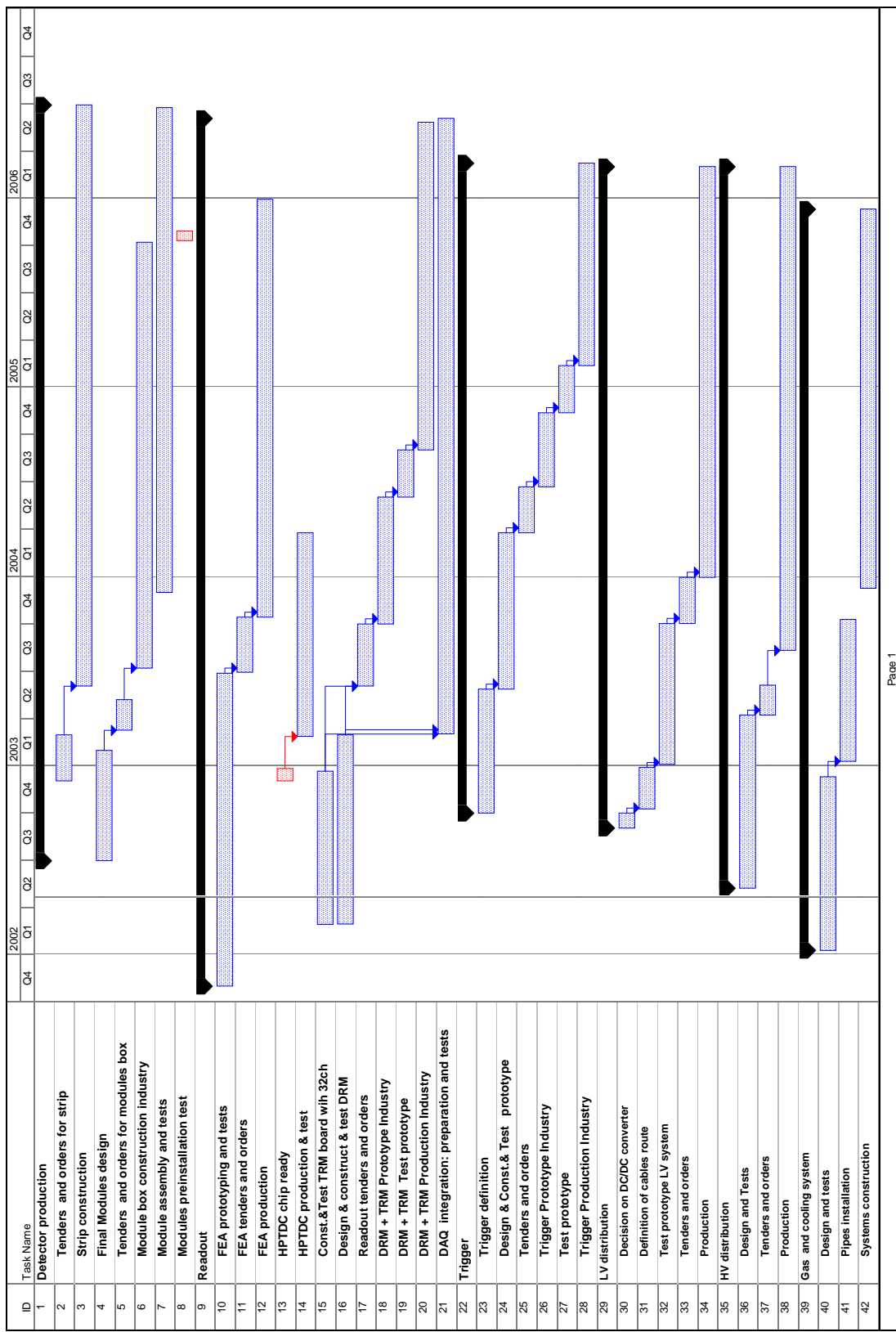


Figure 7.1: The TOF schedule.

Table 7.1: TOF milestones.

Item	Milestone
Strip construction	
Start strip construction	June 2003
30% strip construction	June 2004
100% strip construction	June 2006
Module construction	
Module 0 : results of test	June 2003
Start module assembly	December 2003
Start module cosmics test	June 2004
30% module assembly	December 2004
Module installation test	June 2005
100% module construction	June 2006
Electronics	
FEA final results of test	June 2003
FEA 100% production	December 2005
HPTDC 100% production	March 2004
Readout TRM + DRM final results of test	June 2003
TRM and DRM preproduction: results of test	March 2004
TRM and DRM 100% production	April 2006
DAQ	
DDL data transmission: results of tests	June 2004
ALICE DAQ integration	June 2006
Trigger	
Trigger prototype: results of test	March 2004
Trigger 100% production	March 2006
Services	
LV scheme decision	December 2002
LV system prototype : results of test	September 2003
LV system commissioning	March 2006
HV system prototype : results of test	June 2003
HV system commissioning	March 2006
Gas system definition	December 2002
Gas system commissioning	December 2005
Cooling system definition	December 2002
Cooling system: results of test	June 2003
Cooling system commissioning	December 2005

Table 7.2: TOF budget (assuming that 1 EURO = 1.45 CHF).

Item	Cost in KEURO	Cost in KCHF
MRPC strips construction	808	1172
Modules construction and tools	2503	3629
FE Electronics	2194	3181
Readout electronics	4133	5993
Trigger,DCS,DAQ connections	216	313
LV system	661	959
HV system	210	304
Gas system	250	362
Cables and connectors	982	1424
Total cost	11957	17337

References

Chapter 1

- [1] ALICE Collaboration, Time of Flight System, Technical Design Report, CERN/LHCC 2000-12
ALICE TDR 8, 16 February 2000.

Chapter 2

- [1] E. Cerron Zeballos, I. Crotty, D. Hatzifotiadou, J. Lamas Valverde, S. Neupane, M.C.S. Williams and A. Zichichi, Nucl. Instr. Meth. **A374** (1996) 132.
- [2] ALICE Collaboration, Time of Flight System, Technical Design Report, CERN/LHCC 2000-012
ALICE TDR 8, 16 February 2000.
- [3] E. Cerron Zeballos, I. Crotty, D. Hatzifotiadou, J. Lamas Valverde, M.C.S. Williams, A. Zichichi, Nucl. Instrum. Meth. **A396** (1997) 93-102.
- [4] W. Riegler, R. Veenhof, C. Lippmann, *Simulation of Resistive Plate Chambers*, CERN preprint in preparation.
- [5] I. Smirnov, *HEED, Program to Compute Energy Loss of Fast Particles in Gases*, Version 1.01
CERN W5060.
- [6] S. Biagi, Nucl. Instr. Meth. **A283** (1989) 716.
- [7] S. Biagi, Nucl. Instr. Meth. **A421** (1999) 234-240.
- [8] P. Camarri, R. Cardarelli, A. Di Caccio, R. Santonico, Nucl. Instrum. Meth. **A414** (1998) 317-324.
- [9] V. Radeka, Ann. Rev. Nucl. Part. Sci. **38** (1988) 217-77.
- [10] MAXWELL 3D field simulator, Version 8, Ansoft Corporation, 2001.
- [11] M.C.S. Williams, Nucl. Instr. Meth. **A 478** (2002) 183-186.
- [12] A. Akindinov *et al.*, *A Study of the Multigap RPC at the Gamma Irradiation Facility at CERN*, accepted for publication by Nucl. Instr. Meth. A. (April 2002).
- [13] A. Agosteo *et al.*, Nucl. Instr. Meth. **A452** (2000) 94.

Chapter 3

- [1] The ALICE space frame optimizaation, D. Perini ALICE-PR-2002-02 v.1.
- [2] C. Gavazzi Space SpA, document ALICE-RP-CGS-001, March 2002.
- [3] AMS Collaboration, D. Alvisi *et al.* Nucl.Instrum.Meth.A437:212-221,1999.

Chapter 4

- [1] M. Mota and J. Christiansen, IEEE journal of solid-state circuits, **34** (1999) 1360.
J. Christiansen, High Performance General Purpose TDC Specification, Version 0.5, June 2000,
available online at http://micdigital.web.cern.ch/micdigital/hptdc/hptdc_manual.pdf
J. Christiansen, HPTDC High Performance Time to Digital Converter, Version 2.0 for HPTDC
Version 1.1, September 2001, available online at
http://micdigital.web.cern.ch/micdigital/hptdc/hptdc_manual_ver2.0.pdf
- [2] M. Mota, HPTDC Test Report - v.1, available online at
http://micdigital.web.cern.ch/micdigital/hptdc/hptdc_test.pdf

- [3] ALICE Central Trigger Processor, User Requirement Document, Draft 1.0, October 2001.
- [4] J. Christiansen, private communication, March 2002.
- [5] B.G. Taylor, see <http://ttc.web.cern.ch/TTC/intro.html>
- [6] ALICE T0 based on Cherenkov counters: R&D principle result, ALICE-INT-2001-38 V 1.0.
- [7] G. Stefanini, ALICE document ALICE-PR-2001-64 v.1.

Chapter 5

- [1] ALICE Collaboration, Time of Flight System, Technical Design Report, CERN/LHCC 2000-12 ALICE TDR 8, 16 February 2000;
- [2] ALICE Collaboration, Answers to the Questions of the LHCC Referees, CERN/ALICE, 5 May 2000;
- [3] <http://www.cern.ch/ALICE/Projects/offline/aliroot/Welcome.html>;
- [4] R. Brun *et al.*, <http://root.cern.ch>;
- [5] T. Sjöstrand, Comp. Phys. Commun. **39** (1986) 347.
- [6] H.-U. Bengtsson and T. Sjöstrand, Comp. Phys. Commun. **46** (1987) 43.
- [7] X. N. Wang and M. Gyulassy, Phys. Rev. **D44**(1991) 3501;
X. N. Wang and M. Gyulassy, Phys. Rev. **D45** (1992) 844;
X. N. Wang and M. Gyulassy, Comp. Phys. Comm. **83**(1994) 307.
- [8] F. Antinori, Internal Note ALICE/SIM 93-9, 1993;
N. van Eijndhoven *et al.*, Internal Note ALICE 95-32.
- [9] ALICE Collaboration, ALICE Technical Proposal, CERN/LHCC 95-71, LHCC/P3, 15 December 1995.
- [10] A. Morsch, <http://home.cern.ch/morsch/AliGenerator/AliGenerator.html>
and <http://home.cern.ch/morsch/generator.html>;
- [11] K. Adcox *et al.*, PHENIX Collaboration, arXiv:nucl-ex/0112006 17 December 2001, submitted to Phys. Rev. Lett.;
- [12] ALICE Collaboration, Time Projection Chamber, Technical Design Report, CERN/LHCC 2000-001 ALICE TDR 7, 7 January 2000;
- [13] ALICE Collaboration, Inner Tracking System, Technical Design Report, CERN/LHCC 99-12 ALICE TDR 4, 18 June 1999;
- [14] ALICE Collaboration, Transition Radiation Detector, Technical Design Report, CERN/LHCC 2001-021 ALICE TDR 9, 3 October 2001;
- [15] J. Belikov, Private Communication, September 2001;
- [16] see Fig. 11.11 in N. Ahmad *et al.*, ALICE Technical Proposal, CERN/LHCC 95-71, LHCC/P3, 15 December 1995;
- [17] see Fig. 11.13 in N. Ahmad *et al.*, ALICE Technical Proposal, CERN/LHCC 95-71, LHCC/P3, 15 December 1995;
- [18] see Table 2 in D. Di Bari, D. Elia, E. Nappi, G. Paić, Internal Note ALICE/RICH 97-39, 1997;
- [19] D. Vicinanza, *Ultrarelativistic heavy-ion physics with the ALICE TOF detector*, PhD Thesis, University of Salerno, 2002;
- [20] S. Kiselev, G. Paić, J. Schukraft, A. Smirnitsky and B. Zagreev, Internal Note ALICE/SIM 97-09, 1997;
- [21] S. Kiselev, G. Paić, J. Schukraft, A. Smirnitsky and B. Zagreev, Internal Note ALICE/SIM 96-17, 1996;
- [22] M. Basile *et al.*, Nucl. Instrum. Meth. **179**(1981) 477;
- [23] A.G. Frodesen, O. Skjeggestad and H. Tøfte, *Probability and Statistics in Particle Physics*, UNIVERSITETSFORLAGET, 1979;
- [24] MONARC Phase 2 - CERN/LCB 2000-001 March 2000
and <http://monarc.web.cern.ch/MONARC/docs/phase2report/Phase2Report.pdf>;

- [25] I. Foster and C. Kellerman, The GRID, Blueprint for a New Computing Infrastructure ISBN1-55860-475-8;
- [26] Grid Computing, The European DataGrid Project, Proc. IEEE 2000 Nuclear Science Symposium and Medical Imaging Conference, Lyon, 15-20 October 2000;
- [27] Report of the Steering Group of the LHC Computing Review, CERN/LHCC/2001-004
CERN-RDB-D2001-3-22-Feb-2001;
- [28] <http://www.bo.infn.it/alice/introgrd/introgrdnew.html>,
in particular: http://www.bo.infn.it/alice/introgrd/node5_ct.html.

Chapter 6

- [1] A. Akindinov *et al.*, *A study of the Multigap RPC at the Gamma Irradiation Facility at CERN*, accepted for publication by Nucl. Instr. Meth. A. (April 2002).
- [2] ALICE Collaboration, Time of Flight System, Technical Design Report, CERN/LHCC 2000-012
ALICE TDR 8, 16 February 2000.

